TEL AVIV UNIVERSITY

RAYMOND AND BEVERLY SACKLER

FACULTY OF EXACT SCIENCES

SCHOOL OF PHYSICS & ASTRONOMY

<div dir="rtl">

אוניברסיטת תל אביב

הפקולטה למדעים מדוייקים

ע"ש ריימונד ובברלי סאקלר

בית הספר לפיסיקה ואסטרונומיה

</div>

Quantum pumping in mesoscopic systems

by

Vyacheslavs Kashcheyevs

Thesis submitted towards

the degree of *Doctor of Philosophy*

This work has been carried out under the supervision of

Professor Amnon Aharony and **Professor Ora Entin-Wohlman**

Submitted to the Senate of Tel Aviv University

November 2006

TO   ZAĶIKI

Acknowledgements

Doctoral studies necessarily involve a certain kind of discipleship. My supervisors, professor Amnon Aharony and professor Ora Entin-Wohlman, have been outstanding mentors both in teaching me physics and in providing a superb model of academic excellence. Their focus on critical thinking, independence and pursuit of physical meaning has in many ways defined the physicist in me. Besides physics, I thank warmly my supervisors for their personal support, patience and wise leadership.

I am very grateful to my personal friends-physicists who have added much to my understanding of the subject: Dima Docenko, Adi Shafir, and Jo Smiseth. Numerous discussions with Tomosuke Aono, Andris Guļāns, Adam Németh, Eran Sela, Yaroslav Tserkovnyak and Mikhail Zvonarev have given me valuable lessons and always remain nice occasions to remember. Same is true for the educating discussions with my senior colleagues: professors Ikhiel Kornblit, Yuval Gefen and Jürgen König. I am particularly indebt to professor Avraham Schiller, whose immediate enthusiasm and support for my immature ideas has been crucial in materializing the sixth chapter of the thesis.

And my deepest gratitude, far beyond what words can say, goes to my wife Sanita whose unconditional love and understanding have made all of this possible.

Abstract

The doctoral thesis explores various aspects of electron dynamics in small coherent quantum systems focusing on adiabatic pumping of electrons, conditions for pumped charge quantization, and the role of local Coulomb interactions in single- and multi-level transport. The main body of the work is divided into four chapters that correspond to three published research articles and the one most recently submitted for publication.

Periodic modulation of the external potential acting on a phase coherent electron system can result in charge redistribution between the remote reservoirs which are held at equal chemical potentials. This phenomenon is called quantum pumping, and it is known to be enhanced in systems that support resonant transmission. Under certain conditions, almost integer number of electrons on average can be pumped adiabatically through a resonant system. We explain the mechanism behind this quantization as loading and unloading of elementary charges onto instantaneous quasi-bound energy states. The role of quantum interference in this type of quantization is shown to be restricted to the formation of discrete energy states. It is shown that if the linear conductance of the system remains low throughout the cycle, with a possible exception of distinct resonant peaks, then the total charge transferred per period can be approximately calculated as a sum of individual peak contributions (the resonance approximation).

We explore in details the implications of the resonance approximation for a simple tight-binding model of surface acoustic wave-induced transport in ballistic quasi-1D quantum wires. The influence of experimentally controllable parameters (acoustic wave power, gate voltage, source-drain bias, amplitude and phase of a counter-propagating wave) on the plateau-like structure of the acoustoelectric current is studied. The use of resonance approximation facilitates identification of the relevant model parameters. The results are found to be in good qualitative agreement with existing experimental observations. However, the approximation of spinless non-interacting electrons fails to match the characteristic energy scale of the problem, which can be attributed to the charging energy of a dynamically formed quantum dot.

In order to extend the tools for calculating the dynamical quantities in the relevant models beyond the single-particle approximation, a powerful analytical technique, namely, self-consistent truncation of the equations-of-motion (EOM), is investigated in depth. The

one-particle Green function of a single localized orbital is considered. The physical spin of the electrons and a strong on-site Coulomb repulsion between the opposite spin species is taken into account. We study the EOM hierarchy generated for this Green function by self-consistently decoupling the hierarchy at high order. Exact analytic solutions of the resulting coupled integral equations are presented in several limits. In particular, it is found that at the particle-hole symmetric point the EOM method breaks down due to a discontinuous change in the imaginary part of the interaction-induced self-energy. Away for this special point, the solution for the Green function remains physical.

We benchmark the solution of the truncated EOM hierarchy using a set of known exact results for the Anderson impurity model. Quantities calculated explicitly in the limit of infinite on-site repulsion include the occupation numbers, the density of states, and the local spin susceptibility. The latter is a sensitive test for proper description of interaction-induced correlations, because the spin susceptibility of the Anderson impurity in the single-occupancy regime should saturate at low temperatures due to Kondo screening effect. The self-consistent approximation to EOM is found to be very accurate for quantities related to *charge* dynamics (e.g., the gate voltage dependence of the accumulated charge). In contrast, the description of the Kondo effect (which is caused by dynamical screening of *spin* fluctuations) is valid on a qualitative level only. We show that the widely used simplified version of the EOM method, which does not account fully for the correlations on the network, fails to produce the Kondo correlations even qualitatively.

In the final chapter of the thesis, we consider a two-level model for a quantum dot coupled to two leads. The model features arbitrary tunnelling matrix elements among the two levels and the leads and between the levels themselves (including the effect of Aharonov-Bohm fluxes), as well as inter-level repulsive interactions. A special case — each level coupled to its own lead plus tunnelling between the levels — corresponds to the two-site version of the model for quasi-1D channels studied in the absence of many-body interactions in an earlier chapter. We show that this two-level model is exactly mapped onto a generalized Anderson model of a single impurity, where the electrons acquire a pseudo-spin degree of freedom, which is conserved by the tunnelling but not within the dot. Focusing on the single-occupancy regime, we show that the effective low-energy Hamiltonian is that of the anisotropic Kondo model in the presence of a tilted magnetic field. For moderate values of the (renormalized) field, the Bethe ansatz solution of the isotropic Kondo model

allows us to derive accurate expressions for the dot occupation numbers, and henceforth its zero-temperature transmission. These formulae cover a large variety of phenomena that have been previously considered in the literature in different limits: charge oscillations and population switching, transmission-phase lapses and correlation-induced resonances. We discuss numerous implications for these phenomena, and emphasize their common physical origin.

Contents

Chapter 1

General introduction

We begin by defining and explaining the two key concepts announced in the title. These two concepts are *mesoscopic systems* and *quantum pumping*, and they are discussed in Secs. 1.1 and 1.2 respectively. Sec. 1.2 is the key part of this general introduction as it describes the context and the general direction of the research reported in the thesis. Mini-reviews for the literature on the main topics brought together in this work are given within the corresponding subsections of Sec. 1.2.

1.1 Mesoscopic systems with flexible design and control

The term 'mesoscopic' has been traditionally applied ([1], Chapter 1.1) to condensed matter systems in which the correlation length for the dynamics of the system constituents is comparable to the sample size. Here we will be interested almost exclusively in electronic properties of solid state systems at low temperatures, and the corresponding correlation length can be defined as the distance L_ϕ over which the charge carriers (electrons) maintain their quantum-mechanical phase. On the conceptual level, a system is mesoscopic if it is sufficiently small to behave "quantum-mechanically". Apparently, the answer to the question whether a given system is mesoscopic or not depends on the external parameters (most notably the temperature) and on the way the quantum mechanical properties are probed. A very good introduction to defining and measuring quantum coherency in solid state devices can be found in [1].

Over the history of mesoscopic physics there has been a shift of emphasis from systems with statistically defined properties (such as disordered metals or microgranular composites) towards individually engineered samples (such as quantum wires, rings and dots). It is this latter type of systems, namely, nanostructures with specifically engineered and controlled electronic properties, that the present work addresses. Thus the term "mesoscopic system" in the title refers more to a quantum dot and less to a piece of a dirty metal.

As for a typical experimental realization, we mention just one (but, perhaps, the most versatile and well-developed) platform, namely, the mesoscopic structures formed in a two dimensional electrons gas (2DEG). A great number of detailed reviews of this technique are available, e.g., in Refs. [1, 2, 3]; the basic idea is explained below.

2DEG can be formed on the interface between two semiconductors, typically GaAs and AlGaAs. The mismatch in the electronic properties of the two materials generates a potential well for the mobile electrons in the direction perpendicular to the interface plane. For a sufficiently small electron concentration and at low temperatures, only the lowest level in that potential well is occupied and the electron motion in the transverse direction drops out completely from the dynamical (i.e., Schrödinger) equation. Elaborate crystal growing techniques, such as molecular beam epitaxy, allow for the preparation of 2DEGs with exceptionally high carrier mobilities, corresponding to mean free paths for the in-plane electron motion of several micrometers [3]. Even without further structuring, a 2DEG is an important mesoscopic system in which such effects as localization and the quantum Hall effect (just to name a few) are actively studied (see, e.g. Refs. [3, 4, 5]).

Additional potential barriers in the plane of a 2DEG can be used to restrict the electron motion furthermore, and thus to make what can be called a nanostructure. A common tool for building these extra barriers is the split-gate technique. Narrow metallic gates are formed on the surface of the GaAs/AlGaAs heterostructure using certain fine resolution lithographic techniques (e.g., electron beam lithography). Selectively applying negative voltages to these gates results in potential barriers for the in-plane motion of the electrons. In such a way the electrons can be confined to one (quantum wire) or zero (quantum dot) dimensions. A typical experimental setup for a split-gate formed quantum dot is shown in Fig. 1.1. Lithographically defined quantum dots and channels have been used in the majority of the experimental studies that are cited in the research papers constituting Chapters 3–6.
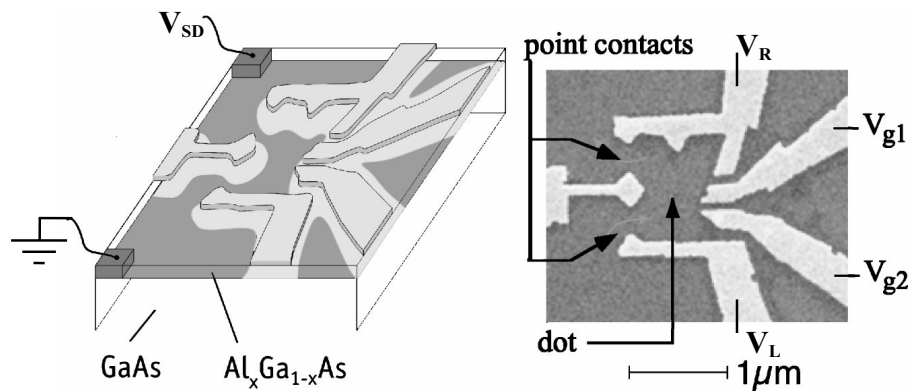
Figure 1.1: Example of a lithographically defined quantum dot [6]. On the right is a scanning electron micrograph of the dot (top view), and on the left is a schematic drawing of the device. Electrons are trapped vertically in the interface of a GaAs/AlGaAs heterostructure, and form a 2D electron gas (darker area). Their lateral confinement to the dot region is achieved by applying a negative voltage to the top metal gate (lighter shade), depleting the electrons underneath. The dot is coupled to two leads (source and drain) through point contacts. Two gate voltages V_{g1} and V_{g2} can be varied to change the number of electrons confined in the dot, and the entrance and exit barriers are tuned by the voltages V_L and V_R. This illustration is taken from Ref. [2].

1.2 Charge pumping in mesoscopic systems: main challenges and overview of the literature

This section first defines the scope and the motivation for the research presented in the thesis, and then gives an overview of the relevant developments in the field.

The term 'pumping' in the context of charge transport can be understood in a variety of ways. In the broadest sense, pumping is any charge redistribution between the terminals of an extended system that is caused by a periodic variation of an external potential. Even an ordinary ac-to-dc transformer[1] falls into the category of pumping devices in this sense. However, in classical systems for which the usual *local* ac voltage, current and conductivity definitions can be applied, the ac-to-dc conversion is usually called rectification.

Crossing into the mesoscopic domain, the wave nature of electrons becomes important. The phase breaking inelastic processes that are crucial for the establishment of a local electrochemical potential no longer take place at a sufficient rate on the lengthscale of the sample size. As a consequence, the effect of a locally applied external perturbation can no longer be described as a simple rectification, and new routes for understanding and calculating the electrical response of the mesoscopic systems become necessary.

In a broad perspective, the majority of these new routes follow two main roads defined by the cases in which quantum effects are relatively easy to incorporate into a theory. The first road is the case of a system in which (a) the electron-electron Coulomb interaction is well-screened, and (b) the electron motion is coherent. The single-particle approximation is adequate in this case, and a set of flexible tools from one-body quantum mechanics becomes applicable. The most important concept in this approach is the description of transport as scattering [7]. We discuss the recent developments in quantum pumping theory within the single-particle approximation in Sec. 1.2.1.

The second case in which much progress can be done is an almost isolated system. If one takes a finite system and neglects coupling to the external world altogether, the electron number and energy inside the sample are described by well-defined discrete observables. One can expect that switching on a weak link to the outside world (e.g., tunnelling into contacts) does not destroy these quantum numbers immediately. Therefore, a perturbative approach

---

[1]For example, the ac adaptor that powers the computer on which this text is typed.

can be built for describing the fluctuations brought about by the external coupling. This way of looking at the system can be very fruitful in a certain range of parameters, most notably in describing the Coulomb blockade phenomenon [8, 9]. We review the Coulomb blockade and its relation to pumping in Sec. 1.2.2 below.

The most important practical application of pumping would be the development of a current standard based on pumped charge quantization. If the number of electrons that are transported between the two terminals can be made sufficiently close to an integer, then the value of the resulting dc current could be tied to the elementary charge and the driving frequency only. This is a very desirable but still unattained goal in the field of metrology [10].

Both of the main approaches mentioned above (the scattering theory, Sec. 1.2.1, and Coulomb-blockade-type approaches, Sec. 1.2.2) have addressed the feasibility and the degree of pumped charge quantization. The relevant results and open questions are reviewed in Sec. 1.2.3.

As we shall see in Chapters 3 and 4, a necessary condition for an accurate charge quantization is to have the number of electrons in the device *at equilibrium* to be as close to an integer as possible. This requirement has directed the research towards understanding the systems in which both the charging energy *and* the single-particle level spacing are large. A prototypical example of such a system is a sufficiently small quantum dot, because both energy scales grow with decreasing the spatial size. So the papers in the second part of the thesis (namely, Chapters 5 and 6) explore the methods of describing quantum dots with a small number of relevant discrete orbitals but a large charging energy. The latter comes from the short-range part of the Coulomb interaction which is explicitly taken into account in the system's Hamiltonian. (See Sec. 1.2.4 for a more detailed discussion of the models involved.)

The need for a flexible theoretical method that properly incorporates both quantum fluctuations and many-body interaction effects for systems with localized degrees of freedom is by no means confined to the pumping problem. On quite a general level, the quest for such theoretical methods has been an active field for more than four decades, ever since the introduction of the Anderson impurity model [11] in 1961. We review briefly the broad spectrum of theoretical methods accumulated in this field in Sec. 1.2.4. To a large extent the goal of the second part of the thesis is to pick and sharpen those techniques that are suitable for the description of transport properties of small quantum dots.

1.2.1 Pumping due to interference

Two important papers [12, 13], published with an interval of several months in 1998/99, have addressed the question of pumping in mesoscopic systems with negligible two-body electron-electron interactions. The physical insight of [12] and the calculational framework of [13] (being based on an earlier work [14]) have paved the way for a surge in the research activity related to quantum pumping in mesoscopic systems.

The paper by Zhou, Spivak and Altshuler [12] has for the first time directly related the physics of conventional mesoscopic effects (such as the universal conductance fluctuations [1]) and the pumping response. Their physical reasoning can be summarized as follows. In a phase coherent metallic system, coupled to reservoirs held at the same equilibrium chemical potentials, the local distribution of charge is determined by standing electronic waves (eigenmodes of the Hamiltonian). As a result, this distribution is very sensitive to changes in the potential landscape which confines the electrons. If this landscape is changed by an external perturbation sufficiently slowly, the electronic distribution will follow adiabatically the instantaneous configuration of the total confining potential. As a result, the charge within the system will be re-distributed, and a non-zero charge transfer between the external reservoirs becomes possible.

The paper by Brouwer [13] essentially addresses the same question — adiabatic pumping response of a phase coherent system, with a chaotic quantum dot as a potential physical realization. The most significant result of [13] has been a formula relating the total charge Q pumped through the system during a single cycle of the modulating potential to a certain contour integral over the derivatives of the scattering matrix. This Brouwer formula for the charge pumping is remarkable in the same way as the celebrated Landauer formula [15, 7] for the conductance – it relates the transport properties to the scattering matrix of the system.

A particularly suggestive result for Q is obtained by applying the Brouwer formula to a two terminal system with single mode leads [16, 17]:

$$Q = \frac{e}{2\pi} \oint \left[1 - \mathcal{T}(t)\right] \frac{d\alpha}{dt} \, dt \,, \tag{1.1}$$

where e is the electron charge, $\mathcal{T}$ is the transmission probability and α is the phase of the reflection amplitude; the integral is taken over one period of the external potential. An explicit dependence on the reflection phase may suggest that pumping in such a system is an intrinsically quantum effect with no simple interpretation in classical terms (e.g., see the

discussion in Refs. [12, 16, 18, 17, 19]).

More general scattering-based approaches have followed soon [17, 20]. Reference [17] develops a systematic expansion of the time-dependent scattering states and extends the results of Brouwer to include external dc bias voltage. The paper [20] addresses the role of adiabaticity and develops a general theory for a finite frequency response based on the Floquet scattering theory. This theory is related to an earlier work on photon-assisted tunnelling (see, e.g., the discussion in Chapter 9 of [21]).

With the help of these formalisms a host of pumping-related phenomena has been explored in recent years: mesoscopic fluctuations of the pumping current [16, 22], noise [23, 24], heat transfer and dissipation [24], symmetries with respect to magnetic field [22, 25, 26]. Several experiments have been conducted as well [25, 27, 28].

1.2.2 Pumping in Coulomb blockaded systems

An intuitively simple scheme for a charge pump capable of transferring electrons one by one can be derived from the concept of Coulomb blockade. This development has been mainly driven by the steady improvement of the experimental techniques in recent decades and pre-dates the discussion of pumping in mesoscopic systems outlined in the previous section.

The term 'Coulomb blockade' [2, 8, 29] is usually invoked when the electron transport is suppressed by the individual charging energy E_c necessary for the addition/removal of a single electron to/from the device (let it be a quantum dot for concreteness). A necessary condition is that the thermal energy[2] T will be low enough in order not to smear out the effect, $T \ll E_c$. The degree of electron confinement is regulated by the contacts to the quantum dot, which are usually quantum point contacts with high tunnelling barriers. The Coulomb blockade becomes *strong*, namely, the number N of confined electrons becomes well-defined, when not only the thermal but also the quantum fluctuations of the electron energy become smaller than E_c [8]. Quantitatively, requiring the energy uncertainty due to the finite RC time of the circuit to be smaller than E_c implies that the conductance of the contacts G_c should be less than the quantum unit of conductance, $G_c \ll e^2/(2\pi\hbar)$. Note that the quantum mechanical Planck constant appears in this condition.

---

[2]We use energetic units for temperature, $k_B \equiv 1$.

A typical energy diagram of a Coulomb blockaded quantum dot is shown in Fig. 1.2. The number of captured electrons corresponds to the highest energy state available below the chemical potential μ, $E_N < \mu < E_{N+1}$. The variation of the voltage V_g on the central gate shifts linearly the quantum dot's energy levels E_N and can be used to change N in discrete steps.

A simple pumping cycle employing periodic variations of the gate voltages coupled to a Coulomb blockaded quantum dot operates as follows (see Fig. 1.3). At the moment when the (equilibrium) number N of electrons on the dot increases by one, one of the barriers (left in Fig. 1.3B) is lowered so that the extra electron tunnels in predominantly from the left. During a later stage of the pumping cycle this additional charge must be released. At this time (Fig. 1.3D), the other barrier is lowered so that the quantum dot opens to the right. Such a quasi-static hopping picture ensures that electrons are transferred one per cycle, with small corrections due to various effects (co-tunnelling, insufficient isolation of the blocked side of the pump, non-adiabaticity etc. [30]).

Simple schemes of the type shown in Fig. 1.3 can nowadays be easily accessed in experiments with a lithographically defined quantum dot. The first successful work of this kind [31] has reported measurements of quantized current through a dot held under a constant source-drain bias, with only V_L and V_R oscillating at the pumping frequency with a well-defined phase difference. More refined schemes with several quantum dots connected in series can be implemented using small metallic islands [32, 33] as the tunnelling barrier heights need not be changed dynamically to achieve the pumping effect [30].

Several theoretical frameworks for a quantitative description of the Coulomb blockage have been formulated (see [8] and [9], also a general review [2]) and tested experimentally. The "orthodox" theory [8] is based on master equations for a ceratin tunnelling Hamiltonian with the charge on the dot described by a continuous collective variable. Alternatively, the theory of Beenakker [9] constructs a probability distribution of the individual level occupation numbers of an isolated dot. A master equation is then obtained by including lowest order tunnelling processes.

A common feature of these theories is that the correlations in the leads induced by tunnelling of individual electrons in and out of the dot are assumed to decay rapidly. On a formal level this assumption means that the density matrix of the leads is not affected by the presence of the dot and remains determined solely by the properties of the external
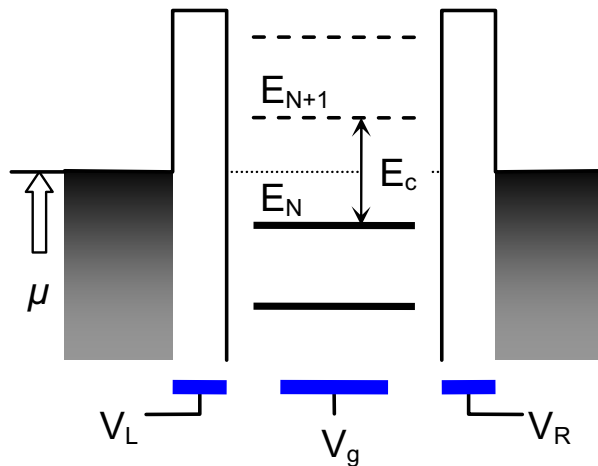
Figure 1.2: Energy diagram of a quantum dot in the Coulomb blockade regime. The typical charging energy $E_c = e^2/C$ is inversely proportional to the dot's capacitance C, and for sufficiently small devices defines the energy difference between the states of fixed electron number N. The number of electrons is controlled by the central gate voltage V_g, while the height of the entrance and the exit barriers depends on the voltages V_L and V_R on the respective gates (cf. Fig. 1.1).
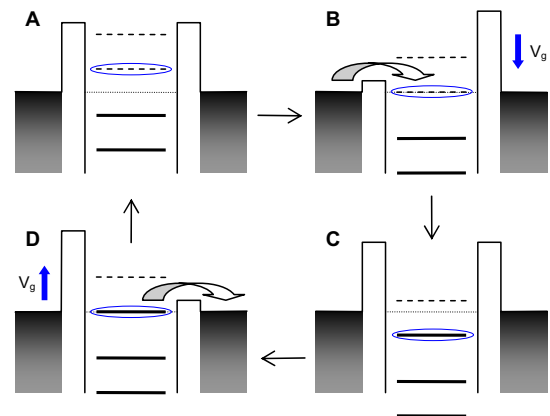

Figure 1.3: Pumping cycle for a device with discrete electronic states. The stages A, B, C, and D represent the energy diagram at consecutive times during one period.

reservoirs. While this "neglect of correlations in the leads" is well justified for temperatures larger than a typical inverse tunnelling rate Γ [9], quantum effects start to play an increasingly important role as the temperature is lowered below Γ. The transport through a Coulomb-blockaded device gets enhanced by co-tunnelling processes [34] which are the lowest order correlation corrections to the single-electron tunnelling probabilities. At even lower temperatures more subtle correlation effects [29] come into play. Systematic inclusion of co-tunnelling corrections into a theory of Coulomb-blockade-based charge pumps [35] improves the agreement for experiments with fixed tunnelling barriers [36], but remains a rather restrictive approach.

Another approach for building a single electron pump has been put forward in experimental studies of surface-acoustic-wave (SAW) driven quasi-one-dimensional channels [37, 38]. The original idea [37] has been to construct dynamically a moving quantum dot using the running electric potential profile induced by SAWs in the direction from the source to the drain. A qualitative explanation for the observed current quantization has been given in Ref. [37]. The reader will find a self-contained review of this work in the introduction to Chapter 4 (see page 36), where we explore an alternative approach [39] which does not require high tunnelling barriers at all stages of the cycle.

1.2.3   Pumped current quantization

An interesting perspective on charge pumping has been suggested in the work of Thouless [40]. He has posed the following question: *"If the potential* [that an electron system is subject to — VK] *is changed slowly in such a way that it returns to its starting value in time T, is the integrated current of electrons across a boundary quantized?"* Thouless has given a positive answer under certain special circumstances: an infinite system in a periodic potential, with the electronic bands filled, subject to an adiabatically varying potential in such a way that the excitation gap never closes. If the above conditions are satisfied, the net charge transferred per period is strictly an integer, and is dictated by topological arguments [40].

If an external periodic perturbation acts on a system *within a finite region* one might expect that such a precise pumped charge quantization becomes unattainable, similar to smearing of sharp thermodynamic phase transitions in finite-size systems. Indeed, soon

after the scattering approach to adiabatic pumping has been formulated (as discussed in Sec. 1.2.1 above), several equivalent geometrical formulations of the Brouwer formula have been investigated [41, 42]. Quite generally, as the system parameters are slowly varied due to external perturbations, the scattering matrix traces a ceratin contour in the corresponding abstract space of unitary matrices [41, 42]. The charge pumped over one period can be expressed then in terms of an integral over the *area* enclosed by this contour [13, 42]. The absence of a topological quantization means that any such contour can be continuously shrunken to zero, with no topological constraints. The pumped charge is closest to a non-zero integer when the integration area inside the contour covers almost the whole space (e.g., the surface of a $3D$ sphere in the simplest case of two single channel leads). This differential geometry approach provides important general answers, but gives limited insight into the actual mechanism of the pumped charge quantization, or the choice of physical parameters that allow to achieve it.

An important connection between pumped charge quantization and resonant transmission has been observed in Refs. [43, 19]. This observation can be summarized as follows. Let us draw the pumping contour directly in the space of parameters that are varied in order to change the Hamiltonian (see an example for two parameters, X_1 and X_2, in Fig. 1 of Chapter 3 on page 26). The transmission probability for the carriers incident in one of the leads is a function of the same parameters as well. References [43, 19] have considered particular models that exhibit sharp peaks in the transmission probability (resonances) as X_1 and X_2 are varied. Typically, a line of enhanced transmission can be identified in the parameter space (the dotted line in Fig. 1 on page 26) with the global maximum of the transmission probability at some point M on that line[3]. It has been found in Refs. [43, 19] that pumping contours that (1) enclose the point M, and (2) go for most of the time far from M and from the resonance line (so that the instantaneous transmission *along* the contour remains small during the whole cycle), transfer the same number of electrons per cycle as the contours' winding number around the point M. The fact that such a protocol should produce on average almost integer charge per cycle can be anticipated from the formula (1.1) on p. 6. More subtle is the condition for this integer to be non-zero. This criterion of "encircling the

---

[3]The point M corresponds to a vanishing reflection coefficient and thus a *singularity* of the reflection phase α [43] which we introduced in Eq. (1.1) on p. 6 [16].
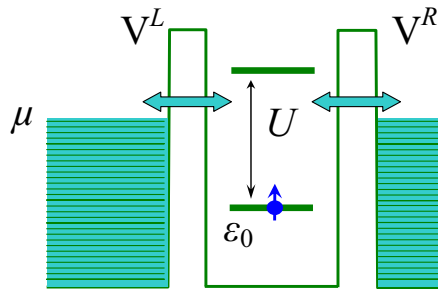
Figure 1.4: Schematic drawing of the Anderson model[4] (cf. Fig. 1.2).

the point of maximal transmission" also goes in line with the maximal area prescription of Ref. [42].

Despite the mathematical beauty of these results, the actual mechanism relating resonant transmission and pumped charge quantization has remained obscure. The simple models of Refs. [43, 19] that lead to non-trivial contours (quantized transport) include out-of-phase modulation of tunnelling barriers, not dissimilar to the turnstile mechanism outlined in Sec. 1.2.2. This similarity is quantitatively explored in Chapter 3.

1.2.4   Strongly interacting dots: models and methods

As we have seen in the previous sections, an interplay between quantum fluctuations and charging effects makes the dynamics of small electronic systems (such as quantum dots) complicated. Theoretical methods capable of describing full crossovers between different regimes of a physical model are quite sophisticated, and usually a delicate trade-off between the simplicity of a model and the variety of properties accessible for calculation is involved.

A great variety of such methods have been developed in relation to the problem of magnetic impurities embedded in a non-magnetic metal. The latter has been actively studied in the 1960s and 70s. There exists a common paradigm which can be applied both to an impurity atom coupled to free electrons of the host, and to a quantum dot connected to leads of a metallic nature.

The main physical components of this paradigm are present in the model of Anderson, suggested in 1961 for magnetic impurities [11, 44] and successfully applied to quantum dots since 1988 [45, 46, 47]. Figure 1.4 shows a schematic drawing of the Anderson model.

We shall describe the model qualitatively below. Some of the Hamiltonians studied in the present work can be viewed as a direct generalization of the Anderson model; their precise form is discussed in Sec. 2.2 below and in the corresponding sections of the research papers. A comprehensive review of the magnetic impurity problem from the theoretical point of view can be found in the book of Hewson [48].

The Anderson model pertains to a single spin-degenerate energy level ϵ_0 corresponding to a d-orbital of the impurity[5] (e.g., an atom of Fe) or a localized state in the quantum dot. The "free" electrons of the host form a continuous band, which in the quantum dots' language describes the leads. Once the impurity atom is placed in the metal, the orbital state corresponding to ϵ_0 is no longer an eigenstate of the full Hamiltonian. Therefore, a transition amplitude V between free and localized electrons is to be included into the model[6]. In the context of the quantum dots, V has the meaning of a tunnelling amplitude. A quantum dot is defined by certain potential barriers that confine the electrons. If the barriers were infinitely high, the states localized in the dot would have remained stationary forever. A finite height of the surrounding barrier (which is the lowest at the contact points between the dot and the leads) implies a ceratin amplitude for tunnelling from a localized state into the continuum. This amplitude is V of the Anderson model [7].

So far the model is a single-particle one, similar to the virtual level model of Friedel [50]. It features a single resonance in the density of states near the energy ϵ_0 (see, e.g., Chapter 1.4 of Ref. [48], or Sec. IV in Chapter 3 of the present thesis).

The crucial component making the Anderson model both challenging and relevant to strongly interacting systems is the inclusion of the direct Coulomb repulsion between the

---

[4]The quantum dot gate voltages $V_{L/R}$ should not be confused with the tunnelling amplitudes $V^{L/R}$ of the Anderson model.

[5]In magnetic alloys, more realistic is the case of several degenerate d- or f-orbitals, that can be more accurately represented by the Coqblin-Schrieffer model [49], see Chapters 7 and 8 of Ref. [48], also Appendix A of Ref. [11].

[6]In the context of the impurity problem, it is essential that the "free" electron band comes mainly from atomic s- and p-states which are "*much more extended throughout the unit cell than the localizeable states near the top of the d-band*" [11].

[7]Possibilities for taking into account the geometry of the mesoscopic structure to which the strongly correlated dot is connected, are addressed in Chapter 5.

electrons of opposite spins occupying the same orbital:

$$\mathcal{H}_{\text{int}} = U \, n_\uparrow n_\downarrow \tag{1.2}$$

(here $n_{\uparrow,\downarrow}$ are the occupation number operators for the two spin-orbitals). For a quantum dot, $U > 0$ corresponds to E_c — the charging energy due to the repulsion between an extra electron and the electrons already in the dot.

To have a feeling of what kind of physics the Anderson model is able to describe, let us consider just one typical experiment[8]: measuring linear conductance of a quantum dot as a function of the gate voltage V_g (compare Figs. 1.2 and 1.4). Typically, the gate voltage has a linear capacitative coupling to the localized electrons, therefore one assumes that $\epsilon_0 \propto -V_g$ (the more negative is the gate voltage, the higher is the energy of the electrons being repelled by the gate). Increasing the gate voltage from highly negative values corresponds to lowering ϵ_0. For ϵ_0, $U + \epsilon_0 \gg \mu$, having either two or one electron on the level is energetically unfavorable. The total occupation number is close to zero. This is the "empty dot regime" in the terminology of Chapters 5 and 6.

As the gate voltage is raised, ϵ_0 goes down. As $\epsilon_0 \approx \mu$ is reached, there forms a convenient "pad" for an electron near the Fermi energy to hop from one of the leads through the dot into the other lead. As a result, the conductance is greatly enhanced, and a peak in the conductance as a function of V_g is observed (the Coulomb blockade peak). The width of this peak (for sufficiently low temperatures) is of order $\Gamma \sim \rho |V|^2$ where ρ is the density of states in the leads. Γ is an energetic measure of quantum fluctuations between the states of different occupancy ('0' and '1' in this case) but the same energy ($= \mu$ at the peak). Γ is also an inverse of the time it takes an electron to tunnel out of the dot, in line with the time-energy uncertainty relation.

Further lowering ϵ_0 but still keeping $\epsilon_0 < \mu < \epsilon_0 + U$ brings the dot again into a state with a relatively well-defined number of electrons on the level, which this time is an odd number (one). The direct sequential tunnelling is energetically unfavorable ("Coulomb-blockaded") again, and the conductance drops. The low[9] conductance region between the Coulomb peaks is called the "Coulomb valley".

---

[8]A much more detailed discussion of the various transport regimes in Coulomb blockaded quantum dots can be found in the review article by Pustilnik and Glazman [51].

[9]For not too small temperatures, see below the discussion of the Kondo effect.

Finally, as the doubly-occupied state comes into degeneracy with the singly occupied one, the conditions for sequential tunnelling are favorable again. A second Coulomb blockade peak is observed in the conductance at $\epsilon_0 + U \approx \mu$, and the dot enters a double-occupied state at $\epsilon_0 + U \ll \mu$.

In the above discussion of the Coulomb blockade we have assumed $\Gamma \ll U$ (quantum charge fluctuations are not too strong as to mask the discreteness of the charging energy), and $T \ll \Gamma$ (electric transport is dominated by quantum and not by thermal fluctuations). Under these conditions there is yet another energy scale, the Kondo temperature $T_K \ll \Gamma$, which can strongly influence the conductance of the dot in the single occupancy ("local moment") regime. One electron on a spin-degenerate level means that if the leads are fully neglected, the quantum dot has a finite spin, $S = 1/2$ (hence the name "local moment"). Slight hybridization of the local state with the continuum in the leads makes spin flips possible. A sequence of such virtual processes generates a cloud of low-energy electron-hole pair excitations in the leads ("the Kondo cloud") which are correlated with one another and with the orientation of the spin on the dot. The eventual result of this dynamical process at $T \to 0$ is the complete screening of the local moment by the itinerant electrons, and the formation of a loosely bound many-body state whose energy is equal to the Fermi energy μ. The typical binding energy of this state is T_K. An equivalent way of characterizing the system [52] is to say that at $T = 0$ it is a Fermi liquid with a singlet (no magnetic moment!) ground state. T_K is the typical energy of the lowest energy elementary excitations and their interactions.

Formation of the Kondo cloud has a profound effect on the electron transport. Incident electrons scatter elastically on the Kondo cloud, which is automatically on resonance, i.e. has the same energy as the incoming electrons, μ. As a result, the transmission is resonant and the conductance reaches[10] the so-called "unitary limit" $2\,e^2/(2\pi\hbar)$. Thus the odd Coulomb valley turns ultimately into a Kondo plateau in the whole local moment regime $\epsilon_0 < \mu < \epsilon_0 + U$, as the temperature goes to zero. Any external factor that drives the system away from the idealized singlet ground state, generally reduces the degree of Kondo screening and brings the conductance in the valley down from the unitary limit. These important factors include finite temperature, source-drain bias, external magnetic field and dephasing due to

---

[10]For a left-right symmetrically coupled quantum dot.

dynamical environment. The typical size of the perturbations that are capable of dispersing the Kondo cloud is given by the Kondo temperature T_K. The latter can be understood as the ferromagnetic bonding energy between the coherent cascade of electron-hole pairs in the leads and the magnetic moment of the localized electron.

The actual models and the physical quantities of interest for modern studies of transport through small nanostructure go way beyond the canonical Anderson model which has been very briefly presented above. A number of such important generalizations is discussed and characterized in the research papers included in this thesis. We note however that most of the intuitive concepts for modelling correlated electron transport comes from the simple version of the Anderson model.

A broad variety of methods and tools exist for calculating different quantities for the Anderson Hamiltonian. Table 1.1 gives a short summary from the author's subjective point of view. Only the methods that in one way or another have influenced the present work are included in the table. Other important techniques, such as slave bosons, non-crossing approximation, quantum Monte Carlo etc., are not discussed.

Some more details are in place here for the methods 'd' and 'e' from Table 1.1, since they are used intensively in Chapters 5 and 6. The equations-of-motion (EOM, method 'd') for the Green functions are derived from the time-evolution equation for operators in the Heisenberg picture [53]. The crucial property of models with many-body interactions is the coupling between the EOM for the Green functions with different number of operators. Therefore, the EOM for the single particle Green function become an infinite hierarchy of coupled equations which is intractable as a whole. The standard way of treating the system of EOM is to apply a ceratin decoupling approximation which makes the hierarchy finite [54, 55, 56].

Successful application of the EOM method to quantum dot systems has been pioneered by Meir, Wingreen and Lee (MWL). In their theory [47] for periodic conductance oscillations, MWL suggest keeping equations for all the Green functions that involve more than one local (quantum dot's) operator, and approximating higher-order Green function using a version of the mean-field decoupling [53, 54]. This approach can accurately describe the emergence of Coulomb blockade in the system as the parameters are changed (e.g., Γ is tuned from $\Gamma \gg U$ to $\Gamma \ll U$). However, MWL do not impose the self-consistency requirement in approximating the thermal averages (mean fields), and therefore miss much of the electron-

hole pair correlations that are essential for the Kondo effect.

A special but very powerful property of the standard Anderson model is its exact integrability (see [57] for a comprehensive review). This allows for the application of the Bethe *ansatz*, and leads to an exact solution (method 'd' in Table 1.1). The exact occupation numbers (for each spin projection separately, if the magnetic field is non-zero), derived from the Bethe *ansatz* equations at $T = 0$, will be of great value in characterizing the two-level model of Chapter 6.

Method	Pro's	Con's	Refs.	Ch.
a. Perturbation in U	Analytic, systematic, usual diagrammatic rules apply	Breaks down at $U/\Gamma \gg 1$	[58], Ch. 5 of [48]	
b. Perturbation in Γ	Analytic, systematic	No Wick theorem, breakdown at the charging points for $T \ll \Gamma$	[59, 60]	5, 6
c. Mean field (Hartee-Fock)	Analytic, simple	Uncontrolled, underestimates correlations	[11, 61]	3 $(U\!=\!0)$
d. Equations of motion	Analytic, more accurate than HF	Uncontrolled, hard to ensure self-consistency	[56, 47]	5
e. Bethe *ansatz*	Exact, many explicit analytic results	No dynamic properties, challenging at $T \neq 0$	[57], Ch.6 of [48]	5, 6
f. Fermi liquid theory	Simple description in terms of a few parameters, exact analytic identities	Valid only if excitations over the ground state are not too strong	[52], Ch. 5 of [48]	5
g. Mapping to a spin model+poor man's scaling	Analytic estimates for Kondo-type effects	Charge fluctuations neglected	[62, 63], Ch.3 of [48]	6
h. Numerical renormalization group	Very accurate, wide parameter range	Numerics only; high calculational demand	[64, 65, 61], Ch.4 of [48]	
i. Functional renormalization group	Accurate up to relatively large U/Γ	Numerical in most cases	[66]	6

Table 1.1: Some of the theoretical methods applicable to Anderson model and its derivatives. Only the basic advantages and drawbacks are mentioned. For each method, a few representative references are given. The last column indicates which chpaters of the thesis use a particular method (either to derive new results, or as a reference).

Chapter 2

Review of the papers

The following four papers constitute Chapters 3 through 6:

(A) V. Kashcheyevs, A. Aharony, and O. Entin-Wohlman, *Resonance approximation and charge loading and unloading in adiabatic quantum pumping*, Physical Review B, vol. **69**, p. 195301, 9 pages, published on 6 May 2004;

(B) V. Kashcheyevs, A. Aharony, and O. Entin-Wohlman, *Quantized charge pumping by surface acoustic waves in ballistic quasi-1D channels*, European Physical Journal B, vol. **39**, p. 385, 12 pages, published on 12 July 2004;

(C) V. Kashcheyevs, A. Aharony, and O. Entin-Wohlman, *Applicability of the equations-of-motion technique for quantum dots*, Physical Review B, vol. **73**, p. 125338, 15 pages, published on 27 March 2006;

(D) V. Kashcheyevs, A. Schiller, A. Aharony, and O. Entin-Wohlman, *Unified description of correlations in double quantum dots*, e-print `arXiv:cond-mat/0610194`, 23 pages, submitted to Physical Review B on 9 October 2006.

2.1 Logical structure and continuity

The four papers presented in the thesis explore electron dynamics in small coherent quantum systems focusing on adiabatic pumping of electrons, conditions for pumped charge quantization, and the role of explicit Coulomb interactions. The following describes briefly

the sequence of milestones achieved on this way, and the connections between the results reported in different papers.

As we explained in Sec. 1.2.3, adiabatic quantum pumping through a structure with sharp transmission resonances may lead to pumped charge quantization. Our first paper (A) raises and answers the following question: what is the charge redistribution associated with moving a system adiabatically through an isolated resonance, and why is it close to one electron transfer? The main idea has been to cast the expression of the pumping current into a form which can serve two purposes. On one hand, it is applicable to a generic resonance triggered by a single level of the nanostructure in question. On the other hand, the instantaneous current formula can be integrated (in a well-defined limit) into a simple expression with clear physical meaning.

To this end, we have translated the scattering states formalism of Ref. [17] into a form involving the local Green function [see Eq. (6) on p. 27]. This form has been applied to a single level with time-dependent position and coupling strength. As a result, a Breit-Wigner resonance (simple pole) appears in the Green function, in the scattering matrix, and in the pumping current formula. What is important is that the transmission is maximal when the pole crosses the Fermi energy. Therefore, the crossing points between the pumping contour and the resonance line [the "resonance points", e.g., points B and D in Fig. 1 on p. 26] correspond to time moments when the instantaneous energy level goes below or above the Fermi surface. This observation has direct implications for pumping, as discussed qualitatively in the introduction to Chapter 3 (paper A) and quantitatively in the main body of that paper.

The analysis of a pumping contour in terms of the individual charge loading and unloading events is not restricted to a single-level model, or to changing just two parameters. For more complex structures with several sites, each resonance may involve a different level. Still, if the system is sufficiently weakly coupled, the resonances are generically well-separated and the total charge pumped per period can be expressed as a sum of the individual contributions, see Sec. III.D of Chapter 3 (paper A) and Sec. 2.3 of Chapter 4 (paper B).

The next step in the research program implemented in the thesis has been to apply the insights of the resonance approximation to a system for which quantized pumping current has been measured experimentally. This system is a SAW-driven quantum channel that has been mentioned at the end of Sec. 1.2.2 in the introductory chapter. The main experimental

observation [38] is the staircase structure of the dc current measured as a function of the gate voltage (the latter controls the degree of depletion of the electron gas in the channel). The value of the current at the plateaus in this staircase is to a good accuracy $I = e \times (1, 2, 3 \ldots) \times f$, where f is the frequency of the SAW (typically a few GHz), and e is the electron charge.

A simple model that captures the basic physics of the quantized current through a SAW-pump device has been proposed in Ref. [39]. The model features a chain of tight-binding sites representing the coherent 1D channel. The effect of a SAW on the electrons in the channel is modelled as a running potential profile, as shown in Fig. 2.1B on p. 24, and discussed in Sec. 2.1 of Chapter 4 (paper B).

Charge pumping generated by SAWs is investigated in detail in Chapter 4. As the results of Chapter 3 suggest, the positions of the instantaneous energy levels as a function of time have to be traced in order to identify the charge loading and unloading events. Each crossing of a particular eigenvalue with the Fermi level gives rise to an adiabatic transfer of a single electron between the reservoirs and the central structure. Whether it is (predominantly) the left or the right reservoir is determined by the shape of the corresponding eigenfunction. This construction is explained in detail in Sec. 3 of Chapter 4, and illustrated in the respective Figs. 2 and 3 on p. 40. We show that the whole dependence of the average current on the gate voltage can be re-constructed from the eigenvalue diagram.

Empowered by the simple framework of the resonance approximation, we investigate the role of the potential profile parameters — such as the SAW power, the ratio between the wavelength and the channel length, the shape of the screening function — on the spectrum of instantaneous eigenvalues, and, subsequently, on the pumped current staircase. A set of almost equidistant states that are responsible for the plateaux structure is found to be localized at the minimum of the travelling potential profile. This means that the pumped electrons are carried adiabatically by a moving potential well. What is important, however, and what distinguishes the results of paper B from related earlier studies [67, 68], is that the existence of such a "moving quantum dot" is not assumed *a priori*. The latter is generated dynamically only if the SAW amplitude is strong enough.

Several novel features of the quantized acoustoelectric current that had been measured [69] but not previously addressed theoretically, are explored in Chapter 4. In particular, classical interference of two counter-propagating SAWs is found to generate in a character-

istic pattern of change in the pumping current curves (see Fig. 5 on page 43), in accrod with the experiment [69].

Despite the successful characterization of the basic experimental features, the approximation of spinless non-interacting electrons is limited both from the conceptual and the practical points of view. The spacing between the current quantization steps is explained within the model as the single-particle level spacing in an approximately harmonic potential well. The corresponding number is significantly smaller than that measured experimentally. The other inconsistency concerns the treatment of electron spin. The channels in the absence of SAW show conductance quantization in units of $2\,e^2/h$, which means that the electrons are spin-degenerate. On the other hand, there are well-defined plateaus both for even and for odd number of electrons transported in a cycle, so that the double degeneracy is effectively lifted for the electrons that are dynamically captured.

Resolution of these difficulties requires a method that takes into account both the local Coulomb repulsion and the hybridization with extended states in a non-perturbative manner. One such method, the equations-of-motion (EOM) technique, is investigated in detail in Chapter 5. Instead of the pumping current, this study concentrates on a more fundamental quantity which is necessarily involved in any characterization of the dynamical properties of the system, namely, on the single-particle Green function.

Similarly to paper A, paper C works out an equation for the local electron's Green function assuming an arbitrary structure in the leads. The latter can be, for example, a grid of tight-binding sites with a certain topology. Both chapters (3 and 5) keep track of the information about the external network by means of the (non-interacting) self-energy function $\Sigma(z)$ as explained in Appendix A of Chapter 5.

One of the principal goals for Chapter 5 is to establish accurately to what extent the EOM method can be trusted. For this sake we pay much attention to the Kondo effect, and compare extensively with the exact results available for the standard Anderson model. Quantities related to charge transport, such as the total occupation number or the broad Lorentzian feature in the local density of state, are captured by the EOM technique remarkably well (see, e.g., Fig. 1 on page 54). Strong Coulomb repulsion indeed prevents double occupancy of the quantum dot, and thus effectively lifts the spin degeneracy. These observations may be seen as a support for the use of the single resonance spinless model employed in Chapter 3.

As discussed qualitatively in the introduction (Sec. 1.2.4), the properties of a quantum dot with an unpaired spinful electron are dominated by its spin fluctuations. In this regime the EOM technique is found to be much less accurate. Although respecting the self-consistency condition improves significantly, the results in the local moment regime fall short of a quantitative description of the Kondo effect.

The next and the final step in the sequence of papers is the transition form a single-site model, considered in papers A and C, to a two-site model, this time with a strong inter-site Coulomb interaction. A schematic drawing of the model considered in Chapter 6 (paper D) is shown in Fig. 2.1D. This kind of general two-level model has been actively studied in recent years within many different contexts, as discussed in the introduction to Chapter 6. The reason for that is that it is a minimal model in which correlated electron transport through more than one energy level can be studied.

Chapter 6 puts forward a crucial observation which unlocks the main physics of the model. The lead and dot degrees of freedom can be independently rotated by a unitary transformation in such a way that the resulting Hamiltonian is of the Anderson type with a certain pseudo-spin degree of freedom. This pseudo-spin is conserved in tunnelling but not necessarily inside the structure, as shown schematically in Fig. 1 on page 66.

Once the new model is mapped to a more familiar Hamiltonian, the experience gained in Chapter 5 can be applied. There is a finite effective magnetic field in the transformed model. It comes from the rotation of the original "Zeeman splitting" of the site energies, and from the renoramlization of the dot levels due to coupling to the leads (the latter are in general "ferromagnetic", as explained in Sec. II of Chapter 6). In analogy to the conventional Kondo effect, we can expect a competition between the dynamical screening of the local pseudo-spin on one hand, and the polarizing magnetic field on the other hand. As we learn from Chapter 5, the EOM method is not good for keeping track of spin fluctuations, therefore a different set of methods has been employed in Chapter 6. These are methods 'g' and 'e' from Table 1.1. These methods do not give as much dynamical information as the EOM technique, but at the same time describe accurately the full crossover from strong to negligible Kondo screening as a function of the effective magnetic field. The latter now depends on many of the original system parameters in a complicated way which is, however, traced analytically in full detail. Two important observables are calculated and discussed extensively in Chapter 6: the occupation numbers and the low-temperature conductance.
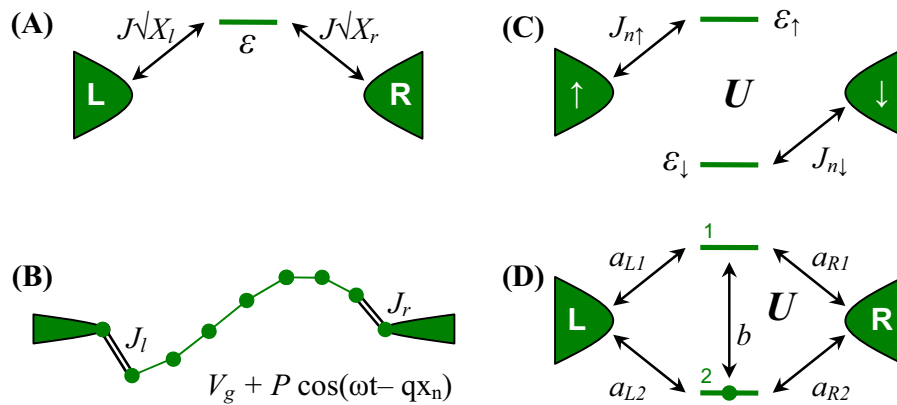
Figure 2.1: An overview of the models studied in the thesis.

In summary, the Chapters 3–6 present a diverse but interconnected picture of the dynamical behavior of electrons in mesoscopic systems with a few active local energy levels.

2.2 A guide to the models explored

We supplement the discussion of the overall structure of the thesis by a visual summary of the models explored. Figures 2.1A through 2.1D relate to Chapters 3 through 6 respectively. The on-site energies in A and B, as well as the tunnelling couplings in A are time-dependent. The number of sites N in the chain of Fig. 2.1B is arbitrary, the case of $N = 2$ is equivalent to a special case of Fig. 2.1D.

Several different models for the leads are discussed throughout this work. The first two papers use a semi-infinite tight-binding chain as a model lead. This results in an energy-dependent self-energy function Σ with a non-vanishing real part (see Sections II and IV.A in Chapter 3 for the definition and discussion of Σ, and also Section II and Appendix A of Chapter 5). In the appropriate limit (namely, $J_{l;r}^2/J \rightarrow$ const and $\sin ka \rightarrow 0$ in the notation of Chapters 3 and 4), the self-energy function becomes energy-independent, and the wide-band limit used in Section IV of Chapter 5, and throughout Chapter 6 is recovered. Note also that the level broadening Γ in Chapters 3 and 4 is twice the value of Γ in Chapters 5 and 6.

Chapter 3

Resonance approximation and charge loading and unloading in adiabatic quantum pumping

The content of this chapter has been previously available as

- a preprint, `arXiv.org:cond-mat/0308382` (19 August 2003);

- a journal article, Phys. Rev. B, **69**, 195301 (6 May 2004).

Resonance approximation and charge loading and unloading in adiabatic quantum pumping

Vyacheslavs Kashcheyevs, Amnon Aharony, and Ora Entin-Wohlman

School of Physics and Astronomy, Raymond and Beverly Sackler faculty of Exact Sciences, Tel Aviv University, Tel Aviv 69978, Israel

Quantum pumping through mesoscopic quantum dots is known to be enhanced by resonant transmission. The pumped charge is close to an integer number of electrons when the pumping contour surrounds a resonance, but the transmission remains small on the contour. For noninteracting electrons, we give a quantitative account of the detailed exchange of electrons between the dot and the leads (to the electron reservoirs) during a pumping cycle. Near isolated distinct resonances, we use approximate Breit-Wigner expressions for the dot's Green function to discuss the loading/unloading picture of the pumping: the fractional charge exchanged between the dot and each lead through a single resonance point is related to the relative couplings of the dot and the leads at this resonance. If each resonance point along the pumping contour is dominated by the coupling to a single lead (which also implies a very small transmission), then the crossing of each such resonance results in a single electron exchange between the dot and that lead, ending up with a net quantized charge. When the resonance approximation is valid, the fractional charges can also be extracted from the peaks of the transmissions between the various leads.

I. INTRODUCTION

There has been much recent experimental[1–3] and theoretical[4–17] interest in adiabatic quantum pumping through mesoscopic electronic devices, such as quantum channels or quantum dots (QD's). Typically, the QD is connected via leads to several electron reservoirs, and is subject to a slowly varying oscillating potential, with period $\mathsf{T} = 2\pi/\omega$. Under appropriate conditions, the device yields a nonzero dc time-averaged current between pairs of terminals, even when the terminals have the same chemical potential. Under ideal conditions, the charge Q transferred between the terminals during a period T may be "quantized," i.e., very close to an integer times the electron charge e. Several recent theoretical studies have considered enhancement of the adiabatic pumping current due to resonant transmission[18] through the QD, both for noninteracting[9,11,16,19,20] and interacting electrons.[21] Connections between pumped charge quantization and resonant transmission have been reported in different contexts.[11,16,19,20,22,23]

Usually, the oscillating potential is characterized by several time-dependent parameters, $\{X_i(t)\}$. As time evolves during one period T, these parameters follow a closed contour in the parameter space. A schematic example is shown in Fig. 1 for two such parameters. In parallel to discussing pumping, one can also consider the conductance between pairs of terminals generated by an appropriate bias. This conductance, which depends on the parameters $\{X_i\}$, may have resonance peaks in the same parameter space. In this context, one freezes the time dependence, and considers the conductance at some instantaneous values of the $\{X_i\}$'s. It has been argued[11] that the pumped charge Q will be close to being quantized if the pumping contour surrounds such a peak (e.g., at the point M in Fig. 1), while staying at points with a low conductance.

In the present paper we present an approximate theory for adiabatic pumping of coherent noninteracting spinless electrons, which is valid for discrete and distinct resonances, and

use this approximation to obtain physical insight into the reasons for this quantization. Given a conductance peak (e.g., at the point M in Fig. 1), one can usually also identify a "resonance line," along which the conductance decreases from its peak more slowly than along other directions.[11,16] Such a line is illustrated by the dashed line in Fig. 1. In the example shown in this figure, the resonance line is crossed by the pumping contour twice, at points B and D. Measuring the instantaneous biased conductance between the two relevant terminals for each time t during the oscillation period, one expects two local peaks at these two resonance points. Under appropriate conditions, which include the limit of weak QD-terminal coupling, most of the pumped current arises when the parameters are close to these resonance points: for example, one can identify a "loading" of the QD by some charge $\Delta Q_\alpha^{\mathrm{res}}$, coming from terminal α, at the point B, and an "unloading" of the QD, by $\Delta Q_{\alpha'}^{\mathrm{res}}$, into terminal α', at the point D. The resulting total pumped charge per period approaches a robust, detail-independent value Q^R, which is determined *only* by the ratios of the coupling strengths between the QD and the different reservoirs at the
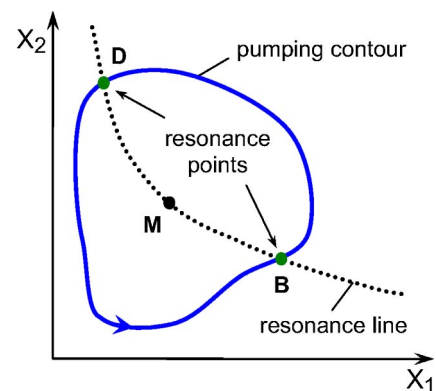

FIG. 1. (Color online) Schematic picture of a two-dimensional pumping contour, crossing the resonance line at two resonance points (B and D). The transmission is maximal at the point M.

resonance points. We also show that Q^R can be related quantitatively to the measured values of the peak conductances. Q^R is (almost) quantized (in units of e) when there is one dominant coupling for each resonance.

Our results can be summarized in a very simple and physically transparent way, by considering the occupation numbers of the quasibound state on the QD, corresponding to each transmission resonance. Each time the energy of such a state crosses the chemical potential μ (which is the same in all reservoirs), the QD gains or loses one electron, so that the total pumped charge flowing into it (per period) is quantized. However, the distribution of the pumped charge between different reservoirs is proportional to the corresponding coupling strengths (tunneling rates). Therefore the pumping current between any two leads can be obtained by summing up individual resonance contributions, with appropriate signs.

A similar "shuttling mechanism" for pumping has been used widely to interpret experiments[2,3] in the Coulomb blockade regime, when the energetics on the QD is dominated by the electron-electron interactions.[24] In that approach, electrons are transferred from a lead to the dot and then from the dot to another lead, whenever such transfers are favored energetically. In contrast, Refs. 11,15,16,25 and 26 presented explicit quantum-mechanical calculations for pumping of noninteracting electrons, calculated the total charge pumped during a full cycle, and emphasized the role played by quantum interference in such processes. In some sense, the present paper bridges between these points of view: in the limit of weak coupling between the QD and the leads, we do end up with a loading/unloading picture, even for noninteracting electrons.[45] However, the details of the charge exchanges during a pumping cycle are found to be more complicated than in the "shuttling" picture: at a given resonance point, charge can usually be shared by several leads. Apart from this, the conditions for the applicability of our loading/unloading picture are similar to those of a single electron transistor,[2] in the sense that the role of quantum interference is restricted to the definition of independent single-particle resonances. In view of this, there is room to conjecture that some of our results may also apply in the presence of electron interactions.

The paper is organized as follows. In Sec. II we review the physical assumptions of the model and the formulas used for the calculation of the adiabatic current. We then use these formulas to derive the current for a single resonant state, by approximating the Green function on the QD by a Breit-Wigner-type formula. In Sec. III we obtain our main result—the adiabatically pumped charge for a sequence of well-defined distinct resonances—and discuss possible applications and experimental verification. To demonstrate this general picture, Sec. IV presents the analysis of the pumped charge for a simple model[15] of a "turnstile" pumping device. A short summary concludes the paper in Sec. V.

II. ADIABATIC CURRENT

We consider a spatially confined nanostructure (the QD) connected by ideal leads to the electronic reservoirs with a common chemical potential μ and temperature T. The total

Hamiltonian for noninteracting spinless electrons is

$$\mathcal{H} = \mathcal{H}^d + \sum_\alpha (\mathcal{H}^l_\alpha + L_\alpha + L^\dagger_\alpha), \qquad (1)$$

$$\mathcal{H}^d = \sum_{mn} h_{mn}(t) d^\dagger_m d_n \quad \text{(dot)}, \qquad (2)$$

$$\mathcal{H}^l_\alpha = \sum_k E_{\alpha k} c^\dagger_{\alpha k} c_{\alpha k} \quad \text{(leads)}, \qquad (3)$$

$$L_\alpha = \lambda_\alpha(t) \sum_{k,n} J_{\alpha k n} c^\dagger_{\alpha k} d_n \quad \text{(hopping)}. \qquad (4)$$

Here $\mathcal{H}^d$ is the Hamiltonian of an N-state isolated QD $(n,m = 1, \ldots, N)$, the index $\alpha = 1, \ldots, L$ enumerates the one-dimensional leads connected to the QD, $c^\dagger_{\alpha k}$ creates a standing wave $|w_{k\alpha}\rangle$ with wave number k and energy $E_{\alpha k}$ in the channel α, the operator L_α describes hopping from the QD into the channel α, and the λ_α's are real dimensionless coefficients. For pumping we allow variation of $\mathcal{H}(t)$ via the time-dependent parameters h_{mn} and λ_α.

The instantaneous adiabatic current in the channel α, directed from a remote reservoir towards the QD, has been expressed in Ref. 15 as

$$I_\alpha(t) = \frac{e}{2\pi} \int dE f'(E) \mathcal{I}_\alpha, \quad \mathcal{I}_\alpha = \frac{1}{\hbar} \langle \chi_{k\alpha} | \dot{\mathcal{H}} | \chi_{k\alpha} \rangle, \quad (5)$$

where $f(E) = 1/[1 + e^{(E-\mu)/k_B T}]$ is the Fermi-Dirac distribution and $|\chi_{k\alpha}\rangle$ is the instantaneous scattering state normalized to a unit flux, $\langle \chi_{k\alpha} | \chi_{k'\alpha} \rangle = (2\pi/v_{k\alpha}) \delta(k - k')$, with $v_{k\alpha} = \partial E_{k\alpha}/\partial(\hbar k)$ being the velocity in the channel α.

In Appendix we use standard scattering theory formulas to rewrite this equation in the form

$$\mathcal{I}_\alpha(E,t) = \text{Tr}_d[G^\dagger_d(\dot{\mathcal{H}}^d + \dot{\hat{\mathcal{E}}}) G_d \hat{\Gamma}_\alpha + (G_d + G^\dagger_d) \dot{\hat{\Gamma}}_\alpha/2]. \quad (6)$$

Here, the operators

$$G_d = (E + i0 - \mathcal{H}^d - \hat{\Sigma})^{-1}, \qquad (7)$$

$$\hat{\Sigma} = \hat{\mathcal{E}} - i\hat{\Gamma}/2, \qquad (8)$$

$$\hat{\Gamma} = \sum_\alpha \hat{\Gamma}_\alpha, \quad \hat{\Gamma}_\alpha = iL^\dagger_\alpha(G^l_\alpha - G^{l\dagger}_\alpha)L_\alpha, \qquad (9)$$

$$\hat{\mathcal{E}} = \sum_\alpha \hat{\mathcal{E}}_\alpha, \quad 2\hat{\mathcal{E}}_\alpha = L^\dagger_\alpha(G^l_\alpha + G^{l\dagger}_\alpha)L_\alpha \qquad (10)$$

act only on the subspace of the QD. Also, G^l_α denotes the retarded Green function of an isolated channel, $G^l_\alpha = (E + i0 - \mathcal{H}^l_\alpha)^{-1}$. We have separated the self-energy operator $\hat{\Sigma}$ into a sum of resonance width and shift operators,[27] $\hat{\Gamma}_\alpha$ and $\hat{\mathcal{E}}_\alpha$, which are Hermitian.

Equation (6) is a generalized version of the pumping current formula derived in Ref. 25 for a particular case of single-mode tight-binding (TB) leads and time-independent couplings.[46]

The adiabatic current (6) can be calculated exactly, provided that one is able to compute the Green function (7) on the QD. We are interested in the regime when the transport is dominated by a single nondegenerate orbital state, and instead of Eq. (2) we consider

$$\mathcal{H}_{\text{res}}^d = \epsilon(t)|\psi\rangle\langle\psi| \equiv \epsilon(t)d^\dagger d. \tag{11}$$

The energy distance to the next resonant state Δ will be assumed to be much larger than all other energies. The Green function corresponding to $\mathcal{H}_{\text{res}}^d$ now assumes the Breit-Wigner-like form[28]

$$G_d = \frac{|\psi\rangle\langle\psi|}{E - \epsilon - \langle\psi|\hat{\Sigma}|\psi\rangle}. \tag{12}$$

The approximation of a single noninteracting energy level, Eq. (12), is valid for resonant tunneling structures with negligible charging energy, and corresponds to the Breit-Wigner treatment of mesoscopic electrical transport initiated in Refs. 29 and 30. For example, our results are directly applicable to the much studied double barrier pumping[9,11,14,31,32] in the resonant tunneling regime.[9,11] We also list several experimental situations when the charging energy is not small, but our noninteracting spinless model can still have some relevance. First, it applies when spin degeneracy is removed either by a constant in-plane magnetic field or by feeding the device with fully polarized electrons form half metallic ferromagnetic leads, e.g., CrO_2 (Ref. 33). In this case the energy scale Δ is set by the level spacing of the effective device Hamiltonian $\mathcal{H}^d$. Second, the Breit-Wigner approximation (12) is relevant for the Coulomb blockade peaks of a strongly pinched quantum dot well above the Kondo temperature.[34,35] Specifically, within the Hartree approximation, a large on-site Coulomb repulsion energy U forbids double occupancy of otherwise spin-degenerate energy levels and sets the interresonance distance $\Delta = U$. Explicit derivation of the Breit-Wigner resonances for a weakly coupled interacting system can be found in Ref. 36.

Substitution of Eq. (12) into Eq. (6) gives

$$\mathcal{I}_\alpha = \frac{\Gamma_\alpha \dot{E}_0 - \dot{\Gamma}_\alpha(E_0 - E)}{(E - E_0)^2 + (\Gamma/2)^2}, \tag{13}$$

where $E_0(E,t) = \epsilon + \langle\psi|\hat{\mathcal{E}}|\psi\rangle$ and $\Gamma_\alpha(E,t) = \langle\psi|\hat{\Gamma}_\alpha|\psi\rangle$. Since the partial "width" Γ_α is of order $\lambda_\alpha^2|J_{\alpha k}|^2$, it represents a measure for the coupling of the QD with the channel α. The exact adiabatic current for a single level given by Eq. (13) will be the starting point for our analysis of the pumped charge in Sec. III. Breit-Wigner-type expressions for the current pumped by a single orbital level have been derived previously in the weak pumping limit,[21] and in the presence of interactions and Zeeman splitting.[22] However, they were not used to discuss the details of the pumped charge quantization.

In the remainder of this section we discuss the physical interpretation of Eq. (13). The total current $I = \Sigma_\alpha I_\alpha$ represents changes in the total charge accumulated both on the dot and in the leads. For small dot-lead couplings, one would expect that the charge on the QD itself is a well-defined quantity and a simple picture of single electrons tunneling between the leads and the QD should apply. In order to clarify the relation between our quantum calculation and this "classical shuttling picture," we comment on the localization of the charge.

Equation (13) implies that the total current in our model is a full time derivative, $I = dQ^F(E_0, \Gamma)/dt$ of some time-dependent charge $Q^F(t)$, where

$$Q^F(t) = -e \int dE f'(E) \left\{ \frac{1}{2} + \frac{1}{\pi}\arctan\frac{2(E - E_0)}{\Gamma} \right\}. \tag{14}$$

(We have chosen the integration constant such that Q^F/e is bounded between 0 and 1.) The charge Q^F represents the integrated Breit-Wigner density of states and can be interpreted[37,38] as the additional charge induced in the system by an extra electronic state $|\psi\rangle$.

This delocalized charge Q^F is to be compared with the local equilibrium occupation inside the QD, which is given by $Q^{\text{occ}}/e = \text{Tr}[\rho|\psi\rangle\langle\psi|]$, where $\rho = h^{-1}\int dE f(E)\Sigma_\alpha|\chi_{k\alpha}\rangle\langle\chi_{k\alpha}|$ is the equilibrium density matrix corresponding to $\mathcal{H}(t)$.[47] Using Eqs. (A1), (A6), and (12) one can show that

$$Q^{\text{occ}} = \frac{e}{2\pi} \int dE f(E) \frac{\Gamma}{(E_0 - E)^2 + (\Gamma/2)^2}. \tag{15}$$

If E_0 and Γ were independent of E, then integration by parts would yield the equality $Q^{\text{occ}} = Q^F$. In general, E_0 and Γ do depend on E, and hence $Q^{\text{occ}} \neq Q^F$.

III. RESONANCE APPROXIMATION

The Breit-Wigner form (13) of the pumping current demonstrates a well-established fact[9,11,16] that pumping is greatly enhanced near a resonance. The resonance condition is $|E_0 - \mu| \lesssim D$, where $D = \max(\Gamma, kT)$ is the energetic width of the resonance. One option, considered in Ref. 21, is to design the pumping contour in such a way that the system stays entirely at resonant transmission. In this case, the Breit-Wigner approximation does not lead to any pumped charge quantization.[21] Here we focus on a more generic case, when the resonance condition is satisfied only during a small fraction of the pumping cycle, as the system goes through a resonance point. As shown in Refs. 11,16,19 and 20, this situation allows for pumped charge quantization. Specifically, we assume that the system remains near a resonance point only during a small fraction of the pumping cycle. This requires relatively narrow resonances, i.e., small widths D and therefore also small Γ.

Consider a resonance time t_R on the pumping contour, identified by the resonance condition $E_0(\mu, t_R) = \mu$. This identifies a "resonance point" on the contour. Assume also that the system "crosses" this resonance point completely

between times t_1 and t_2, such that (1) Γ_α, E_0 are energy independent around the Fermi surface (for $|E - \mu| \lesssim kT$); (2) at the "boundary" times, the system is far from the resonance, $D \ll |E_0(\mu, t_{1,2}) - \mu| \ll \Delta$; (3) while at resonance, the couplings change negligibly, $|\dot\Gamma_\alpha| \ll |\dot E_0|$.

Under these conditions, we can integrate Eq. (13) and get the charge transferred from the reservoir α in a simple form:

$$\Delta Q_\alpha^{\text{res}} = \int_{t_1}^{t_2} dt I_\alpha = -e \frac{\Gamma_\alpha}{\Gamma} \text{sgn} \dot E_0 \quad (\text{at } E_0 = \mu). \quad (16)$$

For this particular resonance point, other parts of the pumping contour contribute negligibly to this charge. Equation (16) is our main result for the pumped charge due to a well-defined resonance point. We will refer to this result as "the resonance approximation." In this approximation, each reservoir contributes on average a fraction of the electronic charge, which is proportional to the corresponding fractional decay width or coupling Γ_α/Γ. The total change in the charge accumulated in the system due to this particular resonance is thus

$$\Delta Q^{\text{res}} \equiv \sum_\alpha \Delta Q_\alpha^{\text{res}} = \pm e. \quad (17)$$

This result can be easily generalized for several independent resonance points. If the pumping contour can be separated into several parts, each containing a single well-defined resonance point, and if the pumping currents on the rest of the contour remain negligible, then the total charge Q_α^R, pumped through the channel α, is given by a sum over the resonances: $Q_\alpha^R = \Sigma_{\text{res}} \Delta Q_\alpha^{\text{res}}$. For a periodic $\mathcal{H}(t)$, the pumping contour is closed, and charge conservation $\Sigma_\alpha Q_\alpha^R = 0$ is ensured by Eq. (17) and the fact that the number of loading ($\dot E_0 < 0$) and unloading ($\dot E_0 > 0$) resonance points is the same.

A. Pumped charge quantization

Equation (17) can be interpreted as the loading/unloading of exactly one electron into/out of the QD, depending on the sign of $\dot E_0$ at the Fermi level. Furthermore, Eq. (16) implies that ΔQ_{res} is dominated by the current from a single channel α, provided that $\Gamma_\alpha \gg \Gamma_{\alpha'}$ for $\alpha \neq \alpha'$. If the same applies to all the resonances, then we end up with a "classical" picture, in which the pumping cycle contains a sequence of individual discrete events, of exchanging electrons one by one between a reservoir and the QD. After a full cycle, the charge on the QD will remain unchanged, and an integer number of electrons will have crossed the QD between any pair of reservoirs. This gives a detailed explanation of the pumped charge quantization within this approximation.

Using the same conditions as used to derive Eq. (16), one can show that both $\Delta Q^F \equiv Q^F(t_2) - Q^F(t_1)$ and ΔQ^{occ} are equal to ΔQ^{res}. This means that every time the system crosses a resonance point, the charge associated with the resonant state changes by $\sim \pm e$. Therefore we stress that if one is interested in the total charge pumped by a single resonance [and not, for example, in the line shape of the current,

Eq. (13)], then the simple picture of loading/unloading of a single electron, as reflected in Eq. (16), is applicable—regardless of the ratio Γ/kT.

We also note that for such an ideal quantization ($Q_\alpha^R \rightarrow e \times$ integer), that is independent of the contour details, one would need to consider the limit $\Gamma_\alpha \approx \Gamma \rightarrow 0$ for each resonance; the resonance approximation becomes exact, with results which are independent of the details of the contour, when $\Gamma \rightarrow 0$, and the charge goes only via channel α when $\Gamma_\alpha/\Gamma \rightarrow 1$. As explained in the following section, this implies a vanishing transmission throughout the whole pumping cycle, in accordance with the conclusions of Refs. 11 and 39.

B. Relation to conductance

The criteria for the validity of the resonance approximation, listed in the preceding section, can be *quantitatively* checked in experiments (or in numerical calculations) by monitoring the conductance between different leads as a function of parameters along the pumping contour.[11,16] A definitive signature of the relevant transport regime (for having a significant nonzero pumped charge) would be the presence of an even number of well-separated peaks in the conductance time trace: each resonance (M in Fig. 1) is associated with two peaks in the instantaneous transmission, encountered at the two resonance points (B and D) where the pumping contour crosses the resonance line on each side of the resonance, as schematically shown in Fig. 1. Note that this measurement is independent of time: one simply measures the conductance at different points on the pumping contour.

The contribution of each particular conductance peak to the pumped charge can be calculated along the following lines. Application of the general expression of the transmission probability[27] from channel α' to channel α, $\mathcal{T}_{\alpha\alpha'} = -\int dE f'(E) \text{Tr}[G_d^\dagger \hat\Gamma_\alpha G_d \hat\Gamma_{\alpha'}]$, to our resonance model [as defined in Eq. (11)] gives the standard Breit-Wigner[28] result (see, e.g., Ref. 34):

$$\mathcal{T}_{\alpha\alpha'} = -\int dE f'(E) \frac{\Gamma_{\alpha'}\Gamma_\alpha}{(E - E_0)^2 + (\Gamma/2)^2}. \quad (18)$$

Let us consider for simplicity an example of L single-mode leads. By using the multiterminal Landauer conductance formula[40] for spinless electrons, $\mathcal{G}_{\alpha\alpha'} = (e^2/h)\mathcal{T}_{\alpha\alpha'}$, in Eq. (18), we recover well-established[34] results for the peak conductance of a strongly pinched QD, that are related to Eq. (16) in an extremely simple way:

$$\mathcal{G}_{\alpha\alpha'}^{\text{peak}} = \frac{e^2}{h} \frac{4\Gamma_\alpha \Gamma_{\alpha'}}{\Gamma D} \equiv \frac{4\Gamma}{hD} \Delta Q_\alpha^{\text{res}} \Delta Q_{\alpha'}^{\text{res}}, \quad (19)$$

where

$$D = \begin{cases} \Gamma, & kT \ll \Gamma, \\ (8/\pi)kT, & kT \gg \Gamma. \end{cases} \quad (20)$$

Measurements of the peak conductance at a particular resonance point for fixed temperature and all possible combinations of source and drain leads would give, in principle, $(L^2 - L)/2$ experimental values to be used in Eqs. (19). Together with Eq. (17), this gives $(L^2 - L)/2 + 1$ equations for the $L + 1$ unknowns ΔQ_α^{res} and Γ/D. Measurement of the temperature dependence of $\mathcal{G}_{\alpha\alpha'}^{peak}(T)$ would yield $D(T)$, and thus determine Γ. We see that even for $L = 2$ it is possible to predict the adiabatically pumped charge from the conductance measurements, and for $L > 2$ different cross checks become feasible.

Additional input of a few bits of information is necessary to make the solution of Eqs. (19) and (17) unique. For a specific resonance "res," all the charges ΔQ_α^{res} (for all α) have the same sign, determined by the type of the resonance: "+" for loading and "−" for unloading, see Eq. (16). An additional sign uncertainty arises in the case of two terminals ($\alpha = l, r$): the respective equation for the pumped charge, $\Delta Q_l (e - \Delta Q_r) = \mathcal{G}_{lr}^{peak}(hD/4\Gamma)$, is symmetric under inversion, $l \leftrightarrow r$. The resolution of these uncertainties depends on the particular experimental situation, and should be easy in simple cases. We illustrate this point in Sec. (IV) below, when we discuss a two-terminal example.

C. Adiabaticity condition

One condition for the validity of the adiabatic picture requires that an electron should have enough time to tunnel under the barriers while the system is at resonance. Thus, the inverse tunneling rate $\hbar/\Gamma$ should be much smaller than the duration of the resonance, $\tau_r = D/|\dot{E}_0|$, yielding the adiabaticity condition,

$$\hbar|\dot{E}_0| \ll \Gamma D. \tag{21}$$

This condition implies that both the amplitude and the frequency of the pumping potential must be sufficiently small for an adiabatic pump.[26] The resonance duration τ_r can be extracted from measurements of the conductance as follows: measuring the variation of the conductance through the resonance, using a very low frequency ω_0, would yield the resonance width τ_{r0} for that frequency. The value of τ_r relevant for the pumping experiments can then be found by rescaling, $\tau_r = \tau_{r0}\omega_0/\omega$.

At zero temperature, $D = \Gamma$ and the condition (21) can be compared to the adiabaticity criterion for coherent pumping formulated recently by Moskalets and Büttiker.[31] They consider the number of sidebands n_{max} required to describe adequately the Fourier transform of the instantaneous scattering matrix. In our case the resonant peak of transmission in the time domain has the width τ_r, and the number of relevant Fourier harmonics n_{max} is at least $(\omega\tau_r)^{-1}$, where ω is the cyclic frequency of the pump. The adiabaticity criterion of Ref. 31 states that the scattering matrix should vary little with energy over the range $E \pm \hbar\omega n_{max}$. Since our characteristic energy scale for the scattering matrix is Γ, the condition of Ref. 31 takes the form $\Gamma \gg \hbar\omega n_{max} = \hbar\tau_r^{-1}$, equivalent to Eq. (21).

D. Application to complicated pumping potentials

In the resonance approximation, the pumped charge is expressed in terms of the resonance *points*, where the pumping contour crosses the resonance lines, and do not require the full information on the contour in the parameter space. We now discuss the conditions under which Eq. (16) can be used to obtain efficient approximate estimates of the pumped charge for a model Hamiltonian $\mathcal{H}^d$, which is complicated enough to render an exact integration[25] of Eq. (6) impractical. Even when the validity of the resonance approximation is marginal, such an approximate estimate could provide a handy tool for exploring complicated pumping models (e.g., Refs. 11,16 and 25) and identifying the relevant physical parameters. For simplicity, we restrict this discussion to zero temperature.

To leading order in the coupling strengths λ_α, the parameters of the resonant level in Eq. (11) are given by the eigenstate of the decoupled $\mathcal{H}^d(t)$ which is the closest to the Fermi energy μ. Therefore, the following algorithm can be formulated.

(1) Diagonalize $\mathcal{H}^d(t)$ (analytically or numerically) to get the spectrum $\{\epsilon_m(t), |\psi_m(t)\rangle\}$.

(2) Calculate the time-dependent decay widths $\Gamma_\alpha^m(t) = \langle\psi_m(t)|\hat{\Gamma}_\alpha(E = \mu)|\psi_m(t)\rangle$ and shifted energy levels $\epsilon_m'(t) = \epsilon_m(t) + \langle\psi_m(t)|\hat{\mathcal{E}}(E = \mu)|\psi_m(t)\rangle$.

(3) For every m, find all such times $t_{m,j}$ when the resonance condition $\epsilon_m'(t_{m,j}) = \mu$ is satisfied.

(4) At each resonance time $t = t_{m,j}$, compute the corresponding partial charge $q_\alpha^{m,j} = e\Gamma_\alpha^m/\Sigma_{\alpha'}\Gamma_{\alpha'}^m$.

(5) Calculate the total pumped charge as

$$Q_\alpha^R = -\sum_{m,j} q_\alpha^{m,j} \text{sgn}\, \dot{\epsilon}_m'(t_{m,j}), \tag{22}$$

or set $Q_\alpha^R = 0$ if no resonances were found in step 3.

The application of this algorithm is justified under the conditions listed in the beginning of this section. The most important condition is the consistency of the perturbation expansion, $\Gamma_\alpha^m(t_{m,j}) \ll \Delta(t_{m,j})$, where $\Delta(t)$ is the level spacing of $\mathcal{H}^d(t)$ at the Fermi surface.

The algorithm will fail for certain values of the adjustable (not pumping) parameters of the model, for which the number of resonance points found in step 3 changes. This change corresponds to the appearance (or annihilation) of a pair of loading/unloading resonances. Such a crossover is usually manifested by a sharp change (a step) (Refs. 16,25) in the total pumped charge, as function of the model parameters.

IV. EXAMPLE: TURNSTILE MODEL

We illustrate the resonance approximation by a simple example of a single energy level with adiabatically varying couplings to the left and right reservoirs (single level turnstile model).[15] Applications to more complicated models, such as pumping by surface acoustic waves,[25] will be reported elsewhere.

A. The turnstile pumping model

The single level turnstile model, discussed in Ref. 15, can be described as a special case of the general Hamiltonian (1), with $N=1$ site (and a single energy $h_{11}=\epsilon$) on the QD and with $L=2$ leads, denoted by $\alpha=l,r$. It is now convenient to use a slightly different notation: Consider an infinite chain of TB sites, enumerated by $n=0,\pm 1,\dots$. The site $n=0$, which represents the QD, has a time-independent energy ϵ and defines $\mathcal{H}_{res}^{d}=\epsilon d^{\dagger}d$, with eigenstate $|\psi\rangle$. The sites with $n>0$ ($n<0$) form the right (left) single-mode TB lead:

$$\mathcal{H}_{\alpha}^{l}=-\sum_{n=\pm 1}^{\pm\infty}J(c_{n}^{\dagger}c_{n\pm 1}+c_{n\pm 1}^{\dagger}c_{n}),\qquad(23)$$

where the upper sign refers to $\alpha=r$. The coupling operators are $L_{\alpha}=\sqrt{X_{\alpha}(t)}Jc_{\pm 1}^{\dagger}d$, with the two time-dependent pumping parameters $X_{\alpha}=\lambda_{\alpha}^{2}$.

The Hamiltonian of the leads (23) is characterized by the dispersion relation $E_{k}=-2J\cos ka$ and the retarded Green function

$$[G_{\alpha}^{l}]_{nm}=\frac{e^{ika|n-m|}-e^{ika|m+n|}}{i2J\sin ka},\qquad(24)$$

where a is the nearest-neighbor distance. The self-energy operator [Eq. (8)] is $\hat{\Sigma}=-(X_{l}+X_{r})Je^{ika}d^{\dagger}d$.

We consider the zero-temperature limit and parametrize the on-site energy as $\epsilon=(-2+\delta)J\cos\kappa a$, where the dimensionless parameter δ is a measure of the detuning of the isolated level ϵ from the Fermi energy $\mu=-2J\cos\kappa a$ in the leads. Near the band bottom one has $\delta\approx(\epsilon-\mu)/J$.

The resonance parameters at the Fermi surface are

$$\Gamma_{\alpha}=2X_{\alpha}J\sin\kappa a,$$

$$E_{0}=(-2+\delta-X_{l}-X_{r})J\cos\kappa a.\qquad(25)$$

Both Γ_{α} and E_{0} depend on time via the time-dependent couplings X_{α}, which span the parameter space $\{X_{l},X_{r}\}$. The resonance condition $E_{0}=\mu$ defines the resonance line, $X_{l}+X_{r}=\delta$. For an explicit calculation, we next choose the pumping contour to be a square with corners at points $A(X_{1};X_{1})$ and $C(X_{2};X_{2})$, as used in Ref. 15. [This is shown in Fig. 2(a), which forms an explicit example of Fig. 1].

The necessary conditions of Sec. III, for having distinct resonances, are satisfied only at the bottom of the TB band ($\sin\kappa a\ll\cos\kappa a$). As we gradually increase δ from zero, the resonance line in Fig. 2(a) moves in the direction indicated by the small arrow. The resonance line crosses the contour only if $2X_{1}\equiv\delta_{1}<\delta<\delta_{3}\equiv 2X_{2}$. Therefore, within the resonance approximation we have

$$Q^{R}/e=0,\quad\text{if}\quad\delta<\delta_{1}\quad\text{or}\quad\delta>\delta_{3}.\qquad(26)$$

For the direction of the contour shown by the arrows in Fig. 2(a), the resonance point B corresponds to loading of the dot mostly from the left ($\Gamma_{l}>\Gamma_{r}$). Its complementary resonance point D is associated with unloading mostly to the right ($\Gamma_{l}<\Gamma_{r}$). This interpretation is illustrated in Fig. 2(b).
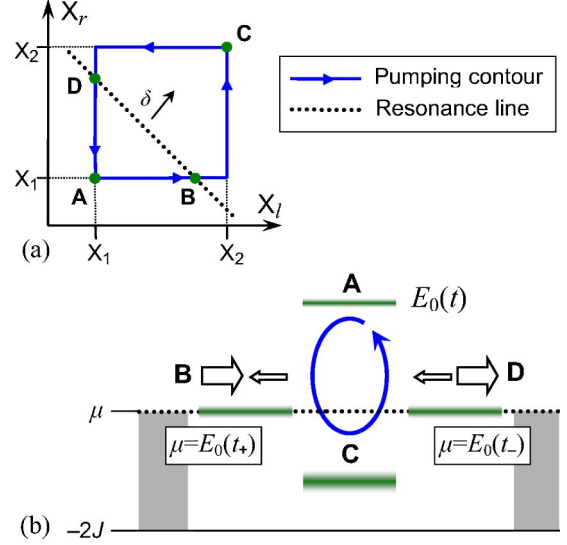

FIG. 2. (Color online) (a) The pumping contour A-B-C-D-A and the resonance line B-D for the single level turnstile model (Ref. 15). (b) Interpretation of the pumping cycle on an energy diagram. (a) The effective energy level E_{0} is above the chemical potential μ, the dot is empty. (b) Loading process with preference to the left-coming electrons. (c) The level E_{0} is below μ, the dot is occupied. (d) Unloading process with preference to the right-going electrons. The asymmetry between B and D creates the nonvanishing total pumped charge. The arrows indicate schematically the direction and the relative magnitude of the current pulses caused by each resonance.

At the lower left part of the contour, $\delta<\delta_{2}=(\delta_{1}+\delta_{3})/2=X_{1}+X_{2}$, the resonance points are $D(X_{1},\delta-X_{1})$ and $B(\delta-X_{1},X_{1})$. The partial charges pumped from the left [using Eqs. (16) and (25)] are

$$\Delta Q_{l}^{D}=-e\frac{2X_{l}J\sin\kappa a}{2(X_{l}+X_{r})J\sin\kappa a}=-e\frac{X_{1}}{\delta},\qquad(27)$$

$$\Delta Q_{l}^{B}=e\frac{\delta-X_{1}}{\delta},\qquad(28)$$

where we have used $\mathrm{sgn}\dot{E}_{0}=\mathrm{sgn}(d/dt)(-X_{l}-X_{r})=+1$ for point D. The net pumped charge is thus

$$Q^{R}/e=Q_{l}^{R}/e=(\Delta Q_{l}^{D}+\Delta Q_{l}^{B})/e=-Q_{r}^{R}/$$

$$e=1-(\delta_{1}/\delta),\quad\text{if}\quad\delta_{1}<\delta<\delta_{2}.\qquad(29)$$

A similar analysis for crossing at $D(\delta-X_{2},X_{2})$ and $B(X_{2},\delta-X_{2})$ (when $\delta_{2}<\delta<\delta_{3}$) yields

$$Q^{R}/e=(\delta_{3}/\delta)-1,\quad\text{if}\quad\delta_{2}<\delta<\delta_{3}.\qquad(30)$$

Our resonance approximation results for Q^{R}/e are shown for some typical parameters (together with the exact results, see below) in Fig. 3. These results agree qualitatively with those of Refs. 11 and 16: Q^{R}/e reaches its maximum value $(X_{2}-X_{1})/(X_{1}+X_{2})$ at $\delta=\delta_{2}$, where the resonance points B and D are farthest away from the resonance point M, which occurs at $X_{1}=X_{2}=\delta/2$. Note that Q^{R}/e approaches the
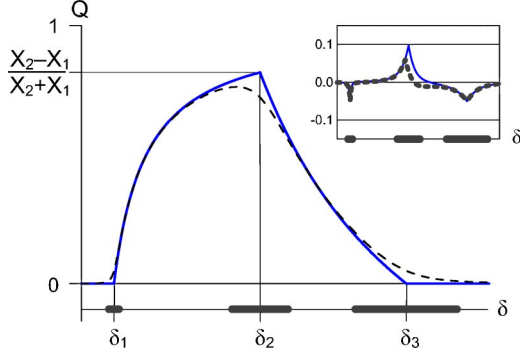
FIG. 3. (Color online) Pumped charge (in units of e) as a function of δ for $X_1 = 1/50$, $X_2 = 1/5$, and $\kappa a = \pi/20$, calculated within the resonance approximation (Q^R, blue continuous line) and exactly (Q, dashed line). Thick bars on the δ axis mark the resonance widths $\pm \Gamma/J$ around the special points $\delta_{1,2,3}$, where deviations from the exact result are anticipated. Inset: Absolute error of the resonance approximation ($Q^R - Q$)/e for the same values of δ. The thick dotted line corresponds to Q^R calculated from the transmission maxima, see text for details.

quantized value 1 when $X_2/X_1 \to \infty$, i.e., when the transmission at the resonance points [related to $4X_1 X_2/(X_1 + X_2)^2$, via Eq. (18)] vanishes. This is consistent with Ref. 11, which required that "a large part of the resonance line" be surrounded by the pumping contour.

B. Comparison with exact results

The formula (13) for the resonance current is exact in our case. Substitution of Eq. (25) into Eq. (13) and integration over the contour A-B-C-D gives the total pumped charge in the form

$$Q = \frac{e}{\pi} \int dX [F(X, X_1) - F(X, X_2)], \qquad (31)$$

where

$$F(X, Z) = \frac{(\delta - 2Z)\sin \kappa a \cos \kappa a}{(\delta - X - Z)^2 \cos^2 \kappa a + (X + Z)^2 \sin^2 \kappa a}. \qquad (32)$$

This result was obtained in Ref. 15 using the time derivatives of the scattering matrix.

In Fig. 3 we compare the exact Q and the approximate Q^R. As the resonance line in Fig. 2(a) moves from point A to C, the pumped charge rises from zero to a maximum, close to $(X_2 - X_1)/(X_2 + X_1)$, and then falls back towards zero. Except for the vicinity of the special points $\delta = \delta_1, \delta_2$, and δ_3, there is an excellent agreement between Eqs. (26), (29), and (30), and Eq. (31).

The most significant source for deviations of the exact pumped charge Q from the separated resonance result Q^R is the term proportional to $\dot{\Gamma}_\alpha$ in the expression of the pumping current (13):

$$Q - Q^R \approx \frac{e}{2\pi} \int \frac{d\Gamma_\alpha(E_0 - \mu)}{(\mu - E_0)^2 + (\Gamma/2)^2}. \qquad (33)$$
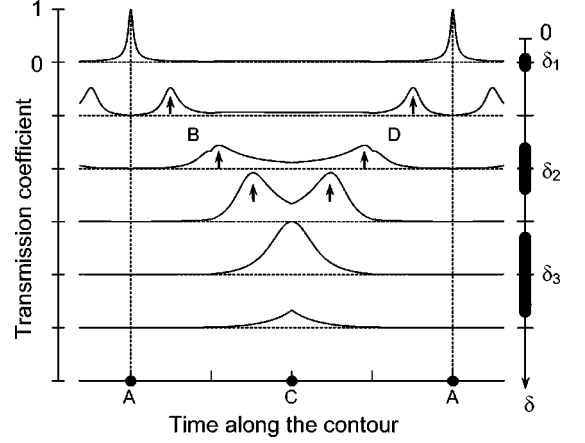

FIG. 4. Time traces of the transmission coefficient $\mathcal{T}_{lr}$ along the pumping contour for six values of δ, increasing with constant intervals from top to bottom. Two complementary resonances B and D (marked with arrows) are observed for $\delta_1 < \delta < \delta_3$ when the pumping contour crosses the resonance line [cf. Fig. 2(a)]. Thick bars on the δ axis mark the regions where the loading/unloading pumping mechanism fails.

In our example, Eq. (25) yields $d\Gamma_\alpha/dE_0 = \Gamma_\alpha/\dot{E}_0 = -2 \tan(\kappa a)$ when the resonance is on an edge of the contour curve where only X_α varies. Thus, the integral in Eq. (33) is negligibly small as long as the distance between the resonance point and a corner of the square contour is larger than Γ/J. Indeed, this agrees with Fig. 3, where the regions $|\delta - \delta_i| < \Gamma/J$ are indicated by horizontal bars on the δ axis.

Figure 4 shows the Breit-Wigner transmission coefficient $\mathcal{T}_{lr}$, calculated from Eqs. (18) and (25) as a function of time (defined homogeneously along the pumping contour) for several values of δ. As δ is increased from zero, a single peak develops at $\delta = \delta_1$, then splits into two independent resonances B and D, which move along the pumping contour and finally merge at $\delta = \delta_3$ and disappear. By comparing Fig. 4 to Fig. 3 one can follow the correlation between the presence of separate well-defined transmission peaks and the validity of the resonance approximation for the pumped charge.

C. Relation to transmission

The quantitative relation between the pumped charge and the transmission (conductance) has been discussed in Sec. III B. In order to illustrate this discussion, let us assume that the transmission traces (Fig. 4) are the *only* available data for our two terminal system. One observes two resonances in the range $\delta_1 < \delta < \delta_3$—both giving the same value of the peak transmission $\mathcal{T}_{max}$. One of the resonances represents loading, contributing $\Delta Q_\alpha^{res} > 0$, while the other one necessarily represents unloading (with $\Delta Q_\alpha^{res} < 0$). If we make a mistake at this stage and take the wrong sign in Eq. (17), it will only change the assumed pumping direction, $Q^R \to -Q^R$. Let us treat the first resonance as loading and calculate the partial charge pumped from the left reservoir, $\Delta Q_l^{res} > 0$. Solution of Eqs. (17) and (19) gives two roots, $\Delta Q^{res} = e(1 \pm \sqrt{1 - \mathcal{T}_{max}})/2$, and one must decide which of the two corresponds to ΔQ_l^{res}. The same dilemma holds for the second

resonance. Considering all four options yields three possible answers $Q^R = \pm Q'$ and 0, where $Q' = e\sqrt{1 - \mathcal{T}_{max}}$. The correct result ($Q^R = Q'$) may be chosen as the one which gives the best fit to the data of the pumping calculation/experiment. Once the uncertain signs have been chosen correctly, there is no need to repeat this "trial-and-error" procedure, since the contour changes continuously. Of course, if some features of the pumping contour design are known (such as which coupling is dominant in different regions), the sign uncertainties are much easier to resolve.

The result of the above calculation $|Q - Q^R|/e$ is shown in the inset of Fig. 3 by a thick dotted line. One can see that both ways of calculating Q^R [from the analytic expressions (26), (29), and (30) and from using the peak transmission] give similar small deviations from the exact value Q of the pumped charge.

We now leave our specific example, and consider Eq. (33) for a general resonance. As seen in the example, the integral in Eq. (33) becomes nonzero whenever $\gamma_\alpha = \dot{\Gamma}_\alpha / \dot{E}_0$ is not a time-independent constant during the whole resonance. For nonconstant γ_α, the largest deviation $|Q - Q^R|$ arises when γ_α changes sign exactly at the resonance point $E_0 = \mu$; one then finds that $|(Q - Q^R)/Q^R| < x \max|\gamma_\alpha|$, where x is a number of order unity, which depends on the details of the contour. These considerations justify condition (3) in the beginning of Sec. III.

V. CONCLUSIONS

We have considered a general model of adiabatic quantum pumping of spinless noninteracting electrons, in the coherent resonant tunneling regime. In the limit of distinct transmission resonances along the pumping contour, the pumped charge is given by a sum of individual contributions due to each resonance. During each resonance one electron either enters or leaves the system, with the probability distribution between different reservoirs given by the corresponding tunneling rates $\Gamma_\alpha / \hbar$.

We have clarified the role of quantum coherence in the resonance-assisted pumped charge quantization by showing that quantization arises due to population of discrete resonant states with preference to a single reservoir in each resonance. A quantitative and experimentally verifiable relation between the pumped charge and the peak conductance has been proposed. The resonance approximation also provides a simple calculational algorithm for analyzing complex pumping potentials.

Our results remain valid if (1) the spacing Δ between different resonant levels is much larger than Γ_α, kT; (2) the relative magnitude of the couplings Γ_α to different reservoirs does not change much during a resonance; (3) the condition $\hbar \dot{E}_0 \ll \max(\Gamma, kT)$ is not violated.

Systematic extension of the resonance approximation to situations when electron-electron interactions play an essential role is a topic for further future study.

APPENDIX: FORMULA FOR THE PUMPED CURRENT

In this appendix, we use standard scattering theory relations[41,27] to derive Eq. (6) from Eq. (5). The scattering states $|\chi_{k\alpha}\rangle$ can be obtained from the Lippman-Schwinger equation

$$|\chi_{k\alpha}\rangle = (1 + GL_\alpha^\dagger)|w_{k\alpha}\rangle, \tag{A1}$$

where $G = (E + i0 - \mathcal{H})^{-1}$ is the retarded Green function taken at energy $E = E_{k\alpha}$. The time t enters Eq. (A1) as a parameter.

Defining projection operators $\hat{P}^d$ and $\hat{P}_\alpha$ onto the QD and onto lead α, one has

$$\mathcal{H}^d = \hat{P}^d \mathcal{H}^d \hat{P}^d, \quad G_d = \hat{P}^d G_d \hat{P}^d, \quad \hat{P}_\alpha \mathcal{H} \hat{P}_{\alpha'} = \delta_{\alpha\alpha'} \mathcal{H}_\alpha^l,$$

$$L_\alpha = L_\alpha \hat{P}^d = \hat{P}_\alpha \mathcal{H} \hat{P}^d, \quad \hat{P}^d|w_{k\alpha}\rangle = 0, \tag{A2}$$

and therefore

$$M_\alpha^d \equiv \langle \chi_{k\alpha}|\dot{\mathcal{H}}^d|\chi_{k\alpha}\rangle = \langle w_{k\alpha}|L_\alpha G_d^\dagger \dot{\mathcal{H}}^d G_d L_\alpha^\dagger|w_{k\alpha}\rangle. \tag{A3}$$

To derive Eq. (7), we start from $(E - \mathcal{H})G = I$, multiply from the right by $\hat{P}^d$ and from the left by $\hat{P}_\alpha$ and—using the identity $\hat{P}^d + \Sigma \hat{P}_\alpha = I$—obtain the relation $\hat{P}_\alpha G \hat{P}^d = G_\alpha^l L_\alpha G_d$. A similar multiplication from the left by $\hat{P}^d$ then yields Eq. (7), with

$$\hat{\Sigma} = \sum_\alpha L_\alpha^\dagger G_\alpha^l L_\alpha, \tag{A4}$$

which is equivalent to Eq. (8).

Similarly, the time dependance of the coupling strengths $\lambda_\alpha(t)$ contributes to the current I_α via the matrix element $M_\alpha^l = \Sigma_{\alpha'} \langle \chi_{k\alpha}|\dot{L}_{\alpha'}|\chi_{k\alpha}\rangle + \text{H.c.}$ Using the trivial relations $\dot{L}_\alpha = (\dot{\lambda}_\alpha/\lambda_\alpha)L_\alpha$ and $\hat{P}_{\alpha'}|w_{k\alpha}\rangle = \delta_{\alpha\alpha'}|w_{k\alpha}\rangle$, a straightforward calculation gives

$$M_\alpha^l = \langle w_{k\alpha}|L_\alpha \left[G_d^\dagger \dot{\mathcal{E}} G_d L_\alpha^\dagger + \frac{\dot{\lambda}_\alpha}{\lambda_\alpha}(G_d + G_d^\dagger) \right] L_\alpha^\dagger|w_{k\alpha}\rangle. \tag{A5}$$

The normalization to the unit flux $\langle w_{k\alpha}|w_{k'\alpha}\rangle = (2\pi/v_{k\alpha})\delta(k - k')$ implies that $\hat{P}_\alpha = \int (dk/2\pi)v_{k\alpha}|w_{k\alpha}\rangle\langle w_{k\alpha}|$. Using also the standard relation $i(G_\alpha^l - G_\alpha^{l\dagger}) = |w_{k\alpha}\rangle\langle w_{k\alpha}|/\hbar$, we find the relation

$$\hbar \hat{\Gamma}_\alpha = L_\alpha^\dagger|w_{k\alpha}\rangle\langle w_{k\alpha}|L_\alpha. \tag{A6}$$

Introducing the trace over the QD's subspace, using Eq. (A6) in Eqs. (A3) and (A5), and substituting the results into $\mathcal{I}_\alpha = (M_\alpha^d + M_\alpha^l)/\hbar$, we finally end up with Eq. (6).

[1] M. Switkes, C.M. Marcus, K. Campman, and A.C. Gossard, Science **283**, 1905 (1999).

[2] L.P. Kouwenhoven, A.T. Johnson, N.C. van der Vaart, C.J.P.M. Harmans, and C.T. Foxon, Phys. Rev. Lett. **67**, 1626 (1991).

[3] R.L. Kautz, M.W. Keller, and J.M. Martinis, Phys. Rev. B **60**, 8199 (1999), and references therein.

[4] I.L. Aleiner and A.V. Andreev, Phys. Rev. Lett. **81**, 1286 (1998).

[5] P.W. Brouwer, Phys. Rev. B **58**, 10 135 (1998).

[6] F. Zhou, B. Spivak, and B. Altshuler, Phys. Rev. Lett. **82**, 608 (1999).

[7] B.L. Altshuler and L.I. Glazman, Science **283**, 1864 (1999).

[8] T.A. Shutenko, I.L. Aleiner, and B.L. Altshuler, Phys. Rev. B **61**, 10 366 (2000).

[9] Y. Wei, J. Wang, and H. Guo, Phys. Rev. B **62**, 9947 (2000).

[10] M. Moskalets and M. Büttiker, Phys. Rev. B **64**, 201305 (2001).

[11] Y. Levinson, O. Entin-Wohlman, and P. Wölfe, Physica A **302**, 335 (2001).

[12] J.E. Avron, A. Elgart, G.M. Graf, and L. Sadun, Phys. Rev. Lett. **87**, 236601 (2001).

[13] Y. Makhlin and A.D. Mirlin, Phys. Rev. Lett. **87**, 276803 (2001).

[14] B. Wang, J. Wang, and H. Guo, Phys. Rev. B **65**, 073306 (2002).

[15] O. Entin-Wohlman, A. Aharony, and Y. Levinson, Phys. Rev. B **65**, 195411 (2002).

[16] O. Entin-Wohlman and A. Aharony, Phys. Rev. B **66**, 035329 (2002).

[17] P. Sharma and C. Chamon, Phys. Rev. B **68**, 035321 (2003).

[18] M. Ya. Azbel', Europhys. Lett. **18**, 537 (1992).

[19] J. Wang and B. Wang, Phys. Rev. B **65**, 153311 (2002).

[20] M. Blaauboer, Phys. Rev. B **65**, 235318 (2002).

[21] M. Blaauboer and E.J. Heller, Phys. Rev. B **64**, 241301 (2001).

[22] T. Aono, Phys. Rev. B **67**, 155303 (2003).

[23] A. Banerjee, S. Das, and S. Rao, cond-mat/0307324 (unpublished).

[24] D.V. Averin and K.K. Likharev, in *Mesoscopic Phenomena in Solids*, edited by B.L. Altshuler, P.A. Lee, and R.A. Webb (Elsevier, Amsterdam, 1991), p. 173.

[25] A. Aharony and O. Entin-Wohlman, Phys. Rev. B **65**, 241401 (2002).

[26] O. Entin-Wohlman, A. Aharony, and V. Kashcheyevs, J. Phys. Soc. Jpn. **72A**, 77 (2003).

[27] S. Datta, *Electronic Transport in Mesoscopic Systems* (Cambridge University Press, Cambridge, 1997).

[28] G. Breit and E. Wigner, Phys. Rev. **49**, 519 (1936).

[29] A.D. Stone and P.A. Lee, Phys. Rev. Lett. **54**, 1196 (1985).

[30] M. Büttiker, IBM J. Res. Dev. **32**, 63 (1988).

[31] M. Moskalets and M. Büttiker, Phys. Rev. B **66**, 205320 (2002).

[32] B. Wang, J. Wang, and H. Guo, Phys. Rev. B **68**, 155326 (2003).

[33] S.A. Wolf, D.D. Awschalom, R.A. Buhrman, J.M. Daughton, S. von Molnár, M.L. Roukes, A.Y. Chtchelkanova, and D.M. Treger, Science **294**, 1488 (2001).

[34] Y. Alhassid, Rev. Mod. Phys. **72**, 895 (2000).

[35] H.A. Weidenmüller, Phys. Rev. B **65**, 245322 (2002).

[36] C.A. Stafford, Phys. Rev. Lett. **77**, 2770 (1996).

[37] A.P. Klein and A.J. Heeger, Phys. Rev. **144**, 458 (1966).

[38] B. Wang and J. Wang, Phys. Rev. B **65**, 233315 (2002).

[39] A. Alekseev, cond-mat/0201474 (unpublished).

[40] M. Büttiker, Phys. Rev. Lett. **57**, 1761 (1986).

[41] M. Paulsson, cond-mat/0210519 (unpublished).

[42] A.-P. Jauho, N.S. Wingreen, and Y. Meir, Phys. Rev. B **50**, 5528 (1994).

[43] B. Wang, J. Wang, and H. Guo, J. Appl. Phys. **86**, 5094 (1999).

[44] M. Büttiker, H. Thomas, and A. Prêtre, Z. Phys. B: Condens. Matter **94**, 133 (1994).

[45] Distinct charge steps during the pumping cycle have been presented in Ref. 25, but with no detailed quantitative discussion of their relation to resonances.

[46] Equation (6) can be used to demonstrate the equivalence between the formalism used in Refs. 15, 25, 16 and 26 and the adiabatic limit of the Keldysh nonequilibrium Green function techniques (Refs. 42,38). Without loss of generality one can set $\dot{\lambda}_\alpha = 0$, and use the cyclic property of the trace in Eq. (6). Extending the trace to the whole system and multiplying the result by 2 to restore spin degeneracy gives the charge injected into the system during an infinitesimal time δt as $\delta Q_\alpha = -(e/\pi)\int dE f'(E)\mathrm{Tr}[G^\dagger \hat{\Gamma}_\alpha G \dot{\mathcal{H}} \delta t]$. This is identical to Eq. (4) of Ref. 38, which in turn was proved (Refs. 38,43) equivalent to the Brouwer formulas (Refs. 5,44).

[47] The use of the equilibrium ρ is justified because adiabatic pumping is invariant to the rescaling of time and can always be performed quasistatically.

Chapter 4

Quantized charge pumping by surface acoustic waves in ballistic quasi-1D channels

The content of this chapter has been previously available as

**THE EUROPEAN
PHYSICAL JOURNAL B**

Quantized charge pumping by surface acoustic waves in ballistic quasi-1D channels

V. Kashcheyevs[1,a], A. Aharony[1,2], and O. Entin-Wohlman[1,2,3]

[1] School of Physics and Astronomy, Raymond and Beverly Sackler faculty of Exact Sciences, Tel Aviv University, Tel Aviv 69978, Israel
[2] Department of Physics, Ben Gurion University, Beer Sheva 84105, Israel
[3] Albert Einstein Minerva Center for Theoretical Physics at the Weizmann Institute of Science, Rehovot 76100, Israel

Abstract. Adiabatic pumping of electrons induced by surface acoustic waves (SAWs) in a ballistic quasi-1D quantum channel is considered using an exactly solvable tight-binding model for non-interacting electrons. The single-electron degrees of freedom, responsible for acoustoelectric current quantization, are related to the transmission resonances. We study the influence of experimentally controllable parameters (SAW power, gate voltage, source-drain bias, amplitude and phase of a secondary SAW beam) on the plateau-like structure of the acoustoelectric current. The results are consistent with existing experimental observations.

PACS. 73.23.-b Electronic transport in mesoscopic systems – 73.50.Rb Acoustoelectric and magnetoacoustic effects – 73.40.Ei Rectification

1 Introduction

Single electron transport through low-dimensional mesoscopic structures, driven by surface acoustic waves (SAWs), is a subject of active experimental [1–9] and theoretical [10–18] research, with potential applications in metrology [19] and new computation technologies [20]. In a typical experimental setup, a quasi-one dimensional ballistic channel is defined in a AlGaAs/GaAs heterostructure and a SAW is launched in the longitudinal direction at a frequency $\omega/2\pi$ of several GHz. Under appropriate conditions, the acoustoelectric dc current I exhibits a staircase plateau-like structure as function of the gate voltage (which controls the depletion of the channel) and of the SAW power. At the plateaus, the current saturates at quantized values $I = e(\omega/2\pi)m$, corresponding to the transfer of an integer number m of electrons per each period of the SAW (here e is the electron charge). The first plateau is the most flat and robust to changes in the control parameters; the higher plateaus become less and less pronounced as the plateau number m is increased. In addition, the effect of factors such as source-drain bias [1,2,5], temperature [1,7], gate geometry [4], a secondary SAW beam [2,4], and perpendicular magnetic field [5] on the staircase structure and the quality of the first plateau have been studied experimentally.

In the experiment, the plateaus are observed below the conductance pinch-off, when electrons in the source

and in the drain reservoirs are separated by a potential barrier. This observation forms the basis for the simple qualitative explanation of the quantized transport which has been proposed in the first experimental report [1] and further refined in references [4,10,11]. They argue that when the wavelength λ of the SAW is comparable with the size of the depleted region L (as it is in the experiments [1,2,4]), a single potential well forms on top of the static barrier. This potential well then acts as a dynamic quantum dot, which can hold an integer number of electrons due to the Coulomb blockade effect. The captured electrons are transferred from one side of the barrier to the other, with possible quantization errors due to back-tunnelling [10,11]. In the above description, the formation of the quantum dot and the transport of the localized electrons are treated separately. Particular effects which have been studied theoretically within this picture are the non-adiabatic effects at the quantum dot's formation stage [12], and the classical dynamics of the already confined interacting electrons [15].

A different perspective on the problem has been suggested in references [16,21]. This approach relates the acoustoelectric transport to adiabatic quantum pumping of non-interacting electrons. The external potential, generated by the SAWs and by the control gates, is viewed as a perturbation acting on a coherent quantum wire [22]. The resulting "staircase" structure of the acoustoelectric current and its dependence on model parameters within this approach have been studied in references [16,18], using

[a] e-mail: `slava@latnet.lv`

the adiabatic approximation in conjunction with an exactly solvable one-dimensional (1D) tight-binding model. This theory yields a crossover from a non-quantized acoustoelectric transport to the quantized limit as the SAW power and/or the static barrier height are increased. Although this picture requires the Coulomb interaction in order to set the energy scale of the problem [11,12,15], the main qualitative features of the experiment can be reproduced within a model of non-interacting spinless electrons [13,16].

In this paper we extend the results of reference [16]. The mechanism of quantized transport is elucidated by using a resonance approximation for adiabatic pumping [23]. Both current quantization and transmission resonances are determined by the quasi-bound states of the electrons captured by a moving potential well. New effects, including the influence of a counter propagating SAW, static potential asymmetry and source-drain bias on the number and shape of the quantization steps, are considered. We compare our qualitative conclusions with the published theoretical and experimental results. In particular, tuning the amplitude and the phase of a weak secondary SAW is found to improve the quantization by accordance with an earlier experimental report [4]. For this effect, we propose a new quantitative relation between the phase and the amplitude of the optimal secondary SAW which can be easily checked using existing experimental setups.

The results are presented as follows. In Section 2, we describe the model [16] and the algorithms for calculating the adiabatic current. In Section 3, we explain the formation of the integer plateaus and make quantitative analytic estimates by applying the resonance approximation [23] to the model of reference [16]. Building on these results we analyze in Section 4 additional factors, not described previously, such as reflected SAWs, source-drain bias and gradual screening of the pumping potential. Finally, a discussion of our results in the context of related work is presented in Section 5, together with several conclusions.

2 The model

2.1 The Hamiltonian

The choice of an adequate theoretical model for a mesoscopic wire is a highly non-trivial task even in the absence of time-dependent potentials. The nanostructures under study are narrow constrictions in a two-dimensional (2D) electron gas, formed either by electrostatic gating [2] or by shallow etching [5]. A realistic modelling of the corresponding 2D potential field requires a self-consistent numerical calculation [10,12], and thus limits the exploration of the parameter space. Suitable analytic approximations (e.g., a saddle-point potential [21] or a combination of Gaussian functions [15]) for the 2D geometry can be used, but the necessary calculations of the acoustoelectric effect are still heavily complicated by the lack of any translational symmetry.
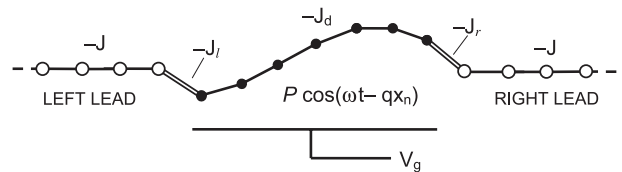
Fig. 1. One-dimensional discrete model for SAW-induced pumping.

In contrast, 1D models of SAW-induced pumping [10,13,16] do not account for the details of the experimental geometry but still capture the basic aspects of quantized transport. The underlying physical assumption is that only electronic states in the lowest transverse mode of a quantum wave-guide play an active role in the transport and the inter-mode scattering can be ignored. The use of this assumption is indirectly supported by two experimental observations: (1) in the absence of SAWs, the samples demonstrate conductance quantization which means that the gradual change in the gate voltage depletes the transversal modes one by one; (2) the relevant regime for the SAW-induced current quantization is just below the depletion threshold where the lowest transversal mode dominates the transport.

In the present paper, the system is described by the simple 1D Hamiltonian of reference [16]. The Hamiltonian is defined on a discrete chain of points (sites) which represent the nanostructrure and the two ideal semi-infinite leads connecting its ends to the electronic reservoirs (Fig. 1). The external potentials due to the gates and the SAWs are assumed to be completely screened in the leads, and act only in the nanostructure.

The leads are characterized by vanishing on-site energies and nearest-neighbors hopping amplitudes $-J$. An electron moving in the lead has the energy $E(k) = -2J\cos ka$, where k is the wave vector and a is the inter-site distance. Note that for $ka \lesssim \pi/2$ the motion is equivalent to that of a free electron with an effective mass $m^* = \hbar^2/(2Ja^2)$. The dynamics of the electrons inside the nanostructure is defined by a three-diagonal $N \times N$ Hamiltonian matrix, $\mathcal{H}_0(t)$, with nearest-neighbors hopping amplitudes $-J_d$ and diagonal on-site energies ϵ_n ($n = 1, 2, \ldots N$ is the site number). The connection between the ideal leads and the perturbed part of the channel is introduced through a hopping amplitude $-J_l$ ($-J_r$) between the left (right) lead and the site 1 (N) of the nanostructure. The resulting full Hamiltonian of the quantum wire is:

$$\mathcal{H} = \sum_{n=1}^{N} \epsilon_n \left|n\right\rangle \left\langle n\right| - \sum_{n=-\infty}^{+\infty} \left(J_n \left|n\right\rangle \left\langle n+1\right| + \text{h.c.}\right), \quad (1)$$

$$\text{where } J_n = \begin{cases} J_l, & n = 0, \\ J_d, & 1 \leq n < N, \\ J_r, & n = N, \\ J, & \text{otherwise.} \end{cases}$$

For the special case of $J_n = \text{const}$ and $\epsilon_n = 0$, equation (1) describes an ideal 1D wire.

V. Kashcheyevs et al.: Quantized charge pumping by surface acoustic waves in ballistic quasi-1D channels   387

The effect of the static gate and the SAW-induced piezoelectric potential is modeled through the space and time dependence of the on-site energies $\epsilon_n(t)$. The simplest case is that of a rectangular barrier and a single running wave, as introduced in reference [16],

$$\epsilon_n(t) = -V_g + P \cos(\omega t - q x_n) . \qquad (2)$$

Here, V_g is the gate voltage (in energy units), q is the wave-vector of the SAW, and P is the amplitude of the piezoelectric potential, induced by a SAW running from left to right (for $q > 0$). The origin of the spatial coordinate $x_n = (n-1)a - L/2$ is chosen to be at the middle of the channel, where $L = (N-1)a$ is an effective channel length.

It is important to emphasize that equation (1) is not a truly microscopic tight-binding description of the underlying crystalline lattice, but rather a discretized version of a continuous 1D Hamiltonian $\mathcal{H}(x,t) = -(\hbar^2/2m^*)(\partial^2/\partial x^2) + V(x,t)$. The matrix elements J_d and J characterize the kinetic energy of the electrons, but not the physical tunneling between spatially localized states. Therefore, it is sufficient to include the time-dependence only in the diagonal part of $\mathcal{H}$ through $\epsilon_n(t) = V(x_n, t)$ and keep the hopping amplitudes constant[1]. In view of this, we expect only the results determined by the lower part of the tight-binding band to have direct physical implications.

The physical interpretation of J_l and J_r is more subtle, since they characterize the (abrupt) boundary between the perturbed and the ideal parts of the channel. In principle, two physically different situations are possible. One is the case of $J_l = J_r = J_d = J$, which means continuity of the effective mass and corresponds to the absence of any static potential barriers on the boundary between the leads and the nanostructure. The other possibility is to consider a closed structure, $|J_{l;r}| \ll |J|, |J_d|$, where $J_{l;r}$ have the meaning of physical tunneling amplitudes. In this case, a SAW-induced time-dependence of $J_{l;r}(t)$ is expected to play a significant role as in turnstile pumping mechanism [22,23].

In the present work, we consider time-independent hopping amplitudes only and find that the ratios $|J_{l;r}^2/(JJ_d)|$ have little influence on the results (see Sect. 3.1 below). Therefore, the simplest assumption, $|JJ_d| = |J_l|^2 = |J_r|^2$, will be used in the exact numerical calculations. The other option, of large *and* SAW-sensitive tunnelling barriers at the channel exits, has been recently considered in experiment [9,24] and constitutes an interesting topic for a separate study.

2.2 The acoustoelectric current

The discrete nature of our model Hamiltonian allows for an exact calculation of the *adiabatic* instantaneous cur-

[1] One could consider, in principle, a SAW-induced time-dependence of $J_n(t)$ coming from some microscopic model. The argumentation of the resonance approximation would still be applicable (Sect. 3.1), but certain specific results may depend on the details of the instantaneous spectrum of $\mathcal{H}_0(t)$.

rent for any strength of the pumping potential. Formally, the adiabatic approximation is justified when the excitation energy $\hbar\omega$ ($10\,\mu$eV for a SAW of several GHz frequency) is less than any other scale governing the energy dependence of the scattering states [21,22]. In practice, the validity regime of the adiabatic approximation in open systems is a rather complicated subject [22,25]. We note that the experimentally observed acoustoelectric current is proportional to ω [2,6], which is a property of an adiabatic current. The next order corrections to the adiabatic current can be derived analytically [22,18]. However, the actual calculation for our Hamiltonian is rather involved and is beyond the scope of the present paper. In view of this, we restrict the following discussion to the adiabatic case.

The adiabatically-pumped current flowing between two reservoirs with equal electrochemical potentials $\mu_l = \mu_r$, is usually calculated using the Brouwer formula [26,27]. We use an equivalent formalism, developed in reference [22], which also includes the effects of a finite bias $eV_{SD} \equiv \mu_l - \mu_r \neq 0$. The total instantaneous current, $I_\alpha(t)$, of spinless electrons from the lead $\alpha = l, r$ into the nanostructure consists of two parts, $I_\alpha(t) = I_\alpha^{\text{pump}} + I_\alpha^{\text{bias}}$. These two parts can be conveniently written down using the instantaneous scattering states $|\Psi_\alpha(t)\rangle$ (normalized to a unit flux), the instantaneous transmission coefficient $\mathcal{T}(t)$ and the overall scattering phase $\theta(t)$ of the nanostructure [22]

$$I_\alpha^{\text{pump}} = \frac{e}{4\pi\hbar} \int dE \, \langle\Psi_\alpha(t)| \dot{\mathcal{H}} |\Psi_\alpha(t)\rangle \frac{\partial(f_l + f_r)}{\partial E} , \qquad (3)$$

$$I_\alpha^{\text{bias}} = \frac{e}{2\pi\hbar} \int dE \left\{ (f_l - f_r)\mathcal{T} + \frac{\hbar}{2}\frac{\partial(f_l - f_r)}{\partial E}\mathcal{T}\dot{\theta} \right\} . \qquad (4)$$

Here $f_\alpha(E) = 1/[1 + e^{\beta(E-\mu_\alpha)}]$ is the Fermi distribution with $\beta = 1/k_B T$ (T is the temperature). If the system is unbiased, then $I_\alpha^{\text{bias}} = 0$ and equation (3) can be shown to reproduce [22,23] the Brouwer formula [26,27]. On the other extreme, if no pumping potential is applied, $I_\alpha^{\text{pump}} = 0$ and equation (4) leads to the Landauer formula [28] for the conductance, $G = (e^2/h)\mathcal{T}$.

For most of the discussion we assume both the bias voltage V_{SD} and the temperature T to be zero. In this case only electrons at the Fermi energy $\mu_l = \mu_r = E_F$ participate in the scattering. Solving the scattering problem for the potential (2) and using equation (3) yields the charge Q pumped over one period (the average dc component of the current) [16],

$$Q = \int_0^{2\pi/\omega} dt \, I_l^{\text{pump}}(t) = \frac{e\tilde{J}_l \sin ka}{\pi} \int_0^{2\pi/\omega} dt \sum_{n=1}^N \dot{\epsilon}_n |g_{n,1}|^2 , \qquad (5)$$

$$[g^{-1}]_{n,n'} = [E\boldsymbol{I} - \mathcal{H}_0]_{n,n'} + \delta_{n,n'} e^{ika} \left(\delta_{n,1}\tilde{J}_l + \delta_{n,N}\tilde{J}_r \right) , \qquad (6)$$

where $\tilde{J}_{l;r} \equiv J_{l;r}^2/J$ and k is the Fermi wavenumber, $E_F \equiv E(k)$. The instantaneous transmission is

$$\mathcal{T}(t) = 4|g_{N,1}|^2 \, \tilde{J}_l \tilde{J}_r \, \sin^2 ka \,. \qquad (7)$$

The integrand in equation (5) is a meromorphic function of $z = \exp(i\omega t)$, with $2N$ pairs of complex conjugate poles. Therefore, the integration of equation (5) may be carried out exactly, once the positions of the poles are determined by solving numerically the corresponding algebraic equation of degree $2N$.

2.3 Resonance approximation

The second term on the r.h.s. of equation (6) is the self-energy addition to the Green's function of the isolated channel, due to the coupling to the external leads. When the latter is sufficiently small, the total pumped charge can be divided into contributions from separate single-particle levels of $\mathcal{H}_0$. A systematic development of this approach leads to the resonance approximation for pumping, which is discussed in detail in reference [23]. Here we summarize the resulting algorithm for calculating the pumped charge in the this approximation.

1. Solve the instantaneous eigenvalue problem $\sum_{n'} [\mathcal{H}_0]_{n,n'} \, \psi_{n'}^{(m)} = E_m \psi_n^{(m)}$ and obtain the approximate resonance energies $E_m(t)$.

2. Calculate the time-dependent decay widths of each resonance into each lead,

$$\left\{ \Gamma_l^{(m)}, \Gamma_r^{(m)} \right\} = \left\{ \tilde{J}_l \big|\psi_1^{(m)}\big|^2, \tilde{J}_r \big|\psi_N^{(m)}\big|^2 \right\} \sin ka \,. \qquad (8)$$

3. For each m, find all such times $t_{m,j}$ at which the resonance condition $E_m(t_{m,j}) = E_F$ is satisfied.

4. At each resonance time $t = t_{m,j}$, compute the partial charge transferred between the left lead and the mth quasibound state in the channel,

$$\Delta Q_{m,j} = \left. \frac{e \, \Gamma_l^{(m)}}{\Gamma_l^{(m)} + \Gamma_r^{(m)}} \right|_{t=t_{m,j}} \,. \qquad (9)$$

5. Calculate the total charge pumped from left to right[2]:

$$Q^{\mathrm{res}} = -\sum_{m,j} \Delta Q_{m,j}\,\mathrm{sgn}\dot{E}_m(t_{m,j}) \,, \qquad (10)$$

or set $Q^{\mathrm{res}} = 0$ if no resonances were found in step 3.

The algorithm has a direct physical interpretation [23]. Whenever the energy E_m of a (quasi-)bound state crosses the Fermi level E_F, an electron either occupies ("loading") or leaves ("unloading") this state. The corresponding unit pulse of current is distributed between the channels proportionally to the $\Gamma_\alpha^{(m)}$'s. Except for specifically designed

---

[2] Due to charge conservation, it is sufficient to calculate the charge transfer from the left reservoir. Therefore, the channel index α is fixed to $\alpha = l$ in equations (9, 10).

Hamiltonians $\mathcal{H}_0(t)$, $Q^{\mathrm{res}} \to Q$ in the limit of vanishing couplings $\Gamma_\alpha^{(m)} \to 0$.

The resonance approximation fails when either (i) the total width of a particular resonance is larger than the distance to the next energy level; or (ii) the partial decay widths $\Gamma_{l;r}^{(m)}$ change considerably while the system is at resonance [23]. As discussed in detail in the following section, these restrictions become significant for the non-quantized transport, but have little influence on the shape of the current quantization steps. In all the cases in which the resonance approximation is inadequate, we rely on the results of an exact calculation.

3 Formation of quantization steps

3.1 Application of the resonance approximation

The results of a full calculation (as outlined in Sect. 2.2) show [16] that the pumped charge, Q, follows a staircase-type dependence on the gate voltage, V_g, and/or on the SAW amplitude, P, for a wide range of the model parameters. This 'quantization' can be related to the structure of the transmission resonances [23,29,30]. We first establish this relation quantitatively and then use it to analyze various aspects of the model.

The calculation of the pumping curve can be visualized using a diagram like the one shown in Figure 2. First, one plots the instantaneous eigenvalues E_m for $V_g = 0$ as function of time ωt (curves in the right panel of Fig. 2). The small circles on the top of each curve show the time evolution of the corresponding partial charge ΔQ: the diameter of each circle is proportional to $|\Delta Q/e| < 1$; shading is determined by the sign — black ($\bullet$) for $\dot{E}_m < 0$ ("loading") and white ($\circ$) for $\dot{E}_m > 0$ ("unloading"). Once the eigenvalue diagram is constructed, the set of resonances for each particular value V_g of the gate voltage is determined graphically: a horizontal line with ordinate $E_F + V_g$ crosses the eigenvalue curves in the right panel at the points where the resonance equation $V_g + E_m(V_g = 0) = E_F$ is satisfied (step 3 of the algorithm). The abscissas of the crossing points determine the resonance times $t_{m,j}$ to be used in equations (9, 10). (The dashed horizontal lines in Figure 2 mark the extrema of the eigenvalue curves, and thus correspond to particular values of V_g at which the number of resonances changes.) Finally, the total pumped charge, $Q^{\mathrm{res}}(V_g)$, is calculated by summing up the contributions to equation (10): the magnitude and the sign of each term is given by the small circle at the respective crossing point in the right panel. The resulting pumping curve $Q^{\mathrm{res}}(V_g)$ is plotted in the left panel of Figure 2.

Several aspects of the model are illustrated by the construction in Figure 2. One can see that the quantization of the pumped charge is caused by electronic (hole) states with the lowest (highest) energy. When resonances occur, (namely, at $\{t_{m,j}\}$), these states are *localized* near one of the channel exits — either $\Gamma_l/\Gamma_r \ll 1$ or $\Gamma_l/\Gamma_r \gg 1$ — and therefore transfer almost integer charges [Eq. (9)].
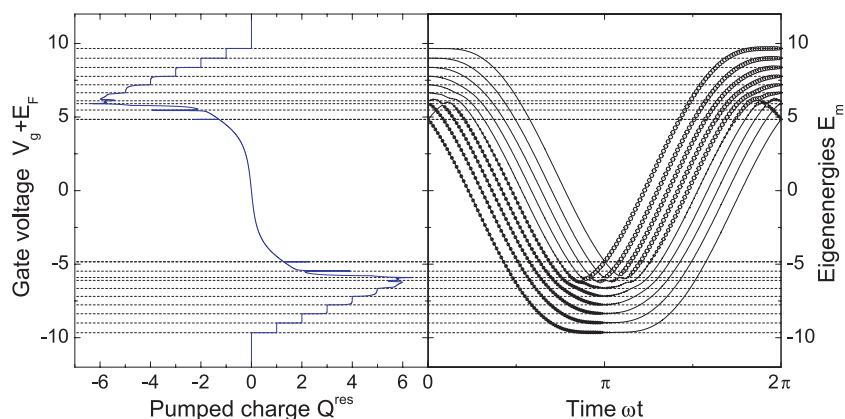
Fig. 2. (Color online) Construction of the pumping curve $Q^{\mathrm{res}}(V_g)$ in the resonance approximation. Right panel: instantaneous energy levels of $\mathcal{H}_0$ at $V_g = 0$ as function of time. Left panel: pumped charge Q^{res} (in units of e) as function of gate voltage. Horizontal dashed lines show the correspondence between sharp features in the pumping curve (left), and the change in the number of energy levels at resonance (right); see text for a detailed discussion. All energies are given in units of J_d; the parameters of the potential are: $P = 8J_d$, $\lambda = 4L$, $N = 10$.
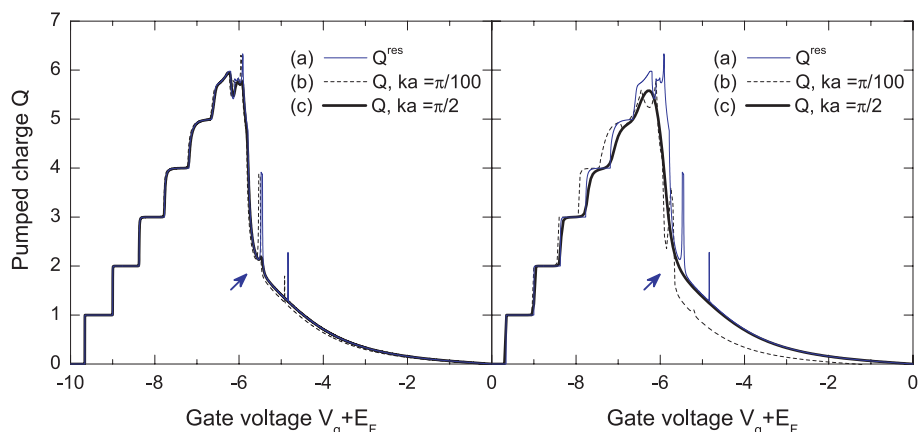
Fig. 3. (Color online) Pumped charge versus gate voltage for different external parameters: $\tilde{J} = 0.16J_d$ (left panel), $\tilde{J} = 1J_d$ (right panel), calculated in the resonance approximation (a) and exactly for the bottom of the band (b) and at the band center (c). Parameters of the potential are the same as in Figure 2.

The number of steps counts the number of localized states involved.

The exact integration [Eq. (5)] takes into account the "external" parameters of the model, ka, $\tilde{J}_l$ and $\tilde{J}_r$, which are ignored in the resonance approximation. In the following, we will consider only symmetric couplings, $\tilde{J}_l = \tilde{J}_r \equiv \tilde{J}$. We have calculated the exact pumped charge, $Q(V_g)$, for several values of the "external" parameters, but with the same pumping potential as in Figure 2. Representative results are shown in Figure 3 along with the approximate $Q^{\mathrm{res}}(V_g)$ from Figure 2 [thin (blue) line]. For sufficiently small $\tilde{J}$, the exactly calculated curves contain integer steps and sharp, non-quantized features at large values of V_g (e.g., the spikes marked by small arrows in Fig. 3). The first steps are robust and do not change their positions as $\tilde{J}$ and ka are varied (except for a trivial shift of E_F). The top of the pumping curve and the spikes are more vulnerable: as $\tilde{J}$ is increased, the upper steps and the sharp features shift and become rounded. Narrow spikes

disappear for $\tilde{J} = J_d$ and ka close to the center of the band [see curve (c) in the right panel of Fig. 3].

The resonance approximation reproduces all the details of the exact calculation for $\tilde{J} \ll J_d$, because the resonance widths in equation (8) vanish in the limit of $\tilde{J} \to 0$. The non-generic sharp features are determined by the surroundings of level anti-crossings (see Fig. 2), where the corresponding level spacings are tiny. As we expect form the validity condition (i) in Section 2.3, the finite resonance width effects are most important in this region. Indeed, the discrepancies between the exact and the approximate curves in Figure 3 are well correlated with the fact that the shifts and the widths of the resonance levels for a tight-binding model are proportional to $\tilde{J} \cos ka$ and $\tilde{J} \sin ka$, respectively [Eq. (8)].

We have made a similar comparison between the exact integration and the resonance approximation for several sets of "internal" parameters, P/J_d, λ/L, and N. The most important conclusion is that the stair-case structure of the pumping curve can be reliably estimated using the

resonance approximation. Hence, we will utilize this useful technique in the following as a source for various analytic estimates that will be further checked versus exact calculations.

3.2 SAW parameters and the number of quantization steps

For the lowest part of the spectrum (which is relevant for the quantized transport), the on-site energies (2) can be treated as a potential function of a continuous spatial coordinate x_n. For $\lambda > L$, only one minimum of this potential can be located inside the SAW-affected part of the channel. The position of this minimum $x_0(t) = (t - t_0)v$ moves with the sound velocity $v = \omega/q$ and passes through the middle of the channel at time $t_0 = \omega^{-1}(\pi + 2\pi \times$ integer). Electronic states localized in this moving potential well can be approximated by simple harmonic oscillator wave-functions [16]. The corresponding energy spectrum is $E_m = -P - 2J_d + \Delta(m - 1/2)$, $m = 1, 2, \ldots$, with a constant spacing $\Delta/J_d = qa\sqrt{2P/J_d}$. The lowest energy wave-function is approximately a Gaussian,

$$\psi_n^{(1)}(t) = \left(\xi^2 \pi/2\right)^{-1/4} \exp\{-[x_n - x_0(t)]^2/\xi^2\}, \quad (11)$$

with $\xi \equiv 2a\sqrt{J_d/\Delta}$. The localization length of the higher levels can be estimated as $\xi_m = \xi\sqrt{m}$.

The harmonic approximation is valid as long as the wave-packet is driven adiabatically by a parabolic well and is not perturbed neither by the ends of the channel, nor by the "hills" of the cosine-shaped potential profile. This implies the validity condition

$$\xi_m \ll \min[L/2 - |x_0(t)|, \lambda/2]. \quad (12)$$

In order to illustrate the above reasoning, we draw the attention of the reader to a set of constant and equidistant energy levels $E_m(t)$ in the right panel of Figure 2, in the vicinity of $\omega t = \pi$. The lowest energy level follows the harmonic approximation as long as the parabolic minimum is located inside the channel, that is for the fraction $\lambda/L = 1/4$ of the full period. Higher energy levels remain constant for shorter times, since their respective localization lengths entering equation (12) are longer. The harmonic structure of the energy levels translates into a sequence of equidistant steps in the pumping curve, $Q(V_g)$, with the same energy spacing Δ, as shown in the left panel of Figure 2. At each value of gate voltage, $V_g^{(m)} = E_m - E_F$, a new pair of resonances and another step in the pumping curve emerge. The plateaus are rather flat because the resonant states at the loading (unloading) moments are well localized at the entrance (exit) of the channel.

The number of quantization steps, N_{steps}, is limited by two competing mechanisms. The first limit is set by the number, N_1, of localized states that can be transferred below the Fermi energy. If x_n can be considered as continuous, the localization condition is roughly the same as
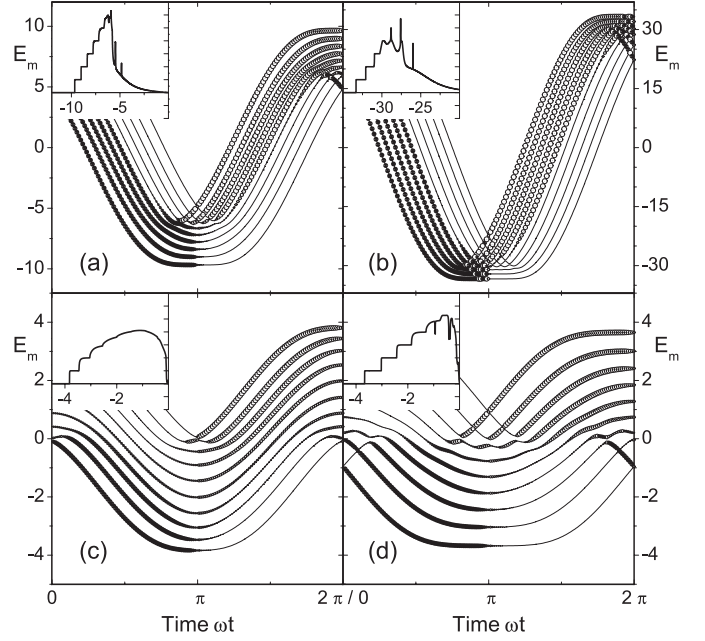
Fig. 4. Instantaneous eigenenergies E_m (in units of J_d) for $V_g = 0$, $N = 10$ and (a) $P = 8J_d$, $\lambda = 4L$; (b) $P = 32J_d$, $\lambda = 4L$; (c) $P = 2J_d$, $\lambda = 4L$; and (d) $P = 2J_d$, $\lambda = 2L$. Insets: the pumped charge Q^{res} as function of the scaled gate voltage $V_g + E_F$; the distance between the ticks on the ordinate axis is equal to a unit charge.

the validity condition (12) for the harmonic approximation. For $L < \lambda$ it follows from $\xi_{N_1} = L/2$ that $N_1 = L^2\Delta/(16J_d a^2) = (\pi\sqrt{2}/8)N(L/\lambda)\sqrt{P/J_d}$. On the other hand, for large enough P the discreteness of the tight-binding grid cannot be neglected. For a rough estimate, we assume that the continuous approximation breaks down if it yields an average distance ξ_m/m between the successive zeros of the mth wave-function, which is smaller than the inter-site spacing a. This happens for $m > N_2$, where $N_2 = N^2/(4N_1)$. Putting the two limits together we estimate the number of quantization steps, N_{steps}, as the integer closest to $\min(N_1, N_2)$. By adjusting the parameters one can obtain at best a sequence of $N/2$ steps. The optimal parameters $L = 0.3\lambda$, $N = 6$, $P = 8J_d$ of reference [16] indeed yield $N_{\text{steps}} \approx N_1 = 2.83 \approx N_2 \approx N/2$. The decrease in the number of steps with increasing L/λ reported in reference [16] corresponds to the tight-binding limited regime $N_{\text{steps}} \approx N_2 \propto \lambda/L$.

Despite a certain inherent uncertainty of our estimates, they prove useful for understanding the effect of changing the amplitude and the wavelength of the SAW (Fig. 4). In Figure 4a, the number of steps is close to optimal, $N/2 = 5$, and is limited by the localization criterion $N_{\text{steps}} \approx N_1 = 3.9$. Increasing P by a factor of 4 (Fig. 4b) reduces the number of steps due to discrete lattice effects: $N_{\text{steps}} \approx N_2 = 3.2$. One can clearly see that for higher energy levels (close to the band center) the tight-binding coupling J_d is no longer relevant: $E_m(t)$ with $m > N_2$ follow a sequence of cosine curves $P\cos(\omega t + \delta\phi)$ with equal phase differences qa. These curves correspond

to the individual on-site energies $\epsilon_n(t)$. In this regime the hopping amplitude J_d leads only to tiny anti-crossings between the energy levels, which in turn give rise to the sharp peak-like structure in the pumping curve. The effects of the tight-binding approximation become less pronounced as P is reduced below the optimum (Fig. 4c). In this case $N_{\text{steps}} \approx N_1 = 1.96$ and the peaks in the pumping curve are suppressed. The missing steps can be brought back by shortening the wave-length, as shown in Figure 4d. The estimated number of steps is now the same as in the original case (a). However, the non-parabolic shape of the potential minimum is more pronounced. Note that in case (d) the flat region for $E_0(t)$ extends over half of the period, since $\lambda = 2L$.

Note that in the physically relevant parameter regime, the tight-binding effects should not dominate. Therefore, the condition $N_1 < N_2 \Rightarrow (L/\lambda)\sqrt{P/J_d} \lesssim 1$ is obeyed in the following calculations.

4 Perturbations of the pumping potential

The pumping potential in equation (2) is of a rather high symmetry. Small perturbations – such as a static impurity or a reflected SAW — can change the shape and the position of the current quantization steps. In order to explore these effects, we add to $\epsilon_n(t)$ a smooth function of x_n and t,

$$\epsilon_n(t) = -V_g + P\cos(\omega t - qx_n) + U(x_n, t)\,. \quad (13)$$

Similarly to the situation discussed above, the structure of the relevant energy levels can be analyzed using the harmonic approximation, provided that $U(x_n, t)$ changes slowly and the travelling wave-packet is well localized: $\xi_m \, \partial U(x,t)/\partial x \ll \Delta$. The first-order approximation for the instantaneous energy,

$$E_m(t) = -P - 2J_d + \Delta(m - 1/2) + U(x_0(t), t)\,, \quad (14)$$

is valid for $|x_0(t)| \lesssim \frac{L}{2} - \xi_m$ (we consider the case $\lambda > L$). Note that $x_0(t)$ is the position of the potential well minimum, and $x_0(t_0) = 0$ (the middle of the channel). Now even within the harmonic approximation $E_m(t)$ is explicitly time-dependent and this time dependence maps onto the shape of the current quantization steps. To make a quantitative statement we note that the instantaneous wave-function remains unperturbed in first-order; $|\psi_N(t)|$ becomes greater than $|\psi_1(t)|$ at $t = t_0$. At this point, the partial decay widths are equal, $\Gamma_l^{(m)} = \Gamma_r^{(m)}$, and the resonance approximation yields a half-integer pumped charge. Therefore, the transition between the consecutive plateaus takes place at the gate voltages $V_g^{(m)} = E_m(t_0) - E_F$. In particular, half of the first step in the pumping curve is reached at the gate voltage

$$V_{1/2} \equiv V_g^{(1)} = V_0 + U(0, t_0)\,, \quad (15)$$

such that $Q(V_{1/2}) = e/2$. Here $V_0 = -E_F - P - 2J_d + \Delta/2$ is the threshold voltage for the first step in the absence of perturbations.

The resonance moment associated with the left-right transition at $V_g = V_{1/2}$ is well defined, since the energy levels $E_m(t)$ are in general no longer constant in the vicinity of $t = t_0$. Therefore, the slope of the first quantization step can be estimated from the resonance approximation. The value of the total pumped charge at $V_g = V_{1/2} + \delta V$ is dominated by the unloading resonance at $t = t_0 + \delta t$, where $\delta V = \dot{E}_1(t_0)\delta t$. The other resonances contribute charges exponentially close to an integer; for simplicity, let us consider only one loading through the left lead (which gives $\Delta Q_1 \approx e = \text{const.}$) before unloading at t_0. The contribution of the latter, $\Delta Q_2(t)$, can be calculated using the Gaussian wave-function (11) in equations (8, 9). The resulting total pumped charge $\Delta Q_1 + \Delta Q_2$ is

$$Q \approx e - \frac{e|\psi_1^{(1)}(t)|^2}{|\psi_1^{(1)}(t)|^2 + |\psi_N^{(1)}(t)|^2} = \frac{e}{2}\left(1 + \tanh\frac{Lv\delta t}{\xi^2}\right)\,. \quad (16)$$

We define the steepness of the first step, S, as

$$S \equiv \left.\frac{dQ}{dV_g}\right|_{V_g = V_{1/2}} \approx \frac{eLv}{\xi^2}\left[\left|v\frac{\partial U}{\partial x} + \frac{\partial U}{\partial t}\right|^{-1}\right]_{\substack{t=t_0 \\ x=0}}\,. \quad (17)$$

The pre-factor in equation (17) is the least accurate, since the applicability of equation (11) at the ends of the channel is marginal. Taking the absolute value in equation (17) makes the result valid for both signs of $\dot{E}_1$ at $t = t_0$. Our derivation is not justified for perturbations that yield small values of the denominator in equation (17). Then, the steepness remains bounded due to the finite resonance width.

The quantization accuracy can be estimated along similar lines. However, the results are less transparent since the energy levels involved are beyond the simple harmonic approximation.

4.1 Sensitivity to the second SAW

For a particular example of a perturbation which mimics the experimental situation, consider the following potential

$$U(x_n, t) = P^-\cos(\omega t + qx_n + \varphi) + b\,x_n/L\,. \quad (18)$$

Here P^- and φ are the amplitude and the phase of a second SAW, propagating in the negative direction. It can be generated either due to reflections of the main beam [2] or by a second transducer [4]. We also include a simple static perturbation [proportional to b in Eq. (18)] which breaks the left-right symmetry of the channel in the absence of the SAW. The estimates in equations (15, 17) become

$$V_{1/2} = V_0 - P^-\cos\varphi\,, \quad (19)$$

$$S = \frac{4N_1 e}{|b + 2qLP^-\sin\varphi|}\,. \quad (20)$$

[We have used the relation $N_1 = L^2/(4\xi^2)$ in Eq. (20).]
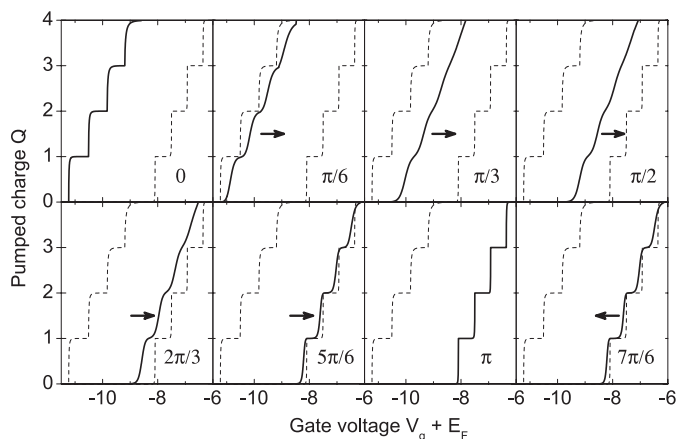
Fig. 5. Interference of two counter-propagating SAWs with an amplitude ratio $P^-/P = 0.2$. The phase difference φ is changed from 0 to $7\pi/6$, in steps of $\pi/6$, as indicated. Solid curves show the pumped charge (in units of e) versus the gate voltage (in units of J_d), the dotted lines mark the best quantization conditions achieved at $\varphi = 0$ and $\varphi = \pi$. For $\varphi \in [\pi, 2\pi]$ the pumping curves repeat the same sequence in reverse order (not shown). The parameters used are: $P = 8J_d$, $\lambda = 4L$, $N = 10$. Curves are computed using the resonance approximation.

First we consider the case of a reflected wave only ($b = 0$). A series of pumping curves for different values of the phase difference is presented in Figure 5. As can be seen from equation (19), the threshold voltage changes periodically in φ, reaching extremal values at $\varphi = 0$ and π. Between these special values of φ, the staircase structure is more smooth, and the steps are more symmetric: the convex and the concave parts of a step become almost congruent. The pumping curves are identical for $\pm\varphi$ due to the symmetry of the potential (13) with $b = 0$.

For a quantitative characterization of the second SAW effect we have determined numerically the positions and the slope of the pumping curves at $Q = e/2$ without any approximations in equation (5). The results are shown in Figure 6. Tuning the phase difference φ for a fixed amplitude ratio P^-/P to the values at which the r.h.s. of equation (20) diverges enhances the steepness of the first step by orders of magnitude. The sharpest steps are achieved at the extrema of the threshold voltage $V_{1/2}$, as shown in the inset in Figure 6 and qualitatively in Figure 5.

The above example shows that a symmetric pumping potential is favorable for quantization: the steepest plateaus are achieved without a secondary SAW or with $P^- \neq 0$ and $\varphi = 0, \pi$, when the total SAW potential $V(x_n, t) \equiv \epsilon_n(t)$ is invariant under $x_n \to -x_n$, $t \to -t + \text{const}$.

Further reduction of symmetry is achieved by choosing $b \neq 0$ and $P^- \neq 0$. Here two regimes are possible. For small b, the situation is similar to the previous case: the steepness is greatly enhanced at two values of φ between 0 and 2π, when the denominator in equation (20) vanishes. In contrast, for $b > 2qLP^-$ it is the static asymmetry of the channel that determines the slope of the steps, which now has only one wide maximum as function of φ. This
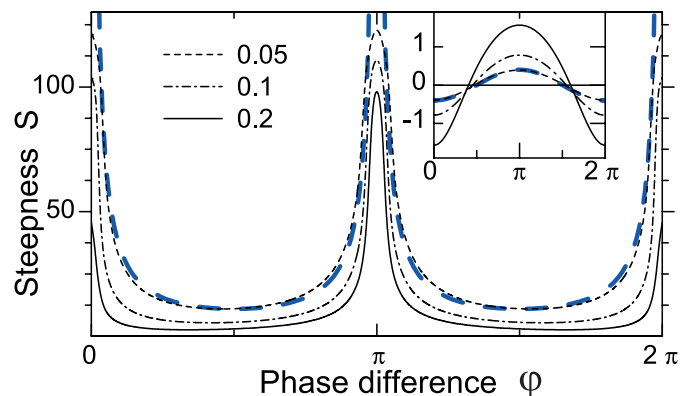
Fig. 6. (Color online) The steepness of the first step $S = dQ/dV_g$ at $Q = e(1/2)$, in units of $e\,J_d^{-1}$ for $P^-/P = 0.05, 0.1, 0.2$ as function of the phase difference φ. The curve for $P^-/P = 0.2$ corresponds to the data presented in Figure 5. Inset: threshold voltage $V_{1/2}(\varphi) - V_0$ versus φ, in units of J_d. Curves are computed exactly from equation (5). Thick dashed (blue) lines show analytic estimates, given by equations (19–20) for the smallest amplitude ratio $P^-/P = 0.05$; the pre-factor N_1 in equation (20) has been treated as a free fitting parameter. The parameters used are: $P = 8J_d$, $\lambda = 4L$, $N = 10$, $ka = \pi/5$, $\tilde{J} = 1$.
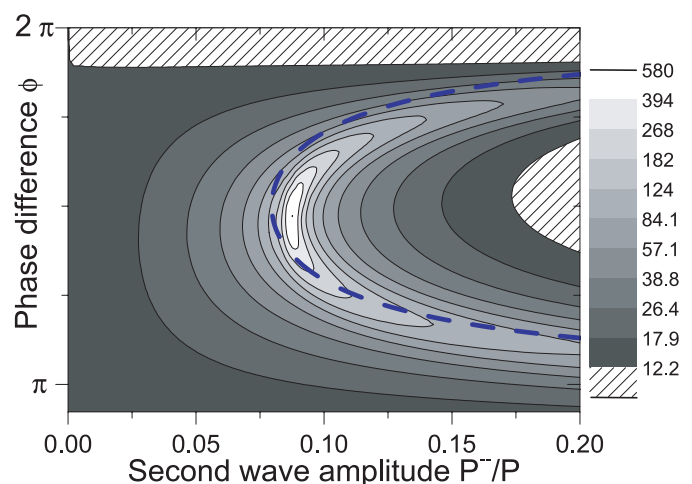
Fig. 7. (Color online) The steepness of the first step for $P = 2J_d$, $\lambda = 2L$, $N = 10$, $b = 1J_d$, as function of P^-/P and φ. The dashed (blue) line marks the combinations of amplitude and phase at which the first order estimate [Eq. (20)] diverges. Note the logarithmic grey-coding scale. The steepness without the perturbation ($P^- = b = 0$) is $S = 613\,e/J_d$.

behavior is illustrated in Figure 7, which shows the slope of the first step as a function of the second SAW amplitude and phase. The initial steepness at $P^- = 0$, $b = 1J_d$ is $S = 12.2(e/J_d)$ for the selected model parameters. That is more than an order of magnitude less than in the unperturbed ($P^- = b = 0$) case. Increasing the amplitude of the second SAW improves the steepness for $\pi \lesssim \varphi \lesssim 2\pi$ with a single wide maximum at $\varphi \approx 3\pi/2$, in agreement with equation (20). At $P^- \approx b/(2qL)$ the steepness peaks sharply, almost reaching the unperturbed value. Further increase of P^- reduces the steepness gradually, which now

has two maxima in φ, approaching $\varphi = \pi$ and $\varphi = 2\pi$ for large P^-, similarly to Figure 6. This example shows that a weak counter-propagating SAW with properly chosen amplitude and phase is able to compensate for the static asymmetry of the pumping potential and significantly improves the sharpness of the current quantization steps.

Available experimental data are consistent with our conclusions. Periodic oscillations of $V_{1/2}$ have been observed in experiments with one active SAW transducer when the frequency of the SAW was varied. The period of these oscillations was found to match a full 2π phase shift between the main SAW and a weak wave reflected from the other (inactive) transducer [2]. Later experiments, with two active transducers on both sides of the constriction, have confirmed this scenario, and a sequence of pumping curves similar to our Figure 5 has been reported [4]. Tuning of the second SAW amplitude and phase has enabled the authors of reference [4] to improve the flatness of the first quantization plateau.

The key argument leading to equation (20) concerns the gate voltage dependence of the potential profile at the point where capture/release of an electron happens with equal probabilities from either side of the barrier. Therefore, the phase and amplitude dependence of the steepness, $S(\varphi, P^-)$, is expected to be insensitive to the particular choice of the pumping potential, as long as it leads to a clear sequence of current quantization steps. We suggest the following generic scenario of the plateau quality improvement, that can be checked by detailed measurements using existing experimental setups. One should measure the traces of the first step steepness $S(\varphi)$ as function of the reflected wave phase φ for a set of gradually increasing secondary beam amplitudes P^-. At small amplitudes, $P^- < P_c^-$, the steepness is expected to have one broad maximum at some $\varphi = \varphi_0$. As P^- is increased, the value at the maximum, $S(\varphi_0)$, increases and at $P^- = P_c^-$, the maximum splits into two, $S(\varphi_1)$ and $S(\varphi_2)$, with $\varphi_{1,2} = \varphi_0 \pm \arccos(P_c^-/P^-)$, as shown in Figure 7 by the dashed line [for our model calculation $\varphi_0 = 3\pi/2$ and $P_c^- \approx b/(2qL)$].

4.2 Source-drain bias and variations of screening

Experimentally, acoustoelectric current can be studied along the full crossover, from the depleted to the transmissive state of the quantum wire, by changing the voltage on the depleting gate. Our discussion so far has been concentrated on the quantized single-electron transport, which is observed in the depleted regime. As the first conduction channel opens, the shape of the pumping potential in real space as well as screening effects become increasingly important [21] and the usefulness of our simplified 1D spinless electron model is very limited. Keeping these limitations in mind, we will choose model parameters that most closely correspond to a point contact near the depletion threshold, and illustrate the breakdown of quantized transport.

For $P > J_d = \tilde{J}$, the tight-binding band is significantly deformed (see Fig. 4), therefore we choose a relatively small SAW amplitude $P = 0.5J_d$, but a large number of sites $N = 24$ to maintain $N_{steps} > 1$ for $\lambda = 2L$. The ratio $(L/\lambda)\sqrt{P/J_d} = 0.35$ is less than 1 (see Sect. 3.2), and we expect the discrete approximation to be adequate. The Fermi wave number $ka = \pi/12$ is taken close to the band bottom.

Consider first the situation before the SAW is applied ($P = 0$). The zero-bias dc conductance of the channel is determined by the transmission coefficient $\mathcal{T}$ (Landauer formula, see Sect. 2.2). There is a potential barrier between the left and the right reservoirs for $-V_g > 0$, therefore the value of $V_g + E_F = -2J_d \cos ka \approx -2J_d$ is expected to be the borderline between transmissive and blocked states of our channel. This corresponds to the depletion threshold of a true point contact. We plot the transmission coefficient in the *absence* of SAW versus gate voltage, $\mathcal{T}(V_g)$, in Figure 8a with a thin (blue) line. For $V_g < 0$, the transmission is exponentially blocked by a rectangular barrier of height $\approx -V_g$ and length L, while above the depletion threshold a Fabry-Perot-like pattern of high transmission is observed due to multiple reflections at the sharp ends of the constriction.

At a non-zero SAW amplitude, the transmission coefficient $\mathcal{T}(t)$ becomes time-dependent and the adiabatic formula [Eq. (4)] should be used to relate it to the conductance. In the linear response regime, the second term in the curly brackets in equation (4) is proportional to $\partial^2 f/\partial E^2$ and can be neglected [22]. This results in a generalized Landauer formula [22], $G = (e^2/h)\,\mathcal{T}_{av}$, where $\mathcal{T}_{av} \equiv (\omega/2\pi)\int_0^{2\pi/\omega} dt\,\mathcal{T}(t)$ is the time average of the instantaneous transmission coefficient $\mathcal{T}(t)$. This quantity is plotted in Figure 8a with a thick black line. One can see that switching on the SAW smears the sharp step in the conductance over the range of $\pm P$ around the depletion threshold. Qualitatively similar smoothing of the conductance quantization steps due to SAW has been observed experimentally [1,2].

Figure 8a also shows some additional structure below the depletion threshold. This structure is correlated with the pumping curve shown by a thick (red) line in Figure 8b. Comparing $Q(V_g)$ and $\mathcal{T}_{av}(V_g)$ we see that each step in the acoustoelectric current is associated with a peak in the time averaged transmission as indicated by arrows in Figure 8a (the first two peaks are too small to be seen on a linear scale). It is easy to explain the origin of these peaks using the resonance approximation diagram (see Fig. 2). At gate voltages between the quantization plateaus the system remains at resonant transmission for a considerable fraction of the period, therefore $\mathcal{T}_{av}$ becomes greatly enhanced.

In the presence of both SAW and source-drain bias, the total charge transfer per period, $Q^{tot} \equiv \int_0^{2\pi/\omega} dt\, I_l(t)$, becomes

$$Q^{tot} = Q + (e^2 V_{SD}/\hbar\omega)\,\mathcal{T}_{av} \qquad (21)$$

(in the linear response regime). The result is a sum of the two terms: pure pumping contribution [thick (red) curve in Fig. 8b]; and the average transmission (thick curve in Fig. 8a), multiplied by a constant. Equation (21) suggests
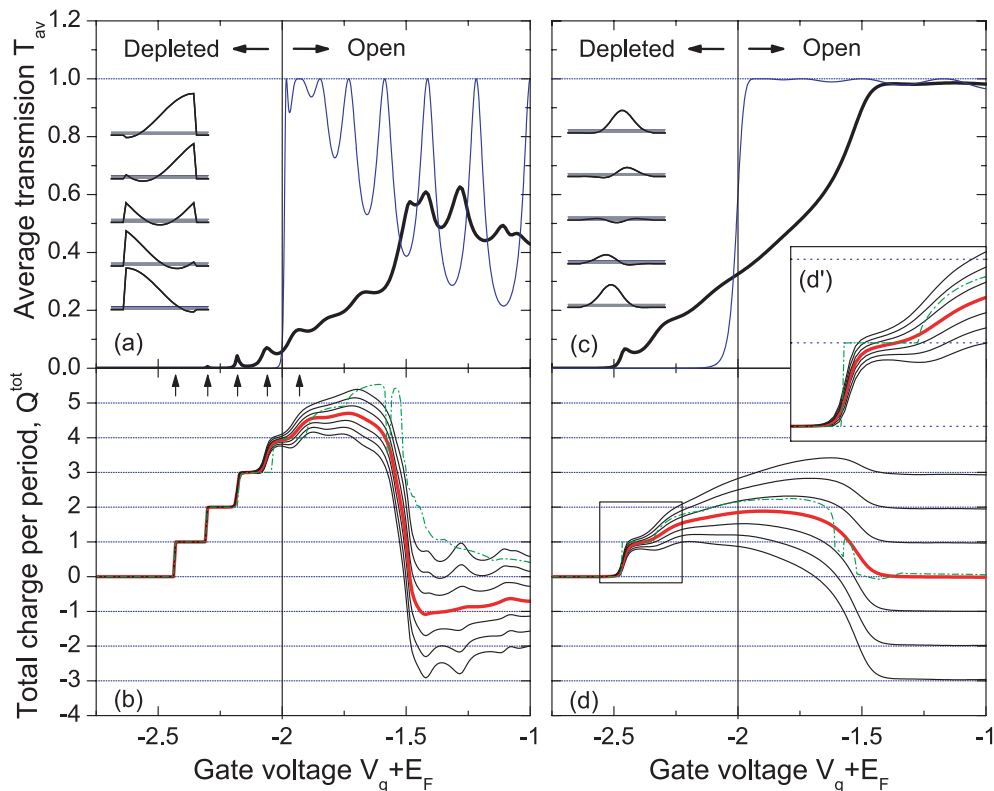
Fig. 8. (Color online) Crossover between the depleted and open regimes of the conduction channel for $N = 24$, $ka = \pi/12$, $\tilde{J} = J_d$. (a) Time-averaged transmission coefficient $\mathcal{T}_{\mathrm{av}}$ in the absence [thin (blue) line] and presence (thick black line) of a SAW with $P = 0.5 J_d$, $\lambda = 2L$. (b) The pumped charge Q [thick (red) line] and the total charge Q^{tot} (thin black lines) for bias voltages $eV_{SD}/(\hbar\omega)$ changing from -3 to 3 in steps of one. The dashed-dotted line shows Q^{res} at no bias [resonance approximation, Eq. (10)]. (c, d) The same as in (a, b), but with an exponentially screened pumping potential [Eq. (22)]. A sequence of snap-shots in panels (a, b) and (c, d) shows the corresponding pumping potential in real space for V_g in the middle of the first plateau; time increases from top to bottom, $\omega t \in [\omega t_0 - \pi/2\omega; \omega t_0 + \pi/2]$.

that $\hbar\omega$ is a natural unit for the source-drain energy mismatch eV_{SD}. In the quantized pumping region, the contribution of the bias, I^{bias}, becomes comparable to that of pumping, I^{pump}, if the bias voltage source transports several electrons per cycle. When $\mathcal{T}_{\mathrm{av}}$ is of order one, this regime is attained for eV equal to several $\hbar\omega$. Thus for a qualitative picture of the pumping curve in the presence of bias, we have plotted Q^{tot} for the bias voltage $eV_{SD}/\hbar\omega$ ranging from -3 to 3 by thin black lines in Figure 8b. The main observation is that the higher is the step number the more sensitive it is to the bias (as one can already appreciate form the average transmission curve). Similar behavior is reported in experimental studies [1,2].

The main results of the above discussion remain unchanged if a phenomenological screening [13,21] is introduced:

$$\epsilon_n(t) = [-V_g + P \cos(\omega t - qx_n)] \exp\left(-x_n^2/L_s^2\right) . \quad (22)$$

We have repeated the previous calculation using the same values of parameters but modified the pumping potential (22) with $L_s = L/4 = \lambda/8$. The results are shown in Figures 8c and 8d. The main qualitative difference is the disappearance of the interference pattern in the transmission curve both with and without the SAW. The number

of steps is reduced to one (shown separately in Fig. 8d′), since the effective amplitude of the SAW is decreased by the screening factor in equation (22). Calculations with larger values of P produce more steps, along the same lines as discussed in Section 3.2 for the unscreened potential (2). We have also checked that the behavior of the first step steepness $S(P^-, \varphi)$ as function of reflected SAW amplitude and phase, follows the general scenario suggested in Section 4.1.

We note that in the above example (Fig. 8) the resonance approximation still holds below the depletion threshold, when a moving quantum well is isolated from the Fermi sea in the leads.

5 Discussion and conclusions

Quantized electronic transport, driven by SAW's, has been considered in several recent theoretical studies [10–15,17]. Here we discuss our approach in relation to those works.

Several models [10–12,15] make a distinction between electrons *already localized* in a moving potential well (dynamic quantum dot) and those belonging to the Fermi sea. The current is then calculated by considering the

loss of electrons from the dynamic quantum dot at the stage of its formation [12, 15] and/or its subsequent motion [10–12, 15]. This approach presupposes the formation of the dynamic quantum dot, but does not require it to be at thermodynamic equilibrium with the reservoirs at all times. Moreover, all the quantization error mechanisms within these models (gradual back-tunneling [10–12], non-adiabaticity at the formation stage [12] and non-equilibrium dynamics during the transfer [15]) consider electrons with energies that can significantly exceed the Fermi energy in the remote reservoirs.

Our adiabatic quantum calculation [16] differs from these studies in two significant aspects: (i) The formation of a dynamic quantum dot is not a necessary condition for the calculation of the acoustoelectric current. We do identify, however, the localized electronic states (whenever such states are present) via the resonance approximation and confirm that they are responsible for the quantized transport. (ii) In the adiabatic pumping approximation [22], the time-dependent potential never excites the carrier by a finite amount of energy away from the Fermi level [25]. Therefore, we never observe quantization steps when the moving potential well rises above the Fermi level upon passing through the middle of the channel.

We find the numerical calculations by Maksym [13] to be the closest to our study. He considers a 1D single-particle model with a pumping potential similar to our equation (22). The current at the quantization plateaus is found to be carried by the lowest energy states of the local potential minimum, in accordance with our results.

The quantization accuracy in our approach is determined by two factors which we expect to become experimentally relevant for sufficiently low tunnelling barriers. The first one is the possibility of *both* reservoirs to participate in the capture/release of an electron. This error mechanism is covered by the resonance approximation and leads to simple estimates like our formulas for the first step steepness discussed in Section 4.1. The second factor concerns mixing of the localized states with the continuum in the leads, which can give significant width to the quasi-stationary states in the moving quantum dot. Compared to the predictions of the loading/unloading scenario (Sect. 2.3), this effect further degrades the flatness of the quantization (see, e.g., Figs. 3b, 6 and 8d) and eventually leads to the breakdown of the quantized transport as the channel opens (Sect. 4.2).

We have not considered explicit Coulomb interactions between electrons in the depleted part of the channel, which set the energy scale of the problem. One can make a naive estimate of the level spacing Δ, which in the continuous limit is [16] $\Delta = \hbar q \sqrt{P/m^*}$. Using typical experimental values [4] for the SAW amplitude $P = 20$ meV, wavelength $\lambda = 1$ μm and GaAs bulk effective mass $m^* = 0.067 m_0$, one gets $\Delta = 1$ meV, which is an order of magnitude less that the distance between the quantization steps observed in experiments [1, 2, 4]. This discrepancy can be qualitatively understood on a mean-field level: if an electron is captured by the moving potential minimum, its unscreened electric field makes the potential well seen by the other electrons much shallower, and thus increases the spacing Δ between resonances by the amount of the charging energy [31, 32]. Such a picture is also supported by the numerical calculation of a two-electron problem by Gumbs and co-workers [11]. It is plausible that the effective values for the parameters of our model can be estimated from a self-consistent realistic calculation.

In conclusion, we have considered a simple model for SAW-driven adiabatic pumping of electrons through a quasi-1D quantum wire. A stair-case structure of the acoustoelectric current has been mapped onto the instantaneous energy spectrum of the pumping potential. Numerical calculations and analytic estimates confirm the experimentally observed behavior of the acoustoelectric current as function of the SAW amplitude, wavelength, source-drain bias, and the parameters of a weak counter-propagating beam. Quantitative measurements of the plateau quality as a function of the second SAW amplitude and phase are proposed to probe the relevance of our model. The presented single-electron picture captures all the main features of the quantized transport.

References

1. J.M. Shilton, V.I. Talyanskii, M. Pepper, D.A. Ritchie, J.E.F. Frost, C.J.B. Ford, C.G. Smith, G.A.C. Jones, J. Phys. C **8**, L531 (1996)

2. V.I. Talyanskii, J.M. Shilton, M. Pepper, C.G. Smith, C.J.B. Ford, E.H. Linfield, D.A. Ritchie, G.A.C. Jones, Phys. Rev. B **56**, 15 180 (1997)

3. V.I. Talyanskii, J.M. Shilton, J. Cunningham, M. Pepper, C.J.B. Ford, C.G. Smith, E.H. Linfield, D.A. Ritchie, G.A.C. Jones, Physica B **249–251**, 140 (1998)

4. J. Cunningham, V.I. Talyanskii, J.M. Shilton, M. Pepper, M.Y. Simmons, D.A. Ritchie, Phys. Rev. B **60**, 4850 (1999)

5. J. Cunningham, V.I. Talyanskii, J.M. Shilton, M. Pepper, A. Kristensen, P.E. Lindelof, Phys. Rev. B **62**, 1564 (2000)

6. J. Ebbecke, G. Bastian, M. Blöcker, K. Pierz, F.J. Ahlers, Appl. Phys. Lett. **77**, 2601 (2000)

7. J.-T. Janssen, A. Hartland, IEEE Transactions on instrumentation and measurement **50**, 227 (2001)

8. A.M. Robinson, V.I. Talyanskii, M. Pepper, J.E. Cunningham, E.H. Linfield, D.A. Ritchie, Phys. Rev. B **65**, 045313 (2002)

9. N.E. Fletcher, J. Ebbecke, T.J.B.M. Janssen, F.J. Ahlers, M. Pepper, H.E. Beere, D.A. Ritchie, Phys. Rev. B **68**, 245310 (2003), cond-mat/0308402

10. G.R. Aĭzin, G. Gumbs, M. Pepper, Phys. Rev. B **58**, 10 589 (1998)

11. G. Gumbs, G.R. Aĭzin, M. Pepper, Phys. Rev. B **60**, 13 954 (1999)

12. K. Flensberg, Q. Niu, M. Pustilnik, Phys. Rev. B **60**, 16 291 (1999)

13. P.A. Maksym, Phys. Rev. B **61**, 4727 (2000)

14. Y.M. Galperin, O. Entin-Wohlman, Y. Levinson, Phys. Rev. B **63**, 153309 (2001)

15. A.M. Robinson, C.H.W. Barnes, Phys. Rev. B **63**, 165418 (2001)
16. A. Aharony, O. Entin-Wohlman, Phys. Rev. B **65**, 241401 (2002), `cond-mat/0111053`
17. V.A. Margulis, M.P. Trushin, A.V. Shorokhov, JETP **94**, 1160 (2002)
18. O. Entin-Wohlman, A. Aharony, V. Kashcheyevs, J. Phys. Soc. Jpn **72A**, 77 (2003), `cond-mat/0201073`
19. J.L. Flowers, B.W. Petley, Rep. Prog. Phys. **64**, 1191 (2001)
20. C.H.W. Barnes, J.M. Shilton, A.M. Robinson, Phys. Rev. B **62**, 8410 (2000)
21. Y. Levinson, O. Entin-Wohlman, P. Wölfle, Phys. Rev. Lett. **85**, 634 (2000)
22. O. Entin-Wohlman, A. Aharony, Y. Levinson, Phys. Rev. B **65**, 195411 (2002), `cond-mat/0201073`
23. V. Kashcheyevs, A. Aharony, O. Entin-Wohlman, Phys. Rev. B **69**, 195301 (2004), `cond-mat/0308382`
24. J. Ebbecke, N.E. Fletcher, T.J.B.M. Janssen, F.J. Ahlers, M. Pepper, H.E. Beere, D.A. Ritchie (2003), unpublished, `cond-mat/0312304`
25. M. Moskalets, M. Büttiker, Phys. Rev. B **66**, 205320 (2002), `cond-mat/0208356`
26. M. Büttiker, H. Thomas, A. Prêtre, Z. Phys. B **94**, 133 (1994)
27. P.W. Brouwer, Phys. Rev. B **58**, 10 135 (1998)
28. R. Landauer, Philosophical Magazine **21**, 863 (1970)
29. O. Entin-Wohlman, A. Aharony, Phys. Rev. B **66**, 035329 (2002)
30. Y. Levinson, O. Entin-Wohlman, P. Wölfle, Physica A **302**, 335 (2001), `cond-mat/0010494`
31. M.V. Moskalets, Phys. Rev. B **63**, 113309 (2001)
32. R. Berkovits, F. von Oppen, J.W. Kantelhardt (2003), unpublished, `cond-mat/0307730`

Chapter 5

Applicability of the equations-of-motion technique for quantum dots

The content of this chapter has been previously available as

- a preprint, `arXiv.org:cond-mat/0511656` (28 November 2005);

- a journal article, Phys. Rev. B, **73**, 125338 (27 March 2006).

Applicability of the equations-of-motion technique for quantum dots

Vyacheslavs Kashcheyevs,[1,*] Amnon Aharony,[1,2] and Ora Entin-Wohlman[1,2,3]

[1]*School of Physics and Astronomy, Raymond and Beverly Sackler Faculty of Exact Sciences, Tel Aviv University, Tel Aviv 69978, Israel*

[2]*Department of Physics, Ben Gurion University, Beer Sheva 84105, Israel*

[3]*Albert Einstein Minerva Center for Theoretical Physics, Weizmann Institute of Science, Rehovot 76100, Israel*

The equations-of-motion (EOM) hierarchy satisfied by the Green functions of a quantum dot embedded in an external mesoscopic network is considered within a high-order decoupling approximation scheme. Exact analytic solutions of the resulting coupled integral equations are presented in several limits. In particular, it is found that at the particle-hole symmetric point the EOM Green function is temperature independent due to a discontinuous change in the imaginary part of the interacting self-energy. However, this imaginary part obeys the Fermi liquid unitarity requirement away from this special point, at zero temperature. Results for the occupation numbers, the density of states, and the local spin susceptibility are compared with exact Fermi liquid relations and the Bethe ansatz solution. The approximation is found to be very accurate far from the Kondo regime. In contrast, the description of the Kondo effect is valid on a qualitative level only. In particular, we find that the Friedel sum-rule is considerably violated, up to 30%, and the spin susceptibility is underestimated. We show that the widely used simplified version of the EOM method, which does not account fully for the correlations on the network, fails to produce the Kondo correlations even qualitatively.

I. INTRODUCTION

Quantum dots embedded in mesoscopic structures are currently of great experimental and theoretical interest, because such systems allow for detailed and controlled studies of the effects of electronic correlations.[1] The theoretical description of these systems is usually based on the Anderson model,[2,3] in which the electronic correlations are confined to few impurities that represent the quantum dots. Although a rich variety of techniques has been developed over the years to treat the Anderson model,[4] their applications to the quantum dot systems are not straightforward. In such systems one would like to be able to study dynamical properties (e.g., transport) as function of the impurity characteristics (which can be tuned experimentally) over a wide range of parameters. This is not easily accomplished by the Bethe ansatz solution, for example.

The theoretical difficulty can be pinned down to the ability to derive a reliable, easy-to-handle, expression for the single-electron Green function on the quantum dot. Because the electronic interactions in the Anderson model take place solely on the dot, this Green function can be shown to determine, under certain conditions, the charge or the spin transmission through the quantum dot, the charge accumulated on it, etc.[3,5] Consequently, much effort has been devoted to finding faithful analytic approximations for this object. Alternative treatments rely on numerical techniques, such as quantum Monte Carlo,[6] or the numerical renormalization group (NRG) method.[7] NRG in particular is considered to be capable of providing accurate estimates of the Green function over a wide parameter range, although at the cost of running iterative diagonalizations for each parameter set, and a limited resolution at high energies and high magnetic fields.

A ubiquitous method to derive an analytical expression for the Green functions is to use the equations-of-motion

(EOM).[8] In the case of the single-impurity Anderson model, the EOM of the (single-particle) impurity Green function gives rise to an infinite hierarchy of EOM of higher-order Green functions. A well-known approximation procedure is then to truncate this hierarchy, thus producing certain thermal averages representing various correlation functions. The latter need to be found self-consistently from the resulting closed set of equations. The level at which the EOM are truncated is chosen such that most of the interaction effects are captured.[9–12] This scheme has been applied to the original Anderson model a long time ago,[9–11,13,14] yielding approximate expressions for the resistivity,[9,10] the spin susceptibility,[10,13] and the magnetotransport[14] of dilute magnetic alloys. For temperatures above the Kondo temperature, T_K, these results agree with perturbation theory calculations.[4] Although several limitations of these self-consistent approaches are known (such as underestimation of the Kondo temperature or the absence of $(T/T_K)^2$ terms in the low-temperature expansion of the results), they still can form a basis for a qualitative analytic treatment of the Kondo effect.

The application of the EOM technique to a quantum dot system has been undertaken by Meir, Wingreen, and Lee[5] (MWL). Neglecting certain correlation functions, they have obtained a closed analytic expression for the dot Green function. Several subsequent studies have employed their scheme to describe various effects of the Kondo correlations in quantum dots in different settings, e.g., ac response of a biased quantum dot,[15] nonequilibrium Andreev tunneling,[16] and coupling to magnetic leads.[17] As we show below, the approximation of MWL fails in various aspects. Recent attempts to improve on that solution turned out to be not completely satisfactory: either requiring further approximations on top of the self-consistent truncation[18] or leading to iterative numerical solutions.[19–22] The truncation of the EOM at

an even higher order has been recently investigated numerically in Ref. 23. It is therefore of interest to examine whether an *exact solution* of the self-consistency equations of the EOM method will improve on the previous results, and will be capable of producing a reliable approximation for the Green function that can be used in the analysis of quantum dot systems.

In this paper we consider a quantum dot embedded in a general complex network, and obtain and solve the truncated EOM for its Green function. This EOM contains all the next-order correlation functions, which we decouple and calculate self-consistently. We first derive (in Sec. II) an integral equation for the Green function, allowing for arbitrary values of the on-site Coulomb interaction, U. We then analyze (in Sec. III) the properties of this EOM solution. We find that in the case of a particle-hole symmetric Hamiltonian the resulting Green function is *temperature independent* (a point which is overlooked in previous treatments of quantum dots, see for example Ref. 5). However, we show that this is a singular point in the parameter space. We also investigate the zero-temperature limit of the EOM solution, and show that it fails to satisfy the Friedel sum-rule. We then turn to the infinite U case (in Sec. IV), and derive an exact analytical solution to the integral equation for the Green function. In Sec. V we use this solution to obtain the total occupation number on the dot, and compare it with the exact solution supplied by the Bethe ansatz. This comparison shows that the EOM solution is faithful outside the Kondo regime, but fails in the regime where Kondo correlations play a dominant role. In particular, the Friedel sum-rule is violated by ~30%, invalidating the assumptions made in previous studies.[11,19,21] We then derive the local spin susceptibility on the dot and demonstrate that the full self-consistent solution of the EOM, as used in this work, is required in order to obtain quantitatively correct results. We also examine the local density of states at the Fermi level, and find that it shows the expected universal behavior as function of T/T_K, though the EOM Kondo temperature lacks a factor of 2 in the exponential dependence on the single-energy level on the dot. Finally, we examine the EOM technique from another point of view (Sec. VI): We expand the Green function derived from the EOM to second order in the dot-network coupling, and compare the results with those obtained from a straightforward perturbation theory.[24,25] This comparison shows again the necessity to include in the EOM solution the full self-consistent calculation of all the correlations. A short summary in Sec. VII concludes the paper.

II. THE GREEN FUNCTION ON THE DOT

As mentioned above, several properties of the Anderson model can be expressed in terms of the Green function on the dot. Here we examine the determination of this function using the EOM method. Our discussion is limited to a single interacting impurity embedded in a general noninteracting network, for which the Hamiltonian can be written in the form

$$\mathcal{H} = \mathcal{H}_{\text{dot}} + \mathcal{H}_{\text{net}} + \mathcal{H}_{\text{net-dot}}. \quad (1)$$

Here, the dot Hamiltonian is given by

$$\mathcal{H}_{\text{dot}} = \sum_{\sigma} (\epsilon_0 + \sigma h) n_{d\sigma} + U n_{d\uparrow} n_{d\downarrow}, \quad n_{d\sigma} = d_{\sigma}^{\dagger} d_{\sigma}, \quad (2)$$

where $d_{\sigma}^{\dagger}$ (d_{σ}) is the creation (annihilation) operator of an electron of spin index $\sigma = \pm 1/2$ on the dot, ϵ_0 is the single-particle energy there, h is the Zeeman splitting, and U denotes the Coulomb repulsion energy. The noninteracting network is described by the tight-binding Hamiltonian

$$\mathcal{H}_{\text{net}} = \sum_{n\sigma} \varepsilon_{n\sigma} a_{n\sigma}^{\dagger} a_{n\sigma} - \sum_{mn\sigma} J_{mn} a_{m\sigma}^{\dagger} a_{n\sigma}, \quad (3)$$

where $a_{n\sigma}^{\dagger}$ ($a_{n\sigma}$) is the creation (annihilation) operator of an electron of spin index σ on the nth site on the network, whose on-site energy is $\varepsilon_{n\sigma}$, and $J_{mn} = J_{nm}^*$ are the hopping amplitudes on the network. Finally, the coupling between the dot and the network is given by

$$\mathcal{H}_{\text{net-dot}} = -\sum_{n\sigma} J_{n\sigma} d_{\sigma}^{\dagger} a_{n\sigma} + \text{H.c.} \quad (4)$$

We have allowed for spin-dependent on-site energies on the network, as well as spin-dependent hopping amplitudes between the dot and the network. In this way, our model includes also the case of spin-polarized leads connected to a quantum dot (see, for example, Refs. 5 and 21). The entire system is assumed to be at equilibrium with a reservoir held at temperature T (in energy units) and chemical potential $\mu = 0$.

Adopting the notations of Ref. 8, we write a general Green function in the form

$$\langle\langle A; B \rangle\rangle_{\omega \pm i\eta} \equiv \mp i \int_{-\infty}^{+\infty} \Theta(\pm t) \langle [A(t); B]_+ \rangle e^{i(\omega \pm i\eta)t} dt, \quad (5)$$

where A and B are operators, Θ is the Heaviside function, and $\eta \to 0^+$. The Green function on the dot is then

$$G_{\sigma}(z) \equiv \langle\langle d_{\sigma}; d_{\sigma}^{\dagger} \rangle\rangle_z, \quad z \equiv \omega \pm i\eta. \quad (6)$$

In conjunction with the definition (5), a thermal average, $\langle BA \rangle$, is related to the corresponding Green function by

$$\langle BA \rangle = i \oint_C \frac{dz}{2\pi} f(z) \langle\langle A; B \rangle\rangle_z, \quad f(z) \equiv \frac{1}{1 + e^{z/T}}, \quad (7)$$

where the contour C runs clockwise around the real axis.

The EOM for the dot Green function is given in Appendix A [see Eq. (A2)]. As is shown there, that equation includes a higher-order Green function, whose EOM gives rise to additional Green functions. The resulting infinite hierarchy of EOM is then truncated according to a scheme proposed originally by Mattis[26] and subsequently used in Refs. 9–11, 13, 14, 18–21, and 27: Each Green function of the type $\langle\langle A^{\dagger}BC; d^{\dagger} \rangle\rangle$ in the EOM hierarchy is replaced by

$$\langle\langle A^{\dagger}BC; d^{\dagger} \rangle\rangle \Rightarrow \langle A^{\dagger}B \rangle \langle\langle C; d^{\dagger} \rangle\rangle - \langle A^{\dagger}C \rangle \langle\langle B; d^{\dagger} \rangle\rangle \quad (8)$$

if at least two of the operators A, B, and C are network operators $a_{n\sigma}$. Explicitly, the Green functions which are decoupled are $\langle\langle a_{n\sigma} d^\dagger_{\bar{\sigma}} a_{m\bar{\sigma}} ; d^\dagger_\sigma \rangle\rangle$, $\langle\langle a^\dagger_{n\bar{\sigma}} d_{\bar{\sigma}} a_{m\sigma} ; d^\dagger_\sigma \rangle\rangle$, and $\langle\langle a^\dagger_{n\bar{\sigma}} a_{m\bar{\sigma}} d_\sigma ; d^\dagger_\sigma \rangle\rangle$ (with $\bar{\sigma}=-\sigma$).[28] Upon calculating the aver-

ages $\langle a^\dagger_{m\sigma} a_{m'\sigma} \rangle$ and $\langle d^\dagger_{\sigma} a_{m\sigma} \rangle$ using Eq. (7), the set of EOM is closed, and can be therefore solved. The details of this calculation are presented in Appendix A. In particular, the resulting equation determining the dot Green function is

$$G_\sigma(z) = \frac{u(z) - \langle n_{d\bar{\sigma}} \rangle - P_{\bar{\sigma}}(z_1) - P_{\bar{\sigma}}(z_2)}{u(z)[z - \epsilon_0 - \sigma h - \Sigma_\sigma(z)] + [P_{\bar{\sigma}}(z_1) + P_{\bar{\sigma}}(z_2)]\Sigma_\sigma(z) - Q_{\bar{\sigma}}(z_1) + Q_{\bar{\sigma}}(z_2)}, \qquad (9)$$

where

$$u(z) \equiv U^{-1}[U - z + \epsilon_0 + \sigma h + \Sigma_\sigma(z) + \Sigma_{\bar{\sigma}}(z_1) - \Sigma_{\bar{\sigma}}(z_2)], \qquad (10)$$

and $z_1 \equiv z - 2\sigma h$, $z_2 \equiv -z + 2\epsilon_0 + U$. The functions P and Q are given in terms of the noninteracting self-energy on the dot, $\Sigma_\sigma(z)$, brought about by its coupling to the network [namely, the self-energy of the noninteracting dot, see Eq. (A7)], and the dot Green function itself [see Eqs. (A25)],

$$P_\sigma(z) = \mathfrak{F}_{\sigma z}[G], \quad Q_\sigma(z) = \mathfrak{F}_{\sigma z}[1 + \Sigma G], \qquad (11)$$

where the notation $\mathfrak{F}_{\sigma z}[g]$ stands for

$$\mathfrak{F}_{\sigma z}[g] \equiv \frac{i}{2\pi} \oint_C f(w) g_\sigma(w) \frac{\Sigma_\sigma(w) - \Sigma_\sigma(z)}{z - w} dw. \qquad (12)$$

Equation (9) generalizes the result of Ref. 11 (see also Refs. 18–21) for the case in which the interaction on the dot is finite, and the entire system is subject to an external magnetic field. Our generalization also corrects a few details in Lacroix's earlier treatment of finite U.[12]

III. PROPERTIES OF THE EOM APPROXIMATION AT FINITE U

As is evident from Eq. (9), the solution of the dot Green function within the EOM scheme cannot be easily obtained over the entire parameter range. However, there are certain limiting cases in which this Green function can be analyzed analytically. We examine those in the subsequent sections.

A. Particle-hole symmetry

Upon replacing the particle operators by the hole ones, $\tilde{d}^\dagger_\sigma \equiv d_\sigma$, $\tilde{a}^\dagger_{n\sigma} \equiv a_{n\sigma}$, the Anderson Hamiltonian (1) attains its original structure, with

$$\tilde{\epsilon}_0 + \sigma\tilde{h} = -\epsilon_0 - \sigma h - U, \quad \tilde{U} = U,$$

$$\tilde{J}_{n\sigma} = -J^*_{n\sigma}, \quad \tilde{\varepsilon}_{n\sigma} = -\varepsilon_{n\sigma}, \quad \tilde{J}_{nm} = -J_{mn}. \qquad (13)$$

(Hole quantities are denoted by a tilde.) The dot Green function in terms of the hole operators is then related to the particle Green function by

$$\tilde{G}_\sigma(z) \equiv \langle\langle \tilde{d}_\sigma ; \tilde{d}^\dagger_\sigma \rangle\rangle_z = -G_\sigma(-z). \qquad (14)$$

One may check that this equivalence holds by introducing the definitions (13) into Eq. (9). Since $\tilde{\Sigma}_\sigma(z) = -\Sigma_\sigma(-z)$ and $\tilde{u}(z) = 1 - u(-z)$, one finds that [see Eqs. (A25) and (A26)] $\tilde{P}_\sigma(z) = -P_\sigma(-z)$ and $\tilde{Q}_\sigma(z) = Q_\sigma(-z) - \Sigma_\sigma(-z)$, reconfirming Eq. (14).

From now on we shall assume that $\Sigma_\sigma(z) = -\Sigma_\sigma(-z)$. This relation is realized, for example, when the network to which the dot is coupled has a wide band spectrum, with the Fermi level at the middle. We next discuss the particular point where $2\epsilon_0 + U = 0$ and $h = 0$. At this point, the Anderson Hamiltonian becomes *particle-hole symmetric*. Then $G_\sigma(z) = -G_\sigma(-z)$, $P_\sigma(z) + P_\sigma(-z) = 0$, $Q_\sigma(z) - Q_\sigma(-z) = \Sigma_\sigma(z)$, and $\langle n_{d\sigma} \rangle = 1/2$. As a result, Eq. (9) becomes

$$[G_\sigma(z)]^{-1} = z - \Sigma_\sigma(z) - \frac{U^2}{4[z - \Sigma_\sigma(z) - 2\Sigma_{\bar{\sigma}}(z)]}. \qquad (15)$$

Namely, at the particle-hole symmetry point of the Anderson model, the EOM results in a *temperature-independent* dot Green function. This implies that the EOM technique at the particle-hole symmetric point *cannot* produce the Kondo singularity. This property of the EOM scheme has been reported a long time ago,[10,29,30] but was ignored in more modern uses of it,[5] which are designed to study the Kondo peak in the density of states.

The failure of the EOM method to describe faithfully the Anderson model at its symmetric point, where the Fermi level lies *exactly* between the states of single and double occupancies, is a very severe drawback of this method. An important question is whether this point is either a singular or a continuous domain, which the EOM method fails totally. We return to this problem in the next section.

B. Zero-temperature relations

The zero-temperature limit is of special importance since the Green function *at the Fermi energy* at $T=0$ satisfies the Fermi-liquid relations[4,31]

$$\text{Im}\,[G^+_\sigma(0)]^{-1} = \Gamma_\sigma, \qquad (16)$$

$$\text{Re}[G_\sigma^+(0)]^{-1} = -\Gamma_\sigma \cot(\pi \tilde{n}_{d\sigma}). \qquad (17)$$

Here and below we use $A^\pm(\omega) \equiv \lim_{\eta \to \pm 0} A(\omega + i\eta)$, so that $G_\sigma^+(\omega) = [G_\sigma^-(\omega)]^*$ is the usual retarded Green function. In Eqs. (16) and (17), Γ_σ is the level broadening,

$$\Gamma_\sigma \equiv -\text{Im} \, \Sigma_\sigma^+(0). \qquad (18)$$

The first relation, Eq. (16), implies[31] number conservation, and therefore is sometimes referred to as the "unitarity" condition. The second one, Eq. (17), is the Friedel sum-rule, in which $\tilde{n}_{d\sigma}$ is the total number of spin σ electrons introduced by the quantum dot,[31]

$$\tilde{n}_{d\sigma} = -\frac{1}{\pi} \, \text{Im} \int f(\omega) \left[1 - \frac{\partial \Sigma_\sigma^+(\omega)}{\partial \omega} \right] G_\sigma^+(\omega) d\omega. \qquad (19)$$

When the self-energy Σ_σ does not depend on the energy, $\tilde{n}_{d\sigma}$ coincides with the single-spin occupation number on the dot, $\langle n_{d\sigma} \rangle$.

It is evident that the EOM solution for the Green function *at the particle-hole symmetric point*, Eq. (15), *violates* the unitarity condition (16). On the Fermi level, the particle-hole symmetric Green function is

$$[G_\sigma^+(0)]^{-1} = i\Gamma_\sigma + i \frac{U^2}{4(\Gamma_\sigma + 2\Gamma_{\bar{\sigma}})}, \qquad (20)$$

and therefore the imaginary part of $[G_\sigma^+(0)]^{-1}$ is *not* determined solely by the noninteracting self-energy (as implied by the unitarity condition), but has also a contribution coming from the interaction. This is contrary to the result of Lacroix,[12] whose EOM differs from our Eq. (9) in several places. On the other hand, the Friedel sum-rule is satisfied by the Green function (15), which yields $\tilde{n}_{d\sigma} = \frac{1}{2}$. This follows from Eq. (19): The imaginary parts of both $G_\sigma(\omega)$ and $\Sigma_\sigma(\omega)$ are even in ω, while (at the symmetric point) the real parts are odd in it. However, $G_\sigma(\omega) \simeq \omega^{-1}$ at large frequencies, whereas $\partial \Sigma_\sigma(\omega)/\partial \omega \simeq \omega^{-2}$. As a result, the second term in the square brackets of Eq. (19) does not contribute. With $\tilde{n}_{d\sigma} = \frac{1}{2}$, the Friedel sum-rule gives $\text{Re}[G_\sigma^+(0)]^{-1} = 0$, which is fulfilled by Eq. (20).

It is rather intricate to study the full EOM solution, Eq. (9), at $T=0$, even on the Fermi level. However, there are cases in which this can be accomplished without constructing the full solution. The investigation of these cases will also allow us to examine the behavior of $G_\sigma(0)$ as the particle-hole symmetric point is approached. To this end we note that at $T=0$ the functions $P(\omega)$ and $Q(\omega)$ acquire logarithmic singularities as $\omega \to 0$,

$$P_\sigma^\pm(\omega) \sim -\frac{1}{\pi} \Gamma_\sigma G_\sigma^\mp(0) \ln|\omega| + \mathcal{O}(1),$$

$$Q_\sigma^\pm(\omega) \sim -\frac{1}{\pi} \Gamma_\sigma [1 + \Sigma_\sigma^\mp(0) G_\sigma^\mp(0)] \ln|\omega| + \mathcal{O}(1). \qquad (21)$$

Therefore, we may examine special points at which the functions P and Q are divergent, keeping only the divergent terms in Eq. (9). Then, that equation reduces to an algebraic

one, which can be easily solved to yield G_σ at those special points.

Let us first consider the case in which the Zeeman field h on the dot vanishes, but $2\epsilon_0 + U \neq 0$. Using Eqs. (21) in Eq. (9) yields

$$[G_\sigma^+(0)]^{-1} + \Sigma_\sigma^+(0) = [G_{\bar{\sigma}}^-(0)]^{-1} + \Sigma_{\bar{\sigma}}^-(0). \qquad (22)$$

By writing the Green function in the general form

$$[G_\sigma(z)]^{-1} = z - \epsilon_0 - \sigma h - \Sigma_\sigma(z) - \Sigma_\sigma^{\text{int}}(z), \qquad (23)$$

in which Σ^{int} is the self-energy due to the interaction, Eq. (22) takes the form

$$\Sigma_\sigma^{\text{int}+}(0) - \Sigma_{\bar{\sigma}}^{\text{int}-}(0) = 0. \qquad (24)$$

When the network is not spin polarized, the spin indices σ and $\bar{\sigma}$ are indistinguishable. Then Eq. (22) implies that $\text{Im} \, \Sigma^{\text{int}}(0)$ vanishes, namely the unitarity condition is satisfied. (In the more general case of possibly ferromagnetic leads, it is only the imaginary part of $[G_\sigma^+(0)]^{-1} - [G_{\bar{\sigma}}^-(0)]^{-1}$ which is determined by the noninteracting self-energy alone.) Had we now sent $2\epsilon_0 + U$ to zero, we would have found that the EOM result at the particle-hole symmetric point *does* satisfy the unitarity condition, in contradiction to our finding, Eq. (20), above. We thus conclude that the failure of the EOM to obey the Fermi-liquid relation (16) at the symmetric point is *confined* to the symmetric point alone, namely, the imaginary part of Σ^{int} on the Fermi level has a discontinuity.

Next we consider the case where $2\epsilon_0 + U = 0$, but $h \neq 0$. Using Eqs. (21) in Eq. (9) we now find the relation

$$[G_\sigma^+(0)]^{-1} + \Sigma_\sigma^+(0) = -\{[G_{\bar{\sigma}}^+(0)]^{-1} + \Sigma_{\bar{\sigma}}^+(0)\}. \qquad (25)$$

Inserting here expression (23), we rewrite this relation in the form

$$\Sigma_\sigma^{\text{int}+}(0) + \Sigma_{\bar{\sigma}}^{\text{int}+}(0) = U. \qquad (26)$$

Therefore, $\text{Im} \, \Sigma^{\text{int}}(0) = 0$, in agreement with the unitarity condition. Sending now the Zeeman field on the dot to zero, yields the result $2\text{Re} \, \Sigma^{\text{int}}(0) = U$, which agrees with the real part of Eq. (20). Thus the EOM result for the real part of Σ^{int} on the Fermi energy does not have a discontinuity. We hence conclude that the EOM technique's failure at the symmetric point is confined to the imaginary part of the interacting self-energy alone and to the symmetric point alone.

Our considerations in this subsection are confined to $\omega = 0$, and therefore do not allow us to investigate the Friedel sum-rule easily. We carry out such an analysis for the infinite-U case below. Alternatively, one may attempt, as has been done in Ref. 21, to *impose* the Friedel sum-rule on the EOM result, assuming that Eq. (17) holds, with $\tilde{n}_{d\sigma} \equiv \langle n_{d\sigma} \rangle$. This is a dangerous procedure, which leads in some cases to unphysical results, as is demonstrated in Sec. V.

IV. EXACT SOLUTION IN THE $U \to \infty$ LIMIT

In this section we present an exact solution of the self-consistently truncated EOM, and obtain the dot Green function, in the limit $U \to \infty$. For this solution, we assume that the

bandwidth D_σ is larger than the other energies in the problem (except U). In the next section we use this function to calculate several physical quantities, and compare the results with those of the Bethe ansatz technique and other calculations. For simplicity, we also assume that the noninteracting self-energy may be approximated by an energy-independent resonance width, i.e.,

$$\Sigma_\sigma^\pm = \mp i\Gamma_\sigma, \tag{27}$$

for all the energies in the band, $-D_\sigma < \omega < D_\sigma$ (the extension to the case where there is also an energy-independent real part to the self-energy is straightforward). This assumption is certainly reasonable for a range of energies near the center of the band. However, using it for the whole band introduces corrections of order $|\omega/D_\sigma|$, thus restricting the solution to $|\omega/D_\sigma| \ll 1$. Then, Eq. (9) for the Green function, together with the definitions (10)–(12), takes the form

$$[\mathcal{G}_\sigma^\pm(\omega)]^{-1}G_\sigma^\pm(\omega + \sigma h) = 1 - \langle n_{d\bar\sigma}\rangle - P_\sigma^\pm(\omega + \bar\sigma h), \tag{28}$$

where

$$\mathcal{G}_\sigma^\pm(\omega) = [\omega - \epsilon_0 \pm i\Gamma_\sigma - I_{\bar\sigma}^\pm(\omega + \bar\sigma h)$$
$$\mp i(\Gamma_{\bar\sigma} + \Gamma_\sigma)P_{\bar\sigma}^\pm(\omega + \bar\sigma h)]^{-1}. \tag{29}$$

Note the shift of energies by σh, compared to Eq. (9). The function I_σ introduced here contains the Kondo singularity,[32]

$$I_\sigma^\pm(\omega) = \frac{\Gamma_\sigma}{\pi}\int_{-D_\sigma}^{D_\sigma} d\omega' \frac{f(\omega')}{\omega \pm i\eta - \omega'}. \tag{30}$$

To order $\mathcal{O}(\omega/D_\sigma)$, one has

$$\pi I_\sigma^\pm(\omega)/\Gamma_\sigma = -\Psi\left(\frac{1}{2} \mp \frac{i\omega}{2\pi T}\right) + \ln\frac{D_\sigma}{2\pi T} \mp \frac{i\pi}{2}, \tag{31}$$

where Ψ is the digamma function. Equation (28) for the Green function also contains the function P_σ, which, using the assumption (27), is given by

$$P_\sigma^\pm(\omega) = \frac{\Gamma_\sigma}{\pi}\int_{-D_\sigma}^{D_\sigma} d\omega' \frac{f(\omega')G_\sigma^\mp(\omega')}{\omega \pm i\eta - \omega'}d\omega'. \tag{32}$$

Physically, all the integrals which contain Σ_σ must be calculated between $-D_\sigma$ and D_σ, and the resulting Green function is calculated only for energies inside the band, $|\omega| < D_\sigma$. However, the integral $P_\sigma^\pm(\omega)$ converges even when one takes the limit $D_\sigma \to \infty$, because $G_\sigma(\omega) \sim 1/\omega$ at large $|\omega|$ [see, e.g., Eq. (28)]. If D_σ is sufficiently large, so that this asymptotic behavior becomes accurate and since $f(\omega) \approx 1$ for $\omega < -D_\sigma$, it is convenient to extend the range of this integral (and all the related integrals below, unless otherwise specified) to the range $-\infty < \omega < \infty$. This introduces errors of order Γ_σ/D_σ or ω/D_σ in the results, which we neglect.

We have thus found that the equation for G_σ^+ involves an integral containing the function $G_{\bar\sigma}^-$, and thus the two functions G_σ^+ and $G_{\bar\sigma}^-$ are coupled. In addition, the occupations $\langle n_{d\sigma}\rangle$ have to be determined self-consistently from the Green functions themselves. Our solution for the Green function follows the method introduced in Refs. 10 and 33. This

method allows one to turn the integral equations into algebraic ones, at the cost of additional quantities which have to be determined self-consistently from the Green function. First, one introduces the functions

$$\Phi_\sigma(z) = z - \epsilon_0 + i\Gamma_\sigma - I_{\bar\sigma}(z + \bar\sigma h) - i(\Gamma_{\bar\sigma} + \Gamma_\sigma)\frac{\Gamma_{\bar\sigma}}{\pi}$$
$$\times \int d\omega' \frac{f(\omega')G_{\bar\sigma}^-(\omega')}{z + \bar\sigma h - \omega'},$$

$$\tilde\Phi_\sigma(z) = z - \epsilon_0 - i\Gamma_{\bar\sigma} - I_\sigma(z + \sigma h) + i(\Gamma_{\bar\sigma} + \Gamma_\sigma)\frac{\Gamma_\sigma}{\pi}$$
$$\times \int d\omega' \frac{f(\omega')G_\sigma^+(\omega')}{z + \sigma h - \omega'}. \tag{33}$$

Note that $\Phi_\sigma^+(\omega)$ is identical to $[\mathcal{G}_\sigma^+(\omega)]^{-1}$ and $\tilde\Phi_\sigma^-(\omega) \equiv [\mathcal{G}_{\bar\sigma}^-(\omega)]^{-1}$, while $\Phi_\sigma^-(\omega)$ and $\tilde\Phi_\sigma^+(\omega)$ are *different* from $[\mathcal{G}_\sigma^-(\omega)]^{-1}$ and $[\mathcal{G}_\sigma^+(\omega)]^{-1}$, respectively. The knowledge of $\Phi_\sigma^\pm$ is sufficient to determine $G_{\bar\sigma}^-$, since

$$\Phi_\sigma^+(\omega) - \Phi_\sigma^-(\omega) = 2i\Gamma_{\bar\sigma}f(\omega + \bar\sigma h)[1 + i(\Gamma_{\bar\sigma} + \Gamma_\sigma)G_{\bar\sigma}^-(\omega + \bar\sigma h)]. \tag{34}$$

Similarly, the functions $\tilde\Phi_\sigma^\pm$ determine G_σ^+, through the relation

$$\tilde\Phi_\sigma^+(\omega) - \tilde\Phi_\sigma^-(\omega) = 2i\Gamma_\sigma f(\omega + \sigma h)[1 - i(\Gamma_{\bar\sigma} + \Gamma_\sigma)G_\sigma^+(\omega + \sigma h)]. \tag{35}$$

Returning now to Eq. (28), we eliminate the Green functions by using Eqs. (34) and (35), and the functions P by using the definitions (33). In this way we find

$$\Phi_\sigma^+(\omega)\frac{\tilde\Phi_\sigma^+(\omega) - \tilde\Phi_\sigma^-(\omega)}{2i\Gamma_\sigma f(\omega + \sigma h)} = X_\sigma^+(\omega),$$

$$\tilde\Phi_\sigma^-(\omega)\frac{\Phi_\sigma^+(\omega) - \Phi_\sigma^-(\omega)}{2i\Gamma_{\bar\sigma}f(\omega + \bar\sigma h)} = \tilde X_\sigma^-(\omega), \tag{36}$$

where

$$X_\sigma(z) = -i(\Gamma_\sigma + \Gamma_{\bar\sigma})(1 - \langle n_{d\bar\sigma}\rangle) + z - \epsilon_0 + i\Gamma_\sigma - I_{\bar\sigma}(z + \bar\sigma h),$$

$$\tilde X_\sigma(z) = i(\Gamma_\sigma + \Gamma_{\bar\sigma})(1 - \langle n_{d\sigma}\rangle) + z - \epsilon_0 - i\Gamma_{\bar\sigma} - I_\sigma(z + \sigma h). \tag{37}$$

So far, we have not achieved much simplification over the original problem at hand. However, noting that

$$X_\sigma^+(\omega) - X_\sigma^-(\omega) = 2i\Gamma_{\bar\sigma}f(\omega + \bar\sigma h),$$

$$\tilde X_\sigma^+(\omega) - \tilde X_\sigma^-(\omega) = 2i\Gamma_\sigma f(\omega + \sigma h), \tag{38}$$

Eqs. (36) yield the remarkable result

$$\Phi_\sigma^+(\omega)\widetilde{\Phi}_\sigma^+(\omega) - X_\sigma^+(\omega)\widetilde{X}_\sigma^+(\omega) = \Phi_\sigma^-(\omega)\widetilde{\Phi}_\sigma^-(\omega) - X_\sigma^-(\omega)\widetilde{X}_\sigma^-(\omega).$$
(39)

Therefore, the combination

$$R(z) \equiv \Phi_\sigma(z)\widetilde{\Phi}_\sigma(z) - X_\sigma(z)\widetilde{X}_\sigma(z)$$
(40)

is *nonsingular* across the real axis. In fact, the only singular point of this combination is at $z=\infty$. This means that $R(z)$ can be written as a polynomial with non-negative powers of z. Moreover, since Φ, $\widetilde{\Phi}$, X, and $\widetilde{X}$ grow only linearly as $z \rightarrow \infty$, that polynomial includes only two terms, $r_0 + r_1 z$. The details of this calculation are given in Appendix B. The result (39) allows one to express the (unknown) functions Φ and $\widetilde{\Phi}$ in terms of the (known) functions X, $\widetilde{X}$, and R,

$$\frac{\Phi_\sigma^+}{\Phi_\sigma^-} = \frac{R + X_\sigma^+ \widetilde{X}_\sigma^-}{R + X_\sigma^- \widetilde{X}_\sigma^-} \equiv H_\sigma(\omega), \quad \frac{\widetilde{\Phi}_\sigma^+}{\widetilde{\Phi}_\sigma^-} = \frac{R + X_\sigma^+ \widetilde{X}_\sigma^+}{R + X_\sigma^+ \widetilde{X}_\sigma^-} \equiv \widetilde{H}_\sigma(\omega).$$
(41)

This reduces our problem into two independent *linear Reimann-Hilbert problems*, for which a rigorous solution is available,[33,34]

$$\Phi_\sigma(z) = (z-a)e^{M_\sigma(z)}, \quad M_\sigma(z) = \int \left(-\frac{d\omega}{2\pi i} \right) \frac{\ln H_\sigma(\omega)}{z-\omega},$$

$$\widetilde{\Phi}_\sigma(z) = (z-\widetilde{a})e^{\widetilde{M}_\sigma(z)}, \quad \widetilde{M}_\sigma(z) = \int \left(-\frac{d\omega}{2\pi i} \right) \frac{\ln \widetilde{H}_\sigma(\omega)}{z-\omega}.$$
(42)

This is a valid solution as long as $\ln H(\omega)$ and $\ln \widetilde{H}(\omega)$ can be chosen to be continuous in ω and to vanish at both ends of the integration interval.[35] All the cases studied in this paper obey this requirement, although we could not prove the absence of solutions other than (42) for a general case with no spin symmetry. The form of the polynomial prefactors, $(z-a)$ and $(z-\widetilde{a})$, in Eq. (42) is dictated by the fact that the leading term in $\Phi_\sigma(z)$ and $\widetilde{\Phi}_\sigma(z)$ must be z [see Eqs. (33)]. The determination of the coefficients a and $\widetilde{a}$, as well as other self-consistent quantities, is detailed in Appendix C.

V. PHYSICAL PROPERTIES IN THE $U \rightarrow \infty$ LIMIT

Once the functions Φ and $\widetilde{\Phi}$ are found, then the Green function is determined from Eq. (34) or Eq. (35). This knowledge enables us to compute various physical quantities, and compare them with the results of other calculations. The first quantity we consider is the total occupation on the dot, $n_0 \equiv \langle n_{d\uparrow} + n_{d\downarrow} \rangle$, at zero temperature. This calculation is carried out for the spin-symmetric case, $h=0$ and spin-independent self-energy. We also denote $D \equiv D_\sigma$, $\Gamma \equiv \Gamma_\sigma$. The result is plotted as function of E_d/Γ, where

$$E_d \equiv \epsilon_0 + (\Gamma/\pi)\ln(D/\Gamma),$$
(43)

and is portrayed in Fig. 1 (full line). It agrees within 3% with the exact universal curve $n_0(E_d/\Gamma)$, as found from the Bethe
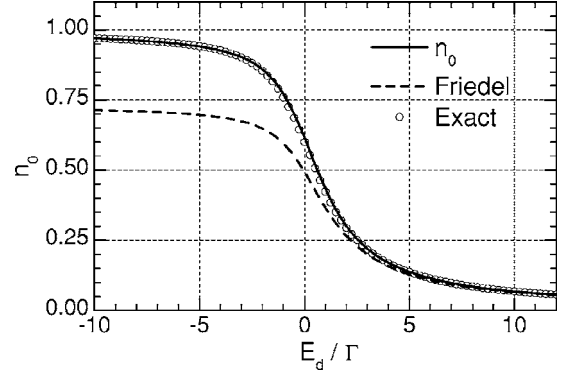

FIG. 1. The zero-temperature occupation number n_0 as function of the renormalized energy E_d calculated self-consistently by the EOM method (solid line), and from the Friedel sum-rule, Eq. (17) (dashed line). Open circles show the exact Bethe ansatz results (Ref. 36).

ansatz,[36] (open circles). Thus, the EOM solution conforms with Haldane's scaling.[37] On the other hand, the EOM solution fails to satisfy the Friedel sum-rule, as has been already discussed above.[38] The total occupation calculated from Eq. (17) (dashed line) deviates systematically from the self-consistent values, in particular in the Kondo regime ($n_0 \rightarrow 1$). Note that Eq. (27) implies that $\widetilde{n}_{d\sigma} = \langle n_{d\sigma} \rangle$ [see Eq. (19)].

As mentioned above, the Fermi-liquid relations are connected with unitarity. In particular, at zero temperature the linear conductance of a symmetrically coupled quantum dot is given by[3,5] $-2(e^2/h)\Gamma_\sigma \text{Im } G_\sigma(\omega=0)$. Thus, the unitary limit $2e^2/h$ is reached only if $\text{Re}[G_\sigma^+(0)] \rightarrow 0$ and the Fermi liquid relation (16) holds. As implied by the dashed line in the figure, the first of these criteria is not obeyed by the self-consistent solution.

Next we consider the local spin susceptibility on the dot. When the leads are nonmagnetic, this quantity is given by $\chi = \frac{1}{2}(g\mu_B)^2 \partial \langle n_{d\downarrow} - n_{d\uparrow} \rangle / \partial h$, with $h = -g\mu_B B$. Here B is the external magnetic field and $g\mu_B$ is the gyromagnetic ratio of electrons in the quantum dot. [The spin susceptibility of the leads adds to the local susceptibility the usual Pauli term, and $\mathcal{O}(\Gamma_\sigma/D_\sigma)$ corrections.[4]] We have calculated $\chi(E_d/\Gamma, T)$ by differentiating the self-consistent equations for $\langle n_{d\sigma} \rangle$ with respect to h, and evaluating the integrals numerically. This procedure is similar to the one which has been used for the Wolff model in Ref. 10(b), but is free from numerical accuracy problems reported there.

The zero-temperature susceptibility derived from the EOM is found to be in a good *quantitative* agreement with the Bethe ansatz results in the mixed valence ($|E_d/\Gamma| \lesssim 1$) and empty orbital ($E_d \gg \Gamma$) regimes, as is shown in Fig. 2. In the local moment regime, $E_d \ll -\Gamma$, a screening cloud is expected to form due to the Kondo effect at[4,37] $T < T_K \sim \Gamma e^{\pi E_d/(2\Gamma)}$, leading to a crossover from a high-temperature Curie law, $\chi \sim (g\mu_B)^2/T$, to a finite ground state value, $\chi \sim (g\mu_B)^2/T_K$. The latter is underestimated by our self-consistent solution, as is manifested by the deviation from the exact Bethe ansatz results depicted in Fig. 2.

Indeed, had we defined the Kondo temperature through the inverse of the zero-temperature susceptibility, we would
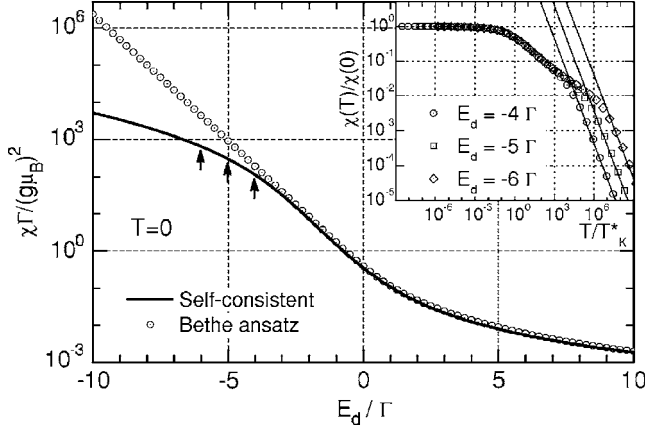
FIG. 2. The local spin susceptibility χ as function of the renormalized energy level E_d, for $T=0$. The EOM result (solid line) is close to the Bethe ansatz one (Ref. 36) (circles) in the empty orbital and mixed valence regimes, but deviates significantly in the strongly correlated region (large negative values of E_d/Γ). Inset: The scaling of the susceptibility with T/T_K^* at three fixed energy level positions (marked by arrows in the main graph). The solid lines indicate the high-temperature asymptotic behavior, $\chi(T) = (g\mu_B)^2/(6T)$.
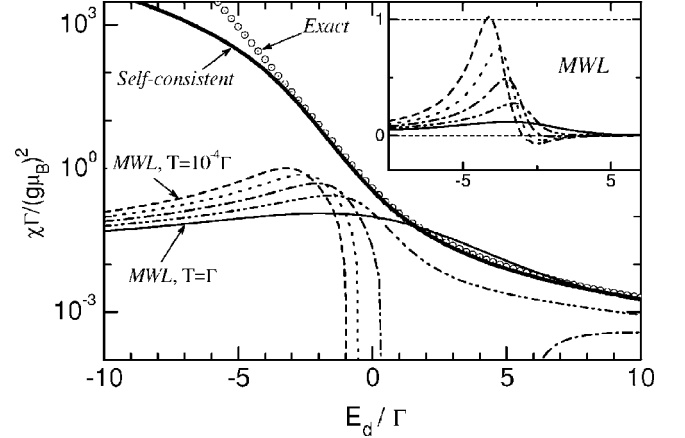

FIG. 3. Data from Fig. 2 compared to the spin susceptibility given by the MWL approximation in the temperature range from $T=1\Gamma$ down to $T=10^{-4}\Gamma$. The inset shows the MWL susceptibilities only, on a linear scale, allowing for the negative values.

have found that the EOM method *overestimates* that temperature. However, within EOM, the relevant energy scale is determined from the leading (real) terms in the denominator of the Green function, i.e., by the temperature at which the real part of $\mathcal{G}$, Eq. (29), vanishes. Using for $I(z)$, Eq. (31), the approximate form[9] $I(z) \approx -(\Gamma/\pi)\ln[(z+i\kappa T)/D]$ where κ is a number of order unity, we find that the leading terms are

$$\omega - E_d + \frac{\Gamma}{\pi}\ln\frac{D}{\Gamma} + \frac{\Gamma}{\pi}\ln\frac{\sqrt{\omega^2+\kappa^2T^2}}{D}, \qquad (44)$$

yielding for the temperature scale

$$T_K^* \sim \Gamma e^{\pi E_d/\Gamma}, \qquad (45)$$

such that the leading terms are

$$\omega + \frac{\Gamma}{\pi}\ln\sqrt{(\omega/T_K^*)^2 + (\kappa T/T_K^*)^2}. \qquad (46)$$

The logarithm in Eq. (46) dominates the properties of the solution close to the Fermi energy at temperatures $T \lesssim T_K^*$. The same energy scale T_K^* has been determined from the analysis of the truncated EOM in Refs. 11 and 18. Note that T_K^* is *smaller* than the true Kondo temperature T_K.

The local spin susceptibility at finite temperatures, calculated from our EOM solution, is shown in the inset of Fig. 2. Indeed, $\chi(T)/\chi(0)$ scales with T/T_K^*, but instead of crossing over to the Curie law, a region of intermediate behavior in which $\chi \sim T^x$ with $-1 < x < 0$ is observed. The high-temperature asymptotic $\chi(T) \sim 1/T$ is approached only for $T \gtrsim \Gamma$. Such a behavior in the intermediate temperature range $T_K^* < T < \Gamma$ is not supported by NRG or Bethe ansatz calculations,[4] which scale with T_K,[39] and has thus to be attributed to the deficiency of the EOM method.

In contrast, neither the Lacroix approximation, as implemented in Ref. 18, nor the MWL[5] approximate Green function leads to comparable results when used to calculate the local spin susceptibility. The Lacroix approximation becomes intrinsically inconsistent at finite magnetic fields, since it results in a logarithmic divergence of $G_\sigma(z)$ as $z \to \sigma h$. Even when ignoring this inconsistency, the zero-temperature spin susceptibility calculated in that approximation attains negative and divergent values regardless of the quantum dot parameters. The MWL approximation leads to finite, but quite unphysical values of χ for $T < \Gamma$, as we demonstrate in Fig. 3. That approximation gives reasonable results at $T=\Gamma$: the susceptibility follows roughly the Curie law $\approx 1/T (=1/\Gamma)$ or the zero-temperature value, whichever is smaller. At lower temperatures one would have expected a gradual increase in the susceptibility in the Kondo region. Instead, a window of a *negative susceptibility* opens, which is widened as the temperature is decreased. At strictly zero temperature χ is negative for all values of E_d. This example shows the necessity of using the full self-consistency of the EOM solution in order to obtain the qualitatively correct behavior.

Finally, we examine the local density of states on the dot, given by

$$\rho(\omega,T) \equiv -\text{Im}\sum_\sigma G_\sigma^+(\omega)/\pi, \qquad (47)$$

as calculated from the EOM. The inset of Fig. 4 shows the Kondo peak at temperatures $T \lesssim T_K^*$. The local density of states at the Fermi energy follows the universal temperature dependence, as can be seen in Fig. 4, with the same scaling factor T_K^* as the spin susceptibility (compare to the inset of Fig. 2). The appearance of a single scale determining the low-energy properties of the system is another hallmark[4] of the Kondo effect which is captured by the fully self-consistent EOM technique.
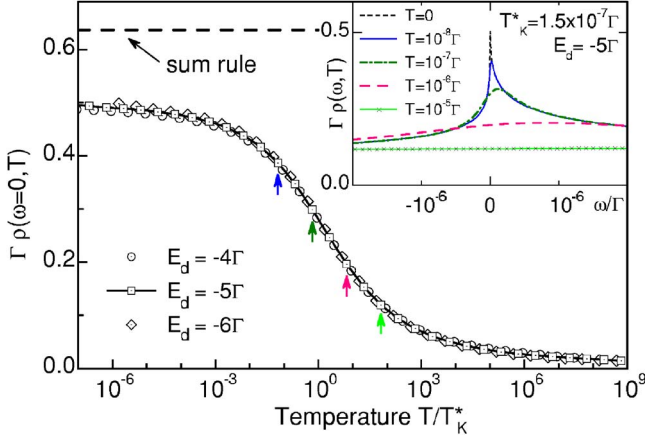
FIG. 4. (Color online) The scaling of the local density of states at the Fermi level as function of the reduced temperature T/T_K^*, is demonstrated by plotting $\rho(\omega=0,T)$ for three different values of the renormalized single-electron energy on the dot, E_d [Eq. (43)]. The dashed line at $\rho=2/(\pi\Gamma)$ corresponds to the limit dictated by the Friedel sum-rule at $E_d/\Gamma \ll -1$. The inset shows the melting of the Kondo peak as the temperature is increased at fixed $E_d/\Gamma=-5$. Temperature values represented in the inset are marked by arrows in the main graph.

VI. PERTURBATION EXPANSION IN THE DOT-NETWORK COUPLINGS

The EOM technique is unfortunately not a systematic expansion. It is therefore very interesting to compare its results with those given by a direct expansion. Here we expand the EOM Green function up to second order in the dot-network couplings $J_{n\sigma}$. For compactness, we confine ourselves to the case $U \to \infty$, and assume for simplicity that the noninteracting self-energy has just an energy-independent imaginary part, i.e., $\Sigma_\sigma(\omega) = -i\Gamma_\sigma$. By comparing with the direct pertur-

bation theory expansion[24,25] we find that, up to second order in $J_{n\sigma}$, our EOM result for the dot Green function is exact. (See also Ref. 23.) On the other hand, the Green function derived in Ref. 5 (which does not include all correlations resulting from the truncated EOM) violates the second-order perturbation theory result, and in fact, predicts a Kondo anomaly in this order (which should not be there).

The $U \to \infty$ Green function of the EOM is given by Eqs. (28)–(30) and (32). Since the noninteracting self-energy Σ_σ, and consequently the width Γ_σ are second order in the coupling $J_{n\sigma}$, the expansion of the Green function reads

$$G_\sigma^{(0)}(z) = \frac{\delta n_{\bar\sigma}^{(0)}}{z - \epsilon_\sigma}, \tag{48}$$

and

$$G_\sigma^{(2)}(z) = \frac{\delta n_{\bar\sigma}^{(2)} - P_{\bar\sigma}^{(2)}(z_1)}{z - \epsilon_\sigma} + G_\sigma^{(0)}(z)\frac{I_\sigma(z_1) + \Sigma_\sigma(z)}{z - \epsilon_\sigma}, \tag{49}$$

where we have denoted

$$\langle n_{\bar\sigma} \rangle \equiv 1 - \delta n_{\bar\sigma}, \quad \epsilon_\sigma = \epsilon_0 + \sigma h \tag{50}$$

and where the superscript (k) denotes the contribution of order k in the couplings. The function $P^{(2)}$ is found by using the zeroth-order of the Green function in Eq. (32),

$$P_\sigma^{(2)}(z) = G_\sigma^{(0)}(z)[I_\sigma(z) - \Gamma_\sigma^-(\epsilon_\sigma) - f(\epsilon_\sigma)\Sigma_\sigma(z) + f(\epsilon_\sigma)\Sigma_\sigma^-(\epsilon_\sigma)]. \tag{51}$$

Using the identities

$$\Gamma_\sigma^-(\epsilon_\sigma) - f(\epsilon_\sigma)\Sigma_\sigma^-(\epsilon_\sigma) = \mathrm{Re}[I_\sigma(\epsilon_\sigma) - f(\epsilon_\sigma)\Sigma_\sigma(\epsilon_\sigma)] \tag{52}$$

and

$$G_{\bar\sigma}^{(0)}(z_1) = \delta n_\sigma^{(0)} G_\sigma^{(0)}(z)/\delta n_{\bar\sigma}^{(0)}, \tag{53}$$

Eq. (49) takes the form

$$G_\sigma^{(2)}(z) = \frac{\delta n_{\bar\sigma}^{(2)}}{z - \epsilon_\sigma} + \frac{-\delta n_\sigma^{(0)}[I_{\bar\sigma}(z_1) - f(\epsilon_{\bar\sigma})\Sigma_{\bar\sigma}(z_1) - \mathrm{Re}\{I_{\bar\sigma}(\epsilon_{\bar\sigma}) - f(\epsilon_{\bar\sigma})\Sigma_{\bar\sigma}(\epsilon_{\bar\sigma})\}] + \delta n_{\bar\sigma}^{(0)}[I_\sigma(z_1) + \Sigma_\sigma(z)]}{(z - \epsilon_\sigma)^2}. \tag{54}$$

In order to complete the second-order calculation, we need to find the occupation numbers $\delta n_\sigma^{(0)}$ and $\delta n_\sigma^{(2)}$ [see Eq. (50)]. From Eq. (48) we find

$$\langle n_\sigma \rangle^{(0)} = \frac{f(\epsilon_\sigma)[1 - f(\epsilon_{\bar\sigma})]}{1 - f(\epsilon_\sigma)f(\epsilon_{\bar\sigma})}. \tag{55}$$

The second-order correction to the occupation number, $\delta n_\sigma^{(2)} \equiv -\langle n_\sigma \rangle^{(2)}$, is obtained by integrating over the Fermi function multiplied by the second-order correction to the density of states, $\rho_\sigma^{(2)}(\omega)$. The latter reads

$$\rho_\sigma^{(2)}(\omega) \equiv \frac{G_\sigma^{+(2)}(\omega) - G_\sigma^{-(2)}(\omega)}{-2\pi i} = \delta(\omega - \epsilon_\sigma)\left(\delta n_{\bar\sigma}^{(2)} + [\langle n_\sigma \rangle^{(0)} - \langle n_{\bar\sigma} \rangle^{(0)}]\frac{\partial \mathrm{Re}\, I_{\bar\sigma}(\epsilon_{\bar\sigma})}{\partial \epsilon_0} \right) - \delta'(\omega - \epsilon_\sigma)\delta n_{\bar\sigma}^{(0)} \mathrm{Re}\, I_{\bar\sigma}(\epsilon_{\bar\sigma})$$

$$+ \frac{\Gamma_\sigma + (\Gamma_{\bar\sigma} - \Gamma_\sigma)\langle n_{\bar\sigma} \rangle^{(0)} + \Gamma_{\bar\sigma} f(\omega - \epsilon_\sigma + \epsilon_{\bar\sigma})[\langle n_\sigma \rangle^{(0)} - \langle n_{\bar\sigma} \rangle^{(0)}]}{\pi(\omega - \epsilon_\sigma)^2}. \tag{56}$$

Apart from the terms representing the second-order modifications of the singularity at ϵ_σ [the first and second members of Eq. (56)], our result reproduces the one of Ref. 24, for the case where the width Γ_σ is spin independent, i.e., $\Gamma_\sigma = \Gamma_{\bar{\sigma}}$.

Note that this density of states remains finite at all temperatures. The Kondo divergence of $\rho_\sigma^{(k)}(0)$ in the limit $T \to 0$ appears only at $k \geq 4$ (see Ref. 24). Using the second-order correction to the density of states, we find

$$\langle n_\sigma \rangle^{(2)} = \int f(\omega) \rho_\sigma^{(2)}(\omega) d\omega = (\langle n_{\bar{\sigma}} \rangle^{(0)} - 1) \mathrm{Re}\, \frac{\partial I_\sigma(\epsilon_\sigma)}{\partial \epsilon_\sigma} + \frac{\partial \langle n_\sigma \rangle^{(0)}}{\partial \epsilon_\sigma} \mathrm{Re}\, I_{\bar{\sigma}}(\epsilon_{\bar{\sigma}}) + \frac{\partial \langle n_\sigma \rangle^{(0)}}{\partial \epsilon_{\bar{\sigma}}} \mathrm{Re}\, I_\sigma(\epsilon_\sigma). \tag{57}$$

This result is identical to the $U \to \infty$ limit of Eq. (5) in Ref. 25 which was obtained by a direct perturbation expansion. Figure 5 depicts the total occupation, $n_0 = \Sigma_\sigma \langle n_\sigma \rangle$, as function of ϵ_0, as found from the EOM technique, and as computed from Eqs. (55) and (57) to first order in the width. The two curves differ by a few percents. The comparison with the exact result is carried out in Sec. IV.

VII. CONCLUSIONS

We have presented a solution for the Green function of an interacting quantum dot embedded in a general noninteracting network. Our solution is derived within the EOM technique, taking into account exactly *all* resulting correlations once those equations are truncated. We have tested our solution by analyzing several limiting cases, and by comparing several physical properties derived from that solution with other results available by the Bethe ansatz method and by NRG computations.

We have found that the EOM Green function is temperature independent at the particle-hole symmetric point (where $h = 0$ and $2\epsilon_0 + U = 0$). We have found that this deficiency of

FIG. 5. The equilibrium occupation number $n_0 = \Sigma_\sigma \langle n_\sigma \rangle$ for the same parameters as in Fig. 1, and $D = 100\Gamma$ (since second-order perturbation theory *does not* scale with E_d, the bandwidth has to be specified), calculated from the self-consistently truncated EOM (solid lines), and by perturbation theory to first order in Γ, Eqs. (55) and (57) (dashed line). The perturbational result diverges at $\epsilon_0 = 0$.

the EOM is related to a discontinuity in the imaginary part of the interacting self-energy at that particular point. However, this imaginary part obeys the Fermi-liquid unitarity requirement away from this special point, at zero temperature. In contrast, even away from the particle-hole symmetric point, the EOM result fails to satisfy the Friedel sum-rule deep inside the Kondo regime, as we have shown explicitly in the infinite interaction limit.

Albeit these problems, the EOM solution reproduces faithfully the low-temperature scaling of the spin susceptibility and the density of states at the Fermi level, though with an energy scale T_K^* which differs from the true Kondo temperature [cf. Eq. (45)]. Zero-temperature results are in excellent agreement with the exact Bethe ansatz solution, except for the Kondo correlated regime. As the temperature is raised, the EOM results become more and more quantitatively correct, and approach high-temperature asymptotics known rigorously from perturbation theory and NRG studies. We have expanded the EOM Green function to second order in the dot-network coupling and found an exact agreement with direct calculations by perturbation theory. Most importantly, we have found that it is crucial to include in the EOM solution *all* the correlations emerging from the truncated scheme. Ignoring part of these correlations, as is ubiquitously done in such studies, results in erroneous behaviors of various physical quantities.

Hence we conclude that the method examined in this paper can provide a reasonable description of a quantum dot system over a wide parameter range, provided that the self-consistency conditions inherent to this technique are fully taken into account.

APPENDIX A: EOM FOR THE FINITE *U* CASE

Here we extend the derivations of Refs. 9, 13, and 18, carried out for an infinite repulsive interaction, to the case in which U is finite. In addition, we allow for a Zeeman field, assuming that the quantization axes of the spins are the same on the dot and on the leads (but the g factors may be differ-
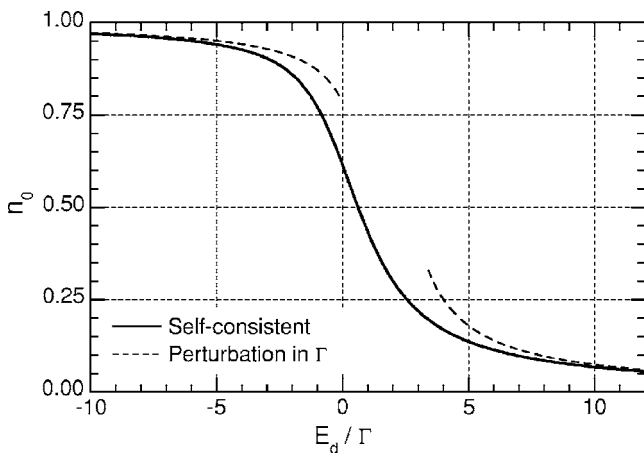
ent). The Hamiltonian of the our system is given in Eq. (1).

The Fourier transform of the EOM for the Green function defined in Eq. (5) can be written in two alternative forms[8] (both will be used in the following),

$$z\langle\langle A;B\rangle\rangle_z = \langle[A,B]_+\rangle + \langle\langle[A,\mathcal{H}]_-;B\rangle\rangle_z$$
$$= \langle[A,B]_+\rangle - \langle\langle A;[B,\mathcal{H}]_-\rangle\rangle_z. \quad (A1)$$

It follows that the EOM for the dot Green function is

$$[z - \epsilon_0 - \sigma h]G_\sigma = 1 + U\langle\langle n_{d\bar\sigma}d_\sigma;d_\sigma^\dagger\rangle\rangle - \sum_n J_{n\sigma}\langle\langle a_{n\sigma};d_\sigma^\dagger\rangle\rangle, \quad (A2)$$

where $\bar\sigma$ is the spin direction opposite to σ. Here and in the following we frequently omit for brevity explicit indications of the argument z. We first consider the last term on the right-hand side of Eq. (A2). The EOM for the Green function appearing there is

$$(z - \varepsilon_{n\sigma})\langle\langle a_{n\sigma};d_\sigma^\dagger\rangle\rangle = -\sum_m J_{nm}\langle\langle a_{m\sigma};d_\sigma^\dagger\rangle\rangle - J_{n\sigma}^*G_\sigma. \quad (A3)$$

Introducing the inverse matrix

$$\mathcal{M}_{nm\sigma}(z) \equiv [(z - \mathcal{H}_{\text{net}}^\sigma)^{-1}]_{nm}, \quad (A4)$$

where $\mathcal{H}_{\text{net}}^\sigma$ is the part of $\mathcal{H}_{\text{net}}$ pertaining to the spin direction σ, we find

$$\langle\langle a_{n\sigma};d_\sigma^\dagger\rangle\rangle = -\sum_m \mathcal{M}_{nm\sigma}(z)J_{m\sigma}^*G_\sigma. \quad (A5)$$

Note that $\mathcal{M}$ is the Green function matrix of the network *in the absence of the coupling to the dot*. Using Eq. (A5), we find that the last term on the right-hand side of Eq. (A2) can be put in the form

$$-\sum_n J_{n\sigma}\langle\langle a_{n\sigma};d_\sigma^\dagger\rangle\rangle = \Sigma_\sigma G_\sigma, \quad (A6)$$

where

$$\Sigma_\sigma(z) \equiv \sum_{nm} J_{n\sigma}\mathcal{M}_{nm\sigma}(z)J_{m\sigma}^* \quad (A7)$$

is the self-energy of the dot Green function coming from the coupling to the (noninteracting) network. Namely, it is the dot self-energy for the $U=0$ case.[18] As such, it can always be calculated, at least in principle (see, for example, Refs. 18 and 40).

We now turn to the interacting part of the EOM for the dot Green function [the second term on the right-hand side of Eq. (A2)]. The EOM for the four-operator Green function appearing there reads

$$[z - \epsilon_0 - \sigma h - U]\langle\langle n_{d\bar\sigma}d_\sigma;d_\sigma^\dagger\rangle\rangle = \langle n_{d\bar\sigma}\rangle - \sum_n [J_{n\sigma}\langle\langle a_{n\sigma}n_{d\bar\sigma};d_\sigma^\dagger\rangle\rangle + J_{n\bar\sigma}\langle\langle d_{\bar\sigma}^\dagger a_{n\bar\sigma}d_\sigma;d_\sigma^\dagger\rangle\rangle - J_{n\bar\sigma}^*\langle\langle a_{n\bar\sigma}^\dagger d_{\bar\sigma}d_\sigma;d_\sigma^\dagger\rangle\rangle], \quad (A8)$$

and gives rise to three new four-operator Green functions (on the right-hand side here). Their EOM are

$$[z - \varepsilon_{n\sigma}]\langle\langle a_{n\sigma}n_{d\bar\sigma};d_\sigma^\dagger\rangle\rangle = -\sum_m J_{nm}\langle\langle a_{m\sigma}n_{d\bar\sigma};d_\sigma^\dagger\rangle\rangle - J_{n\sigma}^*\langle\langle n_{d\bar\sigma}d_\sigma;d_\sigma^\dagger\rangle\rangle - \sum_m [J_{m\bar\sigma}\langle\langle a_{n\sigma}d_{\bar\sigma}^\dagger a_{m\bar\sigma};d_\sigma^\dagger\rangle\rangle - J_{m\bar\sigma}^*\langle\langle a_{m\bar\sigma}^\dagger d_{\bar\sigma}a_{n\sigma};d_\sigma^\dagger\rangle\rangle], \quad (A9)$$

$$[z_1 - \varepsilon_{n\bar\sigma}]\langle\langle d_{\bar\sigma}^\dagger a_{n\bar\sigma}d_\sigma;d_\sigma^\dagger\rangle\rangle = \langle d_{\bar\sigma}^\dagger a_{n\bar\sigma}\rangle - \sum_m J_{nm}\langle\langle d_{\bar\sigma}^\dagger a_{m\bar\sigma}d_\sigma;d_\sigma^\dagger\rangle\rangle - J_{n\bar\sigma}^*\langle\langle n_{d\bar\sigma}d_\sigma;d_\sigma^\dagger\rangle\rangle + \sum_m [J_{m\bar\sigma}^*\langle\langle a_{m\bar\sigma}^\dagger a_{n\bar\sigma}d_\sigma;d_\sigma^\dagger\rangle\rangle$$
$$- J_{m\sigma}\langle\langle d_{\bar\sigma}^\dagger a_{n\bar\sigma}a_{m\sigma};d_\sigma^\dagger\rangle\rangle], \quad (A10)$$

$$[-z_2 + \varepsilon_{n\bar\sigma}]\langle\langle a_{n\bar\sigma}^\dagger d_{\bar\sigma}d_\sigma;d_\sigma^\dagger\rangle\rangle = \langle a_{n\bar\sigma}^\dagger d_{\bar\sigma}\rangle + \sum_m J_{nm}^*\langle\langle a_{m\bar\sigma}^\dagger d_{\bar\sigma}d_\sigma;d_\sigma^\dagger\rangle\rangle + J_{n\bar\sigma}\langle\langle n_{d\bar\sigma}d_\sigma;d_\sigma^\dagger\rangle\rangle - \sum_m [J_{m\sigma}\langle\langle a_{n\bar\sigma}^\dagger d_{\bar\sigma}a_{m\sigma};d_\sigma^\dagger\rangle\rangle$$
$$- J_{m\bar\sigma}\langle\langle a_{n\bar\sigma}^\dagger d_\sigma a_{m\bar\sigma};d_\sigma^\dagger\rangle\rangle], \quad (A11)$$

where we have introduced the definitions

$$z_1 \equiv z - 2\sigma h, \quad z_2 \equiv -z + 2\epsilon_0 + U. \quad (A12)$$

The EOM (A9)–(A11) include four-operator Green functions in which only two of the operators are dot operators. Those are decoupled as detailed in Eq. (8). One then finds

$$-\sum_n J_{n\sigma}\langle\langle a_{n\sigma}n_{\bar\sigma};d_\sigma^\dagger\rangle\rangle = \Sigma_\sigma\langle\langle n_{\bar\sigma}d_\sigma;d_\sigma^\dagger\rangle\rangle + \sum_{nmm'} J_{n\sigma}\mathcal{M}_{nm\sigma}\langle\langle a_{m\sigma};d_\sigma^\dagger\rangle\rangle[J_{m'\bar\sigma}\langle d_{\bar\sigma}^\dagger a_{m'\bar\sigma}\rangle - J_{m'\bar\sigma}^*\langle a_{m'\bar\sigma}^\dagger d_{\bar\sigma}\rangle], \quad (A13)$$

$$-\sum_n J_{n\bar\sigma}\langle\langle d_{\bar\sigma}^\dagger a_{n\bar\sigma}d_\sigma;d_\sigma^\dagger\rangle\rangle = (1 + \Sigma_\sigma G_\sigma)P_{\bar\sigma}(z_1) + \Sigma_{\bar\sigma}(z_1)\langle\langle n_{\bar\sigma}d_\sigma;d_\sigma^\dagger\rangle\rangle - G_\sigma Q_{\bar\sigma}(z_1), \quad (A14)$$

$$\sum_n J_{n\bar{\sigma}}^* \langle\langle a_{n\bar{\sigma}}^\dagger d_{\bar{\sigma}} d_\sigma; d_\sigma^\dagger \rangle\rangle = (1 + \Sigma_\sigma G_\sigma) P_{\bar{\sigma}}(z_2) - \Sigma_{\bar{\sigma}}(z_2) \langle\langle n_{\bar{\sigma}} d_\sigma; d_\sigma^\dagger \rangle\rangle + G_\sigma Q_{\bar{\sigma}}(z_2), \tag{A15}$$

where we have introduced

$$P_\sigma(z) \equiv -\sum_{nm} J_{n\sigma} \mathcal{M}_{nm\sigma}(z) \langle d_\sigma^\dagger a_{m\sigma} \rangle$$

$$= -\sum_{mn} \langle a_{m\sigma}^\dagger d_\sigma \rangle \mathcal{M}_{nm\sigma}(z) J_{n\sigma}^*, \tag{A16}$$

$$Q_\sigma(z) \equiv \sum_{nmm'} J_{n\sigma} \mathcal{M}_{nm\sigma}(z) \langle a_{m'\sigma}^\dagger a_{m\sigma} \rangle J_{m'\sigma}^*$$

$$= \sum_{nmm'} J_{m'\sigma} \langle a_{m\sigma}^\dagger a_{m'\sigma} \rangle \mathcal{M}_{nm\sigma}(z) J_{n\sigma}^*. \tag{A17}$$

The second equality in each of Eqs. (A16) and (A17) is justified below.

Examining Eqs. (A13), (A16), and (A17) reveals that one needs to find thermal averages of two types, the ones belonging to two network operators, $\langle a_{m\sigma}^\dagger a_{m'\sigma} \rangle$, and the ones consisting of a dot and a network operator, $\langle d_\sigma^\dagger a_{m\sigma} \rangle$. These are found [see Eq. (7)] from the corresponding Green's functions, whose EOM are given by Eq. (A3) and

$$(z - \varepsilon_{n\sigma}) \langle\langle d_\sigma; a_{n\sigma}^\dagger \rangle\rangle = -\sum_m \langle\langle d_\sigma; a_{m\sigma}^\dagger \rangle\rangle J_{mn} - J_{n\sigma} G_\sigma, \tag{A18}$$

$$(z - \varepsilon_{m\sigma}) \langle\langle a_{m\sigma}; a_{n\sigma}^\dagger \rangle\rangle$$
$$= \delta_{mn} - \sum_{m'} J_{mm'} \langle\langle a_{m'\sigma}; a_{n\sigma}^\dagger \rangle\rangle - J_{m\sigma}^* \langle\langle d_\sigma; a_{n\sigma}^\dagger \rangle\rangle. \tag{A19}$$

Their solutions in terms of the inverse matrix $\mathcal{M}_{nm\sigma}$ [see Eq. (A4)] are

$$\langle\langle d_\sigma; a_{n\sigma}^\dagger \rangle\rangle = -\sum_m J_{m\sigma} \mathcal{M}_{mn\sigma} G_\sigma, \tag{A20}$$

$$\langle\langle a_{m\sigma}; a_{n\sigma}^\dagger \rangle\rangle = \mathcal{M}_{mn\sigma} + \sum_{ln'} \mathcal{M}_{ml\sigma} J_{l\sigma}^* J_{n'\sigma} \mathcal{M}_{n'n\sigma} G_\sigma. \tag{A21}$$

Employing these solutions to obtain the thermal averages appearing in Eq. (A13), we find

$$\sum_{m'} J_{m'\bar{\sigma}} \langle d_{\bar{\sigma}}^\dagger a_{m'\bar{\sigma}} \rangle = \sum_{m'} J_{m'\bar{\sigma}}^* \langle a_{m'\bar{\sigma}}^\dagger d_{\bar{\sigma}} \rangle.$$

Consequently, the terms in the square brackets of Eq. (A13) are cancelled. Next, we use the first equality in each of the definitions (A16) and (A17) together with the auxiliary Green functions (A5) and (A21), to find P and Q in terms of the dot Green function G,

$$P_\sigma(z) = i \oint_C \frac{dz'}{2\pi} f(z') G_\sigma(z')$$
$$\times \sum_{nm} J_{n\sigma} J_{m\sigma}^* [(z - \mathcal{H}_{\text{net}}^\sigma)^{-1} (z' - \mathcal{H}_{\text{net}}^\sigma)^{-1}]_{nm}, \tag{A22}$$

$$Q_\sigma(z) = i \oint_C \frac{dz'}{2\pi} f(z') [1 + \Sigma_\sigma(z') G_\sigma(z')]$$
$$\times \sum_{nm} J_{n\sigma} J_{m\sigma}^* [(z - \mathcal{H}_{\text{net}}^\sigma)^{-1} (z' - \mathcal{H}_{\text{net}}^\sigma)^{-1}]_{nm}, \tag{A23}$$

where we have used Eq. (A4). Since

$$(z - \mathcal{H}_{\text{net}}^\sigma)^{-1} (z - \mathcal{H}_{\text{net}}^\sigma)^{-1} = \frac{(z' - \mathcal{H}_{\text{net}}^\sigma)^{-1} - (z - \mathcal{H}_{\text{net}}^\sigma)^{-1}}{z - z'}, \tag{A24}$$

we can use Eq. (A7) for the noninteracting self-energy, to write the functions P and Q in terms of that self-energy,

$$P_\sigma(z) = \lim_{\eta' \to 0} \frac{i}{2\pi} \int d\omega \frac{f(\omega)}{z - \omega} (G_\sigma(\omega + i\eta') [\Sigma_\sigma(\omega + i\eta') - \Sigma_\sigma(z)] - G_\sigma(\omega - i\eta') [\Sigma_\sigma(\omega - i\eta') - \Sigma_\sigma(z)])$$

$$\equiv \frac{i}{2\pi} \oint_C f(w) G_\sigma(w) \frac{\Sigma_\sigma(w) - \Sigma_\sigma(z)}{z - w} dw,$$

$$Q_\sigma(z) = \lim_{\eta' \to 0} \frac{i}{2\pi} \int d\omega \frac{f(\omega)}{z - \omega} ([1 + \Sigma_\sigma(\omega + i\eta') G_\sigma(\omega + i\eta')][\Sigma_\sigma(\omega + i\eta') - \Sigma_\sigma(z)] - [1 + \Sigma_\sigma(\omega - i\eta') G_\sigma(\omega - i\eta')]$$

$$\times [\Sigma_\sigma(\omega - i\eta') - \Sigma_\sigma(z)]) \equiv \frac{i}{2\pi} \oint_C f(w) [1 + \Sigma_\sigma(w) G_\sigma(w)] \frac{\Sigma_\sigma(w) - \Sigma_\sigma(z)}{z - w} dw. \tag{A25}$$

Here and elsewhere the imaginary part of z is always greater than η', so that the contour C never encircles the pole at $w = z$. Note that using the same procedure employing the second equalities in Eqs. (A16) and (A17) gives again Eqs. (A22) and (A23), thus proving that the two definitions of P and Q in Eqs. (A16) and (A17) are equivalent. Equation (A8) can be now easily solved. Inserting the solution into Eq. (A2) leads to the expression for the dot Green function, Eq. (9).

In treating the functions P and Q in Sec. III A we have employed several properties of the complex integrals appearing in Eqs. (A25). Consider, for example, the integral

$$\frac{i}{2\pi}\oint_C G(w)\frac{\Sigma(w)-\Sigma(z)}{z-w}dw. \qquad (A26)$$

Since $G(w)$ and $\Sigma(w)$ have no singularities except for a cut along the real axis, it is expedient to complete each half of the contour C by a large-radius semicircle in the upper and lower half-planes. Then, by the residue theorem, Eq. (A26) vanishes provided that $G(w)$ falls as w^{-1} or faster at $w\to\infty$. This means that the Fermi function $f(w)$ in the definition of P can be replaced by $f(w)+\text{const}$. Another important case is

when $G(w)$ is replaced by 1 in Eq. (A26). In this case the contribution of the semicircles does not vanish, and the integral (A26) gives $\Sigma(z)$.

An alternative to the fully self-consistent treatment investigated in this paper has been proposed in Ref. 5. There, the averages of the form $\langle d_\sigma^\dagger a_{m\sigma}\rangle$ were ignored, and those of the type $\langle a_{m\sigma}^\dagger a_{m'\sigma}\rangle$ were approximated by $\delta_{mm'}\langle a_{m\sigma}^\dagger a_{m\sigma}\rangle$. Namely, $\mathcal{H}_{\text{net-dot}}$ was put to zero in the calculation of the averages. Upon such an approximation, $P_\sigma(z)\simeq 0$, and

$$Q_\sigma(z)\simeq\int\text{Im}\left[\frac{\Sigma_\sigma(\omega-i\eta)}{\pi}\right]\frac{f(\omega)}{z-\omega}d\omega, \qquad (A27)$$

reproducing Eq. (8) of Ref. 5. Another approximation of Eqs. (A22) and (A23), originally due to Lacroix,[11] has been recently analyzed in the context of quantum dots in Ref. 18. In this approximation one assumes the dot Green function to vary smoothly enough over the integration regimes in Eqs. (A22) and (A23), so that it can be taken out of the integrals. This ansatz reduces Eq. (9) of the text to a quadratic form. These two approximate solutions are discussed in Secs. III and IV.

APPENDIX B: DERIVATION OF THE POLYNOMIAL FUNCTION R

As explained in Sec. IV, the function

$$R(z)\equiv\Phi_\sigma(z)\widetilde{\Phi}_\sigma(z)-\text{X}_\sigma(z)\widetilde{\text{X}}_\sigma(z)=i(\Gamma_\sigma+\Gamma_{\bar\sigma})[z-\epsilon_0-i\Gamma_{\bar\sigma}-I_\sigma(z+\sigma h)]\left[\langle 1-n_{d\bar\sigma}\rangle-\frac{\Gamma_{\bar\sigma}}{\pi}\int d\omega\frac{f(\omega)G_{\bar\sigma}^-(\omega)}{z+\bar\sigma h-\omega}\right]$$

$$-i(\Gamma_\sigma+\Gamma_{\bar\sigma})[z-\epsilon_0+i\Gamma_\sigma-I_{\bar\sigma}(z+\bar\sigma h)]\left[\langle 1-n_{d\sigma}\rangle-\frac{\Gamma_\sigma}{\pi}\int d\omega\frac{f(\omega)G_\sigma^+(\omega)}{z+\sigma h-\omega}\right]-(\Gamma_\sigma+\Gamma_{\bar\sigma})^2\left[\langle 1-n_{d\bar\sigma}\rangle\langle 1-n_{d\sigma}\rangle\right.$$

$$\left.-\frac{\Gamma_{\bar\sigma}}{\pi}\int d\omega\frac{f(\omega)G_{\bar\sigma}^-(\omega)}{z+\bar\sigma h-\omega}\frac{\Gamma_\sigma}{\pi}\int d\omega\frac{f(\omega)G_\sigma^+(\omega)}{z+\sigma h-\omega}\right] \qquad (B1)$$

is nonsingular across the real axis, and its only singular point is at $z=\infty$. This observation enables one to solve for the Green function in terms of the functions Φ and $\widetilde{\Phi}$. Here we examine $R(z)$ in some detail, and also derive the first two terms of its polynomial expansion.

In the limit $z\to\infty$, the function $I_\sigma(z)$, Eq. (31), is given by

$$I_\sigma(z)\sim\frac{\Gamma_\sigma}{\pi}\ln\frac{D_\sigma}{z}. \qquad (B2)$$

The $z\to\infty$ limit of the integrals appearing in Eq. (B1) has to be taken with care. We write the Green functions appearing in the integrands there in the form $G_\sigma^\pm(\omega)=\text{Re }G_\sigma^+(\omega)\pm i\,\text{Im }G_\sigma^+(\omega)$, and use $\langle n_{d\sigma}\rangle=-(1/\pi)\times\int d\omega f(\omega)\text{Im }G_\sigma^+(\omega)$ to obtain

$$\frac{\Gamma_\sigma}{\pi}\int d\omega\frac{f(\omega)G_\sigma^\pm(\omega)}{z-\omega}\sim\mp i\frac{\Gamma_\sigma\langle n_{d\sigma}\rangle}{z}+A_\sigma(z), \qquad (B3)$$

where

$$A_\sigma(z)=\frac{\Gamma_\sigma}{\pi}\int d\omega\frac{f(\omega)\text{Re }G_\sigma^+(\omega)}{z-\omega}. \qquad (B4)$$

Inserting Eqs. (B2) and (B3) into Eq. (B1), the terms which survive the $z\to\infty$ limit are

$$R(z)\sim(\Gamma_\sigma+\Gamma_{\bar\sigma})^2(\langle n_{d\sigma}\rangle+\langle n_{d\bar\sigma}\rangle-\langle n_{d\sigma}\rangle\langle n_{d\bar\sigma}\rangle)$$

$$+i(\Gamma_\sigma+\Gamma_{\bar\sigma})(z-\epsilon_0)\langle n_{d\sigma}-n_{d\bar\sigma}\rangle$$

$$+i(\Gamma_\sigma+\Gamma_{\bar\sigma})\left(z[A_\sigma(z)-A_{\bar\sigma}(z)]-\langle 1-n_{d\bar\sigma}\rangle\frac{\Gamma_\sigma}{\pi}\ln\frac{D_\sigma}{z}\right.$$

$$+ \langle 1 - n_{d\sigma} \rangle \frac{\Gamma_{\bar{\sigma}}}{\pi} \ln \frac{D_{\bar{\sigma}}}{z} \bigg). \tag{B5}$$

According to the discussion in Sec. IV, the terms logarithmic in z have to disappear. The integral giving $A_\sigma(z)$, Eq. (B4), is well behaved on the positive ω axis, since then for large ω the Fermi function makes it convergent. For very large negative ω values, $\mathrm{Re}\, G_\sigma^+(\omega) \to \langle 1 - n_{d\bar{\sigma}} \rangle / \omega$, and as a result, the contribution from that part of the integration to $A_\sigma(z)$ is $\langle 1 - n_{d\bar{\sigma}} \rangle (\Gamma_\sigma / \pi)(1/z) \ln(\zeta_\sigma / z)$, where $\zeta_\sigma \lesssim D_\sigma$. Hence, the terms logarithmic in z are canceled. In our calculations, we have used

$$A_\sigma(z) \sim -\frac{\Gamma_\sigma}{\pi} \langle 1 - n_{d\bar{\sigma}} \rangle \ln \frac{z}{D_\sigma} + \frac{b_\sigma}{z}, \tag{B6}$$

and have determined the coefficient b_σ self-consistently (see Appendix C). In this way we find

$$R(z) = (\Gamma_\sigma + \Gamma_{\bar{\sigma}})^2 [\langle n_{d\sigma} \rangle + \langle n_{d\bar{\sigma}} \rangle - \langle n_{d\sigma} \rangle \langle n_{d\bar{\sigma}} \rangle]$$
$$+ i(\Gamma_\sigma + \Gamma_{\bar{\sigma}})[(z - \epsilon_0)\langle n_{d\sigma} - n_{d\bar{\sigma}} \rangle + b_\sigma - b_{\bar{\sigma}}]. \tag{B7}$$

APPENDIX C: DETAILS OF THE EXACT SOLUTION

This appendix is devoted to the analysis of the exact solution for the self-consistent EOM, and in particular to the determination of the unknown coefficients b_σ [see Eqs. (B6) and (B7)], a and $\tilde{a}$ [see Eqs. (42)]. This is accomplished by expanding the solution at large frequencies, and equating the coefficients with those of the desired functions Φ and $\tilde{\Phi}$. We give the details for Φ; those of the "tilde" solution are obtained analogously.

As has been the case for the integral (B3), the large negative part of the integral defining $M_\sigma(z)$ has to be taken with care. To this end we write

$$M_\sigma(z) \equiv \int \left(-\frac{d\omega}{2\pi i} \right) \frac{\ln H_\sigma(\omega)}{z - \omega} = \int_{-\infty}^{+\infty} \left(-\frac{d\omega}{2\pi i} \right) \frac{\ln H_\sigma(\omega) - \Theta(-D_{\bar{\sigma}} - \omega)F_\sigma(\omega)(-2\pi i)}{z - \omega} + \int_{-\infty}^{-D_{\bar{\sigma}}} \frac{F_\sigma(\omega)d\omega}{z - \omega}, \tag{C1}$$

where the function $F_\sigma(\omega)$ is defined in such a way that the use of the geometric series $1/(z - \omega) = z^{-1} + z^{-2}\omega + \mathcal{O}(z^{-3})$ in the first integral of Eq. (C1) results in convergent integrals. It is sufficient to include in $F_\sigma(\omega)$ the most slowly decaying terms of $\ln H(\omega)/(-2\pi i)$, which are obtained by expanding $H(\omega)$ for large negative ω,

$$F_\sigma(\omega) = -\frac{\Gamma_{\bar{\sigma}}}{\pi\omega} - \frac{\Gamma_{\bar{\sigma}}}{\pi\omega^2} \left[\frac{\Gamma_{\bar{\sigma}}}{\pi} \ln \frac{D_{\bar{\sigma}}}{|\omega|} + \epsilon_0 - i(\Gamma_\sigma + \Gamma_{\bar{\sigma}})\langle n_{d\sigma} \rangle + i\Gamma_{\bar{\sigma}} \right]. \tag{C2}$$

[In this expansion one has to include terms of the order $\mathcal{O}(\omega^{-2})$ because of the linear term in the prefactor in Eq. (42).] Using Eq. (C2), the second integral in Eq. (C1) is obtained explicitly, and then expanded up to order z^{-2},

$$\int_{-\infty}^{-D_{\bar{\sigma}}} \frac{F_\sigma(\omega)d\omega}{z - \omega} \sim \frac{\Gamma_{\bar{\sigma}}}{\pi z} \ln \frac{z}{D_{\bar{\sigma}}} - \frac{1}{2} \left(\frac{\Gamma_{\bar{\sigma}}}{\pi z} \ln \frac{z}{D_{\bar{\sigma}}} \right)^2 + \frac{\Gamma_{\bar{\sigma}}^2}{\pi^2 D_{\bar{\sigma}} z} - \frac{\Gamma_{\bar{\sigma}}^2}{6z^2} + \frac{D_{\bar{\sigma}}\Gamma_{\bar{\sigma}}}{\pi z^2} - \frac{\Gamma_{\bar{\sigma}}}{\pi} [\epsilon_0 - i(\Gamma_\sigma + \Gamma_{\bar{\sigma}})\langle n_{d\sigma} \rangle + i\Gamma_{\bar{\sigma}}] \left[\frac{1}{zD_{\bar{\sigma}}} - \frac{1}{z^2} \ln \frac{z}{D_{\bar{\sigma}}} \right]. \tag{C3}$$

As a result, the asymptotic expansion of the function $M_\sigma(z)$ becomes

$$M_\sigma(z) \sim [\alpha_\sigma + (\Gamma_{\bar{\sigma}}/\pi)\ln(z/D_{\bar{\sigma}})]/z + \{\beta_\sigma + (\Gamma_{\bar{\sigma}}/\pi)[\epsilon_0 - i(\Gamma_\sigma + \Gamma_{\bar{\sigma}})\langle n_{d\sigma} \rangle + i\Gamma_{\bar{\sigma}}]\ln(z/D_{\bar{\sigma}}) - (\Gamma_{\bar{\sigma}}/\pi)^2(1/2)ln^2(z/D_{\bar{\sigma}})\}/z^2, \tag{C4}$$

where the coefficients α_σ and β_σ are given by

$$\alpha_\sigma = \frac{\Gamma_{\bar{\sigma}}^2}{\pi^2 D_{\bar{\sigma}}} - \frac{\Gamma_{\bar{\sigma}}}{\pi D_{\bar{\sigma}}} [\epsilon_0 - i(\Gamma_\sigma + \Gamma_{\bar{\sigma}})\langle n_{d\sigma} \rangle + i\Gamma_{\bar{\sigma}}]$$
$$+ \int_{-\infty}^{+\infty} [i \ln H_\sigma(\omega)/(2\pi) - \Theta(-D_{\bar{\sigma}} - \omega)F_\sigma(\omega)]d\omega, \tag{C5}$$

$$\beta_\sigma = -\frac{\Gamma_{\bar{\sigma}}^2}{6} + \frac{\Gamma_{\bar{\sigma}}D_{\bar{\sigma}}}{\pi}$$
$$+ \int_{-\infty}^{+\infty} \omega[i \ln H_\sigma(\omega)/(2\pi) - \Theta(-D_{\bar{\sigma}} - \omega)F_\sigma(\omega)]d\omega. \tag{C6}$$

An analogous calculation gives $\tilde{F}_\sigma(\omega) = F_{\bar{\sigma}}(\omega)^*$, leading to

$$\tilde{M}_\sigma(z) \sim [\tilde{\alpha}_\sigma + (\Gamma_\sigma/\pi)\ln(z/D_\sigma)]/z$$
$$+ \{\tilde{\beta}_\sigma + (\Gamma_\sigma/\pi)[\epsilon_0 + i(\Gamma_\sigma + \Gamma_{\bar{\sigma}})\langle n_{d\bar{\sigma}}\rangle - i\Gamma_\sigma]$$
$$\times \ln(z/D_\sigma) - (\Gamma_\sigma/\pi)^2(1/2)\ln^2(z/D_\sigma)\}/z^2, \quad \text{(C7)}$$

$$\tilde{\alpha}_\sigma = \frac{\Gamma_\sigma^2}{\pi^2 D_\sigma} - \frac{\Gamma_\sigma}{\pi D_\sigma}[\epsilon_0 + i(\Gamma_\sigma + \Gamma_{\bar{\sigma}})\langle n_{d\bar{\sigma}}\rangle - i\Gamma_\sigma]$$
$$+ \int_{-\infty}^{+\infty} [i \ln \tilde{H}_\sigma(\omega)/(2\pi) - \Theta(-D_\sigma - \omega)\tilde{F}_\sigma(\omega)]d\omega,$$
$$\text{(C8)}$$

$$\tilde{\beta}_\sigma = -\frac{\Gamma_\sigma^2}{6} + \frac{\Gamma_\sigma D_\sigma}{\pi}$$
$$+ \int_{-\infty}^{+\infty} \omega[i \ln \tilde{H}_\sigma(\omega)/(2\pi) - \Theta(-D_\sigma - \omega)\tilde{F}_\sigma(\omega)]d\omega.$$
$$\text{(C9)}$$

Finally, we use Eqs. (C4) and (C7) in Eq. (42), and then compare term by term with the expansion of Eq. (33). This procedure determines the coefficients a and $\tilde{a}$,

$$a = \alpha_\sigma + \epsilon_0 - i\Gamma_\sigma, \quad \tilde{a} = \tilde{\alpha}_\sigma + \epsilon_0 + i\Gamma_{\bar{\sigma}}, \quad \text{(C10)}$$

and gives the self-consistency equations

$$b_{\bar{\sigma}} + i\Gamma_{\bar{\sigma}}\langle n_{d\bar{\sigma}}\rangle = i(\Gamma_\sigma + \Gamma_{\bar{\sigma}})^{-1}[\beta_\sigma - a\alpha_\sigma + \alpha_\sigma^2/2 + \Gamma_{\bar{\sigma}}h/(2\pi)],$$
$$\text{(C11)}$$

$$b_\sigma - i\Gamma_\sigma\langle n_{d\sigma}\rangle = -i(\Gamma_\sigma + \Gamma_{\bar{\sigma}})^{-1}[\tilde{\beta}_\sigma - \tilde{a}\tilde{\alpha}_\sigma + \tilde{\alpha}_\sigma^2/2 - \Gamma_\sigma h/(2\pi)].$$
$$\text{(C12)}$$

In the case of a full spin symmetry (including $h=0$), one has $\tilde{\alpha}=\alpha^*$, $\tilde{\beta}=\beta^*$, and $\tilde{a}=a^*$, and then Eq. (C11) and Eq. (C12) become complex conjugate.

For a given set of parameters, Eqs. (C11) and (C12) are solved numerically for b_σ and $\langle n_{d\sigma}\rangle$ by an iterative Newton-Raphson algorithm. The initial values are chosen from the solution of the noninteracting ($U=0$) problem.

---

*Electronic address: slava@latnet.lv

[1] L. Kouwenhoven, C. Marcus, P. McEuen, S. Tarucha, R. Westervelt, and N. Wingreen, in *Mesoscopic Electron Transport*, edited by L. L. Sohn, L. P. Kouwenhoven, and G. Schön (Kluwer, Dordrecht, 1997).

[2] P. W. Anderson, Phys. Rev. **124**, 41 (1961).

[3] T. K. Ng and P. A. Lee, Phys. Rev. Lett. **61**, 1768 (1988); L. I. Glazman and M. E. Raĭkh, Pis'ma Zh. Eksp. Teor. Fiz. **47**, 378 (1988) [JETP Lett. **47**, 452 (1988)].

[4] A. C. Hewson, *The Kondo Problem to Heavy Fermions* (Cambridge University Press, Cambridge, England, 1993).

[5] Y. Meir, N. S. Wingreen, and P. A. Lee, Phys. Rev. Lett. **66**, 3048 (1991).

[6] J. E. Hirsch and R. M. Fye, Phys. Rev. Lett. **56**, 2521 (1986); R. N. Silver, J. E. Gubernatis, D. S. Sivia, and M. Jarrell, *ibid.* **65**, 496 (1990).

[7] K. G. Wilson, Rev. Mod. Phys. **47**, 773 (1975); T. A. Costi, A. C. Hewson, and V. Zlatić, J. Phys.: Condens. Matter **6**, 2519 (1994); W. Hofstetter, Phys. Rev. Lett. **85**, 1508 (2000).

[8] D. N. Zubarev, Usp. Fiz. Nauk **71**, 71 (1960) [Sov. Phys. Usp. **3**, 320 (1960)].

[9] A. Theumann, Phys. Rev. **178**, 978 (1969).

[10] (a) J. A. Appelbaum and D. R. Penn, Phys. Rev. **188**, 874 (1969); (b) Phys. Rev. B **3**, 942 (1971).

[11] C. Lacroix, J. Phys. F: Met. Phys. **11**, 2389 (1981).

[12] C. Lacroix, J. Appl. Phys. **53**, 2131 (1982).

[13] H. Mamada and F. Takano, Prog. Theor. Phys. **43**, 1458 (1970).

[14] G. S. Poo, Phys. Rev. B **11**, 4606 (1975); **11**, 4614 (1975).

[15] T. K. Ng, Phys. Rev. Lett. **76**, 487 (1996).

[16] R. Fazio and R. Raimondi, Phys. Rev. Lett. **80**, 2913 (1998); Q. F. Sun, H. Guo, and T. H. Lin, *ibid.* **87**, 176601 (2001).

[17] P. Zhang, Q.-K. Xue, Y. P. Wang, and X. C. Xie, Phys. Rev. Lett. **89**, 286803 (2002); N. Sergueev, Q. F. Sun, H. Guo, B. G. Wang, and J. Wang, Phys. Rev. B **65**, 165303 (2002).

[18] O. Entin-Wohlman, A. Aharony, and Y. Meir, Phys. Rev. B **71**, 035333 (2005).

[19] B. R. Bułka and P. Stefanski, Phys. Rev. Lett. **86**, 5128 (2001).

[20] H.-G. Luo, S.-J. Wang, and C.-L. Jia, Phys. Rev. B **66**, 235311 (2002).

[21] B. R. Bułka and S. Lipiński, Phys. Rev. B **67**, 024404 (2003).

[22] E. C. Goldberg, F. Flores, and R. C. Monreal, Phys. Rev. B **71**, 035112 (2005).

[23] R. C. Monreal and F. Flores, Phys. Rev. B **72**, 195105 (2005).

[24] N. Sivan and N. S. Wingreen, Phys. Rev. B **54**, 11622 (1996).

[25] J. König and Y. Gefen, Phys. Rev. B **71**, 201308(R) (2005).

[26] See footnote 8 in Ref. 9.

[27] H.-G. Luo, J.-J. Ying, and S.-J. Wang, Phys. Rev. B **59**, 9710 (1999).

[28] Keeping the EOM of these Green functions and decoupling the resulting higher-order EOM has been proposed in Ref. 27 as a possible way to improve the present approximation. We have tried to investigate this proposal but could not reproduce the results of that paper. Instead, we have found that the scheme becomes untractable.

[29] L. Dworin, Phys. Rev. **164**, 818 (1967); **164**, 841 (1967).

[30] A. Oguchi, Prog. Theor. Phys. **43**, 257 (1970).

[31] D. C. Langreth, Phys. Rev. **150**, 516 (1966).

[32] In fact, in order to obtain the result (31) it suffices to make the assumption (27) only over an energy scale which is much smaller than the bandwidth, say $[-D_\sigma^{\text{low}}; D_\sigma^{\text{up}}]$. Possible energy dependencies of the self-energy on larger scales can then be incorporated into D_σ, by normalizing the lower cutoff on the band, $D_\sigma \equiv D_\sigma^{\text{low}} \exp \int_{-D^{\text{low}}}^{0}[1 - \text{Im}\,\Sigma_\sigma^-(\omega)/\Gamma_\sigma]/\omega\,d\omega$. This may be necessary when the dot is embedded in a complex mesoscopic network.

[33] P. E. Bloomfield and D. R. Hamann, Phys. Rev. **164**, 856 (1967).

[34] N. I. Muskhelishvili, *Singular Integral Equations*, 2nd ed. (Do-

ver, New York, 1992).

[35] In such a case the so-called index of the Riemann-Hilbert problem (Ref. 34) is zero. If the integration limits in Eq. (42) are to be kept finite, one has to assume $D \equiv D_\sigma$ and possibly consider additional multiplicative powers of $(z \pm D)$, see Ref. 33. We ignore these options since they only affect the corrections of order ω / D_σ.

[36] P. B. Wiegmann and A. M. Tsvelick, J. Phys. C **16**, 2281 (1983); E. Ogievetski, A. M. Tsvelick, and P. B. Wiegmann, *ibid.* **16**, L797 (1983).

[37] F. D. M. Haldane, Phys. Rev. Lett. **40**, 416 (1978); **40**, 911 (1978).

[38] Certain examples of the Friedel sum-rule violation by self-consistent EOM schemes have been discussed recently in Refs. 22 and 23.

[39] S. Kirchner, J. Kroha, and P. Wölfle, Phys. Rev. B **70**, 165102 (2004).

[40] P. Simon, O. Entin-Wohlman, and A. Aharony, Phys. Rev. B **72**, 245313 (2005).

Chapter 6

Unified description of correlations in double quantum dots

The content of this chapter has been previously available as

- a preprint, `arXiv.org:cond-mat/0610194` (9 October 2006).

Unified description of correlations in double quantum dots

Vyacheslavs Kashcheyevs,[1, *] Avraham Schiller,[2] Amnon Aharony,[3] and Ora Entin-Wohlman[3, 4]

[1]*School of Physics and Astronomy, Raymond and Beverly Sackler Faculty of Exact Sciences,*
Tel Aviv University, Tel Aviv 69978, Israel
[2]*Racah Institute of Physics, The Hebrew University, Jerusalem 91904, Israel*
[3]*Department of Physics, Ben Gurion University, Beer Sheva 84105, Israel*
[4]*Albert Einstein Minerva Center for Theoretical Physics,*
Weizmann Institute of Science, Rehovot 76100, Israel

The two-level model for a double quantum dot coupled to two leads, which is ubiquitously used to describe charge oscillations, transmission-phase lapses and correlation-induced resonances, is considered in its general form. The model features arbitrary tunnelling matrix elements among the two levels and the leads and between the levels themselves (including the effect of Aharonov-Bohm fluxes), as well as inter-level repulsive interactions. We show that this model is exactly mapped onto a generalized Anderson model of a single impurity, where the electrons acquire a pseudo-spin degree of freedom, which is conserved by the tunnelling but not within the dot. Focusing on the local-moment regime where the dot is singly occupied, we show that the effective low-energy Hamiltonian is that of the anisotropic Kondo model in the presence of a tilted magnetic field. For moderate values of the (renormalized) field, the Bethe *ansatz* solution of the isotropic Kondo model allows us to derive accurate expressions for the dot occupation numbers, and henceforth its zero-temperature transmission. Our results are in excellent agreement with those obtained from the Bethe *ansatz* for the isotropic Anderson model, and with the functional and numerical renormalization-group calculations of Meden and Marquardt [Phys. Rev. Lett. **96**, 146801 (2006)], which are valid for the general anisotropic case. In addition we present highly accurate estimates for the validity of the Schrieffer-Wolff transformation (which maps the Anderson Hamiltonian onto the low-energy Kondo model) at both the high- and low-magnetic field limits. Perhaps most importantly, we provide a single coherent picture for the host of phenomena to which this model has been applied.

I. INTRODUCTION

The ongoing technological progress in the fabrication and control of nanoscale electronic circuits, such as quantum dots, has stimulated detailed studies of various quantum-impurity models, where a few local degrees of freedom are coupled to a continuum. Of particular interest are models with experimentally verifiable universal properties. One of the best studied examples is the Anderson single impurity model,[1] which describes successfully electronic correlations in small quantum dots.[2,3] The experimental control of most of the parameters of this model, e.g., the impurity energy level position or the level broadening due to hybridization with the continuum, allows for detailed investigations[4,5] of the universal low-temperature behavior of the Anderson model.

In this paper we study the low-energy behavior of a generic model, depicted in Fig. 1a, which pertains either to a single two-level quantum dot or to a double quantum dot where each dot harbors only a single level. The spin degeneracy of the electrons is assumed to be lifted by an external magnetic field. Several variants of this model have been studied intensely in recent years, in conjunction with a plethora of phenomena, such as many-body resonances in the spectral density,[6] phase lapses in the transmission phase,[7,8] charge oscillations,[9,10] and correlation-induced resonances in the conductance.[11,12] Albeit being described by the same model, no clear link-

age has been established between these seemingly different effects. The reason is in part due to the large number of model parameters involved, which so far obscured a clear physical picture. While some exact statements can be made, these are restricted to certain solvable limits,[6] and are apparently nongeneric.[11] Here we construct a framework which encompasses all parameter regimes of the model, and enables a unified description of the various phenomena alluded to above, exposing their common physical origin. For the most interesting regime of strong fluctuations between the two levels, we are able to give: (i) explicit analytical conditions for the occurrence of transmission phase lapses; (ii) an explanation of the population inversion and the charge oscillations[9,10,13] (including a Kondo enhancement of the latter); (iii) a complete account of the correlation-induced resonances[11] as a disguised Kondo phenomenon.

After introducing the details of the double-dot Hamiltonian in Sec. II A, we begin our analysis by constructing a linear transformation of the dot operators, *and* a simultaneous (generally different) linear transformation of the lead operators, such that the 2×2 tunnelling matrix between the two levels on the dot and the leads becomes diagonal (with generally different eigenvalues). As a result, the electrons acquire a pseudo-spin degree of freedom which is conserved upon tunnelling between the dot and the continuum, as shown schematically in Fig. 1b. Concomitantly, the transformation generates a local Zee-
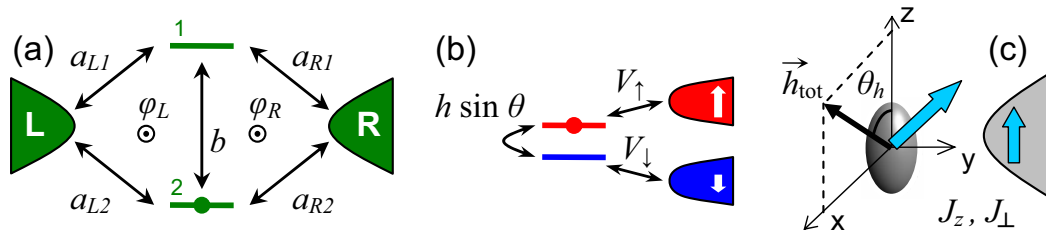
2

FIG. 1: A schematic representation of the double-dot system, along with its reduction in the local-moment regime to an effective Kondo model with a tilted magnetic field. (a) The model system: two localized levels coupled by tunnelling matrix elements to one another and to two separate leads. A constant magnetic flux induces phase factors on those elements. Spinless electrons residing on the two levels experience a repulsive interaction. (b) The mapping onto a spinful generalized Anderson model, with a tilted magnetic field and different tunnelling elements for spin-up and spin-down electrons. (c) The low-energy behavior of the generalized Anderson model is mapped onto an anisotropic Kondo model with a tilted magnetic field, $\vec{h}_{\rm tot}$.

man magnetic field. In this way the original double-dot model system is transformed into a generalized Anderson impurity model in the presence of a (generally tilted) external magnetic field. This first stage is detailed in Sec. II B and Appendix A.

We next analyze in Sec. III the low-energy properties of our generalized Anderson model. We confine ourselves to the local moment regime, in which there is a single electron on the impurity. The fluctuations of the pseudo-spin degree of freedom (which translate into charge fluctuations between the two localized levels in the original model) are determined by two competing effects: the polarizing effect of the local magnetic field, and the Kondo screening by the itinerant electrons. In order to quantitatively analyze this competition, we derive an effective low-energy Kondo Hamiltonian, using Haldane's scaling procedure,[14] together with the Schrieffer-Wolff[15] transformation and Anderson's poor man's scaling.[16] This portion of the derivation resembles recent studies of the Kondo effect in the presence of ferromagnetic leads,[17] although the physical context and implications are quite different.

As is mentioned above, the tunnelling between the impurity and the continuum in the generalized Anderson model is (pseudo) spin dependent. This asymmetry results in two important effects: (a) different renormalizations of the two local levels, which in turn generates an additional local magnetic field.[17] This field is not necessarily aligned with the original Zeeman field that is present in the generalized Anderson model. (b) An anisotropy of the exchange coupling between the conduction electrons and the local moment in the Kondo Hamiltonian. However, since the scaling equations for the anisotropic Kondo model[16,18] imply a flow towards the *isotropic* strong coupling fixed point, the low-energy behavior of the generalized Anderson model can be still described in terms of two competing energy scales, the Kondo temperature, T_K, and the renormalized magnetic field, $h_{\rm tot}$. Our two-stage mapping, double-dot $\Rightarrow$ generalized Anderson model $\Rightarrow$ anisotropic Kondo model (see Fig. 1), allows us to obtain analytic expressions for the original model properties in terms of those of the Kondo

model. We derive in Sec. IV the occupation numbers on the two localized levels by employing the Bethe *ansatz* solution of the magnetization of a Kondo spin in a finite magnetic field.[19,20] This solution also results in a highly accurate expression for the conductance based upon the Friedel-Langreth sum rule.[21] Perhaps most importantly, it provides a single coherent picture for the host of phenomena to which our model has been applied.

Examples of explicit results stemming from our general analysis are presented in Sec. V. First, we consider the case in which the tunnelling is isotropic, being the same for spin-up and spin-down electrons. Then the model is exactly solvable by direct application of the Bethe *ansatz* to the Anderson Hamiltonian.[20,22] We solve the resulting equations[22,23] numerically and obtain the occupation numbers for arbitrary parameter values of the model, and in particular, for arbitrary values of the local Zeeman field. By comparing with the occupation numbers obtained in Sec. IV from the Kondo version of the model, we are able to test the accuracy of the Schrieffer-Wolff mapping onto the Kondo Hamiltonian. We find that this mapping yields extremely precise results over the entire local-moment regime. This exactly solvable example has another virtue. It clearly demonstrates the competition between the Kondo screening of the local spin, which is governed by T_K, and the polarizing effect of the local field $h_{\rm tot}$. This competition is reflected in the charging process of the quantum dot described by the original Hamiltonian. We next proceed to apply our general method to the features for which the anisotropy in the tunnelling is relevant, notably the transmission phase lapses and the correlation-induced resonances.[11] In particular, we derive analytical expressions for the occupation numbers and the conductance employing the mapping onto the Kondo Hamiltonian. These analytical expressions give results which are in a very good agreement with the data presented by Meden and Marquardt,[11] which was obtained by the functional and numerical renormalization-group methods applied to the original model.

As our treatment makes extensive usage of the exact Bethe *ansatz* solutions for the impurity magnetization in the isotropic Kondo and Anderson models with a finite

magnetic field, all relevant details of the solutions are concisely gathered for convenience in Appendix B.

II. THE DOUBLE-DOT SYSTEM AS A GENERALIZED ANDERSON MODEL

A. The model

We consider spinless electrons in a system of two distinct energy levels (a 'quantum dot'), labelled $i = 1, 2$, which are connected by tunnelling to two leads, labelled $\alpha = L, R$. This quantum dot is penetrated by a (constant) magnetic flux. The total Hamiltonian of the system reads

$$\mathcal{H} = \mathcal{H}_l + \mathcal{H}_d + \mathcal{H}_{ld}, \tag{1}$$

in which $\mathcal{H}_l$ is the Hamiltonian of the leads, $\mathcal{H}_d$ is the Hamiltonian of the isolated dot, and $\mathcal{H}_{ld}$ describes the coupling between the dot and the leads. The system is portrayed schematically in Fig. 1a.

Each of the leads is modelled by a continuum of noninteracting energy levels lying within a band of width $2D$, with a constant density of states ρ.[24] The corresponding Hamiltonian is given by

$$\mathcal{H}_l = \sum_{k\alpha} \varepsilon_k c^\dagger_{k\alpha} c_{k\alpha}, \tag{2}$$

where $c^\dagger_{k\alpha}$ $(c_{k\alpha})$ creates (annihilates) an electron of wave vector k on lead α. The two leads are connected to two external reservoirs, held at the same temperature T and having different chemical potentials, μ_L and μ_R, respectively. We take the limit $\mu_L \to \mu_R = 0$ in considering equilibrium properties and the linear conductance.

The isolated dot is described by the Hamiltonian

$$\mathcal{H}_d = \begin{bmatrix} d^\dagger_1 & d^\dagger_2 \end{bmatrix} \cdot \hat{\mathcal{E}}_d \cdot \begin{bmatrix} d_1 \\ d_2 \end{bmatrix} + U\, n_1 n_2, \tag{3}$$

where

$$\hat{\mathcal{E}}_d = \frac{1}{2} \begin{bmatrix} 2\,\epsilon_0 + \Delta & b\, e^{i(\varphi_L - \varphi_R)/2} \\ b\, e^{-i(\varphi_L - \varphi_R)/2} & 2\,\epsilon_0 - \Delta \end{bmatrix}. \tag{4}$$

Here, $d^\dagger_i$ (d_i) creates (annihilates) an electron on the ith level, $n_i \equiv d^\dagger_i d_i$ are the occupation-number operators (representing the local charge), $U > 0$ denotes the

Coulomb repulsion between electrons that occupy the two levels, $\epsilon_0 \pm \Delta/2$ are the (single-particle) energies on the levels, and $b/2$ is the amplitude for tunnelling between them. The phases φ_L and φ_R, respectively, represent the Aharonov-Bohm fluxes (measured in units of the flux quantum $2\pi\hbar c/e$) in the left and in the right hopping loops, such that the total flux in the two loops is $\varphi \equiv \varphi_L + \varphi_R$ [see Fig. 1a].

Gauge invariance grants us the freedom to distribute the Aharonov-Bohm phases among the inter-dot coupling b and the couplings between the dot levels and the leads. With the convention of Eq. (4), the coupling between the quantum dot and the leads is described by the Hamiltonian

$$\mathcal{H}_{ld} = \sum_k \begin{bmatrix} c^\dagger_{kL} & c^\dagger_{kR} \end{bmatrix} \cdot \hat{A} \cdot \begin{bmatrix} d_1 \\ d_2 \end{bmatrix} + \text{H.c.}, \tag{5}$$

where

$$\hat{A} = \begin{bmatrix} a_{L1} e^{i\varphi/2} & a_{L2} \\ a_{R1} & a_{R2} e^{i\varphi/2} \end{bmatrix}, \quad \varphi = \varphi_L + \varphi_R. \tag{6}$$

Here the real (possibly negative) coefficients $a_{\alpha i}$ are the tunnelling amplitudes for transferring an electron from the level i to lead α. Note that the Hamiltonian depends solely on the total Aharonov-Bohm flux φ when the interdot coupling b vanishes. Also, the tunnelling matrix $\hat{A}$ is assumed to be independent of the wave vector k. This assumption considerably simplifies the analysis while keeping the main physical picture intact.

B. Mapping onto a generalized Anderson model

The analysis of the model defined in Sec. II A employs an *exact* mapping of the Hamiltonian of Eq. (1) onto a generalized Anderson Hamiltonian, which pertains to a single-level quantum dot, coupled to a spin-degenerate band of conduction electrons. We show in Appendix A that the model depicted in Fig. 1a is fully described by the Hamiltonian

$$\mathcal{H} = \sum_{k,\sigma} \varepsilon_k c^\dagger_{k\sigma} c_{k\sigma} + \sum_\sigma \left(\epsilon_0 - \sigma \frac{h}{2}\cos\theta\right) n_\sigma - \left(d^\dagger_\uparrow d_\downarrow + d^\dagger_\downarrow d_\uparrow\right)\frac{h}{2}\sin\theta + U n_\uparrow n_\downarrow + \sum_{k,\sigma} V_\sigma\left(c^\dagger_{k\sigma} d_\sigma + \text{H.c.}\right), \tag{7}$$

schematically sketched Fig. 1b, which generalizes the original Anderson model[1] in two aspects. Firstly, it allows for spin-dependent coupling between the dot and

the conduction band. A similar variant of the Anderson model has recently attracted much theoretical and experimental attention in connection with the Kondo effect for ferromagnetic leads.[17,25–28] Secondly, it allows for a Zeeman field whose direction is inclined with respect to the "anisotropy" axis z. For spin-independent tunnelling, one can easily realign the field along the z axis by a simple rotation of the different operators about the y axis. This is no longer the case once $V_\uparrow \neq V_\downarrow$, which precludes the use of some of the exact results available for the Anderson model. As we show below, the main effect of spin-dependent tunnelling is to modify the effective field seen by electrons on the dot, by renormalizing its z-component.

The derivation of Eq. (7) is accomplished by a transformation known as the singular-value decomposition,[29] which allows one to express the tunnelling matrix $\hat{A}$ in the form

$$\hat{A} = R_l^\dagger \cdot \begin{bmatrix} V_\uparrow & 0 \\ 0 & V_\downarrow \end{bmatrix} \cdot R_d \, . \qquad (8)$$

Here R_l and R_d are unitary 2×2 matrices, which are used to independently rotate the lead and the dot operators according to

$$\begin{bmatrix} d_\uparrow \\ d_\downarrow \end{bmatrix} \equiv R_d \cdot \begin{bmatrix} d_1 \\ d_2 \end{bmatrix}, \quad \begin{bmatrix} c_{k\uparrow} \\ c_{k\downarrow} \end{bmatrix} \equiv R_l \cdot \begin{bmatrix} c_{kL} \\ c_{kR} \end{bmatrix} . \qquad (9)$$

To make contact with the conventional Anderson impurity model, we have labelled the linear combinations of the original operators [defined through Eqs. (9)] by the "spin" index $\sigma = \uparrow$ (+1) and $\sigma = \downarrow$ (−1).

The transformation (9) generalizes the one in which the *same* rotation R is applied to both the dot and the lead operators. It is needed in the present, more general, case since the matrix $\hat{A}$ generically lacks an orthogonal basis of eigenvectors. The matrices R_d and R_l can always be chosen uniquely (up to a common overall phase) such that[30] (a) the tunnelling between the dot and the continuum is diagonal in the spin basis (so that the tunnelling conserves the spin); (b) the amplitudes $V_\uparrow \geq V_\downarrow \geq 0$ are real; and (c) the part of the Hamiltonian of Eq. (7) pertaining to the dot has only real matrix elements with $h \sin \theta \geq 0$. The explicit expressions for the rotation matrices R_d and R_l as well as for the model parameters appearing in Eq. (7) in terms of those of the original Hamiltonian are given in Appendix A.

It should be emphasized that partial transformations involving only one rotation matrix, either R_d or R_l, have previously been applied in this context (see, e.g., Refs. 6 and 31). However, excluding special limits, both R_d and R_l are required to expose the formal connection to the Anderson model. A first step in this direction was recently taken by Golosov and Gefen,[8] yet only on a restricted manifold for the tunnelling amplitudes $a_{\alpha i}$. In the following section we discuss in detail the low-energy physics of the Hamiltonian of Eq. (7), focusing on the local-moment regime. Explicit results for the conduc-

tance and the occupations of the levels are then presented in Secs. IV and V.

III.   THE LOCAL-MOMENT REGIME

There are two limits where the model of Eq. (1) has an exact solution:[6] (i) when the spin-down state is decoupled in Eq. (7), i.e., when $V_\downarrow = h \sin \theta = 0$; (ii) when the coupling is isotropic, i.e., $V_\uparrow = V_\downarrow$. In the former case, $n_\downarrow$ is conserved. The Hilbert space separates then into two disconnected sectors with $n_\downarrow = 0$ and $n_\downarrow = 1$. Within each sector, the Hamiltonian can be diagonalized independently as a single-particle problem. In the latter case, one can always align the magnetic field h along the z axis by a simple rotation of the different operators about the y axis. The model of Eq. (7) reduces then to a conventional Anderson model in a magnetic field, for which an exact Bethe *ansatz* solution is available.[20] (This special case will be analyzed in great detail in Sec. V A.)

In terms of the model parameters appearing in the original Hamiltonian, the condition $V_\downarrow = 0$ corresponds to

$$|a_{L1} a_{R2}| = |a_{R1} a_{L2}|, \quad \text{and} \quad \varphi = \beta \bmod 2\pi, \qquad (10)$$

whereas $V_\uparrow = V_\downarrow = V$ corresponds to

$$|a_{L1}| = |a_{R2}|, \ |a_{L2}| = |a_{R1}|, \ \text{and} \ \varphi = (\pi + \beta) \bmod 2\pi. \qquad (11)$$

Here

$$\beta = \begin{cases} 0 & \text{if} \ \ a_{L1} a_{L2} a_{R1} a_{R2} > 0 \\ \pi & \text{if} \ \ a_{L1} a_{L2} a_{R1} a_{R2} < 0 \end{cases} \qquad (12)$$

records the combined signs of the four coefficients $a_{\alpha i}$.[32]

Excluding the two cases mentioned above, no exact solutions to the Hamiltonian of Eq. (1) are known. Nevertheless, we shall argue below that the model displays generic low-energy physics in the "local-moment" regime, corresponding to the Kondo effect in a finite magnetic field. To this end we focus hereafter on $\Gamma_\uparrow, \Gamma_\downarrow, h \ll -\epsilon_0, U + \epsilon_0$, and derive an effective low-energy Hamiltonian for general couplings. Here $\Gamma_\sigma = \pi \rho V_\sigma^2$ is half the tunnelling rate between the spin state σ and the leads.

A.   Effective low-energy Hamiltonian

As is mentioned above, when $V_\uparrow = V_\downarrow$ one is left with a conventional Kondo effect in the presence of a finite magnetic field. Asymmetry in the couplings, $V_\uparrow \neq V_\downarrow$, changes this situation in three aspects. Firstly, the effective magnetic field seen by electrons on the dot is modified, acquiring a renormalized z-component. Secondly, the elimination of the charge fluctuations by means of a Schrieffer-Wolff transformation,[15] results in an anisotropic spin-exchange interaction. Thirdly, a new interaction term is produced, coupling the spin and the

charge. Similar aspects have been previously discussed in the context of the Kondo effect in the presence of ferromagnetic leads,[17] where the source of the asymmetry is the inequivalent density of states for conduction electrons with opposite spin.[28] Below we elaborate on the emergence of these features in the present case.

Before turning to a detailed derivation of the effective low-energy Hamiltonian, we briefly comment on the physical origin of the modified magnetic field. As is well known, the coupling to the continuum renormalizes the bare energy levels of the dot. For $\Gamma_\uparrow, \Gamma_\downarrow, h \ll -\epsilon_0, U + \epsilon_0$, these renormalizations can be accurately estimated using second-order perturbation theory in V_σ. For $V_\uparrow \neq V_\downarrow$, each of the bare levels $\epsilon_\sigma = \epsilon_0 - \frac{1}{2}\sigma h \cos\theta$ is shifted by a different amount, which acts in effect as an excess magnetic field. Explicitly, for $T = 0$ and $D \gg |\epsilon_0|, U$ one obtains[13,17]

$$\Delta h_z = \frac{\Gamma_\uparrow - \Gamma_\downarrow}{\pi} \ln \frac{\epsilon_0 + U}{|\epsilon_0|} . \qquad (13)$$

As ϵ_0 is swept across $-U/2$, $\Delta h_z \propto \Gamma_\uparrow - \Gamma_\downarrow$ changes sign. Had $|\Gamma_\uparrow - \Gamma_\downarrow|$ exceeded h this would have dictated a sign-reversal of the z-component of the combined field as ϵ_0 is tuned across the Coulomb-blockade valley. As originally noted by Silvestrov and Imry,[13] this simple but insightful observation underlies the population inversion discussed in Refs.9,10 and13 for a singly occupied dot. We shall return to this important point in greater detail later on.

A systematic derivation of the effective low-energy Hamiltonian for $\Gamma_\uparrow, \Gamma_\downarrow, h \ll -\epsilon_0, U + \epsilon_0$ involves the combination of Anderson's poor-man's scaling[16] and the Schrieffer-Wolff transformation.[15] For $|\epsilon_0| \sim U + \epsilon_0$, the elimination of high-energy excitations proceeds in three steps. First Haldane's perturbative scaling approach[14] is applied to progressively reduce the bandwidth from its bare value D down to $D_{SW} \sim |\epsilon_0| \sim U + \epsilon_0$. Next a Schrieffer-Wolff transformation is carried out to eliminate charge fluctuations on the dot. At the conclusion of this second step one is left with a generalized Kondo Hamiltonian [Eq. (16) below], featuring an anisotropic spin-exchange interaction and an additional interaction term that couples spin and charge. The Kondo Hamiltonian also includes a finite magnetic field whose direction is inclined with respect to the anisotropy axis z. In the third and final stage, the Kondo Hamiltonian is treated using Anderson's poor-man's scaling[16] to expose its low-energy physics.

The above procedure is further complicated in the case where $|\epsilon_0|$ and $U + \epsilon_0$ are well separated in energy. This situation requires two distinct Schrieffer-Wolff transformations: one at $D_{SW}^{up} \sim \max\{|\epsilon_0|, U + \epsilon_0\}$ and the other at $D_{SW}^{down} \sim \min\{|\epsilon_0|, U + \epsilon_0\}$. Reduction of the bandwidth from D_{SW}^{up} to D_{SW}^{down} is accomplished using yet another (third) segment of the perturbative scaling. It turns out that all possible orderings of $|\epsilon_0|$ and $U + \epsilon_0$ produce the same Kondo Hamiltonian, provided that $\Gamma_\uparrow$, $\Gamma_\downarrow$ and h are sufficiently small. To keep the discussion as concise as possible, we therefore restrict the presentation

to the case $|\epsilon_0| \sim U + \epsilon_0$.

Consider first the energy window between D and D_{SW}, which is treated using Haldane's perturbative scaling.[14] Suppose that the bandwidth has already been lowered from its initial value D to some value $D' = De^{-l}$ with $0 < l < \ln(D/D_{SW})$. Further reducing the bandwidth to $D'(1 - \delta l)$ produces a renormalization of each of the energies $\epsilon_\uparrow$, $\epsilon_\downarrow$, and U. Specifically, the z-component of the magnetic field, $h_z \equiv \epsilon_\downarrow - \epsilon_\uparrow$, is found to obey the scaling equation

$$\frac{dh_z}{dl} = \frac{\Gamma_\uparrow - \Gamma_\downarrow}{\pi} \left[\frac{1}{1 - e^l \epsilon_0/D} - \frac{1}{1 + e^l(U + \epsilon_0)/D} \right]. \qquad (14)$$

Here we have retained ϵ_0 and $U + \epsilon_0$ in the denominators, omitting corrections which are higher-order in $\Gamma_\uparrow$, $\Gamma_\downarrow$, and h (these include also the small renormalizations of ϵ_σ and U that are accumulated in the course of the scaling). The x-component of the field, $h_x = h \sin\theta$, remains unchanged throughout the procedure. Upon reaching $D' = D_{SW}$, the renormalized field h_z becomes

$$h_z^* = h \cos\theta + \frac{\Gamma_\uparrow - \Gamma_\downarrow}{\pi} \ln \frac{D_{SW} + U + \epsilon_0}{D_{SW} - \epsilon_0} , \qquad (15)$$

where we have assumed $D \gg |\epsilon_0|, U$.

Once the scale D_{SW} is reached, charge fluctuations on the dot are eliminated via a Schrieffer-Wolff transformation,[15] which generates among other terms also further renormalizations of ϵ_σ. Neglecting h in the course of the transformation, one arrives at the following Kondo-type Hamiltonian,

$$\begin{aligned}
\mathcal{H}_K &= \sum_{k,\sigma} \varepsilon_k c_{k\sigma}^\dagger c_{k\sigma} + J_\perp (S_x s_x + S_y s_y) + J_z S_z s_z \\
&+ v_{sc} S^z \sum_{k,k',\sigma} :c_{k\sigma}^\dagger c_{k'\sigma}: + \sum_{k,k',\sigma} (v_+ + \sigma v_-):c_{k\sigma}^\dagger c_{k'\sigma}: \\
&- \tilde{h}_z S_z - \tilde{h}_x S_x.
\end{aligned} \qquad (16)$$

Here we have represented the local moment on the dot by the spin-$\frac{1}{2}$ operator

$$\vec{S} = \frac{1}{2} \sum_{\sigma,\sigma'} \vec{\tau}_{\sigma\sigma'} d_\sigma^\dagger d_{\sigma'} \qquad (17)$$

($\vec{\tau}$ being the Pauli matrices), while

$$\vec{s} = \frac{1}{2} \sum_{k,k'} \sum_{\sigma,\sigma'} \vec{\tau}_{\sigma\sigma'} c_{k\sigma}^\dagger c_{k'\sigma'} \qquad (18)$$

are the local conduction-electron spin densities. The symbol $:c_{k\sigma}^\dagger c_{k'\sigma}: = c_{k\sigma}^\dagger c_{k'\sigma} - \delta_{k,k'}\theta(-\epsilon_k)$ stands for normal ordering with respect to the filled Fermi sea. The various couplings that appear in Eq. (16) are given by the explicit expressions

$$\rho J_\perp = \frac{2\sqrt{\Gamma_\uparrow \Gamma_\downarrow}}{\pi} \left(\frac{1}{|\epsilon_0|} + \frac{1}{U + \epsilon_0} \right), \qquad (19)$$

$$\rho J_z = \frac{\Gamma_\uparrow + \Gamma_\downarrow}{\pi} \left(\frac{1}{|\epsilon_0|} + \frac{1}{U + \epsilon_0} \right), \qquad (20)$$

$$\rho v_{\rm sc} = \frac{\Gamma_\uparrow - \Gamma_\downarrow}{4\pi} \left(\frac{1}{|\epsilon_0|} + \frac{1}{U + \epsilon_0} \right), \qquad (21)$$

$$\rho v_\pm = \frac{\Gamma_\uparrow \pm \Gamma_\downarrow}{4\pi} \left(\frac{1}{|\epsilon_0|} - \frac{1}{U + \epsilon_0} \right), \qquad (22)$$

$$\tilde{h}_z = h\cos\theta + \frac{\Gamma_\uparrow - \Gamma_\downarrow}{\pi} \ln \frac{U + \epsilon_0}{|\epsilon_0|}, \qquad (23)$$

and

$$\tilde{h}_x = h\sin\theta. \qquad (24)$$

Equations (19)–(24) are correct to leading order in $\Gamma_\uparrow$, $\Gamma_\downarrow$, and h, in accordance with the inequality $\Gamma_\uparrow, \Gamma_\downarrow, h \ll |\epsilon_0|, U + \epsilon_0$. In fact, additional terms are generated in Eq. (16) when h is kept in the course of the Schrieffer-Wolff transformation. However, the neglected terms are smaller than the ones retained by a factor of $h/\min\{|\epsilon_0|, U + \epsilon_0\} \ll 1$, and are not expected to alter the low-energy physics in any significant way. We also note that $\tilde{h}_z$ accurately reproduces the second-order correction to h_z detailed in Eq. (13). As emphasized above, the same effective Hamiltonian is obtained when $|\epsilon_0|$ and $U + \epsilon_0$ are well separated in energy, although the derivation is notably more cumbersome. In unifying the different possible orderings of $|\epsilon_0|$ and $U + \epsilon_0$, the effective bandwidth in Eq. (16) must be taken to be $D_0 \sim \min\{|\epsilon_0|, U + \epsilon_0\}$.

B. Reduction to the Kondo effect in a finite magnetic field

In addition to spin-exchange anisotropy and a tilted magnetic field, the Hamiltonian of Eq. (16) contains a new interaction term, $v_{\rm sc}$, which couples spin and charge. It also includes spin-dependent potential scattering, represented by the term v_- above. As is well known, spin-exchange anisotropy is irrelevant for the conventional spin-$\frac{1}{2}$ single-channel Kondo problem. As long as one lies within the confines of the antiferromagnetic domain, the system flows to the same strong-coupling fixed point no matter how large the exchange anisotropy is. SU(2) spin symmetry is thus restored at low energies. A finite magnetic field h cuts off the flow to isotropic couplings, as does the temperature T. However, the residual anisotropy is negligibly small if h, T and the bare couplings are small. That is, low-temperature thermodynamic and dynamic quantities follow a single generic dependence on T/T_K and h/T_k, where T_K is the Kondo temperature. All relevant information on the bare spin-exchange anisotropy is contained for weak couplings in the microscopic form of T_K.

The above picture is insensitive to the presence of weak potential scattering, which only slightly modifies the conduction-electron phase shift at the Fermi energy. As we show below, neither is it sensitive to the presence of the weak couplings $v_{\rm sc}$ and v_- in Eq. (16). This observation is central to our discussion, as it enables a very accurate and complete description of the low-energy physics of $\mathcal{H}_K$ in terms of the conventional Kondo model in a finite magnetic field. Given the Kondo temperature T_K and the direction and magnitude of the renormalized field pertaining to Eq. (16), physical observables can be extracted from the exact Bethe *ansatz* solution of the conventional Kondo model. In this manner, one can accurately compute the conductance and the occupation of the levels, as demonstrated in Secs. IV and V.

To establish this important point, we apply poorman's scaling[16] to the Hamiltonian of Eq. (16). Of the different couplings that appear in $\mathcal{H}_K$, only J_z, $J_\perp$, and $\tilde{h}_z$ are renormalized at second order. Converting to the dimensionless exchange couplings $\tilde{J}_z = \rho J_z$ and $\tilde{J}_\perp = \rho J_\perp$, these are found to obey the standard scaling equations[16,18]

$$\frac{d\tilde{J}_z}{dl} = \tilde{J}_\perp^2, \qquad (25)$$

$$\frac{d\tilde{J}_\perp}{dl} = \tilde{J}_z \tilde{J}_\perp, \qquad (26)$$

independent of $v_{\rm sc}$ and $v_\pm$. Indeed, the couplings $v_{\rm sc}$ and $v_\pm$ do not affect the scaling trajectories in any way, other than through a small renormalization to $\tilde{h}_z$:

$$\frac{d\tilde{h}_z}{dl} = D_0\, e^{-l} \left(\tilde{J}_z \tilde{v}_- + 2\tilde{v}_{\rm sc} \tilde{v}_+ \right) 8\ln 2. \qquad (27)$$

Here $\tilde{v}_\mu$ are the dimensionless couplings ρv_μ ($\mu = {\rm sc}, \pm$), and l equals $\ln(D_0/D')$ with D' the running bandwidth.

As stated above, the scaling equations (25)–(26) are identical to those obtained for the conventional anisotropic Kondo model. Hence, the Kondo couplings flow toward strong coupling along the same scaling trajectories and with the same Kondo temperature as in the absence of $v_{\rm sc}$ and $v_\pm$. Straightforward integration of Eqs. (25)–(26) yields

$$T_K = D_0 \exp\left(-\frac{1}{\rho\,\xi} \tanh^{-1} \frac{\xi}{J_z} \right) \qquad (28)$$

with $\xi = \sqrt{J_z^2 - J_\perp^2}$. Here we have exploited the hierarchy $J_z \geq J_\perp > 0$ in deriving Eq. (28). In terms of the original model parameters appearing in Eq. (7), Eq. (28) takes the form

$$T_K = D_0 \exp\left[\frac{\pi\epsilon_0(U + \epsilon_0)}{2U(\Gamma_\uparrow - \Gamma_\downarrow)} \ln\frac{\Gamma_\uparrow}{\Gamma_\downarrow} \right]. \qquad (29)$$

Equation (29) was obtained within second-order scaling, which is known to overestimate the pre-exponential factor that enters T_K. We shall not seek an improved expression for T_K encompassing all parameter regimes of

Eq. (7). More accurate expressions will be given for the particular cases of interest, see Sec. V below. Much of our discussion will not depend, though, on the precise form of T_K. We shall only assume it to be sufficiently small such that the renormalized exchange couplings can be regarded isotropic starting at energies well above T_K.

The other competing scale which enters the low-energy physics is the fully renormalized magnetic field: $\vec{h}_{\text{tot}} = h_{\text{tot}}^x \hat{x} + h_{\text{tot}}^z \hat{z}$. While the transverse field h_{tot}^x remains given by $h \sin\theta$, the longitudinal field h_{tot}^z is obtained by integration of Eq. (27), subject to the initial condition of Eq. (23). Since the running coupling $\tilde{J}_z$ is a slowly varying function of l in the range where Eqs. (25)–(27) apply, it can be replaced for all practical purposes by its bare value in Eq. (27). Straightforward integration of Eq. (27) then yields

$$
\begin{aligned}
h_{\text{tot}}^z &= h\cos\theta + \frac{\Gamma_\uparrow - \Gamma_\downarrow}{\pi} \ln\frac{U + \epsilon_0}{|\epsilon_0|} \\
&+ 3\ln(2)\,D_0 \frac{\Gamma_\uparrow^2 - \Gamma_\downarrow^2}{\pi^2} \times \frac{U(U + 2\epsilon_0)}{(U + \epsilon_0)^2 \epsilon_0^2},
\end{aligned}
\tag{30}
$$

where we have used Eqs. (20)–(22) for J_z, v_{sc}, and $v_\pm$. Note that the third term on the right-hand side of Eq. (30) is generally much smaller than the first two terms, and can typically be neglected.

To conclude this section, we have shown that the Hamiltonian of Eq. (7), and thus that of Eq. (1), is equivalent at sufficiently low temperature and fields to the ordinary *isotropic* Kondo model with a tilted magnetic field, provided that $\Gamma_\uparrow, \Gamma_\downarrow \ll |\epsilon_0|, U + \epsilon_0$. The relevant Kondo temperature is approximately given by Eq. (29), while the components of $\vec{h}_{\text{tot}} = h_{\text{tot}}^x \hat{x} + h_{\text{tot}}^z \hat{z}$ are given by $h_{\text{tot}}^x = h\sin\theta$ and Eq. (30).

IV. PHYSICAL OBSERVABLES

Having established the intimate connection between the generalized Anderson Hamiltonian, Eq. (7), and the standard Kondo model with a tilted magnetic field, we now employ well-known results of the latter model in order to obtain a unified picture for the conductance and the occupation of the levels of our original model, Eq. (1). The analysis extends over a rather broad range of parameters. For example, when $U + 2\epsilon_0 = 0$, then the sole requirement for the applicability of our results is for $\sqrt{\Delta^2 + b^2}$ to be small. The tunnelling matrix $\hat{A}$ can be practically arbitrary as long as the system lies deep in the local-moment regime. The further one departs from the middle of the Coulomb-blockade valley the more restrictive the condition on $\hat{A}$ becomes in order for $\vec{h}_{\text{tot}}$ to stay small. Still, our approach is applicable over a surprisingly broad range of parameters, as demonstrated below. Unless stated otherwise, our discussion is restricted to zero temperature.

A.   Conductance

At zero temperature, a local Fermi liquid is formed in the Kondo model. Only elastic scattering takes place at the Fermi energy, characterized by the scattering phase shifts for the two appropriate conduction-electron modes. For a finite magnetic field h in the z-direction, single-particle scattering is diagonal in the spin index. The corresponding phase shifts, $\delta_\uparrow(h)$ and $\delta_\downarrow(h)$, are given by the Friedel-Langreth sum rule,[21,33] $\delta_\sigma(h) = \pi\langle n_\sigma\rangle$, which when applied to the local-moment regime takes the form

$$
\delta_\sigma(h) = \frac{\pi}{2} + \sigma\pi M(h)\,.
\tag{31}
$$

Here $M(h)$ is the spin magnetization, which reduces[34] in the scaling regime to a universal function of h/T_K,

$$
M(h) = M_K(h/T_K)\,.
\tag{32}
$$

Thus, Eq. (31) becomes $\delta_\sigma(h) = \pi/2 + \sigma\pi M_K(h/T_K)$, where $M_K(h/T_K)$ is given by Eq. (B1)

To apply these results to the problem at hand, one first needs to realign the tilted field along the z axis. This is achieved by a simple rotation of the different operators about the y axis. Writing the field $\vec{h}_{\text{tot}}$ in the polar form

$$
\begin{aligned}
\vec{h}_{\text{tot}} &\equiv h_{\text{tot}}\,(\sin\theta_h\hat{x} + \cos\theta_h\hat{z}) \\
&\approx h\sin\theta\,\hat{x} + \left(h\cos\theta + \frac{\Gamma_\uparrow - \Gamma_\downarrow}{\pi}\ln\frac{U + \epsilon_0}{|\epsilon_0|}\right)\hat{z},
\end{aligned}
\tag{33}
$$

the lead and the dot operators are rotated according to

$$
\begin{bmatrix} \tilde{c}_{k\uparrow} \\ \tilde{c}_{k\downarrow} \end{bmatrix} = R_h \cdot \begin{bmatrix} c_{k\uparrow} \\ c_{k\downarrow} \end{bmatrix} = R_h R_l \cdot \begin{bmatrix} c_{kL} \\ c_{kR} \end{bmatrix}
\tag{34}
$$

and

$$
\begin{bmatrix} \tilde{d}_\uparrow \\ \tilde{d}_\downarrow \end{bmatrix} = R_h \cdot \begin{bmatrix} d_\uparrow \\ d_\downarrow \end{bmatrix} = R_h R_d \cdot \begin{bmatrix} d_1 \\ d_2 \end{bmatrix},
\tag{35}
$$

with

$$
R_h = e^{i(\theta_h/2)\tau_y} = \begin{bmatrix} \cos(\theta_h/2) & \sin(\theta_h/2) \\ -\sin(\theta_h/2) & \cos(\theta_h/2) \end{bmatrix}.
\tag{36}
$$

Here R_l and R_d are the unitary matrices used in Eq. (9) to independently rotate the lead and the dot operators. Note that since $\sin\theta \geq 0$, the range of θ_h is $\theta_h \in [0;\pi]$.

The new dot and lead degrees of freedom have their spins aligned either parallel ($\tilde{d}_\uparrow$ and $\tilde{c}_{k\uparrow}$) or antiparallel ($\tilde{d}_\downarrow$ and $\tilde{c}_{k\downarrow}$) to the field $\vec{h}_{\text{tot}}$. In this basis the single-particle scattering matrix is diagonal,

$$
\tilde{S} = -\begin{bmatrix} e^{i2\pi M_K(h_{\text{tot}}/T_K)} & 0 \\ 0 & e^{-i2\pi M_K(h_{\text{tot}}/T_K)} \end{bmatrix}.
\tag{37}
$$

The conversion back to the original basis set of left- and right-lead electrons is straightforward,

$$
S = R_l^\dagger R_h^\dagger \tilde{S} R_h R_l \equiv \begin{bmatrix} r & t' \\ t & r' \end{bmatrix},
\tag{38}
$$

providing us with the zero-temperature conductance $G = (e^2/2\pi\hbar)|t|^2$.

Equations (37) and (38) were derived employing the mapping of Eq. (1) onto an effective isotropic Kondo model with a tilted magnetic field, in the $v_{sc}, v_{\pm} \to 0$ limit. Within this framework, Eqs. (37) and (38) are exact in the scaling regime, $T_K/D_0 \ll 1$. The extent to which these equations are indeed valid can be appreciated by considering the special case $h \sin\theta = 0$, for which there exists an exact (and independent) solution for the scattering matrix S in terms of the dot "magnetization" $M = \langle n_\uparrow - n_\downarrow \rangle/2$ [see Eq. (41) below]. That solution, which is based on the Friedel-Langreth sum rule[21] applied directly to a spin-conserving Anderson model, reproduces Eqs. (37) and (38) in the Kondo regime.

1. Zero Aharonov-Bohm fluxes

Of particular interest is the case where no Aharonov-Bohm fluxes are present, where further analytic progress can be made. For $\varphi_L = \varphi_R = 0$, the parameters that appear in the Hamiltonian of Eq. (1) are all real. Consequently, the rotation matrices R_d and R_l acquire the simplified forms given by Eqs. (A29) and (A32) (see Appendix A for details). Under these circumstances, the matrix product $R_h R_l$ becomes $\pm e^{i\tau_y(\theta_h + s_R \theta_l)/2} e^{i\pi\tau_z(1-s_R)/4}$, and the elements of the scattering matrix [see Eq. (38)] are

$$t = t' = -i\sin[2\pi M_K(h_{\text{tot}}/T_K)]\sin(\theta_l + s_R\theta_h) ,$$
$$r = (r')^* = -\cos[2\pi M_K(h_{\text{tot}}/T_K)]$$
$$- i\sin[2\pi M_K(h_{\text{tot}}/T_K)]\cos(\theta_l + s_R\theta_h) . \quad (39)$$

Hence, the conductance is

$$G = \frac{e^2}{2\pi\hbar}\sin^2[2\pi M_K(h_{\text{tot}}/T_K)]\sin^2(\theta_l + s_R\theta_h), \quad (40)$$

where the sign s_R and angle θ_l are given by Eqs. (A31) and (A23), respectively. All dependencies of the conductance on the original model parameters that enter Eq. (1) are combined in Eq. (40) into two variables alone, $\theta_l + s_R\theta_h$ and the reduced field h_{tot}/T_K. In particular, θ_l is determined exclusively by the tunnelling matrix $\hat{A}$, while s_R depends additionally on the two dot parameters Δ and b.

The conditions for a phase lapse to occur are particularly transparent from Eq. (40). These lapses correspond to zeroes of t, and, in turn, of the conductance. There are two possibilities for G to vanish: either h_{tot} is zero, or $\theta_l + s_R\theta_h$ equals an integer multiple of π. For example, when the Hamiltonian of Eq. (7) is invariant under the particle-hole transformation $d_\sigma \to d_\sigma^\dagger$ and $c_{k\sigma} \to -c_{k\sigma}^\dagger$ (which happens to be the case whenever $\sqrt{\Delta^2 + b^2} = 0$ and $U + 2\epsilon_0 = 0$), then h_{tot} vanishes, and consequently the conductance vanishes as well. A detailed discussion of the ramifications of Eq. (40) is held in Sec. V B below.

2. Parallel-field configuration

For $h\sin\theta = 0$, spin is conserved by the Hamiltonian of Eq. (7). We refer to this case as the "parallel-field" configuration, since the magnetic field is aligned with the anisotropy axis z. For a parallel field, one can easily generalize the Friedel-Langreth sum rule[21] to the Hamiltonian of Eq. (7).[25] Apart from the need to consider each spin orientation separately, details of the derivation are identical to those for the ordinary Anderson model,[21] and so is the formal result for the $T = 0$ scattering phase shift: $\delta_\sigma = \pi\Delta N_\sigma$, where ΔN_σ is the number of displaced electrons in the spin channel σ. In the wide-band limit, adopted throughout our discussion, ΔN_σ reduces to the occupancy of the corresponding dot level, $\langle n_\sigma \rangle$. The exact single-particle scattering matrix then becomes

$$S = e^{i\pi\langle n_\uparrow + n_\downarrow \rangle} R_l^\dagger \cdot \begin{bmatrix} e^{i2\pi M} & 0 \\ 0 & e^{-i2\pi M} \end{bmatrix} \cdot R_l , \quad (41)$$

where $M = \langle n_\uparrow - n_\downarrow \rangle/2$ is the dot "magnetization."

Equation (41) is quite general. It covers all physical regimes of the dot, whether empty, singly occupied or doubly occupied, and extends to arbitrary fluxes φ_L and φ_R. Although formally exact, it does not specify how the dot "magnetization" M and the total dot occupancy $\langle n_\uparrow + n_\downarrow \rangle$ relate to the microscopic model parameters that appear in Eq. (7). Such information requires an explicit solution for these quantities. In the Kondo regime considered above, $\langle n_\uparrow + n_\downarrow \rangle$ is reduced to one and M is replaced by $\pm M_K(h_{\text{tot}}/T_K)$. Here the sign depends on whether the field $\vec{h}_{\text{tot}}$ is parallel or antiparallel to the z axis (recall that $h_{\text{tot}} \geq 0$ by definition). As a result, Eq. (41) reproduces Eqs. (37)–(38).

To carry out the rotation in Eq. (41), we rewrite it in the form

$$S = e^{i\pi\langle n_\uparrow + n_\downarrow \rangle} R_l^\dagger \left[\cos(2\pi M) + i\sin(2\pi M)\tau_z\right] R_l . \quad (42)$$

Using the general form of Eq. (A3) for the rotation matrix R_l, the single-particle scattering matrix is written as $S = e^{i\pi\langle n_\uparrow + n_\downarrow \rangle}\bar{S}$, where

$$\bar{S} = \cos(2\pi M) + i\sin(2\pi M)\cos\theta_l\,\tau_z$$
$$+ i\sin(2\pi M)\sin\theta_l\left[\cos\phi_l\,\tau_x + \sin\phi_l\,\tau_y\right] . \quad (43)$$

The zero-temperature conductance, $G = (e^2/2\pi\hbar)|t|^2$, takes then the exact form

$$G = \frac{e^2}{2\pi\hbar}\sin^2(2\pi M)\sin^2\theta_l . \quad (44)$$

Two distinct properties of the conductance are apparent form Eq. (44). Firstly, G is bounded by $\sin^2\theta_l$ times the conductance quantum unit $e^2/2\pi\hbar$. Unless θ_l happens to equal $\pm\pi/2$, the maximal conductance is smaller than $e^2/2\pi\hbar$. Secondly, G vanishes for $M = 0$ and is maximal for $M = \pm 1/4$. Consequently, when M is tuned from $M \approx -1/2$ to $M \approx 1/2$ by varying an appropriate

9

control parameter (for example, ϵ_0 when $\Gamma_\uparrow \gg \Gamma_\downarrow$), then G is peaked at the points where $M = \pm 1/4$. In the Kondo regime, when $M \rightarrow \pm M_K(h_{\text{tot}}/T_K)$, this condition is satisfied for $h_{\text{tot}} \approx 2.4 T_K$. As we show in Sec. V B, this is the physical origin of the correlation-induced peaks reported by Meden and Marquardt.[11] Note that for a given fixed tunnelling matrix $\hat{A}$ in the parallel-field configuration, the condition for a phase lapse to occur is simply for M to vanish.

B. Occupation of the dot levels

Similar to the zero-temperature conductance, one can exploit exact results of the standard Kondo model to obtain the occupation of the levels at low temperatures and fields. Defining the two reduced density matrices

$$O_d = \begin{bmatrix} \langle d_1^\dagger d_1 \rangle & \langle d_2^\dagger d_1 \rangle \\ \langle d_1^\dagger d_2 \rangle & \langle d_2^\dagger d_2 \rangle \end{bmatrix} \qquad (45)$$

and

$$\tilde{O}_d = \begin{bmatrix} \langle \tilde{d}_\uparrow^\dagger \tilde{d}_\uparrow \rangle & \langle \tilde{d}_\downarrow^\dagger \tilde{d}_\uparrow \rangle \\ \langle \tilde{d}_\uparrow^\dagger \tilde{d}_\downarrow \rangle & \langle \tilde{d}_\downarrow^\dagger \tilde{d}_\downarrow \rangle \end{bmatrix}, \qquad (46)$$

these are related through

$$O_d = R_d^\dagger R_h^\dagger \tilde{O}_d R_h R_d . \qquad (47)$$

Here $R_h R_d$ is the overall rotation matrix pertaining to the dot degrees of freedom, see Eq. (35).

At low temperatures, the mapping onto an isotropic Kondo model implies

$$\tilde{O}_d = \begin{bmatrix} \langle \tilde{n}_\uparrow \rangle & 0 \\ 0 & \langle \tilde{n}_\downarrow \rangle \end{bmatrix}, \qquad (48)$$

where

$$\langle \tilde{n}_\sigma \rangle = n_{\text{tot}}/2 + \sigma \tilde{M} . \qquad (49)$$

Here we have formally separated the occupancies $\langle \tilde{n}_\sigma \rangle$ into the sum of a spin component and a charge component. The spin component involves the magnetization $\tilde{M}$ along the direction of the total effective field $\vec{h}_{\text{tot}}$. The latter is well described by the universal magnetization curve $M_K(h_{\text{tot}}/T_K)$ of the Kondo model [see Eq. (B1)]. As for the total dot occupancy n_{tot}, deep in the local-moment regime charge fluctuations are mostly quenched at low temperatures, resulting in the near integer valance $n_{\text{tot}} \approx 1$. One can slightly improve on this estimate of n_{tot} by resorting to first-order perturbation theory in Γ_σ (and zeroth order in h):

$$n_{\text{tot}} \approx 1 + \frac{\Gamma_\uparrow + \Gamma_\downarrow}{2\pi} \left(\frac{1}{\epsilon_0} + \frac{1}{U + \epsilon_0} \right) = 1 - 2\rho v_+ . \quad (50)$$

This low-order process does not enter the Kondo effect, and is not contained in $M_K(h_{\text{tot}}/T_K)$.[35] With the above approximations, the combination of Eqs. (47) and (48) yields a general formula for the reduced density matrix

$$O_d = n_{\text{tot}}/2 + M_K(h_{\text{tot}}/T_K) R_d^\dagger R_h^\dagger \tau_z R_h R_d . \qquad (51)$$

1. Zero Aharonov-Bohm fluxes

As in the case of the conductance, Eq. (51) considerably simplifies in the absence of Aharonov-Bohm fluxes, when the combined rotation $R_h R_d$ equals $(s_R s_\theta)^{1/2} e^{i\tau_y(\theta_h + s_\theta \theta_d)/2} e^{i\pi\tau_z(1-s_\theta)/4}$ [see Eqs. (36) and (A29)]. Explicitly, Eq. (51) becomes

$$O_d = n_{\text{tot}}/2 \ + \ M_K(h_{\text{tot}}/T_K)\cos(\theta_d + s_\theta \theta_h)\tau_z$$
$$+ \ M_K(h_{\text{tot}}/T_K)\sin(\theta_d + s_\theta \theta_h)\tau_x , (52)$$

where the sign s_θ and angle θ_d are given by Eqs. (A30) and (A23), respectively.

Several observations are apparent from Eq. (52). Firstly, when written in the original "spin" basis $d_1^\dagger$ and $d_2^\dagger$, the reduced density matrix O_d contains the off-diagonal matrix element $M_K(h_{\text{tot}}/T_K)\sin(\theta_d + s_\theta \theta_h)$. The latter reflects the fact that the original "spin" states are inclined with respect to the anisotropy axis dynamically selected by the system. Secondly, similar to the conductance of Eq. (40), O_d depends on two variables alone: $\theta_d + s_\theta \theta_h$ and the reduced field h_{tot}/T_K. Here, again, the angle θ_d depends solely on the tunnelling matrix $\hat{A}$, while the sign s_θ depends additionally on Δ and b. Thirdly, the original levels $d_1^\dagger$ and $d_2^\dagger$ have the occupation numbers

$$\langle n_1 \rangle = n_{\text{tot}}/2 + M_K(h_{\text{tot}}/T_K)\cos(\theta_d + s_\theta \theta_h), \quad (53a)$$
$$\langle n_2 \rangle = n_{\text{tot}}/2 - M_K(h_{\text{tot}}/T_K)\cos(\theta_d + s_\theta \theta_h). \quad (53b)$$

In particular, equal populations $\langle n_1 \rangle = \langle n_2 \rangle$ are found if either h_{tot} is zero or if $\theta_d + s_\theta \theta_d$ equals $\pi/2$ up to an integer multiple of π. This provides one with a clear criterion for the occurrence of population inversion,[9,10,13] i.e., the crossover from $\langle n_1 \rangle > \langle n_2 \rangle$ to $\langle n_2 \rangle > \langle n_1 \rangle$ or vice versa.

2. Parallel-field configuration

In the parallel-field configuration, the angle θ_h is either zero or π, depending on whether the magnetic field $\vec{h}_{\text{tot}}$ is parallel or antiparallel to the z axis (recall that $h \sin \theta = h_{\text{tot}} \sin \theta_h = 0$ in this case). The occupancies $\langle n_1 \rangle$ and $\langle n_2 \rangle$ acquire the exact representation

$$\langle n_1 \rangle = n_{\text{tot}}/2 + M \cos \theta_d , \qquad (54a)$$
$$\langle n_2 \rangle = n_{\text{tot}}/2 - M \cos \theta_d , \qquad (54b)$$

where n_{tot} is the exact total occupancy of the dot and $M = \langle n_\uparrow - n_\downarrow \rangle/2$ is the dot "magnetization," defined and used previously (not to be confused with $\tilde{M} = \pm M$). As with the conductance, Eqs. (54) encompass all regimes of the dot, and extend to arbitrary Aharonov-Bohm fluxes. They properly reduce to Eqs. (53) in the Kondo regime, when $n_{\text{tot}} \approx 1$ [see Eq. (50)] and $M \rightarrow \pm M_K(h_{\text{tot}}/T_K)$. [Note that Eqs. (53) have been derived for zero Aharonov-Bohm fluxes.]

One particularly revealing observation that follows from Eqs. (54) concerns the connection between the phenomena of population inversion and phase lapses in the parallel-field configuration. For a given fixed tunnelling matrix $\hat{A}$ in the parallel-field configuration, the condition for a population inversion to occur is identical to the condition for a phase lapse to occur. Both require that $M = 0$. Thus, these seemingly unrelated phenomena are synonymous in the parallel-field configuration. This is not generically the case when $h_{\text{tot}}^x \neq 0$, as can be seen, for example, from Eqs. (40) and (53). In the absence of Aharonov-Bohm fluxes, the conductance is proportional to $\sin^2(\theta_l + s_R \theta_h)$. It therefore vanishes for $h_{\text{tot}}^x \neq 0$ only if $\theta_l + s_R \theta_h = 0 \mod \pi$. By contrast, the difference in populations $\langle n_1 - n_2 \rangle$ involves the unrelated factor $\cos(\theta_d + s_\theta \theta_h)$, which generally does not vanish together with $\sin(\theta_l + s_R \theta_h)$.

Another useful result which applies to the parallel-field configuration is an exact expression for the $T = 0$ conductance in terms of the population difference $\langle n_1 - n_2 \rangle$. It follows from Eqs. (54) that $M = \langle n_1 - n_2 \rangle/(2\cos\theta_d)$. Inserting this relation into Eq. (44) yields

$$G = \frac{e^2}{2\pi\hbar} \sin^2\left(\frac{\pi\langle n_1 - n_2 \rangle}{\cos\theta_d}\right) \sin^2\theta_l . \qquad (55)$$

This expression will be used in Sec. V for analyzing the conductance in the presence of isotropic couplings, and for the cases considered by Meden and Marquardt.[11]

V. RESULTS

Up until this point we have developed a general framework for describing the local-moment regime in terms of two competing energy scales, the Kondo temperature T_K and the renormalized magnetic field h_{tot}. We now turn to explicit calculations that exemplify these ideas. To this end, we begin in Sec. V A with the exactly solvable case $V_\uparrow = V_\downarrow$, which corresponds to the conventional Anderson model in a finite magnetic field.[6] Using the exact Bethe *ansatz* solution of the Anderson model,[20] we present a detailed analysis of this special case with three objectives in mind: (i) to benchmark our general treatment against rigorous results; (ii) to follow in great detail the delicate interplay between the two competing energy scales that govern the low-energy physics; (iii) to set the stage for the complete explanation of the charge oscillations[9,10,13] and the correlation-induced resonances in the conductance of this device.[11,12]

We then proceed in Sec. V B to the generic anisotropic case $V_\uparrow \neq V_\downarrow$. Here a coherent explanation is provided for the ubiquitous phase lapses,[8] population inversion,[9,10] and correlation-induced resonances[11,12] that were reported recently in various studies of two-level quantum dots. In particular, we expose the latter resonances as a disguised Kondo phenomenon. The general formulae of Sec. IV are quantitatively compared to the numerical results of Ref.11. The detailed agreement that is obtained nicely illustrates the power of the analytical approach put forward in this paper.

A. Exact treatment of $V_\uparrow = V_\downarrow$

As emphasized in Sec. III, all tunnelling matrices $\hat{A}$ which satisfy Eq. (11) give rise to equal amplitudes $V_\uparrow = V_\downarrow = V$ within the Anderson Hamiltonian description of Eq. (7). Given this extra symmetry, one can always choose the unitary matrices R_l and R_d in such a way that the magnetic field h points along the z direction [namely, $\cos\theta = 1$ in Eq. (7)]. Perhaps the simplest member in this class of tunnelling matrices is the case where $a_{L1} = -a_{L2} = a_{R1} = a_{R2} = V/\sqrt{2}$, $\varphi_L = \varphi_R = 0$ and $b = 0$. One can simply convert the conduction-electron operators to even and odd combinations of the two leads, corresponding to choosing $\theta_l = \pi/2 + \theta_d$. Depending on the sign of Δ, the angle θ_d is either zero (for $\Delta < 0$) or π (for $\Delta > 0$), which leaves us with a conventional Anderson impurity in the presence of the magnetic field $\vec{h} = |\Delta|\,\hat{z}$. All other rotation angle that appear in Eqs. (A2) and (A2) (i.e., χ's and ϕ's) are equal to zero. For concreteness we shall focus hereafter on this particular case, which represents, up to a simple rotation of the $d_\sigma^\dagger$ and $c_{k\sigma}^\dagger$ operators, all tunnelling matrices $\hat{A}$ in this category of interest. Our discussion is restricted to zero temperature.

1. Impurity magnetization

We have solved the exact Bethe *anstaz* equations numerically using the procedure outlined in Appendix B. Our results for the occupation numbers $\langle n_\sigma \rangle$ and the magnetization $M = \langle n_\uparrow - n_\downarrow \rangle/2$ are summarized in Figs. 2 and 3. Figure 2 shows the magnetization of the Anderson impurity as a function of the (average) level position ϵ_0 in a constant magnetic field, $h = \Delta = 10^{-3}U$. The complementary regime $\epsilon_0 < -U/2$ is obtained by a simple reflection about $\epsilon_0 = -U/2$, as follows from the particle-hole transformation $d_\sigma \rightarrow d_{-\sigma}^\dagger$ and $c_{k\sigma} \rightarrow -c_{k-\sigma}^\dagger$. The Bethe *ansatz* curve accurately crosses over from the perturbative domain at large $\epsilon_0 \gg \Gamma$ (when the dot is almost empty) to the local-moment regime with a fully pronounced Kondo effect (when the dot is singly occupied). In the latter regime, we find excellent agreement with the analytical magnetization curve of the Kondo model, Eq. (B1), both as a function of ϵ_0 and as a function of the magnetic field Δ (lower left inset to Fig. 2). The agreement with the universal Kondo curve is in fact quite surprising in that it extends nearly into the mixed-valent regime. As a function of field, the Kondo curve of Eq. (B1) applies up to fields of the order of $h \sim \sqrt{\Gamma U} \gg T_K$.
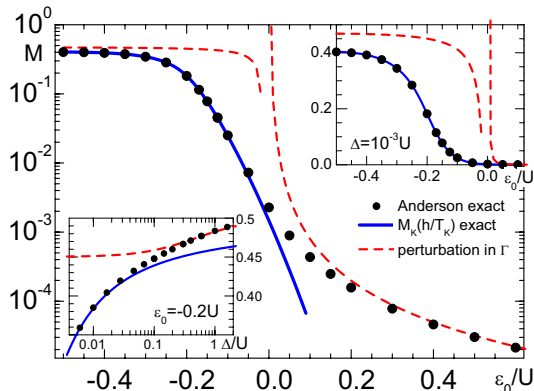
FIG. 2: (Color online) Magnetization of the isotropic case as a function of ϵ_0: exact Bethe *ansatz* curve and comparison with different approximation schemes. Black symbols show the magnetization M derived from the exact Bethe *ansatz* equations; the dashed (red) line marks the result of first-order perturbation theory in Γ (Ref.9, divergent at $\epsilon_0 = 0$); the thick (blue) line is the analytical formula for the magnetization in the Kondo limit, Eq. (B1), with T_K given by Eq. (B4). The model parameters are $\Gamma/U = 0.05$, $\Delta/U = 10^{-3}$ and $T = 0$. The upper right inset shows the same data but on a linear scale. The lower left inset shows the magnetization M as a function of the magnetic field $h = \Delta$ at fixed $\epsilon_0/U = -0.2$. The universal magnetization curve of the Kondo model well describes the exact magnetization up to $M \approx 0.42$ (lower fields not shown), while first-order perturbation theory in Γ fails from $M \approx 0.46$ downwards.

2. Occupation numbers and charge oscillations

Figure 3 displays the individual occupation numbers $\langle n_1 \rangle$ and $\langle n_2 \rangle$ as a function of ϵ_0, for a series of constant fields $h = \Delta$. In going from large $\epsilon_0 \gg \Gamma$ to large $-(\epsilon_0 + U) \gg \Gamma$, the total charge of the quantum dot increases monotonically from nearly zero to nearly two. However, the partial occupancies $\langle n_1 \rangle$ and $\langle n_2 \rangle$ display nonmonotonicities, which have drawn considerable theoretical attention lately.[9,10,13] As seen in Fig. 3, the nonmonotonicities can be quite large, although no population inversion occurs for $\Gamma_\uparrow = \Gamma_\downarrow$.

Our general discussion in Sec. III makes it is easy to interpret these features of the partial occupancies $\langle n_i \rangle$. Indeed, as illustrated in Fig. 3, there is excellent agreement in the local-moment regime between the exact Bethe *ansatz* results and the curves obtained from Eqs. (53) and (50) based on the mapping onto the Kondo Hamiltonian. We therefore utilize Eqs. (53) for analyzing the data. To begin with we note that, for $\Gamma_\uparrow = \Gamma_\downarrow$, there is no renormalization of the effective magnetic field. The latter remains constant and equal to $h = \Delta$ independent of ϵ_0. Combined with the fact that $\cos(\theta_d + s_\theta \theta_h) \equiv -1$ in Eqs. (53), the magnetization $M = \langle n_\uparrow - n_\downarrow \rangle/2 = \langle n_2 - n_1 \rangle/2$ depends exclusively on the ratio Δ/T_K. The sole dependence on ϵ_0 enters through T_K, which varies according to Eq. (B4). Thus, M is positive for all gate voltages ϵ_0, excluding the possibility of a population in-
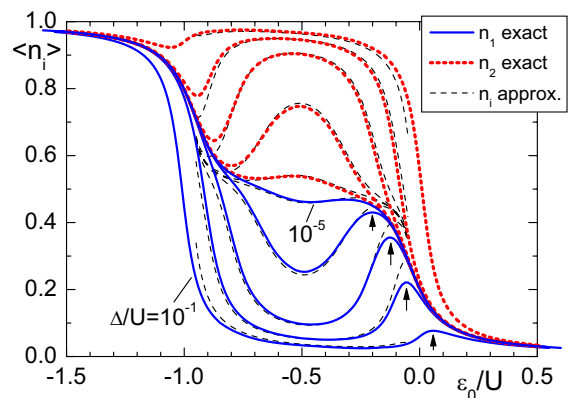

FIG. 3: (Color online) The occupation numbers $\langle n_1 \rangle$ [solid (blue) lines] and $\langle n_2 \rangle$ [dotted (red) lines] versus ϵ_0, as obtained from the solution of the exact Bethe *ansatz* equations. In going from the inner-most to the outer-most pairs of curves, the magnetic field $h = \Delta$ increases by a factor of 10 between each successive pair of curves, with the inner-most (outer-most) curves corresponding to $\Delta/U = 10^{-5}$ ($\Delta/U = 0.1$). The remaining model parameters are $\Gamma/U = 0.05$ and $T = 0$. Non-monotonicities are seen in the process of charging. These are most pronounced for intermediate values of the field. The evolution of the nonmonotonicities with increasing field is tracked by arrows. The dashed black lines show the approximate values calculated from Eqs. (53) and (50) based on the mapping onto the Kondo Hamiltonian (here $\theta_h = 0$ and $\theta_d = \pi$).

version.

The nonmonotonicities in the individual occupancies stem from the explicit dependence of T_K on the gate voltage ϵ_0. According to Eq. (B4), T_K is minimal in the middle of the Coulomb-blockade valley, increasing monotonically as a function of $|\epsilon_0 + U/2|$. Thus, Δ/T_K, and consequently M, is maximal for $\epsilon_0 = -U/2$, decreasing monotonically the farther ϵ_0 departs from $-U/2$. Since $n_{\text{tot}} \approx 1$ is nearly a constant in the local-moment regime, this implies the following evolution of the partial occupancies: $\langle n_1 \rangle$ decreases ($\langle n_2 \rangle$ increases) as ϵ_0 is lowered from roughly zero to $-U/2$. It then increases (decreases) as ϵ_0 is further lowered toward $-U$. Combined with the crossovers to the empty-impurity and doubly occupied regimes, this generates a local maximum (minimum) in $\langle n_1 \rangle$ ($\langle n_2 \rangle$) near $\epsilon_0 \sim 0$ ($\epsilon_0 \sim -U$).

Note that the local extremum in $\langle n_i \rangle$ is most pronounced for intermediate values of the field Δ. This can be understood by examining the two most relevant energy scales in the problem, namely, the minimal Kondo temperature $T_K^{\min} = T_K|_{\epsilon_0 = -U/2}$ and the hybridization width Γ. These two energies govern the spin susceptibility of the impurity in the middle of the Coulomb-blockade valley (when $\epsilon_0 = -U/2$) and in the mixed-valent regime (when either $\epsilon_0 \approx 0$ or $\epsilon \approx -U$), respectively. The charging curves of Fig. 3 stem from an interplay of the three energy scales Δ, $T_K^{\min}$ and Γ as described below.

When $\Delta \ll T_K^{\min}$, exemplified by the pair of curves corresponding to the smallest field $\Delta = 10^{-5}U \approx 0.24 T_K^{\min}$
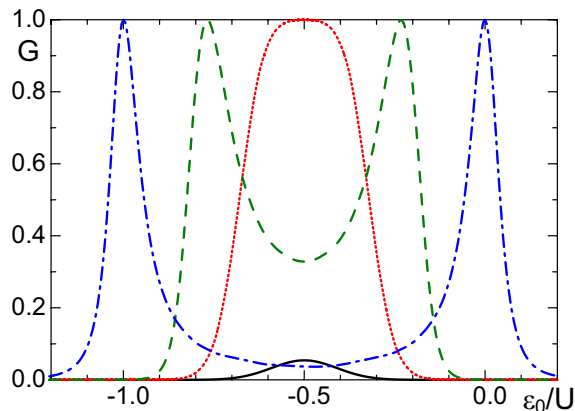
FIG. 4: (Color online) The exact conductance G [in units of $e^2/(2\pi\hbar)$] versus ϵ_0, as obtained from the Bethe *ansatz* magnetization M and Eq. (55) with $\theta_l = 3\pi/2$ and $\theta_d = \pi$. Here Δ/U equals 10^{-5} [full (black) line], 10^{-4} [dotted (red) line], 10^{-3} [dashed (green) line] and 0.1 [dot-dashed (blue) line]. The remaining model parameters are $\Gamma/U = 0.05$ and $T = 0$. Once Δ exceeds the critical field $h_c \approx 2.4 T_K^{\min}$, the single peak at $\epsilon_0 = -U/2$ is split into two correlation-induced peaks, which cross over to Coulomb-blockade peaks at large Δ.

in Fig. 3, the magnetic field remains small throughout the Coulomb-blockade valley and no significant magnetization develops. The two levels are roughly equally populated, showing a plateaux at $\langle n_1 \rangle \approx \langle n_2 \rangle \approx 1/2$ in the regime where the dot is singly occupied. As Δ grows and approaches $T_K^{\min}$, the field becomes sufficiently strong to significantly polarize the impurity in the vicinity of $\epsilon_0 = -U/2$. A gap then rapidly develops between $\langle n_1 \rangle$ and $\langle n_2 \rangle$ near $\epsilon_0 = -U/2$ as Δ is increased. Once Δ reaches the regime $T_K^{\min} \ll \Delta \ll \Gamma$, a crossover from $h \gg T_K$ (fully polarized impurity) to $h \ll T_K$ (unpolarized impurity) occurs as ϵ_0 is tuned away from the middle of the Coulomb-blockade valley. This leads to the development of a pronounced maximum (minimum) in $\langle n_1 \rangle$ ($\langle n_2 \rangle$), as marked by the arrows in Fig. 3. Finally, when $h \gtrsim \Gamma$, the field is sufficiently large to keep the dot polarized throughout the local-moment regime. The extremum in $\langle n_i \rangle$ degenerates into a small bump in the vicinity of either $\epsilon_0 \approx 0$ or $\epsilon_0 \approx -U$, which is the non-monotonic feature first discussed in Ref.9. This regime is exemplified by the pair of curves corresponding to the largest field $\Delta = 0.1U = 2\Gamma$ in Fig. 3, whose parameters match those used in Fig. 2 of Ref.9. Note, however, that the perturbative calculations of Ref.9 will inevitably miss the regime $T_K^{\min} \ll \Delta \ll \Gamma$ where this feature is large.[36]

3. Conductance

The data of Fig. 3 can easily be converted to conductance curves by using the exact formula of Eq. (55) with $\theta_l = 3\pi/2$ and $\theta_d = \pi$. The outcome is presented in Fig. 4. The evolution of $G(\epsilon_0)$ with increasing Δ is quite
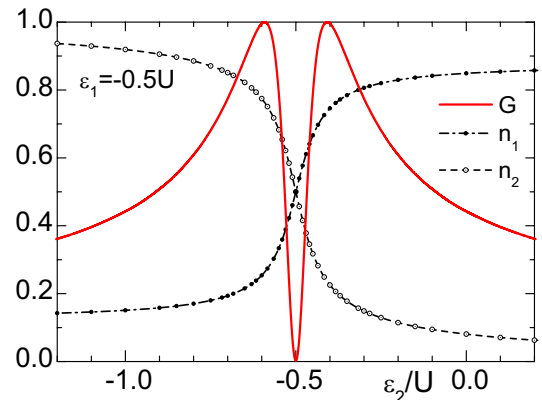

FIG. 5: (Color online) The exact occupation numbers $\langle n_i \rangle$ and conductance G [in units of $e^2/(2\pi\hbar)$] as a function of ϵ_2, for $T = 0$, $\Gamma/U = 0.2$ and fixed $\epsilon_1/U = -1/2$. The population inversion at $\epsilon_2 = \epsilon_1$ leads to a sharp transmission zero (phase lapse). Note the general resemblance between the functional dependence of G on ϵ_2 and the correlation-induced resonances reported by Meden and Marquardt[11] for $\Gamma_\uparrow \neq \Gamma_\downarrow$ (see Fig. 6).

dramatic. When Δ is small, the conductance is likewise small with a shallow peak at $\epsilon_0 = -U/2$. This peak steadily grows with increasing Δ until reaching the unitary limit, at which point it is split in two. Upon further increasing Δ, the two split peaks gradually depart, approaching the peak positions $\epsilon_0 \approx 0$ and $\epsilon_0 \approx -U$ for large Δ. The conductance at each of the two maxima remains pinned at all stages at the unitary limit.

These features of the conductance can be naturally understood based on Eqs. (55) and (53). When $\Delta \ll T_K^{\min}$, the magnetization $M \approx \Delta/(2\pi T_K)$ and the conductance $G \approx (\Delta/T_K)^2 e^2/(2\pi\hbar)$ are uniformly small, with a peak at $\epsilon_0 = -U/2$ where T_K is the smallest. The conductance monotonically grows with increasing Δ until reaching the critical field $\Delta = h_c \approx 2.4 T_K^{\min}$, where $M|_{\epsilon_0=-U/2} = 1/4$ and $G|_{\epsilon_0=-U/2} = e^2/(2\pi\hbar)$. Upon further increasing Δ, the magnetization at $\epsilon_0 = -U/2$ exceeds 1/4, and the associated conductance decreases. The unitarity condition $M = 1/4$ is satisfied at two gate voltages $\epsilon_{\max}^{\pm}$ symmetric about $-U/2$, defined by the relation $T_K \approx \Delta/2.4$. From Eq. (B4) one obtains

$$\epsilon_\pm^{\max} = -\frac{U}{2} \pm \sqrt{\frac{U^2}{4} - \Gamma^2 + \frac{2\Gamma U}{\pi} \ln\left(\frac{\pi\Delta}{2.4\sqrt{2\Gamma U}}\right)}. \quad (56)$$

The width of the two conductance peaks, $\Delta\epsilon$, can be estimated for $T_K^{\min} \ll \Delta \ll \Gamma$ from the inverse of the derivative $d(\Delta/T_K)/d\epsilon_0$, evaluated at $\epsilon_0 = \epsilon_{\max}^{\pm}$. It yields

$$\Delta\epsilon \sim \frac{\Gamma U}{\pi|\epsilon_{\max}^{\pm} + U/2|}. \quad (57)$$

Finally, when $\Delta > \Gamma$, the magnetization exceeds 1/4 throughout the local-moment regime. The resonance condition $M = 1/4$ is met only as charge fluctuations become strong, namely, for either $\epsilon_0 \approx 0$ or $\epsilon_0 \approx -U$. The

resonance width $\Delta\epsilon$ evolves continuously in this limit to the standard result for the Coulomb-blockade resonances, $\Delta\epsilon \sim \Gamma$.

Up until now the energy difference Δ was kept constant while tuning the average level position ϵ_0. This protocol, which precludes population inversion as a function of the control parameter, best suits a single-dot realization of our model, where both levels can be uniformly tuned using a single gate voltage. In the alternative realization of two spatially separated quantum dots, each controlled by its own separate gate voltage, one could fix the energy level $\epsilon_1 = \epsilon_0 + \Delta/2$ and sweep the other level, $\epsilon_2 = \epsilon_0 - \Delta/2$. This setup amounts to changing the field h externally, and is thus well suited for probing the magnetic response of our effective impurity.

An example for such a protocol is presented in Fig. 5, where ϵ_1 is held fixed at $\epsilon_1 = -U/2$. As ϵ_2 is swept through ϵ_1, a population inversion takes place, leading to a narrow dip in the conductance. The width of the conductance dip is exponentially small due to Kondo correlations. Indeed, one can estimate the dip width, $\Delta\epsilon_{\mathrm{dip}}$, from the condition $|\epsilon_1 - \epsilon_2| = T_K|_{\epsilon_2=\epsilon_1}$, which yields

$$\Delta\epsilon_{\mathrm{dip}} \sim \sqrt{U\Gamma}\exp\left(-\frac{\pi U}{8\Gamma}\right). \qquad (58)$$

B. Anisotropic couplings, $\Gamma_\uparrow \neq \Gamma_\downarrow$

As demonstrated at length in Sec. V A, the occurrence of population inversion and a transmission zero for $\Gamma_\uparrow = \Gamma_\downarrow$ requires an external modulation of the effective magnetic field. Any practical device will inevitably involve, though, some tunnelling anisotropy, $V_\uparrow \neq V_\downarrow$. The latter provides a different route for changing the effective magnetic field, through the anisotropy-induced terms in Eq. (30). Implementing the same protocol as in Sec. V A 2 (that is, uniformly sweeping the average level position ϵ_0 while keeping the difference Δ constant) would now generically result both in population inversion and a transmission zero due to the rapid change in direction of the total field $\vec{h}_{\mathrm{tot}}$. As emphasized in Sec. IV B 2, the two phenomena will generally occur at different gate voltages when $V_\uparrow \neq V_\downarrow$.

1. Degenerate levels, $\Delta = b = 0$

We begin our discussion with the case where $\Delta = b = 0$, which was extensively studied in Ref.11. It corresponds to a particular limit of the parallel-field configuration where $h = 0$. In the parallel-field configuration, the conductance G and occupancies $\langle n_i \rangle$ take the exact forms specified in Eqs. (44) and (54), respectively. These expressions reduce in the Kondo regime to Eqs. (40) and (53), with θ_h either equal to zero or π, depending on the sign of h^z_{tot}.
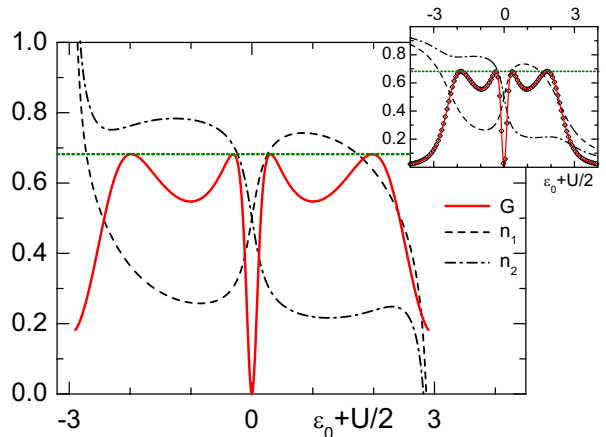

FIG. 6: The occupation numbers $\langle n_i \rangle$ and conductance G [in units of $e^2/(2\pi\hbar)$] as a function of $\epsilon_0 + U/2$ [in units of $\Gamma_{\mathrm{tot}} = (\Gamma_\uparrow + \Gamma_\downarrow)$], calculated from Eqs. (40) and (53) based on the mapping onto the Kondo model. The model parameters are identical to those used in Fig. 2 of Ref.11, lower left panel: $h = \varphi = 0$, $U/\Gamma_{\mathrm{tot}} = 6$, $\Gamma_\uparrow/\Gamma_{\mathrm{tot}} = 0.62415$ and $T = 0$. The explicit tunnelling matrix elements are detailed in Eq. (59), corresponding to the rotation angles $\theta_l = 2.1698$ and $\theta_d = -0.63434$ (measured in radians). The angle θ_h equals zero. The inset shows functional renormalization-group (fRG) data as defined in Ref.11, corrected for the renormalization of the two-particle vertex.[12,37] The small symbols in the inset show the conductance as calculated from the fRG occupation numbers using our Eq. (55). The horizontal dotted lines in each plot mark the maximal conductance predicted by Eq. (55), $(e^2/2\pi\hbar)\sin^2\theta_l$.

Figure 6 shows the occupation numbers and the conductance obtained from Eqs. (40) and (53), for $\Delta = b = 0$ and the particular tunnelling matrix used in Fig. 2 of Ref.11:

$$\hat{A} = A_0 \begin{bmatrix} \sqrt{0.27} & \sqrt{0.16} \\ \sqrt{0.33} & -\sqrt{0.24} \end{bmatrix}. \qquad (59)$$

Here A_0 equals $\sqrt{\Gamma_{\mathrm{tot}}/(\pi\rho)}$, with $\Gamma_{\mathrm{tot}} = \Gamma_\uparrow + \Gamma_\downarrow$ being the combined hybridization width. The Coulomb repulsion U is set equal to $6\Gamma_{\mathrm{tot}}$, matching the value used in the lower left panel of Fig. 2 in Ref.11. For comparison, the corresponding functional renormalization-group (fRG) data of Ref.11 is shown in the inset, after correcting for the renormalization of the two-particle vertex.[12,37] The accuracy of the fRG has been established[11,12] up to moderate values of $U/\Gamma_{\mathrm{tot}} \sim 10$ through a comparison with Wilson's numerical renormalization-group method.[38] Including the renormalization of the two-particle vertex further improves the fRG data as compared to that of Ref.11, as reflected, e.g., in the improved position of the outer pair of conductance resonances.

The agreement between our analytical approach and the fRG is evidently very good in the local-moment regime, despite the rather moderate value of U/Γ_{tot} used. Noticeable deviations develop in $\langle n_i \rangle$ only as the mixed-valent regime is approached (for $\epsilon_0 \gtrsim -\Gamma_{\mathrm{tot}}$ or

$\epsilon + U \lesssim \Gamma_{\text{tot}}$), where our approximations naturally break down. In particular, our approach accurately describes the phase lapse at $\epsilon_0 = -U/2$, the inversion of population at the same gate voltage, the location and height of the correlation-induced resonances, and even the location and height of the outer pair of conductance resonances. Most importantly, our approach provides a coherent analytical picture for the physics underlying these various features, as elaborated below.

Before proceeding to elucidate the underlying physics, we briefly quote the relevant parameters that appear in the conversion to the generalized Anderson model of Eq. (7). Using the prescriptions detailed in Appendix A, the hybridization widths $\Gamma_\sigma = \pi \rho V_\sigma^2$ come out to be

$$\Gamma_\uparrow / \Gamma_{\text{tot}} = 0.62415 \,, \quad \Gamma_\downarrow / \Gamma_{\text{tot}} = 0.36585 \,, \quad (60)$$

while the angles of rotation equal

$$\theta_l = 2.1698 \,, \quad \theta_d = -0.63434 \,. \quad (61)$$

Here θ_l and θ_d are quoted in radians. Using the exact conductance formula of Eq. (44), G is predicted to be bounded by the maximal conductance

$$G_{\text{max}} = \frac{e^2}{2\pi\hbar} \sin^2 \theta_l = 0.68210 \frac{e^2}{2\pi\hbar} \,, \quad (62)$$

obtained whenever the magnetization $M = \langle n_\uparrow - n_\downarrow \rangle / 2$ is equal to $\pm 1/4$. The heights of the fRG resonances are in excellent agreement with Eq. (62). Indeed, as demonstrated in the inset to Fig. 6, the fRG occupancies and conductance comply to within extreme precision with the exact relation of Eq. (55). As for the functional form of the Kondo temperature T_K, its exponential dependence on ϵ_0 is very accurately described by Eq. (29). In the absence of a precise expression for the pre-exponential factor when $\Gamma_\uparrow \neq \Gamma_\downarrow$, we employ the expression

$$T_K = (\sqrt{U\Gamma_{\text{tot}}}/\pi) \exp\left[\frac{\pi\epsilon_0(U+\epsilon_0)}{2U(\Gamma_\uparrow - \Gamma_\downarrow)} \ln \frac{\Gamma_\uparrow}{\Gamma_\downarrow}\right] \,, \quad (63)$$

which properly reduces to Eq. (B4) (up to the small Γ^2 correction in the exponent) when $\Gamma_\uparrow = \Gamma_\downarrow = \Gamma$.

The occupancies and conductance of Fig. 6 can be fully understood from our general discussion in Sec. III. Both quantities follow from the magnetization M, which vanishes at $\epsilon_0 = -U/2$ due to particle-hole symmetry. As a consequence, the two levels are equally populated at $\epsilon_0 = -U/2$ and the conductance vanishes [see Eqs. (44) and (54)]. Thus, there is a simultaneous phase lapse and an inversion of population at $\epsilon_0 = -U/2$, which is a feature generic to $\Delta = b = 0$ and arbitrary $\hat{A}$. As soon as the gate voltage is removed from $-U/2$, i.e., $\epsilon_0 = -U/2 + \delta\epsilon$ with $\delta\epsilon \neq 0$, a finite magnetization develops due to the appearance of a finite effective magnetic field $\vec{h}_{\text{tot}} = h_{\text{tot}}^z \hat{z}$ with

$$h_{\text{tot}}^z \approx \frac{\Gamma_\uparrow - \Gamma_\downarrow}{\pi} \ln \frac{1 + 2\delta\epsilon/U}{1 - 2\delta\epsilon/U} \quad (64)$$

[see Eq. (33)]. Note that the sign of h_{tot}^z coincides with that of $\delta\epsilon$, hence M is positive (negative) for $\epsilon_0 > -U/2$ ($\epsilon_0 < -U/2$). Since $\cos \theta_d > 0$ for the model parameters used in Fig. 6, it follows from Eq. (54) that $\langle n_1 \rangle > \langle n_2 \rangle$ ($\langle n_1 \rangle < \langle n_2 \rangle$) for $\epsilon_0 > -U/2$ ($\epsilon_0 < -U/2$), as is indeed found in Fig. 6. Once again, this result is generic to $\Delta = b = 0$, except for the sign of $\cos \theta_d$ which depends on details of the tunnelling matrix $\hat{A}$.

In contrast with the individual occupancies, the conductance G depends solely on the magnitude of M, and is therefore a symmetric function of $\delta\epsilon$. Similar to the rich structure found for $\Gamma_\uparrow = \Gamma_\downarrow$ and $\Delta > 0$ in Fig. 4, the intricate conductance curve in Fig. 6 is the result of the interplay between h_{tot}^z and T_K, and the nonmonotonic dependence of G on $|M|$. The basic physical picture is identical to that in Fig. 4, except for the fact that the effective magnetic field h_{tot}^z is now itself a function of the gate voltage ϵ_0.

As a rule, the magnetization $|M|$ first increases with $|\delta\epsilon|$ due to the rapid increase in h_{tot}^z. It reaches its maximal value M_{max} at some intermediate $|\delta\epsilon|$ before decreasing again as $|\delta\epsilon|$ is further increased. Inevitably $|M|$ becomes small again once $|\delta\epsilon|$ exceeds $U/2$. The shape of the associated conductance curve depends crucially on the magnitude of M_{max}, which monotonically increases as a function of U. When $M_{\text{max}} < 1/4$, the conductance features two symmetric maxima, one on each side of the particle-hole symmetric point. Each of these peaks is analogous to the one found in Fig. 4 for $\Delta < h_c$. Their height steadily grows with increasing U until the unitarity condition $M_{\text{max}} = 1/4$ is met. This latter condition defines the critical repulsion U_c found in Ref.11. For $U > U_c$, the maximal magnetization M_{max} exceeds one quarter. Hence the unitarity condition $M = \pm 1/4$ is met at two pairs of gate voltages, one pair of gate voltages on either side of the particle-hole symmetric point $\epsilon_0 = -U/2$. Each of the single resonances for $U < U_c$ is therefore split in two, with the inner pair of peaks evolving into the correlation-induced resonances of Ref.11. The point of maximal magnetization now shows up as a local minimum of the conductance, similar to the point $\epsilon_0 = -U/2$ in Fig. 4 when $\Delta > h_c$.

For large $U \gg \Gamma_{\text{tot}}$, the magnetization $|M|$ grows rapidly as one departs from $\epsilon_0 = -U/2$, due to the exponential smallness of the Kondo temperature $T_K|_{\epsilon_0 = -U/2}$. The dot remains polarized throughout the local-moment regime, loosing its polarization only as charge fluctuations become strong. In this limit the inner pair of resonances lie exponentially close to $\epsilon_0 = -U/2$ (see below), while the outer pair of resonances approach $|\delta\epsilon| \approx U/2$ (the regime of the conventional Coulomb blockade).

The description of this regime can be made quantitative by estimating the position $\pm\delta\epsilon_{\text{CIR}}$ of the correlation-induced resonances. Since $M \to M_K(h_{\text{tot}}^z/T_K)$ deep in the local-moment regime, and since $\delta\epsilon_{\text{CIR}} \ll \Gamma_{\text{tot}}$ for $\Gamma_{\text{tot}} \ll U$, the correlation-induced resonances are peaked at the two gate voltages where $h_{\text{tot}}^z \approx \pm 2.4 T_K|_{\epsilon_0 = -U/2}$. Expanding Eq. (64) to linear order in $\delta\epsilon_{\text{CIR}}/U \ll 1$ and

using Eq. (63) one finds

$$\delta\epsilon_{\text{CIR}} \approx 0.6\frac{\pi U}{\Gamma_\uparrow - \Gamma_\downarrow}T_K|_{\epsilon_0=-U/2}$$

$$= 0.6\frac{U\sqrt{U\Gamma_{\text{tot}}}}{\Gamma_\uparrow - \Gamma_\downarrow}\exp\left[\frac{-\pi U \ln(\Gamma_\uparrow/\Gamma_\downarrow)}{8(\Gamma_\uparrow - \Gamma_\downarrow)}\right]. \quad (65)$$

Here the pre-exponential factor in the final expression for $\delta\epsilon_{\text{CIR}}$ is of the same accuracy as that in Eq. (63).

We note in passing that the shape of the correlation-induced resonances and the intervening dip can be conveniently parameterized in terms of the peak position $\delta\epsilon_{\text{CIR}}$ and the peak conductance G_{max}. Expanding Eq. (64) to linear order in $\delta\epsilon/U \ll 1$ and using Eq. (44) one obtains

$$G(\delta\epsilon) = G_{\text{max}}\sin^2\left[2\pi M_K\left(\frac{2.4\delta\epsilon}{\delta\epsilon_{\text{CIR}}}\right)\right], \quad (66)$$

where $M_K(h/T_K)$ is the universal magnetization curve of the Kondo model [given explicitly by (B1)]. This parameterization in terms of two easily extractable parameters may prove useful for analyzing future experiments.

It is instructive to compare Eq. (65) for $\delta\epsilon_{\text{CIR}}$ with the fRG results of Ref.11, which tend to overestimate $\delta\epsilon_{\text{CIR}}$. For the special case where $a_{L1} = a_{R1}$ and $a_{L2} = -a_{R2}$, an analytic expression was derived for $\delta\epsilon_{\text{CIR}}$ based on the fRG.[11] The resulting expression, detailed in Eq. (4) of Ref.11, shows an exponential dependence nearly identical to that of Eq. (65), but with an exponent that is smaller in magnitude by a factor of $\pi^2/8 \approx 1.23$.[39] The same numerical factor appears to distinguish the fRG and the numerical renormalization-group data depicted in Fig. 3 of Ref.11, supporting the accuracy of our Eq. (65). It should be emphasized, however, that Fig. 3 of Ref.11 pertains to the tunnelling matrix of Eq. (59) rather than the special case referred to above.

We conclude the discussion of the case where $\Delta = b = 0$ with accurate results on the renormalized dot levels when the dot is tuned to the peaks of the correlation-induced resonances. The renormalized dot levels, $\tilde{\epsilon}_\uparrow$ and $\tilde{\epsilon}_\downarrow$, can be defined through the $T = 0$ retarded dot Green functions at the Fermi energy:

$$G_\sigma(\epsilon = 0) = \frac{1}{-\tilde{\epsilon}_\sigma + i\Gamma_\sigma}. \quad (67)$$

Here, in writing the Green functions of Eq. (67), we have made use of the fact that the imaginary parts of the retarded dot self-energies, $-\Gamma_\sigma$, are unaffected by the Coulomb repulsion U at zero temperature at the Fermi energy. The energies $\tilde{\epsilon}_\sigma$ have the exact representation[21] $\tilde{\epsilon}_\sigma = \Gamma_\sigma \cot \delta_\sigma$ in terms of the associated phase shifts $\delta_\sigma = \pi\langle n_\sigma\rangle$. Since $M = \pm 1/4$ at the peaks of the correlation-induced resonances, this implies that $\delta_\sigma = \pi/2 \pm \sigma\pi/4$, where we have set $n_{\text{tot}} = 1$.[40] Thus, the renormalized dot levels take the form $\tilde{\epsilon}_\sigma = \mp\sigma\Gamma_\sigma$, resulting in

$$\tilde{\epsilon}_\uparrow\tilde{\epsilon}_\downarrow = -\Gamma_\uparrow\Gamma_\downarrow. \quad (68)$$

The relation specified in Eq. (68) was found in Ref.11, for the special case where $a_{L1} = a_{R1}$ and $a_{L2} = -a_{R2}$.[39] Here it is seen to be a generic feature of the correlation-induced resonances for $\Delta = b = 0$ and arbitrary $\hat{A}$.

2. Nondegenerate levels: arbitrary Δ and b

Once $\sqrt{\Delta^2 + b^2} \neq 0$, the conductance and the partial occupancies can have a rather elaborate dependence on the gate voltage ϵ_0. As implied by the general discussion in Sec. III, the underlying physics remains driven by the competing effects of the polarizing field h_{tot} and the Kondo temperature T_K. However, the detailed dependencies on ϵ_0 can be quite involving and not as revealing. For this reason we shall not seek a complete characterization of the conductance G and the partial occupancies $\langle n_i\rangle$ for arbitrary couplings. Rather, we shall focus on the case where no Aharonov-Bohm fluxes are present and ask two basic questions: (i) under what circumstances is the phenomenon of a phase lapse generic? (ii) under what circumstances is a population inversion generic?

When $\varphi_L = \varphi_R = 0$, the conductance and the partial occupancies are given by Eqs. (40) and (53), respectively. Focusing on G and on $\langle n_1 - n_2\rangle$, these quantities share a common form, with factorized contributions of the magnetization M_K and the rotation angles. The factors containing $M_K(h_{\text{tot}}/T_K)$ never vanish when $h\sin\theta \neq 0$, since h_{tot} always remains positive. This distinguishes the generic case from the parallel-field configuration considered above, where phase lapses and population inversions are synonymous with $M = 0$. Instead, the conditions for phase lapses and population inversions to occur become distinct once $h\sin\theta \neq 0$, originating from the independent factors where the rotation angles appear. For a phase lapse to develop, the combined angle $\theta_l + s_R\theta_h$ must equal an integer multiple of π. By contrast, the inversion of population requires that $\theta_d + s_\theta\theta_h = \pi/2 \mod \pi$. Here the dependence on the gate voltage ϵ_0 enters solely through the angle θ_h, which specifies the orientation of the effective magnetic field $\vec{h}_{\text{tot}}$ [see Eq. (33)]. Since the rotation angles θ_l and θ_d are generally unrelated, this implies that the two phenomena will typically occur, if at all, at different gate voltages.

For phase lapses and population inversions to be ubiquitous, the angle θ_h must change considerably as ϵ_0 is swept across the Coulomb-blockade valley. In other words, the effective magnetic field $\vec{h}_{\text{tot}}$ must nearly flip its orientation in going from $\epsilon_0 \approx 0$ to $\epsilon_0 \approx -U$. Since the x component of the field is held fixed at $h_{\text{tot}}^x = h\sin\theta > 0$, this means that its z component must vary from $h_{\text{tot}}^z \gg h_{\text{tot}}^x$ to $-h_{\text{tot}}^z \gg h_{\text{tot}}^x$ as a function of ϵ_0. When this requirement is met, then both a phase lapse and an inversion of population are essentially guaranteed to occur. Since h_{tot}^z crudely changes by

$$\Delta h_{\text{tot}}^z \sim \frac{2}{\pi}(\Gamma_\uparrow - \Gamma_\downarrow)\ln(U/\Gamma_{\text{tot}}) \quad (69)$$

as ϵ_0 is swept across the Coulomb-blockade valley, this leaves us with the criterion

$$(\Gamma_\uparrow - \Gamma_\downarrow) \ln(U/\Gamma_{\text{tot}}) \gg \sqrt{\Delta^2 + b^2}. \qquad (70)$$

Conversely, if $\sqrt{\Delta^2 + b^2} \gg (\Gamma_\uparrow - \Gamma_\downarrow) \ln(U/\Gamma_{\text{tot}})$, then neither a phase lapse nor an inversion of population will occur unless parameters are fine tuned. Thus, the larger U is, the more ubiquitous phase lapses become.[8,11]

Although the logarithm $\ln(U/\Gamma_{\text{tot}})$ can be made quite large, in reality we expect it to be a moderate factor of order one. Similarly, the difference in widths $\Gamma_\uparrow - \Gamma_\downarrow$ is generally expected to be of comparable magnitude to $\Gamma_\uparrow$. Under these circumstances, the criterion specified in Eq. (70) reduces to $\Gamma_\uparrow \gg \sqrt{\Delta^2 + b^2}$. Namely, phase lapses and population inversions are generic as long as the (maximal) tunnelling rate exceeds the level spacing. This conclusion is in line with that of a recent numerical study of multi-level quantum dots.[41]

Finally, we address the effect of nonzero $h = \sqrt{\Delta^2 + b^2}$ on the correlation-induced resonances. When $h \gg \Gamma_\uparrow \ln(U/\Gamma_{\text{tot}})$, the effective magnetic field $h_{\text{tot}} \approx h$ is large throughout the local-moment regime, always exceeding $\Gamma_\uparrow$ and $\Gamma_\downarrow$. Consequently, the dot is nearly fully polarized for all $-U < \epsilon_0 < 0$, and the correlation-induced resonances are washed out. Again, for practical values of U/Γ_{tot} this regime can equally be characterized by $h \gg \Gamma_\uparrow$.[11]

The picture for $\Gamma_\uparrow \ln(U/\Gamma_{\text{tot}}) \gg h$ is far more elaborate. When $T_K|_{\epsilon_0=-U/2} \gg h$, the magnetic field is uniformly small, and no significant modifications show up as compared with the case where $h = 0$. This leaves us with the regime $T_K|_{\epsilon_0=-U/2} \ll h \ll \Gamma_\uparrow$, where various behaviors can occur. Rather than presenting an exhaustive discussion of this limit, we settle with identifying certain generic features that apply when both components $|h \cos\theta|$ and $h \sin\theta$ exceed $T_K|_{\epsilon_0=-U/2}$. To begin with, whatever remnants of the correlation-induced resonances that are left, these are shifted away from the middle of the Coulomb-blockade valley in the direction where $|h_{\text{tot}}^z|$ acquires its minimal value. Consequently, h_{tot} and T_K no longer obtain their minimal values at the same gate voltage ϵ_0. This has the effect of generating highly asymmetric structures in place of the two symmetric resonances that are found for $h = 0$. The heights of these features are governed by the "geometric" factors $\sin^2(\theta_l + s_R\theta_h)$ at the corresponding gate voltages. Their widths are controlled by the underlying Kondo temperatures, which can differ substantially in magnitude. Since the entire structure is shifted away from the middle of the Coulomb-blockade valley where T_K is minimal, all features are substantially broadened as compared with the correlation-induced resonances for $h = 0$. Indeed, similar tendencies are seen in Fig. 5 of Ref.11, even though the model parameters used in this figure lie on the borderline between the mixed-valent and the local-moment regimes.

VI. CONCLUDING REMARKS

We have presented a comprehensive investigation of the general two-level model for quantum-dot devices. A proper choice of the quantum-mechanical representation of the dot and the lead degrees of freedom reveals an exact mapping onto a generalized Anderson model. In the local-moment regime, the latter Hamiltonian is reduced to an anisotropic Kondo model with a tilted effective magnetic field. As the anisotropic Kondo model flows to the isotropic strong-coupling fixed point, this enables a unified description of all coupling regimes of the original model in terms of the universal magnetization curve of the conventional isotropic Kondo model, for which exact results are available. Various phenomena, such as phase lapses in the transmission phase,[7,8] charge oscillations,[9,10] and correlation-induced resonances[11,12] in the conductance, can thus be accurately and coherently described within a single physical framework.

The enormous reduction in the number of parameters in the system was made possible by the key observation that a general, possibly non-Hermitian tunnelling matrix $\hat{A}$ can always be diagonalized with the help of two simultaneous unitary transformations, one pertaining the dot degrees of freedom, and the other applied to the lead electrons. This transformation, known as the singular-value decomposition, should have applications in other physical problems involving tunnelling or transfer matrices without any special underlying symmetries.

As the two-level model for transport is quite general, it can potentially be realized in many different ways. As already noted in the main text, the model can be used to describe either a single two-level quantum dot or a double quantum dot where each dot harbors only a single level. Such realizations require that the spin degeneracy of the electrons will be lifted by an external magnetic field. Alternative realizations may directly involve the electron spin. For example, consider a single spinful level coupled to two ferromagnetic leads with *non-collinear* magnetizations. Written in a basis with a particular *ad hoc* local spin quantization axis, the Hamiltonian of such a system takes the general form of Eq. (1), after properly combining the electronic degrees of freedom in both leads. As is evident from our discussion, the local spin will therefore experience an effective magnetic field that is not aligned with either of the two magnetizations of the leads. This should be contrasted with the simpler configurations of parallel and antiparallel magnetizations, as considered, e.g., in Refs.17,25 and 27.

Another appealing system for the experimental observation of the subtle correlation effects discussed in the present paper is a carbon nanotube-based quantum dot. In such a device both charging energy and single-particle level spacing can be sufficiently large[42] to provide a set of well-separated discrete electron states. Applying external magnetic field either perpendicular[43] or/and parallel[44] to the nanotube gives great flexibility in tuning the energy level structure, and thus turns the system into a

valuable testground for probing the Kondo physics addressed in this study.

Throughout this paper we confined ourselves to spinless electrons, assuming that spin degeneracy has been lifted by an external magnetic field. Our mapping can equally be applied to spinful electrons by implementing an identical singular-value decomposition to each of the two spin orientations separately (assuming the tunnelling term is diagonal in and independent of the spin orientation). Indeed, there has been considerable interest lately in spinful variants of the Hamiltonian of Eq. (1), whether in connection with lateral quantum dots,[45,46] capacitively coupled quantum dots,[47–49] or carbon nanotube devices.[50] Among the various phenomena that have been discussed in these contexts, let us mention SU(4) variants of the Kondo effect,[47,48,50] and singlet-triplet transitions with two-stage screening on the triplet side.[45,46]

Some of the effects that have been predicted for the spinful case were indeed observed in lateral semiconductor quantum dots[51,52] and in carbon nanotube quantum dots.[44] Still, there remains a distinct gap between the idealized models that have been employed, in which simplified symmetries are often imposed on the tunnelling term, and the actual experimental systems that obviously lack these symmetries. Our mapping should provide a much needed bridge between the idealized models and the actual experimental systems. Similar to the present study, one may expect a single unified description encompassing all coupling regimes in terms of just a few basic low-energy scales. This may provide valuable guidance for analyzing future experiments on such devices.

Acknowledgments

APPENDIX A: MAPPING PARAMETERS

In this Appendix we give the details of the mapping of the original Hamiltonian, Eq. (1), onto the generalized Anderson Hamiltonian of Eq. (7).

The first step is the diagonalization of the matrix $\hat{A}$, Eq. (6), which describes the coupling between the dot and the leads in the original model. Since $\hat{A}$ is generally complex and of no particular symmetry, it cannot be diagonalized by a single similarity transformation. Rather,

two (generally different) unitary matrices, R_d and R_l, are required to achieve a diagonal form,

$$\begin{bmatrix} V_\uparrow & 0 \\ 0 & V_\downarrow \end{bmatrix} = R_l \, \hat{A} \, R_d^\dagger \,. \qquad (A1)$$

This representation, known as the singular-value decomposition, is a standard routine in numerical packages. Here we provide a fully analytical treatment of the 2×2 case relevant to our discussion. To this end we parametrize the two rotation matrices in the form

$$R_d = e^{i\chi_A} e^{i(\chi_d/2)\tau_z} U(\theta_d, \phi_d), \qquad (A2)$$
$$R_l = e^{i(\chi_l/2)\tau_z} U(\theta_l, \phi_l), \qquad (A3)$$

where

$$U(\theta, \phi) \equiv \begin{bmatrix} \cos(\theta/2) & e^{-i\phi}\sin(\theta/2) \\ -e^{i\phi}\sin(\theta/2) & \cos(\theta/2) \end{bmatrix} \qquad (A4)$$

describes a rotation by angle θ about the axis $-\sin(\phi)\,\hat{x} + \cos(\phi)\,\hat{y}$.

The various parameters that enter Eqs. (A2) and (A3) have simple geometrical interpretations. The two sets of angles, (θ_d, ϕ_d) and (θ_l, ϕ_l), are the longitudinal and the azimuthal angles of the vectors pointing along the direction of the z axis which defines the corresponding spin variables in Eq. (7), see Fig. 7. The three angles χ_A, χ_d, and χ_l correspond to the choice of the phases of the single-particle operators $d_\sigma^\dagger$ and $c_{k\sigma}^\dagger$. The latter angles are chosen such that the matrix elements of the transformed Hamiltonian, Eq. (7), will be real with $h\sin\theta \geq 0$. Note that R_d and R_l are determined up to a common overall phase. This degree of freedom has been exhausted in Eqs. (A2) and (A3) by requiring that $\det R_l = 1$.

In order to determine the rotation matrices R_d and R_l, one diagonalizes the hermitian matrices $\hat{A}\hat{A}^\dagger$ and $\hat{A}^\dagger\hat{A}$, whose eigenvalues are evidently real and equal to $|V_\sigma|^2$. This calculation determines the matrices $U(\theta_d, \phi_d)$ and $U(\theta_l, \phi_l)$, and yields the values of $|V_\sigma|$. Indeed, using Eqs. (A1), (A2), and (A3), one obtains

$$\begin{bmatrix} |V_\uparrow|^2 & 0 \\ 0 & |V_\downarrow|^2 \end{bmatrix} = U(\theta_l, \phi_l)\,\hat{A}\hat{A}^\dagger\,U^\dagger(\theta_l, \phi_l)$$
$$= U(\theta_d, \phi_d)\,\hat{A}^\dagger\hat{A}\,U^\dagger(\theta_d, \phi_d). \quad (A5)$$

Assuming $|V_\uparrow| > |V_\downarrow|$ (the case where $|V_\uparrow| = |V_\downarrow|$ is treated separately in Sec. A 2), these two equations give

$$|V_\sigma|^2 = X \pm Y, \qquad (A6)$$

$$\theta_{d/l} = 2\arctan\sqrt{\frac{Y - Z_{d/l}}{Y + Z_{d/l}}}, \qquad (A7)$$

$$\phi_d = \arctan\left(\frac{a_{L1}a_{L2} - a_{R1}a_{R2}}{a_{L1}a_{L2} + a_{R1}a_{R2}}\tan\frac{\varphi}{2}\right) + \pi\eta_d, \quad (A8)$$
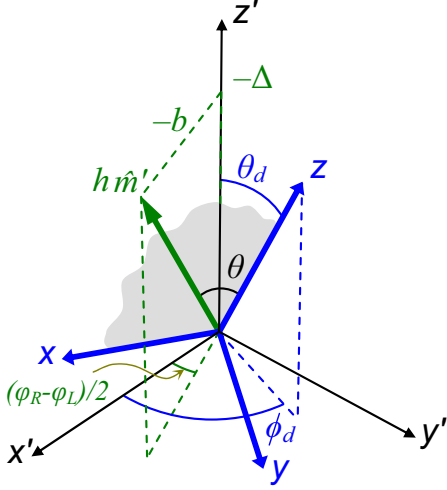
FIG. 7: The original dot degrees of freedom, $d_1^\dagger$ and $d_2^\dagger$, define a pseudo-spin-$\frac{1}{2}$ representation with the axes x', y', and z'. The level indices 1 and 2 are identified in this representation with $\pm\frac{1}{2}$ spin projections on the z' axis. The energy splitting Δ and the hopping b combine to define the magnetic-field vector $h\hat{m}'$. The unitary matrix R_d takes the spin to a new coordinate system whose axes are labelled with x, y, and z. The new "spin" labels $\sigma = \uparrow$ and $\sigma = \downarrow$ represent $\pm\frac{1}{2}$ spin projections on the new z axis, whose direction is defined by the longitudinal and the azimuthal angles θ_d and ϕ_d. The new x axis lies in the plane of vectors $\hat{z}$ and $h\hat{m}'$. A similar picture applies to the conduction-electron degrees of freedom, where the lead index $\alpha = L, R$ plays the same role as the original level index $i = 1, 2$.

$$\phi_l = \arctan\left(\frac{a_{L2}a_{R2} - a_{L1}a_{R1}}{a_{L2}a_{R2} + a_{L1}a_{R1}}\tan\frac{\varphi}{2}\right) + \pi\,\eta_l\,, \quad \text{(A9)}$$

where

$$X = \frac{1}{2}\sum_{\alpha i} a_{\alpha i}^2\,, \tag{A10}$$

$$Y = \sqrt{X^2 - |\det\hat{A}|^2}\,, \tag{A11}$$

$$Z_d = \frac{1}{2}\sum_{\alpha = L, R}(a_{\alpha 1}^2 - a_{\alpha 2}^2)\,, \tag{A12}$$

$$Z_l = \frac{1}{2}\sum_{i=1,2}(a_{Li}^2 - a_{Ri}^2)\,, \tag{A13}$$

and

$$2\,\eta_d = 1 - \text{sgn}\left[(a_{L1}a_{L2} + a_{R1}a_{R2})\cos\frac{\varphi}{2}\right]\,, \text{(A14)}$$

$$2\,\eta_l = 1 - \text{sgn}\left[(a_{L1}a_{R1} + a_{L2}a_{R2})\cos\frac{\varphi}{2}\right]\,. \text{(A15)}$$

The plus sign in Eq. (A6) corresponds to $V_\uparrow$, since the spin-up direction is defined as the one with the larger coupling, $|V_\uparrow|^2 > |V_\downarrow|^2$. The longitudinal angles $0 \leq \theta_d, \theta_l \leq \pi$ are uniquely defined by Eq. (A7), while the quadrants for the azimuthal angles $-\pi/2 < \phi_d, \phi_l \leq 3\pi/2$ must be

chosen according to Eqs. (A14) and (A15). The auxiliary quantities in Eqs. (A10)–(A13) obey the inequalities $X \geq Y$ and $Y \geq |Z_{d/l}|$.

The next step is to determine the angles χ_A, χ_d, and χ_l which come to assure, among other things, that $V_\uparrow > V_\downarrow$ are both real and non-negative. Let us begin with χ_A. When $\det\hat{A} \neq 0$, i.e., for $V_\downarrow > 0$, the angle χ_A is uniquely determined by taking the determinants of both sides of Eq. (A1) and equating their arguments. This yields

$$\chi_A = \frac{1}{2}\arg\det\hat{A}\,. \tag{A16}$$

When $\det\hat{A} = 0$, the angle χ_A can take arbitrary values. This stems from the fact that $V_\downarrow = 0$, and therefore $c_{k\downarrow}$ can be attached an arbitrary phase without affecting the form of Eq. (7). In this case we choose $\chi_A = 0$.

Next we rotate the Hamiltonian term $\hat{\mathcal{E}}_d$, which is the first term of the isolated dot Hamiltonian, Eq. (3). Upon converting to the rotated dot operators $d_\uparrow^\dagger$ and $d_\downarrow^\dagger$, the single-particle term $\hat{\mathcal{E}}_d$ transforms according to

$$\hat{\mathcal{E}}_d \to R_d\,\hat{\mathcal{E}}_d\,R_d^\dagger\,. \tag{A17}$$

Consider first the partial rotation $U(\theta_d, \phi_d)\hat{\mathcal{E}}_d U^\dagger(\theta_d, \phi_d)$ [see Eq. (A2)]. Writing $\hat{\mathcal{E}}_d$ [as defined in Eq. (4)] in the form

$$\hat{\mathcal{E}}_d = \epsilon_0 - \frac{h}{2}\,\hat{m}'\cdot\vec{\tau} \tag{A18}$$

with

$$h = \sqrt{\Delta^2 + b^2} \tag{A19}$$

and

$$\hat{m}' = -\frac{b}{h}\cos\frac{\varphi_L - \varphi_R}{2}\hat{x} + \frac{b}{h}\sin\frac{\varphi_L - \varphi_R}{2}\hat{y} - \frac{\Delta}{h}\hat{z}\,, \text{(A20)}$$

the partial rotation $U(\theta_d, \phi_d)\hat{\mathcal{E}}_d U^\dagger(\theta_d, \phi_d)$ gives

$$\epsilon_0 - \frac{h}{2}\,\hat{m}\cdot\vec{\tau}\,, \tag{A21}$$

where $\hat{m}$ is the unit vector obtained by rotating $\hat{m}'$ by an angle $-\theta_d$ about the axis $-\sin(\phi_d)\,\hat{x} + \cos(\phi_d)\,\hat{y}$. Defining the angle $\theta \in [0, \pi]$ which appears in Eq. (7) according to $\cos\theta = m_z$, it follows from simple geometry that

$$\cos\theta = -\frac{\Delta}{h}\cos\theta_d$$
$$\qquad -\frac{b}{h}\sin\theta_d\cos[\phi_d + (\varphi_L - \varphi_R)/2]\,. \text{(A22)}$$

The full transformation $R_d\hat{\mathcal{E}}_d R_d^\dagger$ corresponds to yet another rotation of $\hat{m}$ by an angle $-\chi_d$ about the z axis. The angle χ_d is chosen such that the projection of $\hat{m}$ onto the xy plane is brought to coincide with the x direction. This fixes χ_d uniquely, unless $h\sin\theta$ happens to be zero (whether because $h = 0$ or because θ is an integer

multiple of π). When $h\sin\theta = 0$, the angle χ_d can take arbitrary values. Physically this stems from the fact that spin-up and spin-down degrees of freedom can be gauged separately within Eq. (7). We choose $\chi_d = 0$ in this case. The explicit expression for χ_d when $h\sin\theta \neq 0$ is quite cumbersome and will not be specified. As for the remaining angle χ_l, it is fixed by the requirement that V_σ will be real and non-negative.

Note that the conditions for the two exactly solvable cases quoted in the main text, Eqs. (10) and (11), are readily derived from our expressions for the eigenvalues V_σ. The first case, Eq. (10), corresponds to $V_\downarrow = 0$, which requires $\det\hat{A} = e^{i\varphi}a_{L1}a_{R2} - a_{L2}a_{R1} = 0$. This immediately leads to Eq. (10). The second solvable case, Eq. (11), corresponds to equal eigenvalues, which implies $Y = 0$ [Eqs. (A6), (A10) and (A11) remain intact for $|V_\uparrow| = |V_\downarrow|$]. By virtue of the inequalities $Y \geq |Z_{d/l}|$, this necessitates that Z_d and Z_l are both zero, which gives rise to the first two conditions in Eq. (11). The remaining condition on the Aharonov-Bohm phase φ follows from substituting the first two conditions into the definition of Y and equating Y to zero.

1. No Aharonov-Bohm fluxes

Of particular interest is the case where no Aharonov-Bohm fluxes are present, $\varphi_L = \varphi_R = 0$. In the absence of a real magnetic field that penetrates the structure, the parameters that appear in the Hamiltonian of Eq. (1) are all real. This greatly simplifies the resulting expressions for the rotation matrices R_d and R_l, as well as for the model parameters that appear in Eq. (7). In this subsection, we provide explicit expression for these quantities in the absence of Aharonov-Bohm fluxes, focusing on the case where $V_\uparrow > V_\downarrow$. The case where $V_\uparrow = V_\downarrow$ is treated separately in Sec. A 2.

As is evident from Eqs. (A8) and (A9), each of the azimuthal angles ϕ_d and ϕ_l is either equal to 0 or π when $\varphi = 0$. (The corresponding y' and y axes are parallel in Fig. 7.) It is therefore advantageous to set both azimuthal angles to zero at the expense of extending the range for the longitudinal angles θ_d and θ_l from $[0,\pi]$ to $(-\pi,\pi]$. Within this convention, Eq. (A7) is replaced with

$$\theta_{d/l} = 2\, s_{d/l} \arctan\sqrt{\frac{Y - Z_{d/l}}{Y + Z_{d/l}}}\,, \qquad (A23)$$

where

$$s_d = \text{sgn}\,(a_{L1}a_{L2} + a_{R1}a_{R2})\,, \qquad (A24)$$
$$s_l = \text{sgn}\,(a_{L1}a_{R1} + a_{L2}a_{R2})\,. \qquad (A25)$$

Similarly, the unit vector $\hat{m}'$ of Eq. (A20) reduces to

$$\hat{m}' = -\frac{b}{h}\hat{x} - \frac{\Delta}{h}\hat{z}\,, \qquad (A26)$$

which results in

$$\hat{m} = \left[-\frac{b}{h}\cos\theta_d + \frac{\Delta}{h}\sin\theta_d\right]\hat{x}$$
$$- \left[\frac{b}{h}\sin\theta_d + \frac{\Delta}{h}\cos\theta_d\right]\hat{z} \qquad (A27)$$

and

$$\theta = \pi - \arccos\left(\frac{b}{h}\sin\theta_d + \frac{\Delta}{h}\cos\theta_d\right). \qquad (A28)$$

Since the rotated unit vector $\hat{m}$ has no y component, the angle χ_d is either equal to 0 or π, depending on the sign of m_x. Assuming $\det\hat{A} \neq 0$ and using Eqs. (A4) and (A16), one can write Eq. (A2) in the form

$$R_d = \left(\text{sgn}\det\hat{A}\right)^{1/2} e^{i\pi(1-s_\theta)\tau_z/4}\, e^{i(\theta_d/2)\tau_y}\,, \qquad (A29)$$

$$s_\theta = \text{sgn}\, m_x = \text{sgn}\,(\Delta\sin\theta_d - b\cos\theta_d)\,. \qquad (A30)$$

Note that the first exponent in Eq. (A29) is equal to 1 for $s_\theta = +1$, and is equal to $e^{i(\pi/2)\tau_z}$ for $s_\theta = -1$. If $\det\hat{A} = 0$ we set $\text{sgn}\det\hat{A} \to 1$ in Eq. (A29), while for $\Delta\sin\theta_d = b\cos\theta_d$ we select $s_\theta = +1$.

Proceeding to the remaining angle χ_l, we note that R_d of Eq. (A29) is either purely real or purely imaginary, depending on whether

$$s_R = s_\theta\,\text{sgn}\det\hat{A} \qquad (A31)$$

is positive or negative. Since both $e^{i(\theta_l/2)\tau_y}$ and $\hat{A}$ are real matrices, then $e^{i(\chi_l/2)\tau_z}$ must also be either purely real or purely imaginary in tandem with R_d in order for the eigenvalues $V_\uparrow$ and $V_\downarrow$ to be real. This consideration dictates that χ_l is an integer multiple of π, with an even (odd) integer for positive (negative) s_R. The end result for R_l is therefore

$$R_l = \eta_R\, e^{i\pi(1-s_R)\tau_z/4}\, e^{i(\theta_l/2)\tau_y}\,, \qquad (A32)$$

Here $\eta_R = \pm 1$ is an overall phase which comes to assure that the eigenvalues $V_\uparrow$ and $V_\downarrow$ are non-negative.

2. Isotropic couplings, $V_\uparrow = V_\downarrow$

Our general construction of the rotation matrices R_d and R_l fails when $|V_\uparrow| = |V_\downarrow| = V$. Equations (A6), (A10) and (A11) remain in tact for $|V_\uparrow| = |V_\downarrow|$, however the angles $\theta_{d/l}$ and $\phi_{d/l}$ are ill-defined in Eqs. (A7)–(A9). This reflects the fact that the matrices $\hat{A}^\dagger\hat{A}$ and $\hat{A}\hat{A}^\dagger$ are both equal to V^2 times the unit matrix, hence any rotation matrix $U(\theta,\phi)$ can be used to "diagonalize" them. There are two alternatives for treating the isotropic case where $|V_\uparrow| = |V_\downarrow|$. The first possibility is to add an infinitesimal matrix $\eta\hat{B}$ that lifts the degeneracy of $|V_\uparrow|$ and $|V_\downarrow|$: $\hat{A} \to \hat{A} + \eta\hat{B}$. Using the general construction outlined above and implementing the limit $\eta \to 0$, a

proper pair of rotation matrices R_d and R_l are obtained. The other alternative is to directly construct the rotation matrices R_d and R_l pertaining to this case. Below we present this second alternative.

A key observation for the isotropic case pertains to the "reduced" matrix

$$\hat{T} = \left(\det \hat{A}\right)^{-1/2} \hat{A}, \tag{A33}$$

which obeys

$$\hat{T}^\dagger \hat{T} = \hat{T}\hat{T}^\dagger = 1, \quad \det \hat{T} = 1. \tag{A34}$$

As a member of the SU(2) group, $\hat{T}$ can be written in the form

$$\hat{T} = U(\theta_T, \phi_T)\, e^{i(\chi_T/2)\tau_z} \tag{A35}$$

with $\theta_T \in [0, \pi]$. Explicitly, the angles θ_T, ϕ_T and χ_T are given by

$$\theta_T = 2 \arccos\left(|\det \hat{A}|^{-1/2}\, |a_{L1}|\right), \tag{A36}$$

$$\chi_T = 2 \arg\left[(\det \hat{A})^{-1/2}\, a_{L1}\right], \tag{A37}$$

and

$$\phi_T = \arg\left[(\det \hat{A})^{-1/2}\, a_{R1}\right] - \pi - \chi_T/2. \tag{A38}$$

Exploiting the fact that $\det \hat{A} = V^2$, the matrix $\hat{A}$ takes then the form

$$\hat{A} = V\, R_l^\dagger R_d = V\, e^{i\chi_A}\, U(\theta_T, \phi_T)\, e^{i(\chi_T/2)\tau_z}, \tag{A39}$$

where the angle χ_A is defined in Eq. (A16).

Equation (A39) determines the matrix product $R_l^\dagger R_d$. Any two rotation matrices that satisfy the right-most equality in Eq. (A39) transform the tunnelling matrix $\hat{A}$ to V times the unit matrix, as is required. The rotation matrix R_d is subject to yet another constraint, which stems from the requirement that $h \sin\theta \geq 0$ in Eq. (7). We note that this constraint as well does not uniquely determine the matrix R_d.[30] Perhaps the simplest choice for R_d is given by

$$R_d = e^{i\chi_A} e^{i(\chi_d/2)\tau_z} \tag{A40}$$

with

$$\chi_d = \frac{1}{2}(\varphi_L - \varphi_R) + \frac{\pi}{2}(1 - \operatorname{sgn} b), \tag{A41}$$

which corresponds to

$$h \cos\theta = -\Delta, \quad h \sin\theta = |b|. \tag{A42}$$

Adopting the choice of Eq. (A40), the rotation matrix R_l takes the form

$$R_l = e^{i\tau_z(\chi_d - \chi_T)/2}\, U(\theta_T, -\phi_T), \tag{A43}$$

where θ_T, ϕ_T, χ_T and χ_d are listed above.

APPENDIX B: BETHE *ANSATZ* FORMULAE

In this appendix we gather for convenience all relevant details of the exact Bethe *ansatz* solutions for the impurity magnetization in the isotropic Kondo and Anderson models in the presence of a finite magnetic field. Extensive reviews of these solutions (including the anisotropic Kondo model) are available in the literature.[19,20,22] Here we only summarize the main results of relevance to our analysis, and briefly comment on the numerical procedure. We confine ourselves to zero temperature, although explicit equations do exist also at finite temperature. Throughout the Appendix we employ units in which $\mu_B g = 1$.

1. Isotropic Kondo model

We begin the presentation with the case of a Kondo impurity, before turning to the more elaborate case of an Anderson impurity. As a function of the magnetic field h, the magnetization of an isotropic spin-$\frac{1}{2}$ Kondo impurity is given by the explicit expression [see, e.g., Eq. (6.23) of Ref.22]

$$M(h) =$$
$$\frac{-i}{4\sqrt{\pi}} \int_{-\infty}^{+\infty} d\omega \frac{(i\omega + 0)^{i\omega/2\pi} \operatorname{sech}\left(\frac{\omega}{2}\right)}{(\omega - i0)\Gamma(\frac{1}{2} + i\frac{\omega}{2\pi})} \left(\frac{h}{2\pi T_K}\right)^{i\omega/\pi}. \tag{B1}$$

Here $\Gamma(z)$ is the complex gamma function. The Kondo temperature, T_K, is defined via the inverse of the spin susceptibility,

$$T_K^{-1} \equiv 2\pi \lim_{h \to 0} M(h)/h. \tag{B2}$$

Evidently, Eq. (B1) is a universal function of the ratio h/T_K, which is denoted in the main text by $M_K(h/T_K)$. It has the asymptotic expansion

$$M(h) \simeq \begin{cases} h/(2\pi T_K), & h \ll T_K, \\ \frac{1}{2} - \frac{1}{4\ln(h/T_H)} - \frac{\ln\ln(h/T_H)}{8\ln^2(h/T_H)}, & h \gg T_K, \end{cases} \tag{B3}$$

where $T_H \equiv \sqrt{\pi/e}\, T_K$.

2. Isotropic Anderson model

In contrast to the Kondo model, there are no closed-form expressions for the total impurity occupancy $n_{\text{tot}} = \langle n_\uparrow + n_\downarrow \rangle$ and magnetization $M = \langle n_\uparrow - n_\downarrow \rangle/2$ in the isotropic Anderson model. The exact Bethe *anstaz* solution of the model provides a set of coupled linear integral equations from which n_{tot} and M can be computed. Below we summarize the equations involved and comment on the numerical procedure that is required for solving these equations. The expressions detailed below apply to

arbitrary ϵ_0, U, h, and Γ at zero temperature. In terms of the Hamiltonian of Eq. (7), we restrict the discussion to $\Gamma = \Gamma_\uparrow = \Gamma_\downarrow$ (isotropic Anderson model) and $\sin\theta = 0$ (parallel-field configuration). The case $\sin\theta \neq 0$ follows straightforwardly from a simple rotation of the dot and the conduction-electron operators about the y axis.

a. Kondo temperature

The most accurate analytical expression that is available for the Kondo temperature of the isotropic Anderson model can be written as

$$T_K = (\sqrt{2U\Gamma}/\pi)\, \exp\!\left[\pi\left(\Gamma^2 + \epsilon_0\, U + \epsilon_0^2\right)/(2\, U\, \Gamma)\right],$$
(B4)

where $\Gamma = \pi\rho|V|^2$. This expression for T_K exactly reproduces Eq. (6.22) of Ref.22 for the symmetric Anderson model, $\epsilon_0 = -U/2$. It also coincides with Eq. (7.11) of Ref.22 for the Kondo temperature of the asymmetric model when $U \gg \Gamma$. Note that the Γ^2 term in the exponent is usually omitted from Eq. (B4) on the basis of it being small. It does in general improve the estimate for T_K.

In the local-moment regime, where Eq. (B4) is valid, the impurity magnetization of the isotropic Anderson model is dominated by the universal magnetization curve of Eq. (B1) up to fields of the order of $h \sim \sqrt{\Gamma U} \gg T_K$ (see, e.g., lower left inset to Fig. 2). At yet larger fields, $h \gg \sqrt{\Gamma U}$, the magnetization of the Anderson model can no longer be described by that of the Kondo model, as charge fluctuations become exceedingly more important than spin flips. Rather, M is well described by perturbation theory in Γ. Importantly, the asymptotic expansion of Eq. (B3) properly matches (to leading order in Γ/U) the perturbative result[9] for M when $h \sim \sqrt{\Gamma U}$. Thus,

the two approaches combine to cover the entire range in h for the Anderson model.

b. Bethe ansatz equations for the occupancy and magnetization

The Bethe *ansatz* solution of the Anderson model features four key quantities, which are the distributions of the charge and spin rapidities, $\tilde{\rho}_{i/h}(k)$ and $\tilde{\sigma}_{i/h}(\lambda)$, respectively, for the impurity (i) and the host (h) band. The total impurity occupancy and magnetization are expressed as integrals over the distributions of the charge and spin rapidities for the impurity:

$$M \;=\; \frac{1}{2}\int_{-\infty}^{B}\tilde{\rho}_i(k)\,dk\,,$$
(B5)

$$n_d \;=\; 1 - \int_{-\infty}^{Q}\tilde{\sigma}_i(\lambda)\,d\lambda\,.$$
(B6)

The upper limits of integration in Eqs. (B5) and (B6) are determined through implicit conditions on the corresponding distribution functions for the host band,

$$\frac{h}{2\pi} \;=\; \int_{-\infty}^{B}\tilde{\rho}_h(k)\,dk\,,$$
(B7)

$$\frac{U + 2\epsilon_0}{2\pi} \;=\; \int_{-\infty}^{Q}\tilde{\sigma}_h(\lambda)\,d\lambda\,.$$
(B8)

As for the distributions of the rapidities for the impurity and the host, these are determined by the same pair of linear integral equations, only with different inhomogeneous parts:

$$\tilde{\rho}(k) + \frac{dg(k)}{dk}\int_{-\infty}^{B} R[g(k) - g(k')]\,\tilde{\rho}(k')\,dk' + \frac{dg(k)}{dk}\int_{-\infty}^{Q} S[g(k) - \lambda]\,\tilde{\sigma}(\lambda)d\lambda = \tilde{\rho}^{(0)}(k)\,,$$
(B9)

$$\tilde{\sigma}(\lambda) - \int_{-\infty}^{Q} R(\lambda - \lambda')\,\tilde{\sigma}(\lambda')\,d\lambda' + \int_{-\infty}^{B} S[\lambda - g(k)]\,\tilde{\rho}(k)\,dk = \tilde{\sigma}^{(0)}(\lambda)\,,$$
(B10)

where[54]

$$S(x) = \frac{1}{2\cosh(\pi x)}\,,$$
(B11)

$$R(x) = \frac{1}{2\pi}\,\mathrm{Re}\!\left[\Psi\!\left(1 + i\frac{x}{2}\right) - \Psi\!\left(\frac{1}{2} + i\frac{x}{2}\right)\right],$$
(B12)

$$g(k) = \frac{(k - \epsilon_0 - U/2)^2}{2U\Gamma}$$
(B13)

(here Ψ is the digamma function). The inhomogeneous

parts in Eqs. (B9) and (B10) are given in turn by

$$\tilde{\rho}_i^{(0)}(k) = \tilde{\Delta}(k) + \frac{dg(k)}{dk}\int_{-\infty}^{+\infty} R[g(k) - g(k')]\,\tilde{\Delta}(k')\,dk'\,,$$
(B14)

$$\tilde{\rho}_h^{(0)}(k) = \frac{1}{2\pi}\left\{1 + \frac{dg(k)}{dk}\int_{-\infty}^{+\infty} R[g(k) - g(k')]\,dk'\right\},$$
(B15)

22

$$\tilde{\sigma}_{\rm i}^{(0)}(\lambda) = \int_{-\infty}^{+\infty} S[\lambda - g(k)]\, \tilde{\Delta}(k)\, dk\,, \qquad (B16)$$

$$\tilde{\sigma}_{\rm h}^{(0)}(\lambda) = \frac{1}{2\pi} \int_{-\infty}^{+\infty} S[\lambda - g(k)]\, dk\,, \qquad (B17)$$

where $\tilde{\Delta}(k)$ is the Lorentzian function

$$\tilde{\Delta}(k) = \frac{1}{\pi}\frac{\Gamma}{\Gamma^2 + (k - \epsilon_0)^2}\,. \qquad (B18)$$

c. Details of the numerical procedure

The main obstacle faced with in a numerical solution of the Bethe *ansatz* equations is the self-consistent determination of the upper integration bounds that appear in Eqs. (B5)–(B10). These are computed iteratively according to the scheme

$$\tilde{\rho}_{\rm h}^{(n-1)},\tilde{\sigma}_{\rm h}^{(n-1)} \Rightarrow B^{(n)},Q^{(n)} \Rightarrow \tilde{\rho}_{\rm h}^{(n)},\tilde{\sigma}_{\rm h}^{(n)}\,. \qquad (B19)$$

Starting with $\tilde{\rho}_{\rm h}^{(n-1)}$ and $\tilde{\sigma}_{\rm h}^{(n-1)}$ as input for the nth iteration, $B^{(n)}$ and $Q^{(n)}$ are extracted from Eqs. (B7) and (B8). Using the updated values for B and Q, $\tilde{\rho}_{\rm h}^{(n)}(k)$ and $\tilde{\sigma}_{\rm h}^{(n)}(\lambda)$ are then obtained from the solution of Eqs. (B9) and (B10). This cycle is repeated until convergence is reached. The first iteration in this procedure is usually initialized with $\tilde{\rho}_{\rm h}^{(0)}(k)$ and $\tilde{\sigma}_{\rm h}^{(0)}(\lambda)$ as input. Standard techniques are then used to ensure rapid convergence of the iterative solution. Typically 15 to 30 iterations are required to achieve a relative accuracy of 10^{-4} for the vector (B,Q).

The core of this cycle is the solution of Eqs. (B9) and (B10). These are solved (for given values of B and Q) by discretizing the integration interval with adaptively chosen $500 \div 1000$ mesh points. Once a self-consistent solution is reached for B, Q, $\tilde{\rho}_{\rm h}(k)$ and $\tilde{\sigma}_{\rm h}(\lambda)$, the corresponding distributions of rapidities for the impurity are obtained from a single solution of Eqs. (B9) and (B10). The impurity occupancy and magnetization are calculated in turn from Eqs. (B5) and (B6).

To test the accuracy of our numerical results, we have extensively checked them against the analytical solution for the zero-field occupancy $n_d(h = 0)$ and the zero-field susceptibility $dM/dh|_{h=0}$. In suitable parameter regimes, we have also compared our results to perturbation theory in both U and Γ. In all cases tested the relative errors in n_d and M were less than 0.05% and 0.5%, respectively. This accuracy can be systematically improved by increasing the number of discretization points used in solving Eqs. (B9) and (B10) for the distributions. Our results were also in full agreement with those reported by Okiji and Kawasaki,[23] except for $M(h)$ where up to 10% differences were found. Considering the extensive set of checks that were applied to our results, it appears that the discrepancy is due to lower numerical accuracy in the solution of Ref. 23.

* Electronic address: slava@latnet.lv

[1] P. W. Anderson, Phys. Rev. **124**, 41 (1961).

[2] T. K. Ng and P. A. Lee, Phys. Rev. Lett. **61**, 1768 (1988).

[3] L. I. Glazman and M. E. Raĭkh, Pis'ma Zh. Eksp. Teor. Fiz. **47**, 378 (1988), [JETP Lett. **47**, 452 (1988)].

[4] D. Goldhaber-Gordon, J. Göres, M. A. Kastner, H. Shtrikman, D. Mahalu, and U. Meirav, Phys. Rev. Lett. **81**, 5225 (1998).

[5] W. G. van der Wiel, S. De Franceschi, T. Fujisawa, J. M. Elzerman, S. Tarucha, and L. P. Kouwenhoven, Science **289**, 2105 (2000).

[6] D. Boese, W. Hofstetter, and H. Schoeller, Phys. Rev. B **64**, 125309 (2001).

[7] A. Silva, Y. Oreg, and Y. Gefen, Phys. Rev. B **66**, 195316 (2002).

[8] D. I. Golosov and Y. Gefen (2006), unpublished, cond-mat/0601342.

[9] J. König and Y. Gefen, Phys. Rev. B **71**, 201308(R) (2005).

[10] M. Sindel, A. Silva, Y. Oreg, and J. von Delft, Phys. Rev. B **72**, 125316 (2005).

[11] V. Meden and F. Marquardt, Phys. Rev. Lett. **96**, 146801 (2006).

[12] C. Karrasch, T. Enss, and V. Meden, Phys. Rev. B **73**, 235337 (2006).

[13] P. G. Silvestrov and Y. Imry, Phys. Rev. Lett. **85**, 2565 (2000).

[14] F. D. M. Haldane, Phys. Rev. Lett. **40**, 416 (1978).

[15] J. R. Schrieffer and P. A. Wolff, Phys. Rev. **149**, 491 (1966).

[16] P. W. Anderson, J. Phys. C **3**, 2436 (1970).

[17] J. Martinek, Y. Utsumi, H. Imamura, J. Barnaś, S. Maekawa, J. König, and G. Schön, Phys. Rev. Lett. **91**, 127203 (2003).

[18] P. W. Anderson, G. Yuval, and D. R. Hamann, Phys. Rev. B **1**, 4464 (1970).

[19] N. Andrei, K. Furuya, and J. H. Lowenstein, Rev. Mod. Phys. **55**, 331 (1983).

[20] A. M. Tsvelick and P. B. Wiegmann, Adv. Phys. **32**, 453 (1983).

[21] D. C. Langreth, Phys. Rev. **150**, 516 (1966).

[22] P. B. Wiegmann and A. M. Tsvelick, J. Phys. C **16**, 2281 (1983).

[23] A. Okiji and N. Kawakami, J. Phys. Soc. Jpn. **51**, 3192 (1982).

[24] Assigning the same density of states, ρ, to both leads does not restrict the generality of our model, since the case of $\rho_L \neq \rho_R$ can be accounted for by an appropriate rescaling of the tunnelling matrix $\hat{A}$.

[25] J. Martinek, M. Sindel, L. Borda, J. Barnaś, J. König, G. Schön, and J. von Delft, Phys. Rev. Lett. **91**, 247202 (2003).

[26] A. N. Pasupathy, R. C. Bialczak, J. Martinek, J. E. Grose, L. A. K. Donev, P. L. McEuen, and D. C. Ralph, Science **306**, 86 (2004).

[27] J. Martinek, M. Sindel, L. Borda, J. Barnaś, R. Bulla, J. König, G. Schön, S. Maekawa, and J. von Delft, Phys. Rev. B **72**, 121302(R) (2005).

[28] For ferromagnetic leads, the conduction-electron density of states, ρ_σ, is spin dependent, which can be converted into spin-dependent tunnelling amplitudes V_σ by appropriate rescaling.

[29] G. H. Golub and C. F. Van Loan, *Matrix Computations* (Johns Hopkins University Press, Baltimore, MD, 1996), pp. 70–71, 3rd ed.

[30] If either det $\hat{A} = 0$, $h \sin\theta = 0$, or $V_\uparrow = V_\downarrow$, then there is an additional degree of freedom in constructing the unitary matrices R_l and R_d. As detailed in Appendix A, when det $\hat{A} = 0$ the angle χ_A can take arbitrary values, while for $h \sin\theta = 0$ the angle χ_d can be arbitrary [see Eqs. (A2) and (A3) for the definitions of these angles]. If $V_\uparrow = V_\downarrow$, then the angle θ can take any value in the range $0 \le \theta \le \pi$.

[31] M. Pustilnik and L. I. Glazman, Phys. Rev. B **64**, 045328 (2001).

[32] The phase φ is ill-defined when any of the coefficients a_{L1}, a_{L2}, a_{R1}, and a_{R2} is zero.

[33] Note that the Friedel-Langreth sum rule was derived for the Anderson impurity model rather than the Kondo model.

[34] The universal function $M_K(h/T_K)$ pertains, strictly speaking, to a global magnetic field that couples simultaneously to the impurity and the conduction electrons with equal g-factors. Here, by contrast, one is dealing with a local magnetic field that couples solely to the impurity. However, in the scaling regime of interest here, the impurity magnetization is the same for a local and a global magnetic field.

[35] Formally, these corrections to the dot charge follow quantitatively from the fact that, when properly transformed under the Schrieffer-Wolff transformation, the local dot operators $d_\sigma^\dagger$ are slightly mixed with the conduction-electron degrees of freedom. Note also that to first order in Γ_α the total charge $n_{\rm tot}$ is independent of basis rotation.

[36] Only small nonmonotonicities in the charging are reported in the nonperturbative numerical renormalization-group calculations of Ref.10 for $\Gamma_\uparrow = \Gamma_\downarrow$. The regime of nearly degenerate levels, which is required for the appearance of the large feature reported here, has not been studied in Ref.10.

[37] The improved fRG data for the inset have been kindly provided to us by V. Meden.

[38] K. G. Wilson, Rev. Mod. Phys. **47**, 773 (1975).

[39] For the special case where $a_{L1} = a_{R1}$ and $a_{L2} = -a_{R2}$, our $\Gamma_\uparrow$ and $\Gamma_\downarrow$ are related to those of Ref.11 though $\Gamma_\uparrow = 2\max\{\Gamma_1^L, \Gamma_2^L\}$ and $\Gamma_\downarrow = 2\min\{\Gamma_1^L, \Gamma_2^L\}$.

[40] Here we have neglected exponentially small corrections of order $\Gamma_{\rm tot}\delta\epsilon_{\rm CIR}/U^2$ to the total dot occupancy. These stem from the fact that ϵ_0 is sightly removed from the middle of the Coulomb-blockade valley, i.e., $\epsilon_0 \to \pm\delta\epsilon_{\rm CIR}$ in Eq. (50).

[41] C. Karrasch, T. Hecht, Y. Oreg, J. von Delft, and V. Meden (2006), unpublished, cond-mat/0609191.

[42] M. R. Buitelaar, A. Bachtold, T. Nussbaumer, M. Iqbal, and C. Schönenberger, Phys. Rev. Lett. **88**, 156801 (2002).

[43] J. Nygård, D. H. Cobden, and P. E. Lindelof, Nature **408**, 342 (2000).

[44] P. Jarillo-Herrero, J. Kong, H. S. J. van der Zant, C. Dekker, L. P. Kouwenhoven, and S. De Franceschi, Nature **434**, 484 (2005).

[45] W. Hofstetter and H. Schoeller, Phys. Rev. Lett. **88**, 016803 (2002).

[46] W. Hofstetter and G. Zaránd, Phys. Rev. B **69**, 235301 (2004).

[47] L. Borda, G. Zaránd, W. Hofstetter, B. I. Halperin, and J. von Delft, Phys. Rev. Lett. **90**, 026602 (2003).

[48] R. López, D. Sánchez, M. Lee, M.-S. Choi, P. Simon, and K. Le Hur, Phys. Rev. B **71**, 115312 (2005).

[49] M. R. Galpin, D. E. Logan, and H. R. Krishnamurthy, J. Phys. C **18**, 6545 (2006).

[50] M.-S. Choi, R. López, and R. Aguado, Phys. Rev. Lett. **95**, 067204 (2005).

[51] W. G. van der Wiel, S. De Franceschi, J. M. Elzerman, S. Tarucha, L. P. Kouwenhoven, J. Motohisa, F. Nakajima, and T. Fukui, Phys. Rev. Lett. **88**, 126803 (2002).

[52] G. Granger, M. A. Kastner, I. Radu, M. P. Hanson, and A. C. Gossard, Phys. Rev. B **72**, 165309 (2005).

[53] P. G. Silvestrov and Y. Imry (2006), unpublished, cond-mat/0609355.

[54] To evaluate $R(x)$, we have performed analytic integration of Eq. (4.35) of Ref.22.

Chapter 7

Results and discussion

The main new results reported in the thesis can be summarized as follows:

✓ Scattering states formalism for adiabatic transport is translated into a convenient Green function form, and applied to a generic single-level (Breit-Wigner) resonance.

✓ The pumped charge quantization in resonant structures is explained in terms of dynamical loading and unloading of quasi-bound states, and a quantitative approximation based on this insight (the resonance approximation for quantum pumping) is proposed.

✓ The resonance approximation is applied to a model of surface acoustic wave driven quasi-1D channels. All main qualitative features of the experimental data are reproduced, and the influence of each of the control parameters is clarified.

✓ A self-consistent equation for the local Green function of a small quantum dot embedded in a general mesoscopic network is derived and solved exactly in several physically relevant limits, including an explicit analytic solution for the asymmetric Anderson model. The solution demonstrates correct physical behavior in a wide parameter range.

✓ The role of self-consistency in the widely used equations-of-motion technique is clarified by calculating different properties of a single level quantum dot with and without the self-consistency condition. Breakdown of the simplified approximation in the the strongly correlated regime is quantified.

✓ A new way of analyzing a generic two-site model with strong inter-site Coulomb repulsion is proposed. The model is mapped exactly onto a generalized Anderson model

using a singular value decomposition of the tunnelling matrix. The low-energy properties of the physically most interesting regime of single total occupancy are described by a further mapping onto an anisotropic Kondo model in a title effective magnetic field.

✓ Based on the mapping to an effective magnetic impurity model, analytical expressions for the population numbers and the conductance of the two-site model are put forward. The results are shown to be extremely accurate in a wide parameter range.

✓ Conditions for the population switching, transmission-phase lapses and correlation-induced resonances in strongly interacting quantum dots are formulated analytically, and explained in numerous examples.

✓ High-accuracy numerical solution to the exact equations for the accumulated charge and magnetization of the standard Anderson model in the presence of an external magnetic field is constructed for the first time. The results are used as a reference to quantify the accuracy of the Schrieffer-Wolff transformation.

These results may have strong implications for a number of active research areas in the field of correlated transport in nanostructure. Bearing in mind that guesses of this kind are necessarily speculative, we expect the following insights to have to strongest impact:

- The results concerning the resonance approximation imply that the notion of "interference-induced quantization", which had been often seen as a contraintuitive quantum phenomenon, can be understood in simple physical terms.

- The in-depth investigation of the equations-of-motion technique has clearly shown that the simple non-self-consistent version of the method fails to describe even the most basic features of the Kondo effect. This has implications for numerous studies that attempt drawing conclusions for non-conventional Kondo physics using this technique.

- All previous studies of the correlated two-level transport had either to assume some degree of fine-tuned symmetry for the dot-lead couplings, or to explore numerically a prohibitively large parameter space. The singular value decomposition technique applied to the tunnelling matrix in Chapter 6 dramatically reduces the number of

parameters, and facilitates identification of universal physics. We expect this transformation to be useful for other models involving tunnelling and transfer matrices.

The convenient calculational framework presented in Chapter 3 together with the physical understanding of the pumping mechanism (Chapter 4) and of the role of inter-site capacitive interactions (Chapter 6) has stimulated new experiments on pumping through double quantum dot devices that are currently underway [70] at the National Physics Laboratory in Teddington, UK, and at PTB Institute in Braunschweig, Germany. Preliminary results in the regime of strong tunnelling coupling between the dots show very good agreement with the models explored in the thesis. Prospects for experimental investigation of the strongly correlated regime (Chapter 6) in a double quantum dot are being investigated.

Bibliography

[1] Y. Imry, *Introduction to mesoscopic physics*, Mesoscopic Physics and Nanotechnology (Oxford University Press, New York, 1997).

[2] Y. Alhassid, *The statistical theory of quantum dots*, Rev. Mod. Phys. **72**, 895 (2000), `cond-mat/0102268`.

[3] H. L. Stormer, *Nobel lecture: The fractional quantum Hall effect*, Rev. Mod. Phys. **71**, 875 (1999).

[4] T. Ando, A. B. Fowler, and F. Stern, *Electronic properties of two-dimensional systems*, Rev. Mod. Phys. **54**, 437 (1982).

[5] E. Abrahams, S. V. Kravchenko, and M. P. Sarachik, *Metallic behavior and related phenomena in two dimensions*, Rev. Mod. Phys. **73**, 251 (2001), `cond-mat/0006055`.

[6] J. A. Folk, S. R. Patel, S. F. Godijn, A. G. Huibers, S. M. Cronenwett, C. M. Marcus, K. Campman, and A. C. Gossard, *Statistics and parametric correlations of Coulomb Blockade peak fluctuations in quantum dots*, Phys. Rev. Lett. **76**, 1699 (1996).

[7] Y. Imry and R. Landauer, *Conductance viewed as transmission*, Rev. Mod. Phys. **71**, S306 (1999).

[8] D. V. Averin and K. K. Likharev, in *Mesoscopic Phenomena in Solids*, edited by B. L. Altshuler, P. A. Lee, and R. A. Webb (Elsevier, Amsterdam, 1991), pp. 173–271.

[9] C. W. J. Beenakker, *Theory of Coulomb-blockade oscillations in the conductance of a quantum dot*, Phys. Rev. B **44**, 1646 (1991).

[10] K. Flensberg, A. A. Odintsov, F. Liefrink, and P. Teunissen, *Towards single-electron metrology*, Int. J. Mod. Phys. B **13**, 2651 (1999), `cond-mat/9908219`.

[11] P. W. Anderson, *Localized magnetic states in metals*, Phys. Rev. **124**, 41 (1961).

[12] F. Zhou, B. Spivak, and B. Altshuler, *Mesoscopic mechanism of adiabatic charge transport*, Phys. Rev. Lett. **82**, 608 (1999), `cond-mat/9809189`.

[13] P. W. Brouwer, *Scattering approach to parametric pumping*, Phys. Rev. B **58**, 10135(R) (1998), `cond-mat/9808347`.

[14] M. Büttiker, H. Thomas, and A. Prêtre, *Current partition in multi-probe conductors in the presence of slowly oscillating external potentials*, Z. Phys. B **94**, 133 (1994).

[15] R. Landauer, *Electrical resistance of disordered one-dimensional lattices*, Philosophical Magazine **21**, 863 (1970).

[16] T. A. Shutenko, I. L. Aleiner, and B. L. Altshuler, *Mesoscopic fluctuations of adiabatic charge pumping in quantum dots*, Phys. Rev. B **61**, 10366 (2000), `cond-mat/9911019`.

[17] O. Entin-Wohlman, A. Aharony, and Y. Levinson, *Adiabatic transport in nanostructures*, Phys. Rev. B **65**, 195411 (2002), `cond-mat/0201073`.

[18] I. L. Aleiner and A. V. Andreev, *Adiabatic charge pumping in almost open dots*, Phys. Rev. Lett. **81**, 1286 (1998), `cond-mat/9805181`.

[19] O. Entin-Wohlman and A. Aharony, *Quantized adiabatic charge pumping and resonant transmission*, Phys. Rev. B **66**, 035329 (2002), `cond-mat/0202289`.

[20] M. Moskalets and M. Büttiker, *Floquet scattering theory of quantum pumps*, Phys. Rev. B **66**, 205320 (2002), `cond-mat/0208356`.

[21] G. Platero and R. Aguado, *Photon-assisted transport in semiconductor nanostructures*, Phys. Rep. **395**, 1 (2004), `cond-mat/0311001`.

[22] M. L. Polianski and P. W. Brouwer, *Pumped current and voltage for an adiabatic quantum pump*, Phys. Rev. B **64**, 075304 (2001), `cond-mat/0102159`.

[23] M. L. Polianski, M. G. Vavilov, and P. W. Brouwer, *Noise through quantum pumps*, Phys. Rev. B **65**, 245314 (2002), `cond-mat/0202241`.

[24] M. Moskalets and M. Büttiker, *Dissipation and noise in adiabatic quantum pumps*, Phys. Rev. B **66**, 035306 (2002), `cond-mat/0201259`.

[25] L. DiCarlo, C. M. Marcus, and J. J. S. Harris, *Photocurrent, rectification, and magnetic field symmetry of induced current through quantum dots*, Phys. Rev. Lett. **91**, 246804 (2003), `cond-mat/0304397`.

[26] M. Moskalets and M. Büttiker, *Magnetic-field symmetry of pump currents of adiabatically driven mesoscopic structures*, Phys. Rev. B **72**, 035324 (2005), `cond-mat/0502106`.

[27] M. Switkes, C. M. Marcus, K. Campman, and A. C. Gossard, *An adiabatic quantum electron pump*, Science **283**, 1905 (1999), `cond-mat/9904238`.

[28] S. K. Watson, R. M. Potok, C. M. Marcus, and V. Umansky, *Experimental realization of a quantum spin pump*, Phys. Rev. Lett. **91**, 258301 (2003), `cond-mat/0302492`.

[29] I. L. Aleiner, P. W. Brouwer, and L. I. Glazman, *Quantum effects in Coulomb blockade*, Physics Reports **358**, 309 (2002), `cond-mat/0103008`.

[30] M. W. Keller, J. M. Martinis, and R. L. Kautz, *Rare errors in a well-characterized electron pump: comparison of experiment and theory*, Phys. Rev. Lett. **80**, 4530 (1998).

[31] L. P. Kouwenhoven, A. T. Johnson, N. C. van der Vaart, C. J. P. M. Harmans, and C. T. Foxon, *Quantized current in a quantum-dot turnstile using oscillating tunnel barriers*, Phys. Rev. Lett. **67**, 1626 (1991).

[32] L. J. Geerligs, V. F. Anderegg, P. A. M. Holweg, J. E. Mooij, H. Pothier, D. Esteve, C. Urbina, and M. H. Devoret, *Frequency-locked turnstile device for single electrons*, Phys. Rev. Lett. **64**, 2691 (1990).

[33] H. Pothier, P. Lafarge, C. Urbina, D. Esteve, and M. H. Devoret, *Single-electron pump based on charging effects*, Europhys. Lett. **17**, 249 (1992).

[34] D. V. Averin and Y. V. Nazarov, *Virtual electron diffusion during quantum tunneling of the electric charge*, Phys. Rev. Lett. **65**, 2446 (1990).

[35] H. D. Jensen and J. M. Martinis, *Accuracy of the electron pump*, Phys. Rev. B **46**, 13407 (1992).

[36] R. L. Kautz, M. W. Keller, and J. M. Martinis, *Leakage and counting errors in a seven-junction electron pump*, Phys. Rev. B. **60**, 8199 (1999), and references there-in.

[37] J. M. Shilton, V. I. Talyanskii, M. Pepper, D. A. Ritchie, J. E. F. Frost, C. J. B. Ford, C. G. Smith, and G. A. C. Jones, *High-frequency single-electron transport in a quasi-one-dimensional GaAs channel induced by surface acoustic waves*, J. Phys. C **8**, L531 (1996).

[38] V. I. Talyanskii, J. M. Shilton, M. Pepper, C. G. Smith, C. J. B. Ford, E. H. Linfield, D. A. Ritchie, and G. A. C. Jones, *Single electron transport in a one-dimensional channel by high-frequency surface acoustic waves*, Phys. Rev. B **56**, 15 180 (1997).

[39] A. Aharony and O. Entin-Wohlman, *Quantized pumped charge due to surface acoustic waves in a one-dimensional channel*, Phys. Rev. B **65**, 241401 (2002), cond-mat/0111053.

[40] D. J. Thouless, *Quantization of particle transport*, Phys. Rev. B **27**, 6083 (1983).

[41] J. E. Avron, A. Elgart, G. M. Graf, and L. Sadun, *Geometry, statistics, and asymptotics of quantum pumps*, Phys. Rev. B **62**, 10618 (2000), cond-mat/0002194.

[42] Y. Makhlin and A. D. Mirlin, *Counting statistics for arbitrary cycles in quantum pumps*, Phys. Rev. Lett. **87**, 276803 (2001), cond-mat/0105414.

[43] Y. Levinson, O. Entin-Wohlman, and P. Wölfle, *Pumping at resonant transmission and transferred charge quantization*, Physica A **302**, 335 (2001), cond-mat/0010494.

[44] P. A. Wolff, *Localized moments in metals*, Phys. Rev. **124**, 1030 (1961).

[45] T. K. Ng and P. A. Lee, *On-site Coulomb repulsion and resonant tunneling*, Phys. Rev. Lett. **61**, 1768 (1988).

[46] L. I. Glazman and M. E. Raĭkh, *Resonant Kondo transparency of a barrier with quasilocal impurity states*, Pis'ma Zh. Eksp. Teor. Fiz. **47**, 378 (1988), [JETP Lett. **47**, 452 (1988)].

[47] Y. Meir, N. S. Wingreen, and P. A. Lee, *Transport through a strongly interacting electron system: Theory of periodic conductance oscillations*, Phys. Rev. Lett. **66**, 3048 (1991).

[48] A. C. Hewson, *The Kondo problem to heavy fermions* (Cambridge University Press, Cambridge, 1993).

[49] B. Coqblin and J. R. Schrieffer, *Exchange interaction in alloys with cerium impurities*, Phys. Rev. **185**, 847 (1969).

[50] J. Friedel, *Some electrical and magnetic properties of metallic solid solutions*, Can. J. Phys. **34**, 1190 (1956).

[51] M. Pustilnik and L. Glazman, *Kondo effect in quantum dots*, J. Phys. C **16**, R513 (2004), `cond-mat/0401517`.

[52] P. Nozières, *A "Fermi-liquid" description of the Kondo problem at low temperatures*, J. Low. Temp. Phys. **17**, 31 (1974).

[53] D. N. Zubarev, *Double-time Green functions in statistical physics*, Usp. Fiz. Nauk **71**, 71 (1960).

[54] A. Theumann, *Self-consistent solution of the Anderson model*, Phys. Rev. **178**, 978 (1969).

[55] J. A. Appelbaum and D. R. Penn, *Localized correlations in narrow conduction bands*, Phys. Rev. **188**, 874 (1969), Phys. Rev. B, **3**, 942 (1971).

[56] C. Lacroix, *Density of states for the Anderson model*, J. Phys. F **11**, 2389 (1981).

[57] A. M. Tsvelick and P. B. Wiegmann, *Exact results in the theory of magnetic alloys*, Adv. Phys. **32**, 453 (1983).

[58] B. Horvatić and V. Zlatić, *Perturbation expansion for the asymmetric Anderson Hamiltonian*, Phys. Stat. Solidi B **99**, 251 (1980).

[59] F. D. M. Haldane, *Theory of the atomic limit of the Anderson model. I. Perturbation expansions re-examined*, J. Phys. C **11**, 5015 (1978).

[60] J. König and Y. Gefen, *Nonmonotonic charge occupation in double dots*, Phys. Rev. B **71**, 201308(R) (2005), `cond-mat/0408691`.

[61] M. Sindel, A. Silva, Y. Oreg, and J. von Delft, *Charge oscillations in quantum dots: Renormalization group and Hartree method calculations*, Phys. Rev. B **72**, 125316 (2005), `cond-mat/0510686`.

[62] J. R. Schrieffer and P. A. Wolff, *Relation between the Anderson and Kondo Hamiltonians*, Phys. Rev. **149**, 491 (1966).

[63] P. W. Anderson, *A poor man's derivation of scaling laws for the Kondo problem*, J. Phys. C **3**, 2436 (1970).

[64] H. R. Krishna-murthy, J. W. Wilkins, and K. G. Wilson, *Renormalization-group approach to the Anderson model of dilute magnetic alloys*, Phys. Rev. B **21**, 1003 (1980).

[65] W. Hofstetter, *Generalized numerical renormalization group for dynamical quantities*, Phys. Rev. Lett. **85**, 1508 (2000), `cond-mat/0004458`.

[66] C. Karrasch, T. Enss, and V. Meden, *A novel approach to transport through correlated quantum dots*, Phys. Rev. B **73**, 235337 (2006), `cond-mat/0603510`.

[67] G. R. Aǐzin, G. Gumbs, and M. Pepper, *Screening of the surface-acoustic-wave potential by a metal gate and the quantization of the acoustoelectric current in a narrow channel*, Phys. Rev. B **58**, 10 589 (1998).

[68] A. M. Robinson and C. H. W. Barnes, *Classical dynamics of electrons in quantized-acoustoelectric-current devices*, Phys. Rev. B **63**, 165418 (2001).

[69] J. Cunningham, V. I. Talyanskii, J. M. Shilton, M. Pepper, M. Y. Simmons, and D. A. Ritchie, *Single-electron acoustic charge transport by two counterpropagating surface acoustic wave beams*, Phys. Rev. B **60**, 4850 (1999).

[70] B. Kästner and J. T. Janssen (2006), private communication.

הממוקמת. התכונה האחרונה היא המיוחד רגישה לטיב התיאור של קורלציות אלקטרוניות מכיוון שסוספטיביליות הספין של אטום אנדרסון נעשית רווייה בטמפרטורות נמוכות עקב תופעת קונדו. הקירוב הקונסיסטנטי של משוואות התנועה נמצא מדויק מאד עבור תכונות הקשורות לדינמיקת המטען (לדוגמא, התלות במתח השער של אכלוס הרמה). לעומת זאת, תיאור תופעת קונדו (הנגרמת עקב סיכוך דינמי של פלוקטואציות הספין) הוא אמין רק באופן איכותי. אנו מראים כי הגרסה הפשטנית הנפוצה של טכניקת משוואות התנועה נכשלת בתיאור קורלציות קונדו אפילו באופן איכותי.

בפרק האחרון של התיזה אנו דנים במודל שתי רמות לנקודה קוונטית הצמודה לשני מובילים. אנו מניחים צימודים כלליים של מנהור בין שתי הרמות למובילים ובין הרמות לבין עצמן (אנו מאפשרים גם שטף מגנטי הגורם לתופעת אהרונוב-בוהם), וכן דחייה קולונית בין שתי הרמות. המקרה המיוחד שבו כל רמה צמודה למוביל שלה, וקיים מנהור בין שתי הרמות, תואם גרסה של המודל הקווזי-חד-ממדי עבור שני אתרים אשר הוצג (ללא אינטראקציות אלקטרוניות) בפרק קודם. אנו מראים כי מודל שתי הרמות ממופה במדויק על מודל אנדרסון המוכלל שבו האלקטרונים רוכשים דרגת חופש של קווזי-ספין, אשר נשמרת בתהליך המנהור אך לא בתוך הנקודה הקוונטית. אנו מתמקדים בתחום בו הנקודה מאוכלסת על ידי אלקטרון בודד, ומראים כי ההמילטוניאן התואם עירורים מעוטי אנרגיה הוא זה של מודל קונדו הלא-איזוטרופי בנוכחות שדה מגנטי מוטה. עבור ערכים מתונים של שדה (מנורמל) זה, הפתרון המשתמש בהנחת בתה של מודל קונדו האיזוטרופי מאפשר לנו להשיג ביטויים מדויקים עבור אכלוס הנקודה, ומתוך כך גם את מקדם ההעברה שלה באפס המוחלט. נוסחאות אלה כוללות בחובן תופעות רבות ושונות, אשר קודם לכן נחשבו בספרות כמייצגות גבולות שונים: תנודות מטען ושינויי אכלוס, קפיצות מופע מקדם ההעברה, ותנודות הנגרמות עקב קורלציות. אנו דנים במספר היבטים של תופעות אלה, ומדגישים את מקורן המשותף.

תקציר

התיזה עוסקת בהיבטים שונים של דינמיקת אלקטרונים במערכות קוונטיות קטנות וקוהרנטיות, תוך שהיא מתמקדת בשאיבה אדיאבטית של אלקטרונים. במיוחד נחקרים התנאים לשאיבה מקוונטטת, ותפקידן של איטראקציות קולון ממוקמות בתובלה דרך רמה אחת או מספר רמות. גוף העבודה מחולק לארבעה פרקים, התואמים את שלושת המאמרים שכבר פורסמו, ואת המאמר הרביעי שהוגש לפרסום.

שינוי מחזורי של פוטנציאל חיצוני הפועל על מערכת אלקטרונים קוהרנטיים גורר חלוקה מחדש של המטען בה (המערכת מחוברת לאמבטי חלקיקים המוחזקים באותו פוטנציאל כימי). תופעה זו נקראת שאיבה קוונטית, והיא נכרת במיוחד כאשר מקדם ההעברה של המערכת הוא בעל תהודה. תחת תנאים מסוימים המספר הממוצע של האלקטרונים הנשאבים אדיאבטית הוא כמעט שלם. אנו מסבירים את אופן הפעולה הנמצא ברקע קוויטוט זה כהעמסה ופריקה של מטענים אלמנטרים לתוך קווזי-רמות קשורות רגעית. תפקיד ההתאבכות הקוונטית בקוויטוט המטען מוגבל ליצירת קווזי-רמות אלו. אנו מראים כי אם המוליכות הלינארית של המערכת נשארת נמוכה במשך רוב המחזור, למעט מספר שיאי תהודה, אזי המטען הכולל העובר במשך מחזור אחד יכול להיות מחושב מתוך סכום תרומות השיאים בנפרד) קירוב התהודה).

אנו חוקרים בפירוט את הפירוט והשלכות של קירוב התהודה במודל קשר-חזק פשוט עבור תובלה הנגרמת עקב צימוד לגלים אקוסטיים של פני השטח בתילים קוונטים חד-ממדיים בליסטיים. ההשפעה של גורמים הניתנים לשליטה בניסיון (עוצמת הגלים, מתח השער, מתח מקור-ספיגה, מהירות ומופע הגלים החוזרים) על מבנה המדרגות של הזרם החשמלי-אקוסטי נלמדת בפרוטרוט. התוצאות מתאימות באופן איכותי לתצפיות הניסיוניות. אולם ההנחה של אלקטרונים חסרי ספין וללא אינטראקציות ביניהם נכשלת בהתאמת סקאלת האנרגיה האופיינית של הבעיה. זו האחרונה יכולה להיות מיוחסת לאנרגית הטעינה של הנקודה הקוונטית הנוצרת באופן דינאמי.

כדי להרחיב את מגוון הכלים המתאימים לחישוב תכונות דינאמיות של מודלים הכוללים אינטראקציות אלקטרוניות, בחנו לעומק את השיטה המבוססת על קטיעת משוואות התנועה. במיוחד התרכזנו בפונקצית גרין החד-חלקיקית של רמה ממוקמת, כאשר אנו מביאים בחשבון את הספין ואת אינטראקצית הדחייה החזקה על הרמה. חקרנו את היררכית המשוואות של פונקצית גרין זו עד לסדר גבוה, תוך כדי קטיעתן באופן קונסיסטנטי. פתרנו במדויק את המשוואות שהתקבלו במספר גבולות. במיוחד מצאנו כי בנקודת הסימטריה בין אלקטרון לחור, השיטה נכשלת עקב קפיצה בחלק הדמיוני של האנרגיה העצמית הנובעת מאינטראקציות. אולם מנקודה זו והלאה השיטה נותנת פתרון פיסיקאלי לפונקצית גרין.

השוויונו את הפתרון שלנו למשוואות התנועה לתוצאות מדויקות המצויות בספרות למודל אנדרסון. הגדלים שחושבו, בגבול בו האינטראקציה הדוחה היא אינסופית, כללו את האכלוס, צפיפות המצבים, וסוספטיביליות ספין על הרמה

TEL AVIV UNIVERSITY

RAYMOND AND BEVERLY SACKLER
FACULTY OF EXACT SCIENCES
SCHOOL OF PHYSICS & ASTRONOMY

אוניברסיטת תל אביב

הפקולטה למדעים מדוייקים
ע"ש ריימונד ובברלי סאקלר
בית הספר לפיזיקה ואסטרונומיה

שאיבה קוונטית במערכות מזוסקופיות

מאת

ויאצ'סלבס קשצ'ייבס

חבור לשם קבלת תואר "דוקטור לפילוסופיה"

עבודה זאת נעשתה בהדרכת
פרופסור אמנון אהרוני ופרופסור אורה אנטין-וולמן

הוגש לסנאט של אוניברסיטת תל-אביב

נובמבר 2006